UPPSALA
UNIVERSITET

Digital Comprehensive Summaries of Uppsala Dissertations
from the Faculty of Science and Technology 556

Neutron Spectroscopy

Instrumentation and Methods for Fusion Plasmas

HENRIK SJÖSTRAND

ACTA
UNIVERSITATIS
UPSALIENSIS
UPPSALA
2008

ISSN 1651-6214
ISBN 978-91-554-7292-4
urn:nbn:se:uu:diva-9296

Dissertation presented at Uppsala University to be publicly examined in Polhemsalen, Ångströmlaboratoriet, Lägerhyddsvägen 1, Uppsala, Friday, October 24, 2008 at 13:15 for the degree of Doctor of Philosophy. The examination will be conducted in English.

Abstract

Sjöstrand, H. 2008. Neutron Spectroscopy. Instrumentation and Methods for Fusion Plasmas. Acta Universitatis Upsaliensis. *Digital Comprehensive Summaries of Uppsala Dissertations from the Faculty of Science and Technology* 556. 74 pp. Uppsala. ISBN 978-91-554-7292-4.

When the heavy hydrogen isotopes deuterium (D) and tritium (T) undergo nuclear fusion large amounts of energy are released. At the Joint European Torus (JET) research is performed on how to harvest this energy. Two of the most important fusion reactions, $d+d \rightarrow {}^3He+n$ (E_n = 2.5 MeV) and $d+t \rightarrow {}^4He+n$ (E_n = 14 MeV), produce neutrons. This thesis investigates how measurements of these neutrons can provide information on the fusion performance.

The Magnetic Proton Recoil (MPR) neutron spectrometer has operated at JET since 1996. The spectrometer was designed to provide measurements on the 14 MeV neutron emission in DT operation, thereby conveying information on the state of the fuel ions. However, a majority of today's fusion experiments are performed with pure D fuel. Under such conditions, the measurements with the MPR were severely hampered due to interfering background. This prompted an upgrade of the instrument. The upgrade, described in this thesis, included a new focal plane detector, a phoswich scintillator array, and new data acquisition electronics, based on transient recorder cards. This combination allows for pulse shape discrimination techniques to be applied and a signal to background of 5/1 has been achieved in measurements of the 2.5-MeV neutrons in D experiments. The upgrade also includes a new control and monitoring system, which enables the monitoring and correction of gain variations in the spectrometer's photo multiplier tubes. Such corrections are vital for obtaining good data quality.

In addition, this thesis describes a new method for determining the total neutron yield and hence the fusion power by using a MPR spectrometer in combination with a neutron emission profile monitor. The system has been operated at JET both during DT and D experiments. It is found that the systematic uncertainties are considerably lower (≈6 %) than for traditional systems. For a dedicated system designed for the next generation fusion experiments, i.e, ITER, uncertainties of 4 % could be attained.

Neutron spectroscopy can also be an important tool for determining the neutron emission from residual tritium in D plasmas. This information is combined with other measurements at JET in order to determine the confinement of the 1 MeV tritons from the $d+d \rightarrow t+p$ reactions.

Keywords: Neutron spectroscopy, plasma diagnostics, fusion power, fusion, plasma heating, MPRu, JET, triton burn-up, ITER, neutron yield, calibration

Henrik Sjöstrand, Department of Physics and Astronomy, Lägerhyddsvägen 1, Box 516,
Uppsala University, SE-751 20 Uppsala, Sweden

© Henrik Sjöstrand 2008

ISSN 1651-6214
ISBN 978-91-554-7292-4
urn:nbn:se:uu:diva-9296 (http://urn.kb.se/resolve?urn=urn:nbn:se:uu:diva-9296)

Till min älskade familj
Anna, Alexandra, Lena och Ulf

List of Papers

This thesis is based on the following papers which are referred to in the text by their Roman numerals.

I **H. Sjöstrand**, L. Giacomelli, E. Andersson Sundén, S. Conroy, G. Ericsson, M. Gatu Johnson, C. Hellesen, A. Hjalmarsson, J. Källne, E. Ronchi, M.Weiszflog, G. Wikström, G. Gorini, M.Tardocchi, A. Murari, G. Kaveney, S. Popovichev, J. Sousa, R.C. Pereira, A. Combo, N. Cruz and JET EFDA contributors
The New MPRu Instrument for Neutron Emission Spectroscopy at JET
Review of Scientific Instruments **77** 10E717 (2006)

II **H. Sjöstrand**, E. Andersson Sundén, S. Conroy, G. Ericsson, M. Gatu Johnson, L. Giacomelli, G. Gorini, C. Hellesen, A. Hjalmarsson, S. Popovichev, E. Ronchi, M. Tardocchi, M. Weiszflog and JET EFDA contributors
Control and Monitoring System of the Upgraded Magnetic Proton Recoil Neutron Spectrometer at JET
EFDA–JET–Preprint (08)07 submitted for publication in
Review of Scientific Instruments (2008)

III E. Andersson Sundén, **H. Sjöstrand**, S. Conroy, G. Ericsson, M. Gatu Johnson, L. Giacomelli, C. Hellesen, A. Hjalmarsson, E. Ronchi, M. Weiszflog, J. Källne, G.Gorini, M. Tardocchi, A. Combo, N. Cruz, A. Batista, R. Pereira, P. Ricardo, J. Sousa, S. Popovichev and JET-EFDA contributors
The thin foil magnetic proton recoil neutron spectrometer MPRu
To be submitted to Nuclear Instrumentation and Methods

IV L. Giacomelli, E. Andersson Sundén, S. Conroy, G. Ericsson, M. Gatu Johnson, C. Hellesen, A. Hjalmarsson, J. Källne, E. Ronchi, **H. Sjöstrand**, M. Weiszflog, G. Gorini, M. Tardocchi, A. Murari, S. Popovichev, J. Sousa, R.C. Pereira, A. Combo, N. Cruz and JET EFDA contributors
Development and Characterization of the Proton Recoil Detector for the MPRu Neutron Spectrometer
Review of Scientific Instruments **77** 10E708 (2006)

V **H. Sjöstrand**, E. Andersson Sundén, L. Bertalot, S. Conroy, G. Ericsson, M. Gatu Johnson, L. Giacomelli, G. Gorini, C. Hellesen, A. Hjalmarsson, J. Källne, S. Popovichev, E. Ronchi, M. Weiszflog, M. Tardocchi and JET EFDA contributors
Fusion Power Measurement using a Combined Neutron Spectrometer-Camera System at JET
EFDA–JET–Preprint (08)02 submitted for publication in Nuclear Instrumentation and Methods (2008)

VI **H. Sjöstrand**, E. Andersson Sundén, S. Conroy, G. Ericsson, M. Gatu Johnson, L. Giacomelli, C. Hellesen, A. Hjalmarsson, J. Källne, E. Ronchi, M. Weiszflog and JET EFDA contributors
Fusion Power Measurement Using a Combined Neutron Spectrometer - Camera System at ITER
Proceedings of the International Workshop on Burning Plasma Diagnostics Varenna Italy CP988 p. 319-322 (2007)

VII **H. Sjöstrand**, G. Gorini, S. Conroy, G. Ericsson, L. Giacomelli, H. Henriksson, A. Hjalmarsson, J. Källne, D. Palma, S. Popovichev, M. Tardocchi, M.Weiszflog and JET EFDA contributors
Triton Burn Up Neutron Emission in JET Low Current Plasmas
Journal of Physics D: Applied Physics **41** 115208 10pp (2008)

All papers are printed with the permission of the copyright holder

Paper I is reprinted with permission from H. Sjöstrand, Review of Scientific Instruments, 77, 10E717 (2006). Copyright 2006 American Institute of Physics

Paper IV is reprinted with permission from L. Giacomelli, Review of Scientific Instruments, 77, 10E708 (2006). Copyright 2006 American Institute of Physics

Paper VI is reprinted with permission from H. Sjöstrand, Proceedings of the International Workshop on Burning Plasma Diagnostics, Varenna, Italy, CP988 p. 319-322 (2007). Copyright 2007 American Institute of Physics

Paper VII is reprinted with permission from H. Sjöstrand, Journal of Physics D: Applied Physics 41 115208 10pp (2008), www.iop.org/journals/jphys,d Copyright 2008 IOP Publishing Ltd

Content

1 Introduction 11
  1.1 Fusion as an energy source 11
  1.2 The Tokamak 13
  1.3 Plasma heating 15
  1.4 Burn Criteria 16

2 Fusion Neutrons 18
  2.1 Neutron flux 18
  2.2 Scattered and direct neutrons 22

3 Plasma Diagnostics 24
  3.1 Calibration and errors 25

4 Neutron diagnostics 27
  4.1 np scattering 28
  4.2 Neutron intensity measurements 28
    4.2.1 Activation system 31
    4.2.2 Fission chambers 31
    4.2.3 Semiconductor detectors 32
  4.3 Neutron spectroscopy 33
    4.3.1 Measurement Criteria 34
    4.3.2 Measurement techniques 36
  4.4 Neutron emission profile measurements – The Neutron Camera ... 38

5 The Magnetic Proton Recoil Neutron Spectrometer 40
  5.1 The background 41
  5.2 The new scintillator array 44
  5.3 Data reduction and background subtraction 45
  5.4 Control and monitoring 48
  5.5 Results and discussion 49

6 MPR -Camera fusion power measurement system 53
  6.1 Results 54
  6.2 Discussion 56

7 Charged fusion product confinement measurements 58
  7.1 TBN model 58

7.2 Experiments and result 59
7.3 Discussion and outlook 60

8 Conclusions 62

9 Summary of papers 63

10 Sammanfattning på svenska 66

11 Acknowledgments 69

References 71

Abbreviations

ADC	Analogue to Digital Converter
CM-system	Center of Mass system
C&M	Control and Monitoring
D	Deuterium
d	deuteron
FC	Fission Chamber
FWHM	Full Width Half Maximum
$I(E_n)$	Neutron Energy spectrum
ICRH	Ion Cyclotron Resonance Heating
ITER	International Thermonuclear Test Reactor
JET	Joint European Torus
LOS	Line Of Sight
MCNP	Monte Carlo N-Particle transport code
MPR	Magnetic Proton Recoil neutron spectrometer
MPRu	MPR upgrade
N	Number of counts
NBI	Neutral Beam Injection
PMT	Photo Multiplier Tuber
PSD	Pulse shape Discrimination
Q	integrated charge
ROI	Region Of Interest
S/B	Signal to Background ratio
T	Tritium
t	triton
TFTR	Tokamak Fusion Test Reactor
TOF	Time Of Flight
TOFOR	TOF neutron spectrometer Optimized for Rate
TBN	Triton Burn-up Neutrons
TRC	Transient Recorder Card
TRIGA	Training, Research, Isotopes, General Atomics
UV-light	Ultra violet light
Y	neuron Yield
YAP	Yttrium Aluminium Pervoskite
ε_{col}	photon collection efficiency
$\psi(E_n,q)$	Spectral response function
$\Psi(R,Z,\varphi)$	Spatial flux response function
$y(R,Z,\varphi)$	neutron emission spatial distribution

1 Introduction

Time is not our friend

Kurt Russell

1.1 Fusion as an energy source

A scientific effort in fusion energy research has been pursued for five decades, with the ultimate aim to deliver clean and safe energy. When fusing light nuclei, the total mass of the nuclei is reduced and a large amount of energy is released as given by Einstein's famous formula $E=mc^2$ [1].

In general, it is fusion of the lightest nuclei that gives the largest mass reduction and hence the largest energy release. Therefore, the hydrogen isotopes, protium, i.e., regular hydrogen (^{1}H or p), deuterium, (^{2}H or d), and tritium, (^{3}H or t) as well as 'light' helium (^{3}He), are suitable candidates for fusion fuel. The fusion power output, P_{fusion}, from a fusion fuel depends both on the fuel density, n_i, the energy release from each reaction, E_{tot}, and the fuel's reactivity:

$$P_{\mathrm{fusion}} = \int_{V_{\mathrm{plasma}}} n_1 \cdot n_2 \langle \sigma v \rangle_{1,2} \cdot E_{\mathrm{tot}} \partial V\,, \qquad (1)$$

where n_1 and n_2 are the densities of the fuel ion species, V_{plasma} is the plasma volume and $\langle \sigma v \rangle$ is the fuel reactivity given by

$$\langle \sigma v \rangle_{1,2} = \int\int f_1(v_1) f_2(v_2) |v_1 - v_2| \sigma(|v_1 - v_2|) \partial^3 v_1 \partial^3 v_2\ ,(2)$$

where v_i is the fuel ions velocity, $\sigma(|v_1\text{-}v_2|)$, is the reaction cross section as a function of the relative ions velocity and $f(v_i)$ is the normalized ion velocity distribution. If only one fuel species is present Equation 1 becomes:

$$P_{\mathrm{fusion}} = \int_{V_{\mathrm{plasma}}} \frac{1}{2} n_1^2 \langle \sigma v \rangle_{1,1} \cdot E_{\mathrm{tot}} \partial V\,. \qquad (3)$$

When investigating different possible fusion reactions, one finds that the reactions listed in Table 1 have sufficiently high reactivity and could therefore be used in fusion experiments.

Table 1. Candidate fusion reactions for fusion energy applications. The total energy release is listed, as well as the energy given to charged and neutral particles, respectively.

#	Reaction	Fusion product energy [MeV]		
		Charged (E_C)	Neutron (E_n)	Total (E_{tot})
1	d + d → t + p	4.0	-	4.0
2	d + d → ^{3}He + n	0.82	2.5	3.3
3	d + ^{3}He → ^{4}He + p	18.4	-	18.4
4	d + t → ^{4}He + n	3.5	14.0	17.6

It is interesting to note that the two branches of the dd-reaction, reactions 1 and 2, have approximately the same branching ratios. Regarding reactions 3 and 4 of Table 1, it can be noted that ^{3}He has a limited natural abundance and is therefore unsuitable as fusion fuel. Tritium is a radioactive isotope with a half life of 12 years and not naturally occurring. It can be produced by neutron capture in deuterium, $n+d \rightarrow t+\gamma$, most commonly done in CANDU reactors [2], which makes it very expensive ($\approx 30 \cdot 10^6$ \$/kg). The dt-reaction is envisaged for the first generation fusion reactors due to its high reactivity (see Figure 1) and the large energy release per reaction (see Table 1). Consequently, a mixture of deuterium and tritium is used in advanced reactor relevant experiments. The tritium for future reactors will be produced through absorption of fusion neutrons in lithium:

$$\mathrm{n} + {}^6\mathrm{Li} \rightarrow \mathrm{t} + \alpha \tag{4}$$

$$\mathrm{n} + {}^7\mathrm{Li} \rightarrow \mathrm{t} + \alpha + \mathrm{n}\,. \tag{5}$$

For the fusion reactions to take place, the two nuclei have to come sufficiently close for the short-range, attractive, nuclear force to act on the nuclei. In order to do so, the nuclei must have sufficient energy to overcome the repulsive Coulomb force. This gives the reactivity a strong positive dependence on the fuel ion temperature as illustrated in Figure 1.

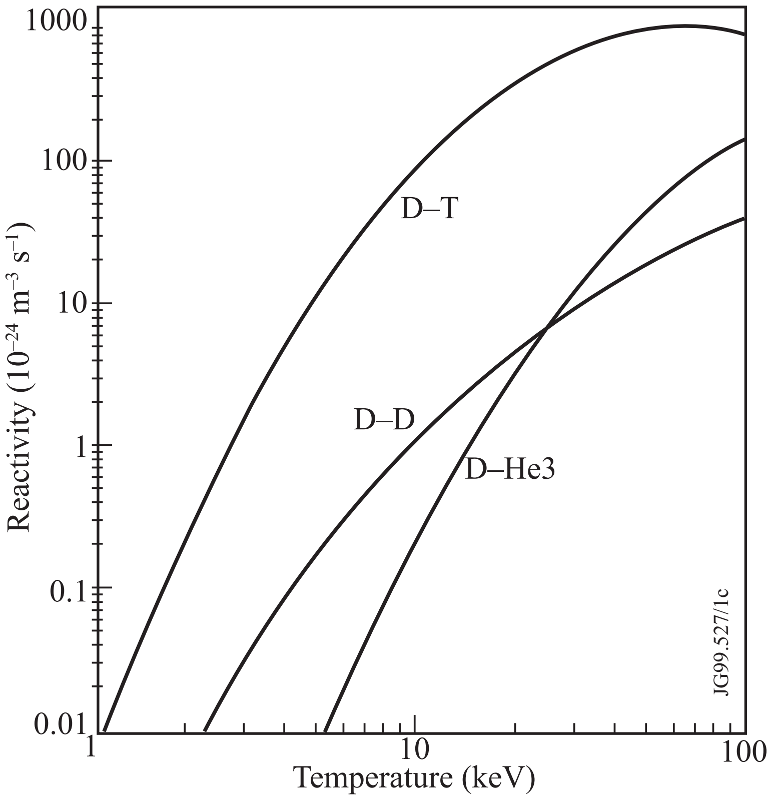

Figure 1. The temperature dependence of the reactivity for different fuel mixtures. Figure courtesy of EFDA-JET.

1.2 The Tokamak

At the temperatures of maximum reactivity (i.e., around 60-80 keV for DT plasmas), the fuel nuclei are stripped of their electrons and the fuel is ionized into a plasma mostly consisting of free charged particles. No material walls can withstand these high temperatures, but in a magnetic field the charged particles are forced to spiral along the magnetic field lines due to the Lorentz force as shown in Figure 2.

By bending the B-field in a torus-shaped configuration end losses can be avoided. One such toroidal configuration is the tokamak[1]. In a tokamak an induced toroidal current produces a poloidal field and together with an externally produced toroidal field a resultant helical field is obtained as shown in Figure 2. It has been found that this field configuration has properties that are beneficial for confining the fuel (plasma) and its energy [3].

---

[1] The tokamak was invented in the 1950s by Soviet physicists. The term is an abbreviation of the Russian word “**to**roidal'naya **ka**mera s **ma**gnitnymi **k**atushkami”, which translates to ”toroidal chamber with magnetic coils”.

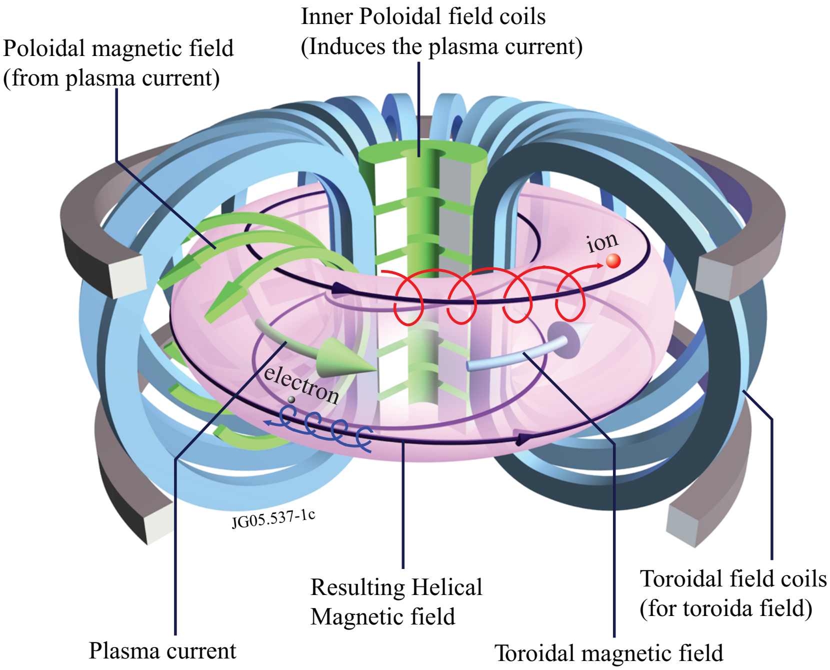
Inner Poloidal field coils
(Induces the plasma current)
Poloidal magnetic field
(from plasma current)
ion
electron
JG05.537-1c
Resulting Helical
Magnetic field
Toroidal field coils
(for toroida field)
Plasma current
Toroidal magnetic field

Figure 2. The torus-shaped tokamak and its magnetic fields and current. The gyro orbits of magnetically confined ions and electrons are shown. The figure is not to scale. Figure courtesy of EFDA-JET.

The first tokamak to explore the use of high levels of tritium was the TFTR situated in Princeton, USA. Today, however, the Joint European Torus, JET outside Oxford, UK, is the only fusion machine that can handle tritium and hence the only fusion device that can produce MW of fusion power. Due to the high price of tritium and its radioactivity, most fusion experiments operate with pure deuterium. One such example is JT-60U, a Japanese tokamak of similar size as JET.

The next step in fusion research is to build an even bigger fusion experiment, ITER, with a predicted fusion power production of 500 MW. This is of the same magnitude as the electrical output from a midsize nuclear reactor like the Swedish Oskarshamn 1 reactor. In high power experiments ITER will operate with DT fuel; however, in an initial phase ITER will also be operated with pure deuterium plasmas. To set the magnitude of the ITER construction in perspective some of the machine parameters of JET and ITER are given in Table 2.

Table 2. *Machine parameters of JET and ITER.*

Parameter	**JET**	**ITER**
Max current (*I*)	5 MA	15 MA
Volume	80 m^3	840m^3
Toroidal B-field (B_T)	4 T	5.3 T
Fusion power	16 MW	500 MW
Discharge length	20 s	400 s
Energy confinement time	1 s	4 s

This thesis is concerned with diagnostics and experiments at such magnetically confined fusion plasmas.

1.3 Plasma heating

There are several ways the plasma can be heated in order to increase the temperature and thereby reach the point of maximum reactivity (see Figure 1).

- Ohmic heating: The plasma current (*I*) in the tokamak heats the plasma through ohmic heating due to the resistivity (*R*) of the plasma. The heating power is proportional to $I^2 \cdot R$, but since *R* is proportional to $1/T^{3/2}$ it is only possible to reach temperatures of a few keV [3].
- Neutral beam injection (NBI) [4]: A particle accelerator outside the tokamak accelerates deuterons or tritons to high energies. The ions are neutralized and can subsequently enter the plasma, where they are again ionized. The ions need to acquire sufficiently high energies to reach the core of the plasma; this is typically ≈ 150 keV for JET [5] and ≈ 1 MeV for ITER [6].
- Ion cyclotron resonance heating (ICRH): High frequency electromagnetic waves are generated and launched into the plasma by antennas located on the machine walls facing the plasma. The waves couple to the plasma ions[2], which can be accelerated to very high energies.

NBI and ICRH are normally referred to as auxiliary heating schemes. The high-energy particles resulting from the auxiliary heating generally constitute a minority of the plasma ions and they slow down by transferring their energy to the electrons and ions of the bulk plasma. This slowing down process is described by a Fokker-Planck type equation. With a Maxwellian energy distribution of the background plasma, the slowing down of the particle, dE/dt, can be written in the following form [7],

---

[2] ICRH heating is similar to what we experience when we heat something in a microwave oven. The dedicated experimentalist can put a lighted candled in a microwave oven and experience how the microwaves heats the plasma (the fire).

$$-\frac{dE}{dt} = \frac{\alpha}{\sqrt{E}} + \beta E\,, \qquad (6)$$

where E is the energy of the particle. The α term describes the slowing down due to ion collisions where α is proportional to the ion density and the β term describes the slowing down due to interactions between the particle and the plasma electrons, where $\beta \propto n_\mathrm{e} \cdot T_\mathrm{e}^{3/2}$. Consequently, for a specific plasma, the magnitudes of the parameters α and β determine the slowing down time for the energetic ion.

The different heating schemes give rise to different ion velocity distributions. The NBI heating gives a practically square distribution with the maximum energy given by the NBI energy, whereas the ICRH heating gives rise to a quasi-exponential distribution of high energy ions. These high energy particles have an anisotropic velocity distribution. Their motion is normally described by a parallel and a perpendicular velocity component relative to the magnetic field line.

The bulk of the ions, heated either by the ohmic or the auxiliary heating, normally have a Maxwellian energy distribution, i.e., a thermal distribution which can be described with one parameter, its temperature.

Besides the external heating the plasma has a self heating mechanism. This internal heating in a fusion plasma is provided by the charged fusion products (α–particles in the case of dt-fusion) slowing down and transferring their kinetic energy to the plasma.

For this thesis new instrumentation for studying the effects of plasma heating has been developed.

1.4 Burn Criteria

A high temperature fusion plasma continuously loses energy to the surroundings. In order for the plasma to be in thermal equilibrium the power loss, P_L, has to be balanced by internal and external heating:

$$P_e + P_\mathrm{i} = P_\mathrm{L}\,, \qquad (7)$$

where P_e is the amount of power from external heating and P_i is the power from internal heating. The power losses are due to heat transport and radiation. The power loss due to transport is driven by the temperature gradient between the centre and the edge of the plasma, whereas the radiation losses are dominated by bremsstrahlung [8], which is produced when the free electrons experience acceleration in collisions with the free ions.

One of the major scientific goals of ITER is to prove that machines of this size can confine the plasma energy sufficiently well for a future reactor to produce a net amount of electricity. To reach this goal the plasma has to reach a condition close to nuclear “ignition”, where the “fusion fire” is sustained by its internal heating, with no or only little externally supplied heating. The internal heating that should balance these losses is proportional to the fusion power, P_{fusion}:

$$P_{\mathrm{i}} = \eta \cdot f_c \cdot P_{\text{fusion}} , \tag{8}$$

where η is the fraction of energy from the fusion reactions going to the charged particle(s) and f_c is the fraction of charged particle energy confined by the plasma. Obviously, it is of great importance to determine the different quantities of Equations 7 and 8. The fast charged particle confinement at JET is described in [VII] and a new method for fusion power measurements is described in [V] and [VI]. Instrumentation for providing information on heating effects is described in [I]-[IV]

2 Fusion Neutrons

Three things cannot be long hidden, the sun, the moon and the truth.

Buddha

As can be seen in Table 1, fusion plasmas produce neutrons. These are neutral particles and can therefore escape the magnetic field of the tokamak. The neutron production is both a blessing and a curse for fusion applications. On the one hand, the fusion neutrons cause radiation damage and induce activation in the reactor walls; solving these issues is one of the more challenging quests in fusion research. On the other hand, the neutrons have many positive functions: they breed tritium (see Equations 4 and 5); they deposit their energy into a large volume, thereby reducing the problems of surface heat loads; and they carry important information from the core of the fusion process (which is the main topic for this thesis). Furthermore, a fusion neutron source is an excellent candidate for incinerating the long lived actinides in fission nuclear waste [9] or for breeding fissile material [10] in fission-fusion hybrids. The advantage of such hybrids is that the fission part of the reactor system produces the energy and consequently the burn criterium discussed previously does not have to be fulfilled in order for the system to give a positive energy output. Finally, fusion neutrons can be used in applications outside the energy field, such as medicine through fast neutron therapy and in airport safety through detection of explosives; in these applications small DD or DT sources are used [11].

2.1 Neutron flux

The neutron flux from fusion plasmas originate either from the d+d→^{3}He+n (E_n= 2.5 MeV) or the d+t→^{4}He+n (E_n= 14 MeV) reactions, or a combination of the two, and the neutron emissivities, y [neutrons/m^3], from the two reactions are given by the reaction rates in the plasma:

$$y_{\mathrm{14MeV}} = n_\mathrm{d} \cdot n_\mathrm{t} \left\langle \sigma v \right\rangle_{\mathrm{d,t}} \tag{9}$$

$$y_{\mathrm{2.5MeV}} = \frac{1}{2} n_\mathrm{d}^2 \left\langle \sigma v \right\rangle_{\mathrm{d,d}} \cdot \beta_2, \tag{10}$$

where β_2 is the branching ratio of the neutron producing reaction number 2 in Table 1. The dd-reaction is also possible in DT plasmas and consequently

DT plasmas emit both 2.5-MeV and 14-MeV neutrons. The fraction of 2.5-MeV neutrons is given by:

$$\frac{y_{2.5\mathrm{MeV}}}{y_{14\mathrm{Mev}}}=\frac{1/2\,n_d^2\left\langle \sigma v\right\rangle_{\mathrm{d,d}}\cdot\beta_2}{n_{\mathrm{d}}\cdot n_{\mathrm{t}}\left\langle \sigma v\right\rangle_{\mathrm{d,t}}}=\frac{n_{\mathrm{d}}\left\langle \sigma v\right\rangle_{\mathrm{d,d}}\cdot\beta_2}{2\cdot n_{\mathrm{t}}\left\langle \sigma v\right\rangle_{\mathrm{d,t}}}. \qquad (11)$$

For all realistic temperatures the dd-reactivity is much smaller than the dt-reactivity and consequently the 2.5-MeV neutron emission is roughly two orders of magnitude weaker than the 14-MeV neutron emission.

The fuel density and temperature are functions of the position in the plasma, which results in a spatial distribution of the neutron emission intensity, $y(R,Z,\varphi)$, where Z, R, and φ are the vertical, radial and the toroidal position in the plasma, respectively. Integrating $y(R,Z,\varphi)$, over the plasma volume gives the total neutron emission, Y:

$$Y=\int_{V_{\mathrm{plasma}}} y\left(R,Z,\varphi\right)\partial V\,. \qquad (12)$$

Tokamak plasmas are toroidally symmetric, and so is $y(R,Z,\varphi)$. Consequently, y is only a function of R and Z.

The fusion product energies in Table 1 are given assuming reactants at rest. However, the sum of the energies of the fusion products equals the sum of the energies of the reactants and the reaction Q-value (E_{tot} in Table 1). Moreover, since the fuel ions are moving at high velocities, the CM-system moves in relation to the Lab frame, hence the lab velocity of the neutron is a superposition of the CM-system velocity and the neutron velocity in the CM-system. As a consequence, the fuel ion's velocity distribution determines the neutron energy distribution, i.e., the neutron energy spectrum, $I(E_{\mathrm{n}})$.

Since the ion velocity distribution depends on the heating mechanisms $I(E_{\mathrm{n}})$ is closely linked to the type of heating applied. The thermal motion of the ions in the Maxwellian bulk plasma gives rise to a Doppler broadened $I(E_{\mathrm{n}})$ [12] which can be described by a Gaussian distribution (see Figure 3). The width of $I(E_{\mathrm{n}})$ depends on the ion temperature (T_{i}) and the reaction type. For 2.5-MeV neutrons the FWHM=$82.5\cdot\sqrt{(T_{\mathrm{i}})}$ [keV] and for 14-MeV neutrons the FWHM=$177\cdot\sqrt{(T_{\mathrm{i}})}$[keV] [13], where T_{i} is given in keV. The increased energy in the fusion products also gives rise to a kinematical spectral shift. The ion velocity distribution of auxiliary heated plasmas gives a directionally anisotropic $I(E_{\mathrm{n}})$ [14] and in D plasma also the neutron emission intensity can be directionally anisotropic [15].

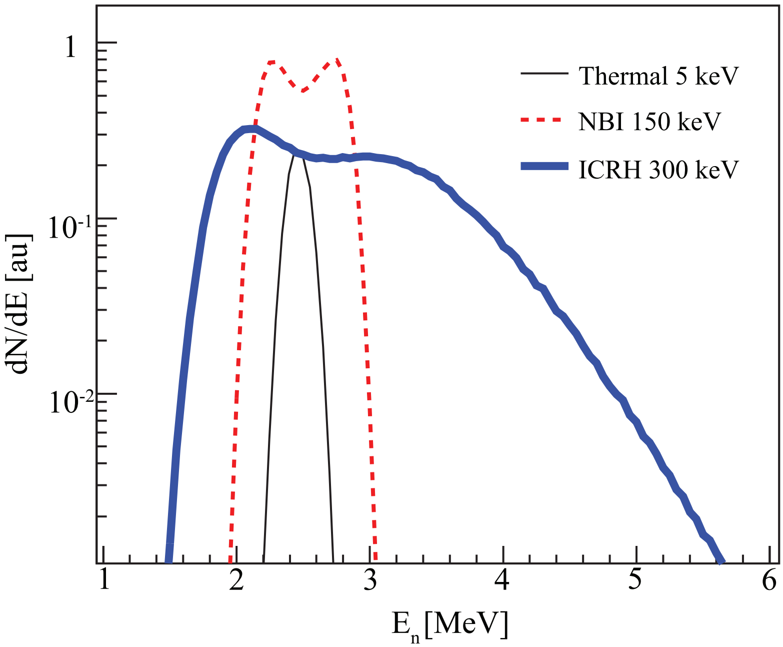

Figure 3. (Color online) Neutron energy spectrums from a thermal (black narrow), ICRH (blue broad) and NBI heated (red broken) plasma when viewed from a radial direction.

Deuterium plasmas produce mainly 2.5-MeV neutrons, but also neutrons from dt-reactions are present due to a two-step process as illustrated in Figure 9. The 1-MeV triton from the d+d→p+t reaction slows down by collisions with ions and electrons. In the course of this process, there is a probability for a d+t→^{4}He+n reaction to occur, where the neutron produced is called a triton burn-up neutron (TBN). The TBN process is illustrated in Figure 4.

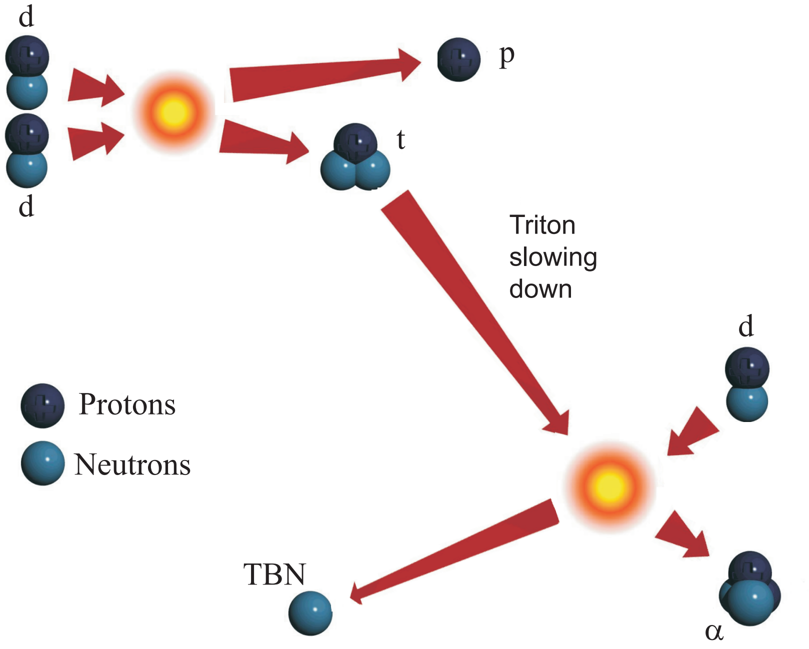

Figure 4. The triton burn-up process.

The ratio, ρ, between the TBN emission and 2.5-MeV neutron emission is normally between 0.005 and 0.015 as can be seen in [VII, Figure 7] and scales as:

$$\rho = \frac{TBN}{Y_{2.5MeV}} \propto T_{\mathrm{e}} \cdot n_d / n_e \, . \tag{13}$$

From Equation 13 it is clear that information on the deuterium density can be derived by measuring the neutron fluxes and electron temperature and density.

Due to the high energy of the tritons the TBN-emission is associated with a characteristic, very broad, neutron energy spectrum [16], as can be seen in Figure 5. Deuterium plasmas can also contain traces of tritium. Experience from JET has shown that residual tritium from previous DT experiments resides in the fusion machine for very long periods of time and is released back into the plasma during plasma discharges. Additionally, in high power pulses with good particle confinement tritium from the dd-reaction that is not burnt in the triton burn-up process is accumulated in the plasma. Such pulses are expected in the ITER deuterium advanced scenario, when ITER is operated with pure deuterium and high heating power is used. During these experiments the accumulated tritium is expected to contribute to a significant part of the neutron emission [17]. $I(E_{\mathrm{n}})$ from the residual and accumulated tritium has normally a Gaussian shape characterized by parameters similar to those of the bulk D plasma. The thermal emission, Y_{thermal}, can therefore be distinguished from the TBN emission using neutron spectroscopy. This is illustrated in Figure 5 and this feature was used in [VII] to account for the residual tritium in the JET machine.

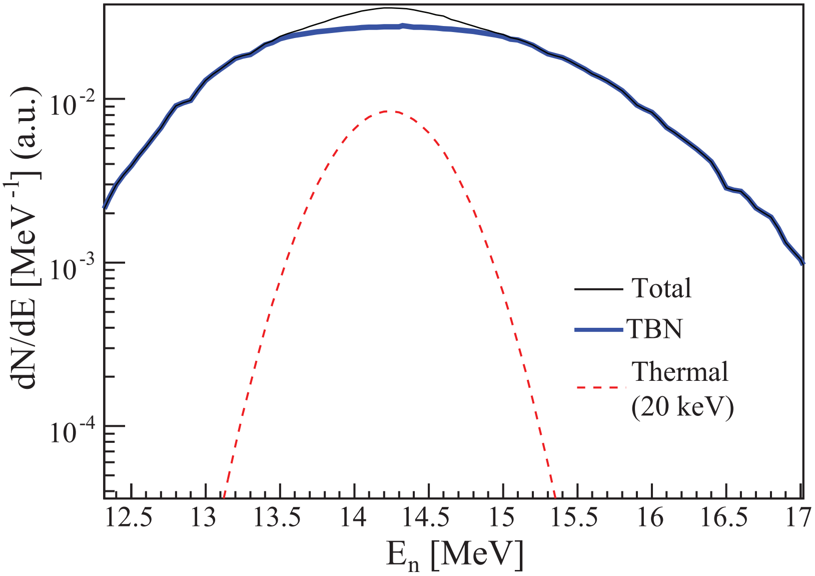

Figure 5. (Color online) Neutron spectrum from TBN (blue thick line) together with the thermal spectrum (red broken line) from residual tritium.

Combining Equation 11 and 13 one finds that the ratio between the emission from residual tritium and the TBN scales as

$$\frac{TBN}{Y_{\text{thermal}}} \propto T_{\text{e}} \left(\frac{n_{\text{d}}}{n_{\text{e}}} \right) \cdot \frac{n_{\text{d}}}{n_{\text{t}}} . \qquad (14)$$

As can be seen the ratio is dependent on the amount of impurities in the plasma (n_{d}/n_e).

2.2 Scattered and direct neutrons

The neutron flux in and around a fusion device has two components, a scattered flux and a direct flux. Neutrons that have not undergone any reaction constitute the direct flux.

The scattered neutrons have interacted with the fusion machine or surrounding support structures (e.g., diagnostics, walls etc.). Almost all scattering processes are endothermic, so the scattered flux is degraded in energy. The energy distribution of these neutrons extends from the emission energy all the way down to thermal energies, where the neutrons decay or, more commonly, are absorbed in and around the torus. The scattered neutron flux can be assessed using neutron transport codes such as MCNP [18] or Attila [19].

An example of the scattered flux is shown in Figure 6, where the scattered flux is evaluated with MCNP. It shows the expected energy distribution of the scattered neutron flux from the inner column (the back scattered flux) for ITER when viewed through a radial line of sight (LOS) in the horizontal plane. It has been claimed that the scattered flux in the region 2-5 MeV will be small [20]. This is unfortunately wrong[3] as shown by Figure 6. The data in Figure 6 is in good agreement with the results from previous simulations [21].

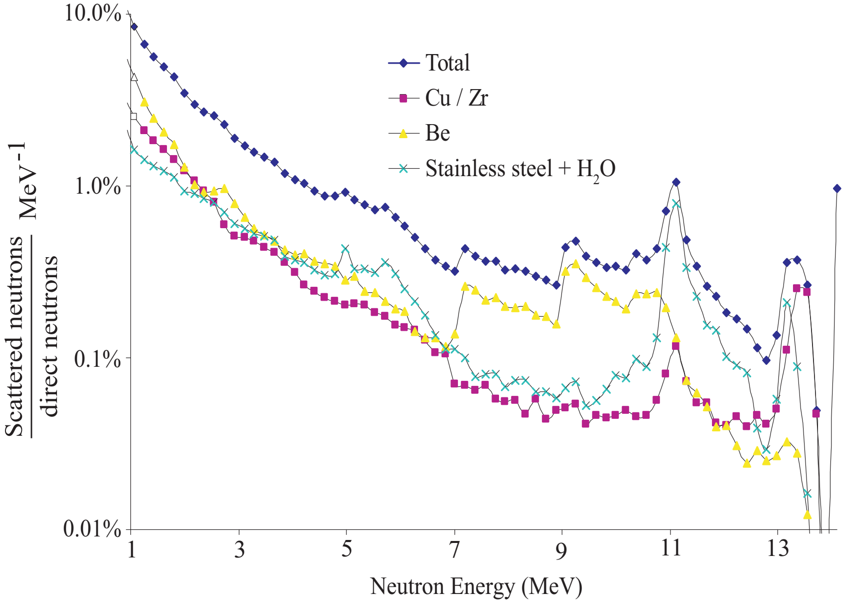

Figure 6. (Color online) Scattered flux from ITER's inner column when viewed through a radial line of sight in the horizontal plane. The structures in the graph are due to structures in the neutron cross section for the different materials (see figure legend) of the inner column. The data was derived using MCNP and a mono energetic 14 MeV neutron source.

---

[3] Ref [20] used a limited toroidal coverage and used reflecting surfaces to compensate for this. From MCNP5 user manual [18]: "Reflecting planes are valuable because they can simplify a geometry setup (and also tracking) in a problem. They can, however, make it difficult (or even impossible) to get the correct answer."

3 Plasma Diagnostics

Man kan inte rösta
om sanningen

J.Källne

In order to perform fusion research, plasma diagnostics are crucial for several reasons:

- Plasma control. Accurate knowledge of plasma parameters such as plasma position and magnetic fields is necessary for feedback system to maintain stable plasma condition.
- Machine protection. Phenomena such as disruptions (a sudden loss of plasma confinement) have to be predicted in order to be mitigated.
- Plasma optimization. Information concerning plasma performance parameters, such as temperature, density and fusion power is necessary in order to optimize the operation of the fusion machine.
- Safety and regulatory demands. The amounts of residual tritium and neutron activation are necessary to know in order to meet regulatory demands and maintain a safe operation for the public and operating staff.
- Model benchmarking. Physic models of the plasma behavior have to be tested against information from plasma experiments. This information can only be channelled through diagnostics.

Plasma diagnostics can be divided into five different categories from which important information about the plasma can be derived:

- Passive photon detection. The plasma emits photons from different processes. One example is the bremsstrahlung spectroscopy which measures the radiation emitted from the plasma produced when the free electrons experience acceleration in collisions with the free ions. In [VII] bremsstrahlung spectroscopy [22] is used to determine the effective charge of the plasma, which in turn can be used to determine the deuterium density.
- Active photon detection. By emitting radiation into the plasma and investigating how the radiation is absorbed and scattered information on mainly the plasma electrons can be derived. One example of this is Thomson scattering diagnostics which emits laser light into the plasma. The electron density and temperature can be derived by measuring the amount of scattered light and its Doppler broad-

ening. Data from the JET Thomson Scattering system, LIDAR [23], was used in [VII], for determining the electron density and temperature.

- Coils [24] are used to measure the magnetic flux outside the plasma and by doing so the magnetic and current profile inside the vessel can be determined.
- Particle detectors measure particles when they have escaped the plasma. Neutron diagnostics, which are described in Section 4, is one example. Faraday cups, scintillator probes or thin-foil methods are examples of diagnostics which measures the escaping charged particles.
- Surface diagnostics are used to investigate how the machine is affected by the amount of material that is deposited on a certain surface or how the surface is eroded through sputtering and other processes.

3.1 Calibration and errors

Independent of the field of science or the type of measurement the output, q, from a measurement cannot be related directly to the sought physical parameter, λ, without the instrument being calibrated. Examples of parameters q are the number of ticks on a ruler, the amount of light from a scintillator or the number of events registered in a detector; examples of corresponding λ could be the length of an object, the energy of an incoming particle or the fusion power. The relation $\lambda=f(q)$, where f is the instrumental response function, has to be found. This process is called calibration, and can be divided into cross-calibration, *ab initio* (from first principles) calibration or direct calibration against a standard. When an instrument is *ab initio* calibrated, the instrument's response is characterized from known physical laws (e.g., conservation of momentum), constants (e.g., speed of light) and by measuring physical properties of the instrument (e.g., volume, length etc). However, the instruments response to the sought physical parameter is not directly measured as is done when the instrument is directly calibrated against a standard. On the other hand, in a cross calibration the instrumental response is compared to the instrumental response of a calibrated instrument.

Independent of the type of calibration the concept of traceability is important, which means that it must be possible to trace all quantities that go into the calibration to international standards. In the case of calibration against a standard, the determination of the standard has to be traceable. In an *ab initio* calibration the measurements of the physical parameters which go into the calibration have to be performed with calibrated instruments.

After a calibration, the instrument is either absolutely calibrated or relatively calibrated. From the measurement of an absolutely calibrated instrument the actual value of the sought parameter can be determined whereas a relative calibration only gives the relation between different objects or events.

The quality of a measurement is not determined by the type of calibration, but rather from the magnitude of its errors. These can be divided into two categories: random errors (precision) and systematic errors (accuracy). The precision of a measurement describes its reproducibility and the accuracy its average error [25] as shown in Figure 7.

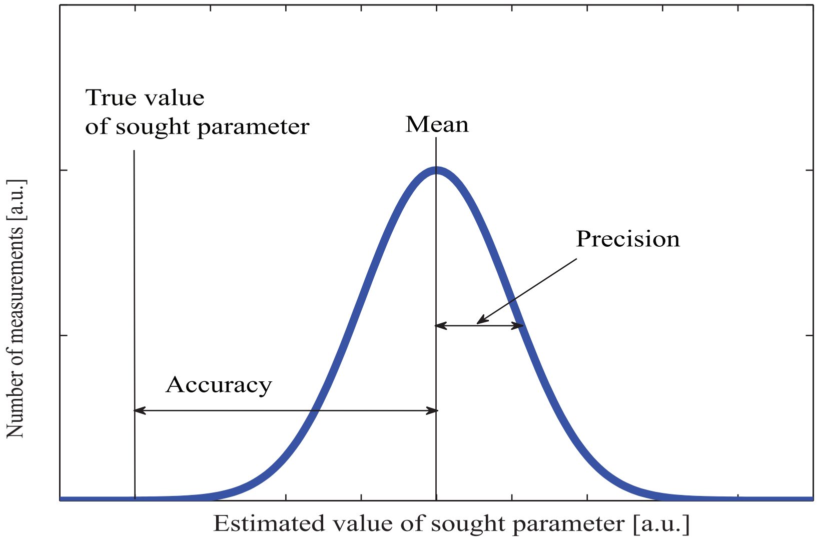
True value
of sought parameter
Mean
Precision
Accuracy
Number of measurements [a.u.]
Estimated value of sought parameter [a.u.]

Figure 7. Illustration of the difference between precision and accuracy.

The estimated magnitude of the errors is the uncertainty of the measurement. The systematic uncertainly is determined by careful investigation of the calibration procedure. The random uncertainties, as the name indicates, are given by random effects in the measurement situation. Sources of random uncertainties can be statistical fluctuations in the measurement, instrumental instabilities or a requirement of human input when determining q. The size of the random error can sometimes be evaluated by reaped measurements of a single object.

4 Neutron diagnostics

> *The root of all superstition is*
> *that men observe when a thing*
> *hits but not when it misses*
>
> Francis Bacon

Neutron diagnostics play a prominent part in this thesis and are discussed in detail in this chapter. The neutron emission from a fusion plasma is characterized by its intensity, its spatial distribution and its energy distribution. These are strong functions of the most important reactivity parameters and consequently neutron diagnostics are excellent tools when determining important plasma parameters and benchmarking fusion modelling codes [26]. At large fusion machines such as JET and ITER, each of the neutron emission characteristics has its own diagnostics.

To understand the fundaments of neutron diagnostics, some principles of neutron detection have to be discussed. The neutron carries no charge [27] and since only charged particles can be detected, the neutral neutron has to undergo a nuclear reaction to be observed. There are in principle three kinds of processes through which the neutron can be detected:

1. Nuclear scattering: Here the neutron transfers part of its momentum to a charged particle, which in turn can be detected. Protons and other light nuclei are preferred, since more energy can be transferred to these (see Section 4.1).
2. Direct charged particle production. When a neutron reacts with a target nucleus a charged particle might be emitted directly. Normally, the charged particle is a proton or an α-particle.
3. Nuclear excitation: When a target nucleus absorbs a neutron, the resulting nucleus may be excited above its ground state. The excited nucleus subsequently decays by emitting some kind of radiation. If the nucleus emits a charged particle the reaction can be detected, whereas an emitted photon has to interact with matter in order to be detected. A special case of nuclear de-excitation is fission, where the excited nucleus decays into two charged fission fragments, which can be detected.

While reactions of type 1 or 2 are prompt (e.g., instantaneous on the time scales governing the response of the detector devices), some reactions of type 3 can be “delayed”, taking place on a time scale of seconds or minutes.

Detectors using these different processes are discussed in Sections 4.2 to 4.4 and Chapter 5.

4.1 np scattering

Since neutron scattering on protons is used in many neutron detection applications some further properties of this type of scattering are discussed here. For reactions of type 1 the recoil proton energy (E_p), can be related to E_n by the kinematics of elastic scattering, i.e., for n+p→n'+p':

$$E_p = 4 \cdot E_n \frac{\frac{m_n}{m_p}}{\left(1+\frac{m_n}{m_p}\right)^2} \cos^2 \theta_{p,lab}, \qquad (15)$$

where m_n is the neutron mass, m_p is the proton mass and $\Theta_{p,lab}$ is the angle between the incoming neutron and the outgoing proton in the lab frame. For the purpose of this thesis we can assume the proton and neutron masses to be the same, in which case Equation 15 reduces to

$$E_p = E_n \cdot \cos^2 \theta_{p,lab}. \qquad (16)$$

The *np*-elastic cross section in the CM system, $\sigma_{\mathrm{np,CM}}$, is (approximately) independent of the angle of the outgoing proton. The lab frame cross section $\sigma_{\mathrm{np,lab}}$ can be approximated with

$$\sigma_{\mathrm{np,lab}} = 4 \cdot \sigma_{\mathrm{np,CM}} \cdot \cos\left(\theta_{p,lab}\right). \qquad (17)$$

It is important to note that for a given angular segment, $d\Theta$, the solid angle segment, $d\Omega$, increases with the angle:

$$d\Omega = 2\pi \sin\left(\theta_{p,lab}\right) d\theta. \qquad (18\ )$$

Combining 17 and 18 one finds that the maximum number of protons are emitted in $\Theta_{p,lab}$=45°. Furthermore combining Equations 16, 17 and 18, one finds that the recoil protons have a uniform energy distribution from the incoming neutron energy and extending all the way down to zero.

4.2 Neutron intensity measurements

From the neutron rates, the reactions' energy release (see Table 1) and their branching ratios, β, the fusion power can be calculated:

$$P_{\text{fusion}} = Y_{14\text{MeV}} \cdot E_{\text{tot}(4)} + Y_{2.5\text{MeV}} \cdot \left(E_{\text{tot}(2)} + E_{\text{tot}(1)} \frac{\beta_{(1)}}{\beta_{(2)}} \right), \quad (19)$$

where the indices in parentheses relate to the reaction numbers in Table 1.

Besides determining the fusion power the neutron rates have to be measured for several reasons. Regulatory demands require that the neutron intensity is measured, since it determines neutron activation of the machine and hence constitutes both an occupational health problem as well as a waste problem. From the intensity of the 2.5-MeV and 14-MeV neutrons, the ion temperature and densities can be determined. It has been proposed [28] that it should be possible to infer the fuel ion density ratio by measuring the ratio between the 2.5-MeV and 14-MeV emission in DT plasmas (as indicated by Equation 10). However, since the neutron flux around 2.5-MeV is dominated by the scattered flux from the 14-MeV emission (see Figure 6), this measurement is very challenging and can probably only been performed in trace tritium (i.e., n_t/n_d <5 %) experiments. For large fusion machines such as ITER the measurement of the neutron intensity is an important input in the residual tritium calculation. The amount of residual tritium is given by:

$$\Delta t_{\text{residual}} = \left(t_{\text{in}} - t_{\text{out}} \right) - Y_{14\text{MeV}} + Y_{2.5\text{MeV}}, \quad (20)$$

where $\Delta t_{\text{residual}}$ [number of atoms] is the change in the residual tritium inventory, t_{in} is the amount of tritium entering the machine, t_{out}, is the amount of tritium leaving the machine. $Y_{14\text{MeV}}$ is the 14-MeV neutron yield and hence a measurement of the amount of burnt tritium. $Y_{2.5\text{MeV}}$ is the 2.5-MeV neutron yield, which is an approximation of the amount of produced tritium. The amount of residual tritium accumulates over time with the consequence that any systematic errors in the measurement of the parameters in Equation 20 accumulate to a large error in the estimation amount of residual tritium left in the machine. For example, a 10% error in $Y_{14\text{MeV}}$ propagates to approximately 1 kg uncertainty in the amount of residual tritium at the end of the ITER lifetime.

In order to establish the relation between Y and the number of events (N) registered by a detector several fundamental processes need to be understood:

1. The energy dependent efficiency $e(E_n)$ of the detector must be known in order to relate the measured count rate to the local flux, F_n:

$$N = F_n \cdot A \cdot \int I\left(E_n\right)_{\text{detector}} \cdot e\left(E_n\right) \cdot dE_n, \quad (21)$$

where A is the area of the detector and $I(E_\mathrm{n})_\mathrm{detector}$ is the normalized neutron energy spectrum at the detector. The parameter $e(E_\mathrm{n})$ can be found either by an *ab intio* calibration or through a source calibration using a standard.

2. The spatial flux response, $\Psi(R,Z,\varphi)$, has to be identified. This describes how the local neutron emission $y(R,Z,\varphi)$ affects the flux at the detector. The flux response is discussed in detail in [V, Equation 13 to 15] and is summarized by the expression:

$$F_\mathrm{n} \cdot A = \int y(R,Z,\varphi) \cdot \Psi(R,Z,\varphi)\, dRdZd\varphi . \qquad (22)$$

   $\Psi(R,Z,\varphi)$ is normally determined using a neutron transport codes such as MCNP.

3. The normalized function of $y(R,Z,\varphi)$ has to be known:

$$y_{norm}(R,Z,\varphi) = \frac{y(R,Z,\varphi)}{Y} . \qquad (23)$$

   From Equation 22 and 23 the ratio, p, between the number of neutrons on the detector and the neutron yield can be calculated:

$$p = \frac{F_\mathrm{n} \cdot A}{Y} = \int y_{norm}(R,Z,\varphi) \cdot \Psi(R,Z,\varphi)\, dRdZd\varphi . (24)$$

4. The energy distribution at the detector $I(E_\mathrm{n})_\mathrm{detector}$ has to be determined since there normally is an energy dependence in the efficiency of the detector (see point 1). $I(E_\mathrm{n})_\mathrm{detector}$ is determined by the ratio between 2.5-MeV and 14-MeV neutrons; the amount of scattered flux; and the initial neutron emission spectrum, $I(E_\mathrm{n})$.

Points 1 and 2 above can be combined into a single calibration step, either by using *in situ* calibration or by cross calibrating the detector against an already calibrated instrument. For *in situ* calibration, a neutron source is placed in the torus and the instrumental response to the source is measured. By moving the neutron source around the torus the product $e(E_\mathrm{n})\cdot \Psi(R,Z,\varphi)$ is measured. As neutron source either a dd- or dt-generator is preferred, but alternatively a Californium source can be used. The advantage of *in situ* calibration is that the traceability to international standards is facilitated. However, an *in situ* calibration takes a long time to perform and delays the physics program. Furthermore the calibration has to be redone after any change in the machine hardware. An alternative approach is to use the neutron sources to benchmark the neutron transport calculations.

Finally, the detector can be cross-calibrated to other already calibrated instruments. It is important to note that the systematic uncertainty from the calibrated instrument propagates to the cross-calibrated instrument.

One of the main goals of this thesis is to improve the neutron intensity measurements and a detailed discussion of this is given in Chapter 5. A summary of today's most common methods in determining the neutron emission intensity is given below.

4.2.1 Activation system

An activation system uses the physical property of certain nuclei to emit gamma rays or delayed neutrons after being excited by neutron absorption. A sample of suitable nuclei is placed in the neutron flux, normally close to the plasma. After irradiation the sample is transported to a measurement station where the induced radiation is measured. Knowing the energy-dependent neutron reaction cross section, the measurement station's detection efficiency, the half life of the excited nucleus and the time between irradiation and measurement, one can calculate the time-integrated neutron flux at the sample position. The required $\Psi(R,Z,\varphi)$ is normally determined using neutron transport codes.

By using foils composed of nuclei with threshold reactions, which are activated only by neutrons with energies above ~5 MeV and therefore discriminating against 2.5-MeV neutrons, an activation system can also be used to measure the 14-MeV yield.

The activation foil technique is an established method in fusion research and is or has been used at both JET [29], JT60U [30] and TFTR [31][32]. There is also a proposed neutron activation system for ITER [33].

Activation foils provide time-integrate yield measurements and other methods have to be used to obtain time resolved data.

4.2.2 Fission chambers

Fission chambers (FC) can be used to determine the time evolution of the neutron emission. A FC consists of a thin foil of fissionable material (normally Uranium) placed around or in an ion chamber. The chamber is further surrounded by hydrogen-rich polythene, where the neutrons are moderated before inducing fission in the uranium. The energetic fission fragments are counted in the ion chamber. In this way, the local neutron flux variation at the FC position can be estimated (i.e., the FC is relatively calibrated). The efficiency of the FC is normally not determined when using FC in fusion applications, so other means are necessary in order to obtain an absolute calibration.

At TFTR *in situ* calibration was performed using both dd-generators, dt-generators and Californium sources [34], and at JT60U Californium sources were used [35]. *In situ* calibrations have also been tried at JET [36]. However, when new hardware was installed the response of the FCs changed and the *in situ* calibration was abandoned. *In situ* calibration is also proposed for ITER [37].

Instead of *in situ* calibration cross-calibration with the activation system is the preferred method at JET and a similar system is also proposed for ITER. The calibration accuracies for the different systems at different machines are given in Table 3.

Table 3. Accuracies in the determination of the neutron yield for different large fusion devices.

Method	Measurement	JET	TFTR	JT60 U	ITER
Activation foils	14-MeV	7%[29]-10%[38]	8%[4][32]	20 %[30]	7-10%[41]
	2.5-MeV	7% [29]	9%[32]	15 %[30]	7-10%[41]
In situ	14-MeV	NA	13%[39]	NA	10%[37]
	2.5-MeV	10%[36]	10%[40]	11%[35]	25%[37]

The accuracies given in Table 3 are for a particular calibration method. It is also possible to combine different independent measurements and make a best estimate of the neutron emission, which reduces the uncertainty. This was done at TFTR and accuracies of 7% were reached [34].

4.2.3 Semiconductor detectors

FCs can only be used to determine the total neutron flux, since they have no energy resolution or energy discrimination capability; specifically, they are unable to distinguish between the 14-MeV and the 2.5-MeV neutron emission. Semiconductor detectors, such as silicon (Si) diodes [42], on the other hand, detect charged-particles with good energy resolution, and neutron-induced charged-particle production can therefore be used for neutron flux measurements.

In a Si semiconductor two neutron-induced threshold reactions take place: $^{28}\text{Si}+\text{n}\rightarrow{}^{25}\text{Mg}+\alpha$ and $^{28}\text{Si}+\text{n}\rightarrow{}^{28}\text{Al}+\text{p}$. The energy dependence of the reaction cross section, with its abrupt onset at about 5 MeV [43], provides the necessary energy discrimination between the 2.5-MeV and 14-MeV neutron flux. At JET the Si-detectors are used to measure the local 14-MeV flux. The count rate in the Si-detectors is cross-calibrated with 14-MeV activation foils to provide the absolute 14-MeV yield.

---

[4] Excluding uncertainties in the cross section of the particular reactions.

One drawback of Si detectors is that they suffer from radiation damage and an alternative is to use diamonds as semiconductors [44].

4.3 Neutron spectroscopy

In addition to the absolute intensity of the neutron emission the energy distribution has to be determined for the neutron emission to be fully characterized. In order to derive the neutron energy spectrum, $I(E_\mathrm{n})$, a neutron spectrometer is needed. As stated in Section 3.1 a sought parameter, in this case $I(E_\mathrm{n})$, cannot be measured directly. As a consequence a measurable parameter q (e.g., pulse height, time, spatial distribution etc.), which can be related to $I(E_\mathrm{n})$, must be found. The convolution [45] below is a specific type of the response function discussed in Section 3.1:

$$g(q)=F_\mathrm{n}\cdot A\cdot\int_{-\infty}^{\infty} I(E_\mathrm{n})\cdot\psi(E_\mathrm{n},q)\partial E_n, \qquad (25)$$

where $g(q)$ is the distribution of the measured parameter q and $\psi(E_\mathrm{n},q)$ is the convolution (response) function relating $I(E_\mathrm{n})$ to $g(q)$. In practice $g(q)$ is normally discretized, $g[q]$, so it is convenient to express $\psi(E_\mathrm{n},q)$ and $I(E_\mathrm{n})$ in matrix form:

$$g[q]=F_\mathrm{n}\cdot A\cdot I[E_\mathrm{n}]'\cdot\psi[E_\mathrm{n},q], \qquad (26)$$

where $\psi[E_\mathrm{n},q]$ is the response matrix, and $\mathrm{I}[E_\mathrm{n}]$ is the discretized energy spectrum vector. In principle, $\psi[E_\mathrm{n},q]$ could be inverted to find $I[E_\mathrm{n}]$:

$$F_\mathrm{n}\cdot A\cdot I[E_\mathrm{n}]=\psi[q,E_\mathrm{n}]^{-1}\cdot g[q]. \qquad (27)$$

In practice, an inversion magnifies the errors in $\psi[E_\mathrm{n},q]$ and $g[q]$, resulting in unacceptably large errors in $I[E_\mathrm{n}]$. More advanced mathematical inversion methods, such as maximum entropy methods, have been tried in order to obtain $I[E_\mathrm{n}]$ [46]. However these methods can introduce large errors [47].

A more feasible method is to fit $I[E_\mathrm{n}]$ to $g[q]$, but since there is no one-to-one correspondence between $I[E_\mathrm{n}]$ and $g[q]$, such fitting procedures require assumptions to be made regarding the shape of $I(E_\mathrm{n})$. One method is to fit spectral components such as those illustrated in Figure 3 to the data. These spectral components are associated with a number of free parameters (e.g., width, energy shift and intensity), and by varying these parameters the $I[E_\mathrm{n}]_\mathrm{fitted}$ that best describes the data is found [48]; normally Chi-square or C-stat is used as the goodness-of-fit arbiter.

An alternative approach is to calculate the ion velocity distribution from plasma codes such as TRANSP [49], and by coupling these to reactivity codes, such as FPS [14] or Controlroom [50] $I(E_n)$ can be calculated. The calculated $I(E_n)$ is then convoluted with the response function and a simulated measurement result $g(q)_{\text{simulated}}$ is obtained. The distribution $g(q)_{\text{simulated}}$ is subsequently compared to the measured $g(q)$. This method is conceptually simple; a model (hypothesis) of the plasma and its reactivity is constructed and the hypothesis is tested with the measurement. It is also the most inclusive way to treat the problem, since many different aspects of the plasma behavior can be taken into account. However, the method is very computer and manpower intensive, and is therefore not suitable if large data sets are to be analyzed. Moreover, the method does not necessarily find the spectrum that best explains the data, i.e., there is normally an ion velocity distribution that would give a better fit to the data.

4.3.1 Measurement Criteria

Important plasma parameters can be determined from $I(E_n)$. Among these parameters you find such diverse elements as the ion temperature, T_i, the collective motion of the main plasma, the fuel ion densities and their velocity distributions [48][51][52]. A spectrometer should determine these parameters with good precision and accuracy in a wide range of plasma scenarios. A number of characteristics that determines the performance of the instrument are listed in [III]. Among those are:

- Accuracy of the response function.
- Rate capability, i.e., the number of useful counts in the spectrometer before saturation effects occur.
- Energy bite, i.e., the energy range covered by the instrument.
- Operational and calibration stability.
- Energy resolution, i.e., the width of the line shape of a mono energetic neutron source.
- Efficiency as defined by Equation 21.
- Immunity to background (see also section 5.1).

Traditionally neutron spectrometers were designed to measure T_i which is closely related to the FWHM (W) of $I(E_n)$ (see Section 2.1) and an analytical expression has been derived linking the resolution, R, and the number of counts, N, in the spectrometer to the uncertainty in the ion temperature determination [53]:

$$\frac{\Delta T_{\mathrm{i}}}{T_{\mathrm{i}}} = 2\frac{\Delta W}{W} = 2\sqrt{\left(\frac{R^2+W^2}{W^2}\right)^2 \cdot \frac{1}{2N} + \left(\frac{R^2}{W^2}\right)^2 \left(\frac{\Delta R}{R}\right)^2}\ , \tag{28}$$

where Δ is the uncertainty in the different parameters. In case the response function is well known, i.e., ΔR is small, Equation 28 simplifies to:

$$\frac{\Delta T_{\mathrm{i}}}{T_{\mathrm{i}}} = \frac{R^2+W^2}{W^2}\sqrt{\frac{2}{N}}\ . \tag{29}$$

Equations 28 and 29 were derived under the assumption of a Gaussian response function, zero background interference and only counting statistics as the source of error.

In reality, response functions are never completely Gaussian, there are many different sources of error and the uncertainties of other parameters than $\mathrm{T_i}$ have to be assessed. Consequently, today, numerical simulations are done in order to evaluate errors associated with different spectrometers techniques. In order to estimate the errors the following procedure is performed:

1. A plasma model is set up, i.e., a parameterized ion velocity distribution is selected.
2. From the ion velocity distribution a reactivity code calculates a synthetic neutron spectrum. Since the plasma model is well-defined the shape of the neutron spectrum is unambiguous.
3. The synthetic $I(E_{\mathrm{n}})$ is convoluted with the response function resulting in a synthetic measured distribution $g(q)_{\mathrm{synthetic}}$.
4. Measurements of $g(q)$ are normally associated with a known or assumed error distribution. From this distribution a randomized synthetic error is generated. These synthetic errors are added to $g(q)_{\mathrm{synthetic}}$. The errors normally come from counting statistics, but other contributions can be included.
5. In a similar way as in step 4 the response function is distorted. Since in general the response function is assumed to be well known, this step is normally omitted.
6. Given $g(q)_{\mathrm{synthetic}}$ with errors and the distorted response function a $I(E_{\mathrm{n}})_{\mathrm{estimated}}$ is derived. From $I(E_{\mathrm{n}})_{\mathrm{estimated}}$ an estimation of the sought parameters is derived.
7. Steps 4 to 6 are repeated until enough synthetic data is derived to perform a statistical analysis of the data set.
8. The result is distributions of estimated sought parameters (Figure 7). Ideally these distributions should be narrow and their mean values should be the same as was given by the plasma model in step 1. Systematic differences could be an indication that the method to reconstruct the

neutron spectrum is introducing a bias, but it could also be a feature of the response function. The spreads in the resulting distributions are the total uncertainties in the estimated parameters, i.e., the spreads are the total errors of the sought parameters propagated from the errors in steps 3 and 4. If there is an interest to know whether the found errors are systematic or random the evaluation technique has to be performed twice: once with only random errors as input and once with only systematic errors as input.

The evaluation techniques described above can be used when designing spectrometers, choosing the type of convolution method to derive the neutron spectrum [47] or as decision support when choosing a specific spectroscopic technique for an experiment [54].

Similar techniques can be used when performing error analyses of other types of diagnostic systems. For exemple the technique above was used when evaluating how the uncertainty in the neutron camera (see Section 4.4) data propagated to the uncertainty in the neutron yield determination in [V] and [VI].

4.3.2 Measurement techniques

In order to make an educated decision on which type of spectrometer to opt for one has to know which measurement techniques are available. Over the years, a number of different spectroscopic approaches have been tested at large fusion machines such as JET [55], TFTR [56][57] and JT60U [58]. Today, there are in principle four different approaches to measuring $I(E_\mathrm{n})$: scintillator, semiconductor, time of flight (TOF) and thin foil proton recoil. The different techniques are illustrated in Figure 8.

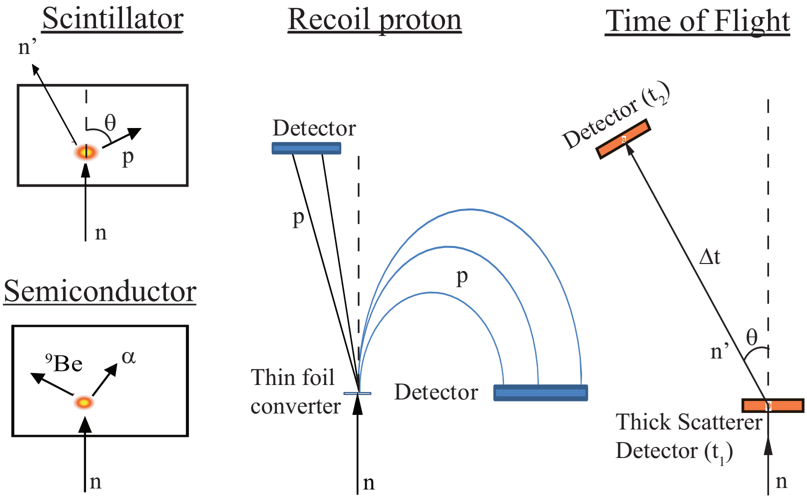

Figure 8 Measurement principles for neutron spectroscopy. Note that the "semiconductor" illustration depicts the situation for a diamond detector. See text for descriptions of the different techniques.

4.3.2.1 Semiconductor detectors

Semiconductor detectors are placed directly in the neutron beam. As described in Section 4.2.3 these detectors use charged particle production in order to detect neutrons. The energy of the charged particle(s) is the sum of the energy of the incoming neutron and the reaction Q-value. By measuring the energy of the residuals the neutron energy can be inferred. Si-diodes [42] as well as both artificial [59] and natural diamonds [56] have favorable properties for neutron spectroscopy and have been proposed for ITER [60].

4.3.2.2 Scintillator detectors

As for semiconductors detectors, the scintillator is placed directly into a collimated neutron beam where neutrons scatter on the scintillator protons. The amount of scintillator light is proportional to the amount of energy deposited by the recoil proton, which can be related to the incoming neutron energy (see Equation 16). Thus by measuring the light distribution one can derive $I(E_n)$. Since normally all scattering angles are allowed, the recoil proton distribution is uniform in the range $0<E_p<E_n$ (as shown in Section 4.1). This results in a broad response function, which complicates the determination of $I(E_n)$.

The liquid NE213 scintillator [61] is commonly used for neutron spectroscopy applications due to its ability for pulse shape discrimination between gammas and neutrons; carefully calibrated NE213 scintillators have been exploited at JET for some time [62].

The advantage of scintillator detectors is that they are small in size and conceptually simple. However, the broad response function can introduce large errors into the analysis and it is therefore difficult to measure weak spectral components. Furthermore, they are sensitive to gain drifts and noise and have limited dynamical range.

4.3.2.3 Time of flight

Time of flight, TOF, measurements are done by measuring the time it takes for a neutron to travel (fly) between two different detectors. This flight time is closely related to the velocity of the particle, which can be related back to its energy. TOF measurement can be performed on 14-MeV neutrons [63] although the technique is best suited for 2.5-MeV neutrons [64]. A recent important addition to the neutron diagnostics of JET is the TOFOR 2.5-MeV neutron TOF spectrometer [65][66].

4.3.2.4 Recoil Proton

In this technique collimated fusion neutrons scatter elastically on hydrogen nuclei (protons) in a thin hydrogen-rich conversion foil, often made of polythene (CH_2). By selecting protons in a limited angular range the proton energy can be related back to the neutron energy. The proton energy can be determined either by direct measurement using, e.g., a semiconductor detector [67][68] or by using a magnetic field to spatially separate the protons by momentum (energy). The later technique is used by the MPR spectrometer described in detail in Chapter 5, and in [I] and [III].

4.4 Neutron emission profile measurements – The Neutron Camera

The final component in characterizing the neutron emission is to determine $y(R,Z,\varphi)$; this task can be completed with a neutron camera by measuring the collimated neutron emission from different regions of the plasma. At JET, the camera system [69] consists of a pair of fan-like neutron collimator arrays placed in the torus hall closely coupled to the plasma vessel. One of these is situated above the tokamak (the vertical camera) and the other is located to the side of the torus (the horizontal/radial camera) attached to one of the diagnostic ports. There are nine vertical LOS and ten horizontal ones and all are in the radial direction. Each LOS is equipped with a NE213 scintillator and a plastic scintillator for detecting the incoming neutrons. The detectors' fields-of-view are defined by adjustable neutron collimators.

By knowing the efficiency of the scintillators, the resulting pulse-height spectrum can be related back to the neutron flux at each detector. In order to relate the neutron emission in a camera's field-of-view to the evaluated flux at the detector, MCNP calculations are necessary to correct for different scattering processes.

Using the evaluated neutron emission from the cameras' 19 fields-of-view the $y(R,Z,\varphi)$ can be reconstructed. The problem of reconstructing the $y(R,Z,\varphi)$ is similar to the problem of reconstructing $I(E_n)$, since they are both underdetermined problems; hence similar techniques can be used in the two cases. At JET the $y(R,Z,\varphi)$ is parameterized and fitted by using a chi-square minimization procedure [70]. It is important to note that only the relative emission in each field-of-view has to be determined in order to find the shape of $y(R,Z,\varphi)$. This facilitates the calibration of the instrument. The absolute level of $y(R,Z,\varphi)$ can then be determined by an instrument absolutely calibrated in flux (see Chapter 6) or against the activation foils system. An independent absolute calibration of the JET neutron camera has been performed [71] and the results were consistent with the JET activation foils.

The NE213 scintillator has the ability to separate 2.5-MeV and 14-MeV neutrons, so in principle both the 2.5-MeV and the 14-MeV $y(R,Z,\varphi)$ can be determined. However, in practice the data from the plastic scintillators are normally used for 14-MeV measurements and the NE213 is used for 2.5-MeV measurements. The 2.5-MeV $y(R,Z,\varphi)$ becomes hard to determine in cases where significant amounts of tritium are mixed into the plasma, because of the broad uniform response function of the detectors and the high level of scattered 14-MeV neutrons.

5 The Magnetic Proton Recoil Neutron Spectrometer

The Magnetic Proton Recoil (MPR) neutron spectrometer is a thin-foil spectrometer which was installed at JET in 1996 and upgraded (MPRu) 2001-2005. The principle and components of the MPR technique are illustrated in Figure 9. The fusion neutrons are collimated into a neutron beam. At the end of the neutron collimator np-scattering in a thin-foil (CH_2) conversion foil takes place. The recoil protons emitted in the forward direction enter the magnetic part of the spectrometer where they are momentum analyzed and focused onto the focal plane. An array of plastic scintillators coupled to photomultiplier tubes (PMTs) register the spatial distribution of the protons. All these steps depend on well-known physical constants (e.g., np cross sections), well-understood physical laws (e.g., the Lorenz force and conservation of momentum) and measurable quantities (e.g., the B-field and the geometry). Consequently an *ab initio* calculated response function can be derived with which the spatial proton distribution can be related back to the neutron energy distribution at the foil. At JET, the MPR has a semi-tangential line of sight through the plasma. The MPR has a 700 mm long cylindrical steel neutron collimator with a 10-cm^2 bore. At a distance 170 mm behind the end of the collimator is placed the 10 cm^2 polythene conversion foil, defining the active area of the spectrometer. The collimator-foil arrangement defines the spectrometers field-of-view into the plasma.

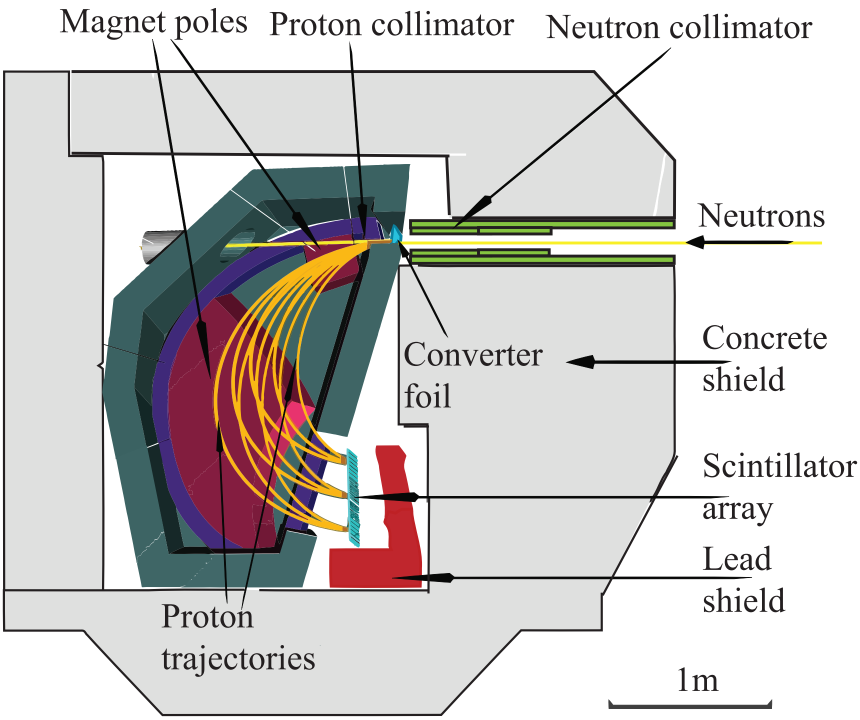
Magnet poles
Proton collimator
Neutron collimator
Neutrons
Converter foil
Concrete shield
Scintillator array
Lead shield
Proton trajectories
1m

Figure 9. Schematic figure of the MPR spectrometer and its components together with its radiation shield.

The geometry and the performance of the MPR is discussed in detail in [I], [II], [III] and [IV]. This chapter focuses on the measurement criteria that guided the upgrade of the instrument.

5.1 The background

Close to a fusion machine there are strong levels of radiation (neutrons and gammas) that can constitute a background in the measurement situation. As discussed in Section 2.2 there is a direct, a scattered and a thermal flux of neutrons. Gammas normally originate from neutron induced reactions, but are also produced directly in the fusion plasma. Gammas can produce high energy electrons through Compton scattering. Therefore, besides protons, also gammas, neutrons and Compton electrons impinge on the scintillator array and constitute a background in the measurement. In [V], three criteria were put up for performing measurements despite the background:

- The instrument should be physically shielded from background radiation, so that only few background events are registered. Nor-

mally concrete, preferably borated, is used for neutrons, high Z materials are used for gammas and low Z material are used for Compton electrons.
- Even if detected, background events should be well separated from signal events.
- The background that remains indistinguishable from the signal should be possible to estimate, so that the observed signal can be corrected.

One of the advantages with the MPR technique is that proton detection is well separated from the neutron beam entering the spectrometer, hence limiting the amount of neutrons coming directly from the neutron beam to the detector location. The MPR is shielded using 60 tons of (non borated) concrete around the spectrometer and a lead shield placed close to the scintillators. When particles enter the MPR scintillators, light is emitted, which is converted to charge in a PMT. The amount of charge is registered, either in an analogue to digital converter, ADC, (original MPR) or by a transient recorder card (MPRu). By analyzing the resulting pulse height spectrum a particle identification can be done. The original MPR was designed to operate in DT plasmas and the 14-MeV protons could be distinguished from the background events since they in general deposited more energy. An example of the original MPR pulse height spectrum is given in Figure 10, where the shape of both protons and background is shown. The amount of background under the signal peak was determined by fitting an exponential to the background. It was found that a signal to background ratio (S/B) of 2000 was achieved.

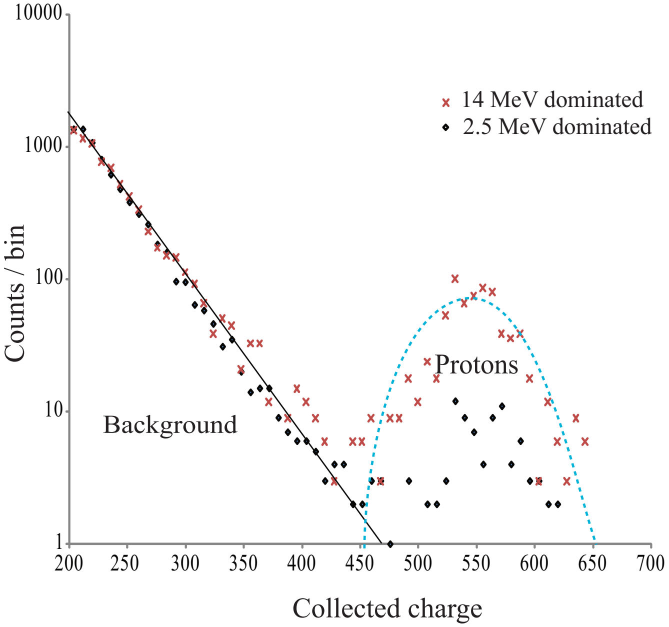

Figure 10. (Color online) ADC spectra of the MPR from the JET trace tritium experiments when the spectrometer is set to measure 14 MeV neutrons. A spectrum for a plasma dominated (to 80 %) by 2.5 MeV emission (blue diamonds), together with a spectrum from a plasma dominated (to 80 %) by 14 MeV neutron emission (red crosses) are shown.

When measuring the 2.5-MeV neutrons in D-operation a S/B = 0.1 was obtained [72]; this is a level that prevents any detailed interpretation of the neutron spectrum. The level and the spectral shape of the background were best explained by penetrating electrons and it was concluded that these were the major cause of background in 2.5-MeV measurements. When constructing the original MPR it was believed that 2.5-MeV neutrons would give rise to less background than 14-MeV neutrons, since they have a lower probability of penetrating the radiation shield. This hypothesis was later tested during the trace tritium experiment and as shown in Figure 11 the level of background does not depend strongly on the neutron source. It is also shown that the shape of the background is independent of the type of neutron emission (see Figure 10). Another hypothesis was that thermal neutrons due to the thermalization of the neutron beam entering the spectrometer cavity were the main source of the background. However, when changing the collimator length and thereby the intensity of the neutron beam entering the neutron spectrometer, no change in the absolute background[5] level was found. The current hypothesis is that thermal neutrons leak into the spectrometer's cavity, where they induce gammas, which in turn contribute to the background both directly and indirectly through Compton electrons.

---

[5] The absolute background is the number of registered background events per emitted JET neutron.

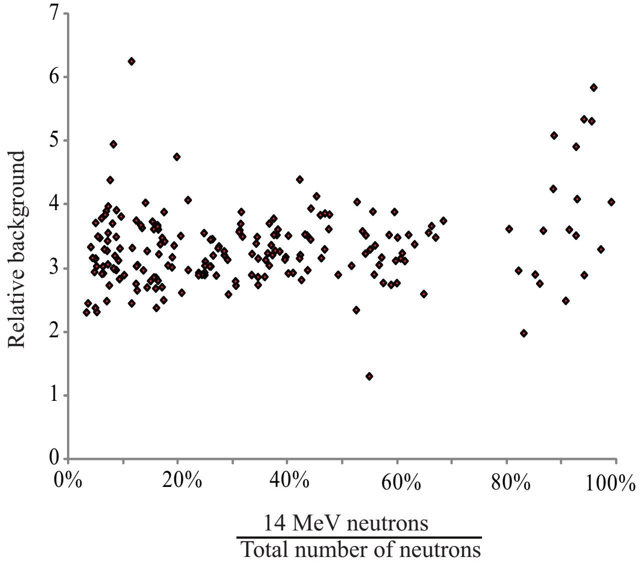

Figure 11. The relative background level (AU) as a function of the 14-MeV emission fraction of the neutron source.

In order to measure the 2.5-MeV neutron spectrum and to improve measurements of weak components in the 14-MeV neutron spectrum (e.g., the α knock-on tail [73]) an upgrade of the spectrometer was performed. The goal of the upgrade was to reduce the background and noise sensitivity of the instrument and to improve the calibration and the control and monitoring system. The full upgrade with its first results is described in [I] to [IV].

5.2 The new scintillator array

One of the major components of the upgrade was a new scintillator array. The new array consists of 32 scintillators each coupled to two PMTs. The original MPR used monolithic scintillators, whereas for the MPRu two-layered phoswich scintillators are used. The different timing properties of the two layers make pulse shape discrimination possible. The MPRu scintillators consist of a thin fast scintillating layer which faces the incoming protons and is in optical contact with a thicker slow scintillating layer as illustrated in Figure 12. The thickness is such that 2.5-MeV protons only give signals in the fast layer; this make them distinguishable from penetrating gammas and electrons, which in most cases give signals in both layers. Background neutrons interact in the scintillators primarily through np scattering with constituent hydrogen nuclei; the produced recoil protons have a limited energy and range. As a consequence they normally deposit their energy in only one of the two scintillator layers. Only neutrons interacting in the fast scintillator layer give signals with pulse shapes similar to those of incoming signal protons and therefore the background from neutrons scales with the volume of the fast scintillator. Hence by using a thin fast scintillator layer the neutron interference in both 2.5-MeV and 14-MeV measurements are reduced.

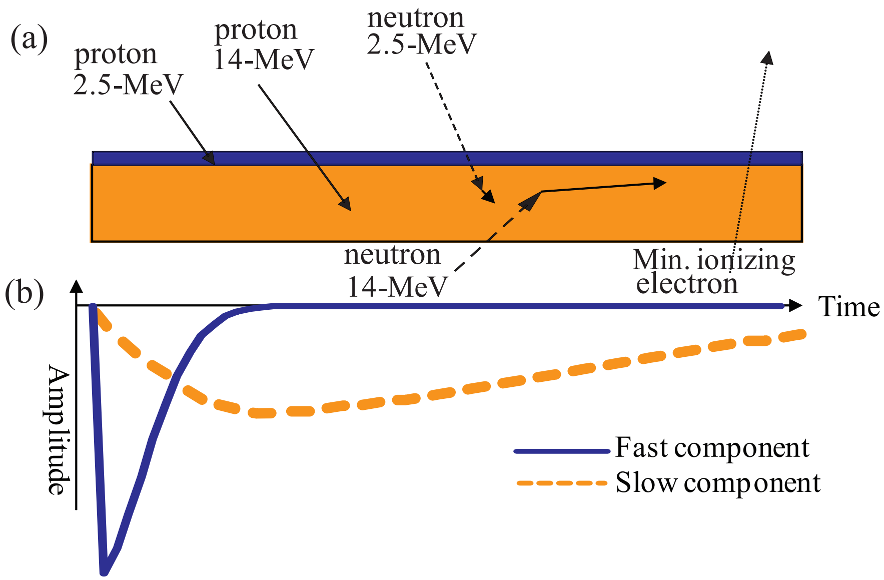

Figure 12 (Color online) (a) Interaction of different particles in an MPRu phoswich scintillator. The fast scintillator layer (dark blue) faces the incoming protons is backed with a slow scintillator layer (yellow). (b) Illustration of the timing properties of the two phoswich layers.

5.3 Data reduction and background subtraction

Transient recorder cards (TRC) [74] were installed in order to record the pulse shape of each individual scintillator event. Examples of the difference in shapes between a proton and an electron induced PMT signal are shown in Figure 13. The pulse shape discrimination method used here is a traditional long gate vs. short gate technique where the pulse of each event is integrated over an early short gate and a later long gate as indicated in Figure 13(a).

The corresponding charges from the short gate (Q_S) and the long gate (Q_L) identify each event. The set of (Q_S,Q_L) is used to produce a 2D histogram as illustrated in Figure 13(b). In this 2D histogram the number of events inside a region of interest (ROI) is counted. The ROI is chosen to include all protons. Background recordings are performed when the spectrometer is operated with zero B-field, preventing any recoil protons from reaching the scintillators. This background recording is used to estimate the background level in subsequent measurements.

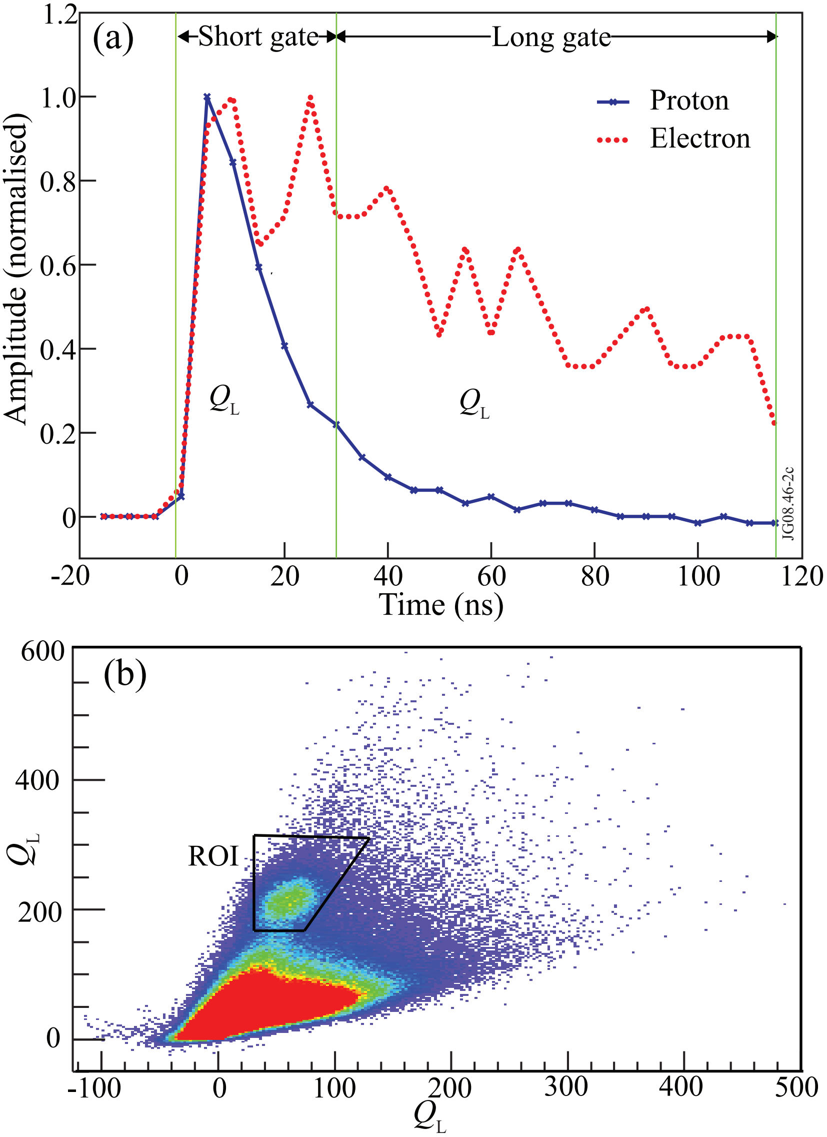

Figure 13. (a) The pulse shapes from a proton (blue solid line) and an electron (red broken). The integration intervals used to calculate Q_S and Q_L are indicated with vertical lines. (b) The resulting 2D histogram where the ROI used for proton selection is shown.

To maximize the S/B it is desirable to minimize the width, σ, of the collected charge, Q, distribution. A narrower signal distribution covers a smaller area in the (Q_S, Q_L) space and hence picks up less background. There are in principle three reasons for the broadening of $\sigma(Q)$. Firstly, there is an energy distribution of the protons impinging on a particular phoswich detector. However, in the MPR this is a minor effect, since the energy distribution is only 0.8% and 1.6%, for the two types of scintillators employed. Secondly, photo electron statistics has a significant effect. The number of photo electrons, n_{PE} is given by:

$$n_{\mathrm{PE}} = n_\gamma \cdot \varepsilon_{\mathrm{col}} \cdot q_{\mathrm{e}}, \tag{30}$$

where n_γ is the number of photons produced in the scintillator, $\varepsilon_{\mathrm{col}}$ is the scintillator light collection efficiency and q_e is the quantum efficiency of the PMT. The number of photo electrons can then be related to $\sigma(Q)$:

$$\frac{\sigma(Q)}{\bar{Q}} = \frac{\sqrt{n_{\mathrm{PE}}}}{n_{\mathrm{PE}}}. \tag{31}$$

The third contribution to $\sigma(Q)$ is due to the fact that $\varepsilon_{\mathrm{col}}$ is a function of the position on the scintillator where the protons impinge, which also contributes to the broadening. The parameter $\varepsilon_{\mathrm{col}}$ normally decreases with the distance to the PMT. This was found to have a quite large effect in the original MPR, and consequently each scintillator in the MPRu was fitted with two PMTs, per scintillator instead of one, which flattened the $\varepsilon_{\mathrm{col}}$ distribution.

The scintillator’s response to radiation was tested with protons, α-particles, electrons and UV-light. The tests are described in [IV]. In Figure 14 an example of the $\varepsilon_{\mathrm{col}}$ distribution derived with α-tests can be seen. Figure 14 shows the achieved $\varepsilon_{\mathrm{col}}$ distribution when summing the signals from the two PMTs. The $\varepsilon_{\mathrm{col}}$ distributions when only one of the two PMTs is switched on are also shown.

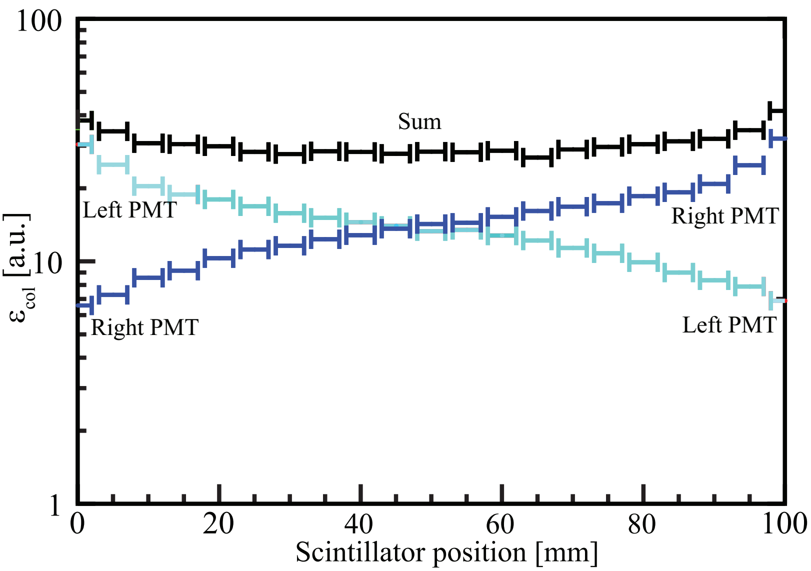

Figure 14. (Color online) The ε_{col} distribution for one of the scintillators with both PMTs active as a function of the position of the incoming radiation. The ε_{col} distribution for each individual PMTs is also shown.

5.4 Control and monitoring

During the TTE experiments it was found that many of the PMTs experienced gain variations. This complicated the background subtraction. Since the new data acquisition system, using TRCs, enables more advanced post discharge analysis a more advanced gain monitoring system was installed with the MPR upgrade. The new system consists of a YAP [75] scintillator with an embedded ^{241}Am source attached to the scintillator corresponding to the lowest energy (scintillator 0) and a LED light source coupled to all scintillators. The details of the gain monitoring are described in [II] and it is only briefly summarized here. The gain, G, is in this thesis is defined as:

$$G = \frac{Q}{e \cdot \gamma}, \tag{32}$$

where γ is the amount of light incident on the photocathode and e is the electron charge. The magnitude of G is given by

$$G = A_{\mathrm{PMT}} \cdot A_{\mathrm{other}} \cdot t \cdot q_{\mathrm{e}}, \tag{33}$$

where A_{PMT} is the amplification in the PMT, A_{other} is amplification in other parts of the system, t is the transmission of charge in the cables and q_{e} is the PMT quantum efficiency.

Since the output of the YAP source is based on the physical process of alpha particles interacting in the scintillator material, this source provides an absolute stable reference point from which the scintillator 0 can be calibrated. Since the same LED is coupled to all the scintillators the scintillator 0 together with the information from the LED can be used to correct for gain variations in all the scintillators. This method for gain correction is applicable not only for the MPR spectrometer, but for all measurements using a combination of scintillators and PMTs.

5.5 Results and discussion

The MPR upgrade allows for measurements of 2.5-MeV neutrons and such measurements have been performed at JET. With the new scintillator array and transient recorder cards a S/B of 5 was achieved, which is an improvement by a factor of 50 compared to the 2.5-MeV measurements performed with the original MPR and in good agreement with simulations [76].

The gain monitoring system detected significant gain drifts as can be seen in Figure 15(a). In [II] different possibilities for these changes in gain are examined. A reduction in the quantum efficiency could be discarded. It is believed that the loss in gain is due to a reduction in the amplification of the PMTs or some other part of the systems. Due to the large gain variations it would have been almost impossible to analyze the data without gain corrections. It was found that the gain corrections worked adequately as can be seen in Figure 15(b), where the position of the proton peak is restored after the corrections.

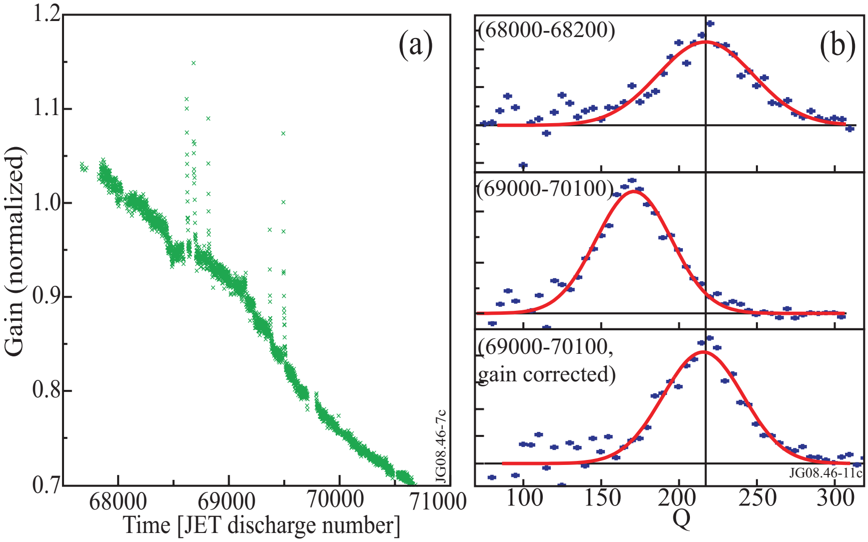

Figure 15 (a) Time traces of the gain for one of the MPR scintillator PMT assemblies. The dramatic decrease in gain is not typical, this is the worst case. The spikes in the data are due to PMT over-current trips and subsequent reapplication of the PMT high-voltage. (b) Distribution of the total collected charge per proton event, *Q,* for two different sets of JET plasma discharges (same scintillator as in panel a). The bottom panel shows the gain corrected *Q*-distribution after using the information from panel a. The red full lines are Gaussian fits to the data.

After the background has been subtracted and the gain variations have been corrected for the spatial distribution of the protons, the proton position histogram can be extracted. Examples of the proton histograms from 2.5-MeV neutrons operations are shown in Figure 16 for JET discharge 68569, heated with only NBI, and discharge 68379, subjected to both NBI and ICRH. For the NBI-only pulse the tokamak was operated with a deuterium plasma into which was injected 16 MW of 80+140 keV deuterium beams during a period of 9s. The integrated yield of the discharge was $6.0 \cdot 10^{16}$ neutrons, which resulted in 1770 extracted proton counts in the MPRu position histogram. The ICRH+NBI discharge employed 10 MW of NBI and 9 MW of ICRH (at 55 MHz, e.g., tuned to the fundamental frequency of hydrogen and the 2nd harmonic of deuterium at the centre of the plasma) over a period of 9s into a D plasma. The total neutron yield was $3.5 \cdot 10^{16}$, resulting in a MPRu position histogram with 1183 protons.

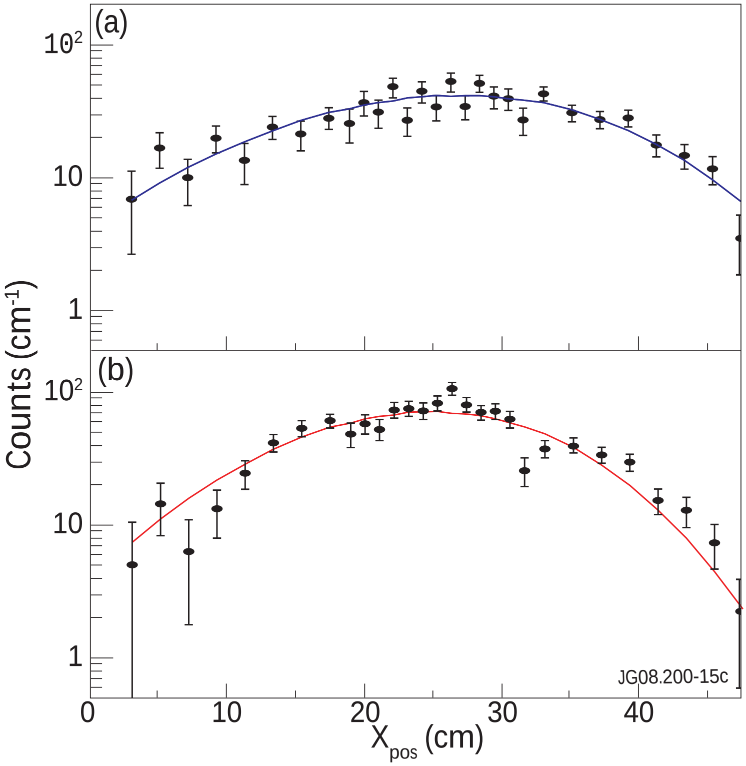

Figure 16. The proton histogram from the NBI heated plasma with a Gaussian fit. (b) The proton histogram from the NBI+ICRH heated plasma with a Gaussian fit.

One can note that the proton distribution from the NBI case is narrower than for the ICRH+NBI plasma, due to the lower energies of the fuel ions. It was found that the derived neutron energy spectra, if modeled with a Gaussian, had a $FWHM_{ICRH}$ = 476 keV compared to $FWHM_{NBI}$=357 keV. This is consistent with expectations, since ICRH heating can accelerate the fuel ions to MeV energies while NBI heating is restricted by the maximum energy of the beams (here 130 keV).

The MPRu was also set to measure the 14-MeV neutron spectrum in D-plasmas. As discussed in Section 2.1 the neutron spectrum is composed of both a triton burn-up component and a thermal component as was shown in Figure 5. The neutron spectrum was taken with the MPRu spectrometer and the corresponding proton histogram, with 3139 proton events, is shown in Figure 17.

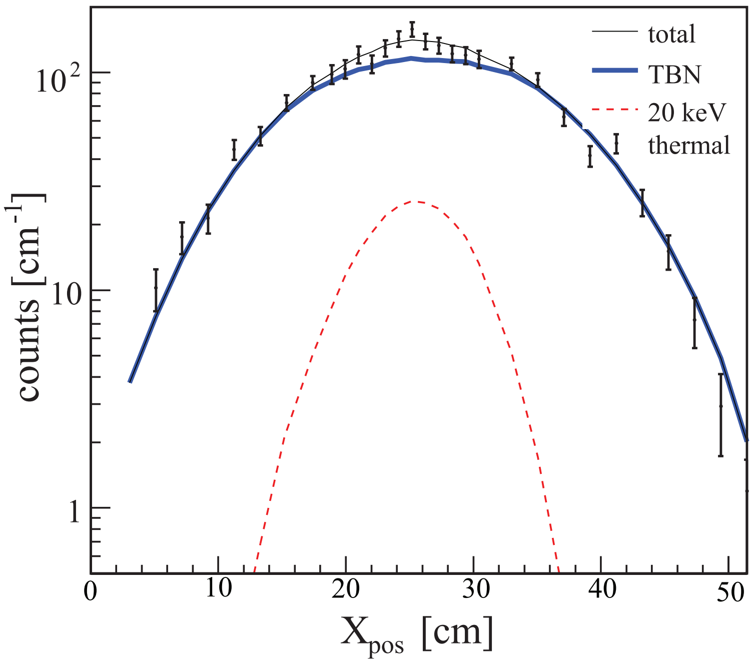

Figure 17. (Colors online) The proton position distribution for the TBN + residual tritium neutron spectrum shown in Figure 5. The fit from the thermal (red broken) and TBN (blue broad line) components are also shown.

The TOFOR spectrometer is the key instrument for measurements of 2.5-MeV neutron spectra at JET, due to its high efficiency. However the MPRu has a different LOS than TOFOR and using the dual sight lines of the two instruments can reduce ambiguities in the interpretation of the data [26].

Moreover, the MPRu instrument is *ab initio* calibrated in flux, a characteristic that is used when determining Y as discussed in the next section.

6 MPR -Camera fusion power measurement system

The importance of neutron yield measurements is outlined in Section 4.2. A new independent method for determining the neutron yield has been developed for this thesis, with the goal to increase the accuracy in such measurements. The method is presented in detail in [V] and has the potential to meet the demands of high-accuracy measurements of the fusion power for future fusion experiments such as ITER [VI]. The goal is to correlate the count rate of a spectrometer to the total neutron emission, and hence the fusion power and internal heating as described in Section 3.3.

The method relies on a spectrometer that is absolutely calibrated in flux and energy and a neutron camera. Both of these instruments are present at JET and, consequently, the method has been developed and tested there. The relation between the JET neutron emission, Y, and the spectrometer count rate is given by combing Equations 21 and 24:

$$Y = F \cdot A \cdot p^{-1} = \frac{N}{e} \cdot p^{-1}, \qquad (34)$$

where e is the average efficiency. The parameter p has a few different components. The major component to p is the direct flux from the spectrometer's field-of-view. The direct flux is estimated with an optical model, where the neutron flux is treated as if it behaved like light (hence the name) and machine structures are either opaque or transparent [V, Section 2]. However, the direct flux has to be corrected for due to the ability of neutrons to penetrate materials without undergoing any interaction. The effective field-of-view is increased due to transmission of neutrons, mainly through the edges of the neutron collimator. On the other hand, neutrons are lost due to attenuation in intervening material. In addition, p, has a component due to the scattered flux. The calculations of the attenuation, transmission and the scattered flux have been done using the neutron transport code MCNP. The attenuation part of the calculations was also checked with a simple exponential attenuation model. The parameter p depends on the shape of $y_{\mathrm{norm}}(R,Z,\varphi)$ as described in Equation 24. The shape of $y_{\mathrm{norm}}(R,Z,\varphi)$ is determined by using a neutron camera. The schematics of the entire system are illustrated in Figure 18.

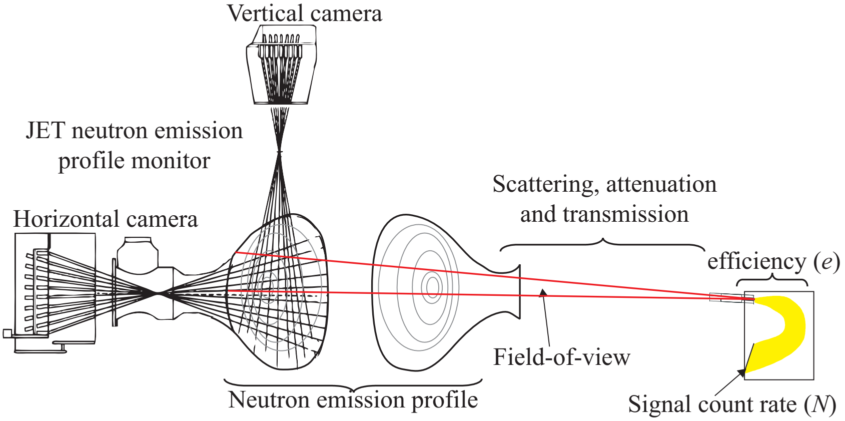
Vertical camera
JET neutron emission profile monitor
Horizontal camera
Scattering, attenuation and transmission
efficiency (e)
Field-of-view
Neutron emission profile
Signal count rate (N)

Figure 18. The MPR and the neutron cameras at JET together with their fields-of-view. The different quantities important for the yield determination are also presented in the figure.

Based on this established method a detailed error analysis is performed. It is found that the total systematic uncertainty is 6%, and the random uncertainties are dominated by the counting statistics in the spectrometer.

A performance evaluation for a similar system for ITER has been done [VI], and the different contributions to the uncertainty are given in [VI, Table 1]. It is found that a total systematic uncertainty of 3.0% is achievable, dominated by the uncertainty in the efficiency of the spectrometer. These results rely on the assumption that the centre of the neutron emission profile could be determined with an accuracy of 1 cm. However it has been suggested that the center will be determined with an accuracy of 10 cm [77]. This would increase the total accuracy to 4.2% for the system. It should be noted that the final design of the JET neutron camera is still to be completed and consequently the uncertainty in $y(R,Z,\varphi)$ in ITER is still difficult to predict.

6.1 Results

The first application of the method was for data from the 1997 JET deuterium tritium experiments DTE1 and the results are presented in Ref x. During the JET Trace Tritium Experiments, TTE, in 2003 the method was fully developed and it could be applied as a routine control room diagnostic. A comparison of TTE data from the MPR-Camera system and the calibrated silicon diode system (see Section 4.2.3) is shown in Figure 19 where a difference of 9 % between the two systems is found. This difference is within the uncertainties of the two data sets. Figure 19 also shows the random errors in the MPR-Camera data.

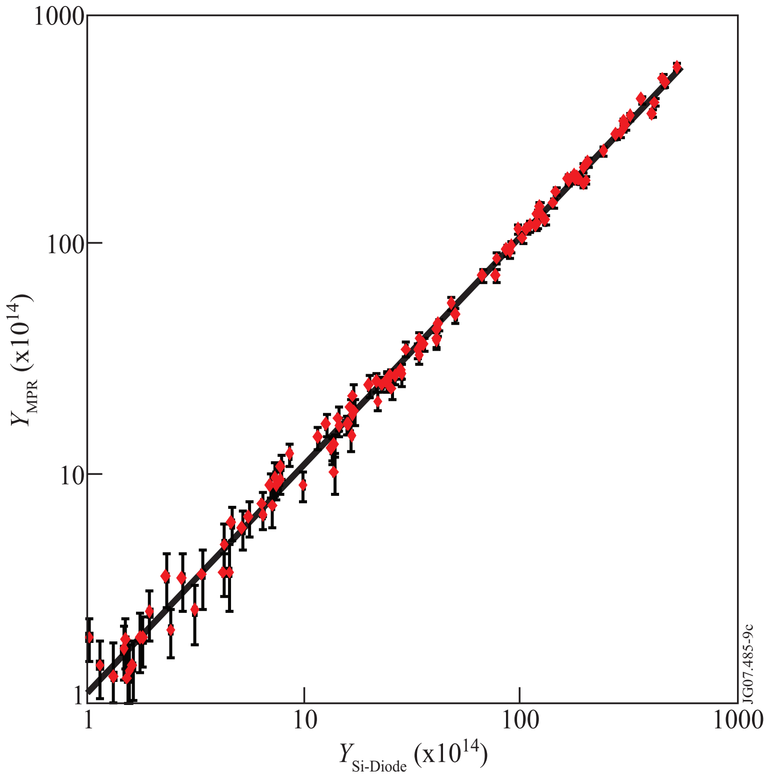

Figure 19. Comparison of pulse-integrated 14 MeV neutron yield data from the MPR-camera and silicon diode systems for 110 TTE pulses. The random uncertainties for the MPR-camera data are also shown. The silicon diode and MPR data sets are independent and no cross-calibration has been performed.

With the MPRu upgrade it is also possible to measure the 2.5-MeV neutron yield. Time has not permitted to make a detailed analysis of $y(R,Z,\varphi)$, so the results presented in [III] uses a fixed $y(R,Z,\varphi)$ from the TTE. This increases both the random and the systematic uncertainties. However, an attempt was made to calculate the $y(R,Z,\varphi)$ from the neutron camera data available. With this information a preliminary analyses was performed and the integrated neutron yields for 101 pulses were determined. The results can be seen in Figure 20, where a systematic difference of only 2 % between the MPR and the calibrated FCs are found. This is consistent with the results presented in [III] given the increased errors when not using neutron camera data.

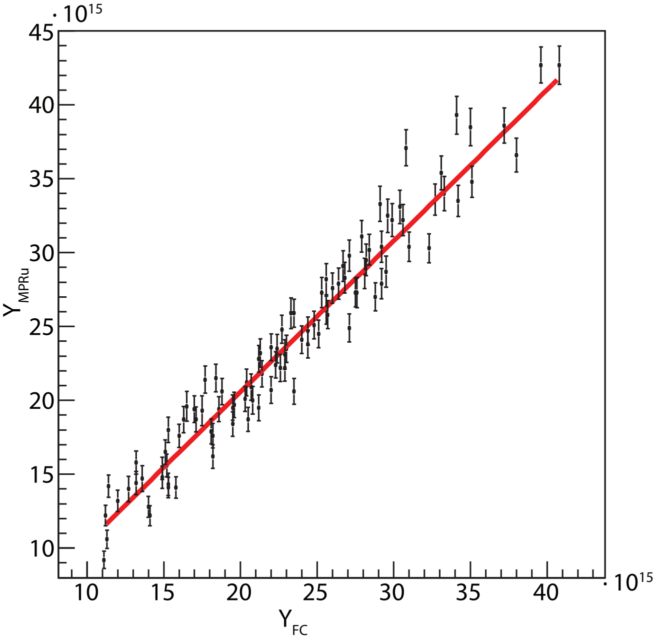

Figure 20. Comparison of pulse-integrated 2.5-MeV neutron yield data from the MPRu (Y_{MPR}) and JET fission chambers (Y_{FC}) for 101 JET pulses. Uncertainties due to counting statistics for the MPRu data are also shown.

6.2 Discussion

One of the major reasons that the systematic uncertainties are lower for the ITER system than for JET is that a dedicated, hypothetical, neutron collimator is used. Simulations show that in order to minimize the uncertainty in the calculations the transmission and the scattering should be reduced. To achieve this, a long broad tapered neutron collimator is used for the ITER case Figure 21. Such a collimator, instead of a short cylindrical one (see Figure 9), has many advantages. The flux on the spectrometer increases, since the ratio between the area of the umbra and the penumbra is enhanced. The tapered collimator results in a more well-defined field-of-view, which decreases the uncertainty in the flux. Furthermore, a tapered collimator reduces the amount of neutrons penetrating the collimator. It is also important to have some distance between the collimator and the foil, since this decreases the number of scattered neutrons on the detector. Finally, by increasing the angle of the tapering close to the plasma the amount of scattered neutrons in the collimator is further reduced.

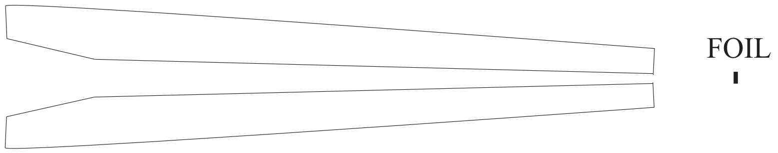

Figure 21 Shape of an optimal neutron collimator for determining the neutron yield.

Using a neutron spectrometer-camera system allows the low-energy scattered neutrons to be studied and excluded experimentally. Furthermore, the spectroscopic information makes it possible to correct for any energy dependence in the flux detection efficiency. A collimated neutron flux also decreases the influence of the scattered flux at the detector, which is difficult to model.

The $y(R,Z,\varphi)$ should always be included when neutron yield measurements are performed, independent of the method. However using a collimated neutron flux measurement simplifies the propagation of uncertainties in the $y(R,Z,\varphi)$ to the final result. Furthermore, using a neutron camera for determining the $y(R,Z,\varphi)$ minimizes the associated errors.

Using an MPR spectrometer has some added advantages. The MPR is *ab initio* absolutely calibrated both in flux and in energy, so no *in situ* calibration or cross-calibration of the instrument is needed. This makes the new method independent of other methods for fusion power determination, such as the traditional one based on FCs calibrated with activation foils.

The present system at JET was not optimized for neutron yield measurement. And as shown in [VI], in a dedicated system the uncertainties can be substantially reduced.

7 Charged fusion product confinement measurements

The previous chapter gave examples on how the neutron yield could be determined with an accuracy of 4% when different neutron systems were combined. In this chapter it is shown that a combination of information from a broad range of plasma diagnostics can provide a measurement of the internal heating of the plasma.

The internal heating of the plasma depends both on the released fusion power and the confinement of the charged fusion products (CFP) as shown in Equation 8. In Section 6, [V] and [VI] a new method for measuring the fusion power is outlined. An approach to determine the CFP confinement based on neutron measurements, by measuring the triton burn-up neutrons (TBN) is presented in [VII].

The confinement of 1-MeV tritons has previously been studied by means of TBN measurements [78] for operation in high current mode at JET. Lately, JET has been operated with lower plasma currents in order to investigate new operating scenarios. This thesis describes a set of TBN measurements done under these new operating conditions. There have been previous studies of TBN at low currents at other fusion machines [79]; however this is the first attempt to study the TBN at JET for these conditions.

7.1 TBN model

The TBN model is described in detail in [VII] and is only summarized here. The triton from the d+d reaction is born at an energy of approximately 1-MeV and moves in a gyro-motion orbit where the triton orbits around a magnetic field line. If a triton does not slow down or undergo any collisions, it continues to follow the same gyro-motion orbit as long as the tokamak magnetic field is stable. However, a fraction of the tritons enters into orbits that are intersected by a vessel wall; those tritons are lost. Due to the high velocity of a 1-MeV triton (≈6000km/s), it is lost within a couple of μs after being "born"; this is therefore referred to as a prompt loss. The confined tritons slow down by collisions with the electrons and ions of the background plasma. This slowing down process is described by Equation 6.

After the prompt losses have been estimated, the TBN rate has to be measured and compared to simulated values in order to see if there are any other triton loss processes. The simulated TBN emission is found using the reactivity code TRAPT [78], which simulates the time dependence of the tritons slowing down and reacting with the background plasma.

7.2 Experiments and result

The deuterium experiments at JET in the period October 2000-May 2002 offered an excellent opportunity to study the ion confinement in new operation scenarios. During this period, the ion confinement was studied by means of TBN measurements, prompt loss calculations and TBN simulations.

In these experiments, the 14-MeV neutron rate was monitored by JET's silicon diodes. In order to calculate the TBN rate from the 14-MeV neutron rate, the residual tritium from previous experiments, namely the major DT experiment in 1997, has to be taken into account. Using the MPR spectrometer the contribution of the neutron flux from the thermal tritons is distinguished from the TBN emission.

It is found that there are significant losses of tritons at low currents. At currents of 3 MA about 10% of the tritons are lost and losses of 60% (mostly prompt losses) were observed at 1 MA current. After correcting for the amount of residual tritium and the number of prompt losses the ratio between the number of measured TBN neutrons and the number of expected TBN neutrons can be derived as shown in Figure 12.

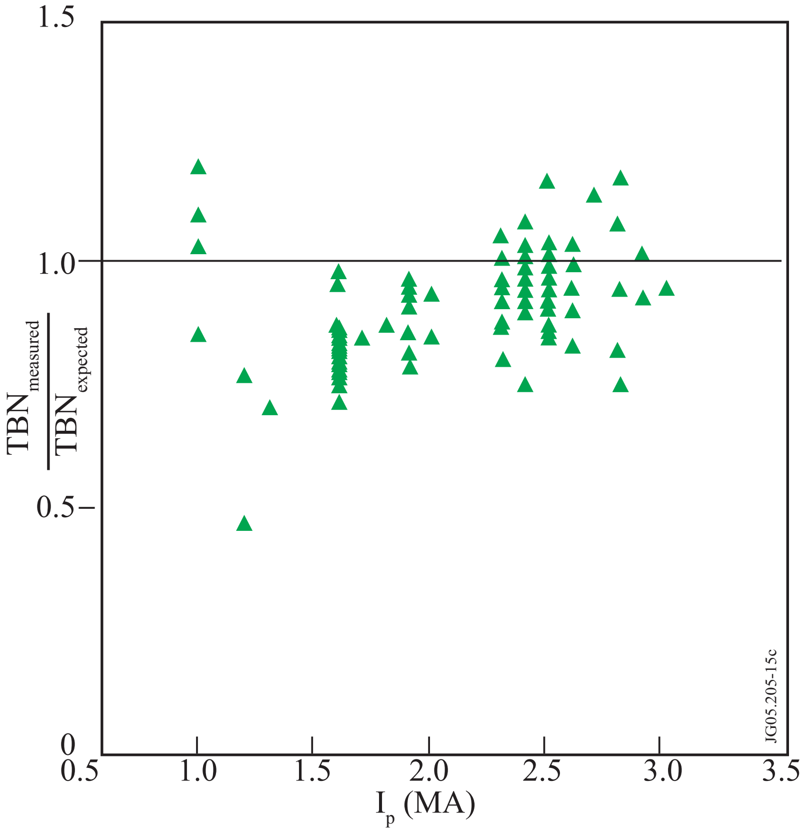

Figure 12 The ratio between the number of measured TBN and the number of expected TBN as function of plasma current.

Furthermore it was found that the ratio, TBN/$Y_{thermal,}$ was affected by the amount of impurities in the plasma as expected from Equation 14.

7.3 Discussion and outlook

The confinement of tritons is a measure on how well α-particles are confined. The losses experienced at low currents imply reduced plasma heating in DT-plasmas at low currents (see Equation 8). At currents larger than 2.2 MA, there is no evidence for non-prompt losses; for lower currents other loss-mechanisms could not be excluded. Mechanisms responsible for such losses could be, for example, field ripple diffusion, MHD activity or large-angle Coulomb scattering, but an investigation of this has not been within the scope of this thesis.

In general, the uncertainties associated with the TBN method are to a large degree given by the uncertainties in the input parameters to the simulations. In [VII] the problems to determine the deuterium density were discussed, due to large uncertainties in the effective charge of the plasma. Previously, experiments have shown that the deuterium density can be determined using neutron spectroscopy [80]; a method that could be pursuit for current JET experiments. Since the 14-MeV neutron flux is one of the most important input parameters for the ion confinement measurements the developed 14-MeV method outlined in [V], [VI] and in Section 6 could reduce the systematic uncertainties in the TBN-method.

8 Conclusions

The work with this thesis has led to: a MPR neutron spectrometer that is less sensitive to background and gain-drifts; a new method to determine the neutron yield; and a further understanding of the confinement of ions at low currents in large tokamaks.

The results from the confinement study verify findings from other machines, but also highlight the possibilities offered by neutron measurements to supply information outside their traditional field of study. In particular, the ability of a high-resolution neutron spectrometer to separate the triton burn-up and residual triton neutron emission components is of fundamental importance in this context.

The instrumental upgrade allows the MPRu to measure both the 2.5-MeV and 14-MeV neutron spectrum. Consequently, the spectrometer can provide important information on the fuel ion population both in D and DT operation. The possibility to operate in D plasmas allows the spectrometer to be fine tuned and fully characterized prior to the next JET (trace or full) tritium experiment. This possibility is also ITER relevant, since neutron data will be needed from day one of ITER DT experiments. In the planned ITER advanced D experiments and any trace tritium experiments a mixed flux of 2.5-MeV and 14-MeV neutrons is present. The capability to distinguish and measure both these species makes the MPR a rare candidate to study such scenarios.

The results from the developed spectrometer-camera system for yield measurements show that the systematic errors in fusion power measurements can be greatly reduced in comparison to standard methods using activation foils or *in situ* calibration. Reducing the need of *in situ* calibration can bring ITER into plasma operation at an earlier date, and consequently speed up the progress in fusion research. The method was originally developed for 14-MeV neutron measurements; however, with the upgraded MPRu spectrometer it is also possible to measure the 2.5-MeV neutron yield. This method has great implications for future fusion power measurements in both D and DT-operation, most notably in that the uncertainty in the residual tritium inventory of ITER can be dramatically reduced.

9 Summary of papers

Paper I

The New MPRu Instrument for Neutron Emission Spectroscopy at JET

This paper presents the upgrade of the Magnetic Proton Recoil (MPR) neutron spectrometer and its improved signal to background capability. This improvement is made possible by the use of a new proton recoil detector in combination with transient recorder data acquisition cards. The importance of these instrumental improvements for extending the use of the MPRu in diagnosis of D and DT plasmas is discussed. Results from the first 2.5-MeV measurements performed with the MPRu during JET's high level commissioning in April 2006 are presented.

My contribution to Paper I: Building and installing the MPRu at JET. Taking part in the data taking during the JET experimental campaigns. Writing the paper.

Paper II

Control and Monitoring System of the Upgraded Magnetic Proton Recoil Neutron Spectrometer at JET

This paper describes the control and monitoring system of the upgraded MPR neutron spectrometer installed at JET, focusing in particular on a technique for the stabilization of the gain of the photomultipliers coupled to the focal plane scintillator detectors. The technique described is of general interest for all instruments that employ scintillators coupled to photomultiplier tubes.

My contribution in Paper II is participation in the assembly and tests of the different components of the C&M system. I developed and implemented the method for gain corrections, made the data analyses, drew the conclusions and, finally, wrote the paper.

Paper III

The thin foil magnetic proton recoil spectrometer MPRu

The paper gives a full description of the completed MPRu spectrometer. Examples are given of its capabilities to measure both 2.5-MeV and 14-MeV neutrons in D plasmas. The new instrument is also used to measure the absolute 2.5 MeV neutron flux.

My contribution in Paper III has been constructing and installing the MPRu spectrometer at JET. Paper III has been a true group effort all the way from the design of the spectrometer to the completion of the paper. I have participated in all aspects of this effort.

Paper IV

Development and Characterization of the Proton Recoil Detector for the MPRu Neutron Spectrometer

The paper describes the development of the focal plane detector for the MPRu spectrometer. This was partly done by tests of prototype scintillators to reach the final design. The paper reports on the tests conducted and the projected performance.

My contribution to paper IV is participating in the design of the test procedure and the actual tests of the phoswich detectors. I also participated in the data analyses.

Paper V

Fusion Power Measurement using a Combined Neutron Spectrometer-Camera System at JET

In this paper the principles of collimated neutron flux measurements for fusion plasma power determination are described. A method combining information from a neutron spectrometer and a neutron profile monitor to obtain the neutron yield is presented. Particular care is taken to estimate the uncertainties involved. The method has been put to practical use at JET and results from JET's Trace Tritium experimental campaign in 2003 are presented.

My contribution to paper V is participating in the TTE experiment, developing the method, analyzing the data and writing the paper.

Paper VI

Fusion Power Measurement Using a Combined Neutron Spectrometer - Camera System at ITER

In this paper, we present how the system presented in **paper V** could be implemented on ITER and how well it would perform under different assumptions of plasma scenarios and diagnostic capabilities.

My contribution to paper VI is developing the method for error analyses at ITER and building a MCNP model of ITER, interpreting the results, writing the paper and, finally, presenting the paper at the Burning Plasmas Conference in Varenna Italy 2007.

Paper VII

Triton Burn Up Neutron Emission in JET Low Current Plasmas

The paper describes measurements and simulations of the charged particle confinement at JET. By measuring the triton burn-up neutrons and comparing to simulations the amount of lost tritons is estimated for low current plasmas in JET. The level of 14 MeV neutrons due to residual tritium is estimated using data from the MPR neutron spectrometer.

My contribution to paper VI is performing preliminary analysis of the data and completing the paper.

10 Sammanfattning på svenska

En av vår generations största frågor är hur vi ska kunna försörja en växande världsbefolkning med energi. Växthuseffekten begränsar vår vilja att använda olja, gas och kol; i stora delar av värden finns det en folklig rädsla för traditionell kärnkraft; och det finns stora frågetecken kring hur mycket energi som kan levereras från förnyelsebara resurser. Fusionskraft skulle kunna tillgodose vårt behov av en obegränsad mängd med ren och säker energi.

Fusion är den process som driver vår sol. Om denna process kunde kontrolleras på jorden skulle våra energiproblem vara lösta för all framtid. I fusionsprocessen utvinns energi genom termonukleär förbränning där lätta atomkärnor slås ihop. I den processen omvandlas en del massa (m) till energi (E) enligt Einsteins berömda formel:

$$E = mc^2 \tag{35}$$

där c är ljushastigheten. Eftersom ljushastigheten är hög (300 000 km/s), behöver bara en liten mängd massa omvandlas för att frigöra en stor mängd energi.

Det mest troliga bränslet i en framtida fusions reaktor är en blandning av två tunga former av väte, deuterium och tritium. När tritium och deuterium slås ihop frigörs stora mängder energi och en heliumkärna och en neutron bildas, vilket visas i Figur 22.

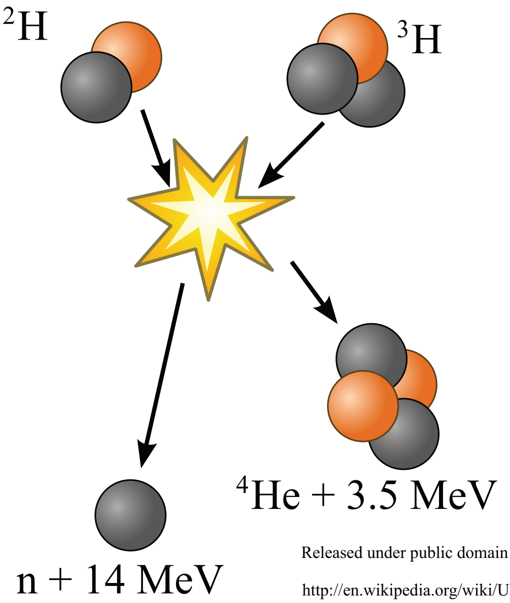

Released under public domain by
http://en.wikipedia.org/wiki/User:Wykis

Figur 22. Fusionsprocessen där en tritium (^{3}H) och en deuterium (^{2}H) kärna slås ihop. Produkten blir en heliumkärna (^{4}He) och en neutron (n). Processen frigör så mycket energi att 25 gram bränsle kan producera den mängd elenergi som en person behöver för hela sin livstid.

Tritium finns inte naturligt i vår miljö utan måste tillverkas i speciella kärnkraftverk av tungvattentyp. Detta gör tritium väldigt dyrt (ca 200 000 000 kr/kg). Tritium är dessutom radioaktivt och därför används ofta rent deuterium i dagens fusionsforskningsexperiment. Även med rent deuterium bildas neutroner när atomkärnorna slås ihop. Förhoppningen är att i framtidens reaktorer kunna tillverka tritium direkt i reaktorn genom att ”klyva” litium med fusionsneutroner. Litium, i sin tur, är en relativt vanligt förekommande metall i jordskorpan.

Forskare försöker idag bemästra den svårtämjda fusionskraften. Ett stort problem är att bränslet måste vara flera hundra miljoner grader för att antända. Detta gör det väldigt svårt att hantera bränslet. Ett sätt är att ha bränslet inneslutet med hjälp av kraftiga magnetfält i en badringsformad magnetisk torus. En sådan magnetisk torus är Joint European Torus (JET) som finns England. JET är idag det enda fusions-magnet-experiment som kan hantera tritium.

I en bilmotor bestämmer trycket och temperaturen bilmotorns effekt. På liknande sätt bestämmer tryck och temperatur den effekt som kan fås ut ur ett fusionskraftverk. För att kontinuerligt kunna kontrollera och förstå förbränningsprocessen måste tryck, temperatur och effekt i ett framtida fusionskraftverk kunna mätas. Eftersom bränslet är väldigt varmt kan inga ”vanliga” mätverktyg (t.ex. en kvicksilvertermometer) föras in i bränslet.

Dessa skulle omedelbart förstöras och förorena bränslet. Bränslets egenskaper måste alltså kunna mätas på distans. Det är i det sammanhanget som forskningsresultaten som presenteras i denna avhandling kommer in.

Oavsett bränslesammansättning kan de elektriskt oladdade neutronerna som kommer från fusionsreaktionerna ta med sig viktig information om förbränningsprocessen ut ur den magnetiska inneslutningen. Genom att mäta neutronernas energi kan man få fram bränslets temperatur och information om hur plasmat är upphettat.

Ett prototypinstrument som mäter egenskaperna hos de neutroner som kommer ut från bränslet installerades på JET redan 1996. Instrumentet är en neutronspektrometer av MPR-typ (Magnetisk Proton-Rekyl-spektrometer). Den byggdes för att mäta energin på de neutroner som kommer från deuterium-tritium reaktionerna. MPR-spektrometern har uppgraderats för att även kunna användas till de vanligare deuteriumexperimenten. Denna uppgradering beskrivs i den här avhandlingen.

En viktig del av mitt arbete har varit själva uppgraderingen av spektrometern där både design, utveckling och byggande har ingått. Jag, tillsammans med kollegor, har installerat MPR-spektrometerns nya detektorsystem. Ny toppmodern datainsamlingselektronik har också installerats. Vi har även uppgraderat instrumentets kontrollsystem. Syftet med uppgraderingarna har varit att göra instrumentet mindre känsligt för de störningar som finns i närheten av ett fusionsexperiment. Med det uppgraderade instrumentet har vi lyckats bestämma temperaturen på fusionsbränslen som har varit flera hundra miljoner grader varmt.

I den här avhandlingen beskrivs också utvecklingen av en ny metod som gör det möjligt att med hjälp av MPR-spektrometern bestämma JETs totala neutronproduktion. Genom att bestämma neutronproduktionen med stor noggrannhet går det att bestämma fusionseffekten och bränslets sammansättning.

För att föra fusionsforskningen vidare har det bestämts att det ska byggas en ny testreaktor, ITER. Den kommer att producera en termisk effekt på upp till 1.5 GW (motsvarande den elektriska effekten man får ut av ett stort kärnkraftverk) och vid reaktorn kommer forskare att kunna göra experiment som varar i flera minuter. Detta gör att enorma mängder neutroner kommer att produceras. Att kunna mäta dessa neutroner kommer att vara av yttersta vikt för att ITER-projektet ska bli en succé. I avhandlingen visas att det går att bestämma neutronproduktionen med väldigt god noggrannhet med instrumentet och metoden som har utvecklats.

11 Acknowledgments

None of us is as smart
as all of us

Japanese proverb

In this chapter I will try to thank all the people who have contributed to this work.

First, I want to thank to my supervisor Göran. You have taught me how to build neutron diagnostics, analyze data, write articles, choose good wines and be true to science. It has been an honor to work with you. Göran has also been the group leader for the MPRu project and led it to a successful conclusion together with the rest of the team. My co-supervisor, Dr Conroy, have been a tough teacher, but I have learnt a lot, MCNP, Python, Plasma Physics and never to solve anything analytically. “We have computers.”

The completion of the MPRu project has been a true group effort. First I want to thank Erik; you have always given me a helping hand when things needed to be finished. And your ideas have been truly valuable. Luca, Wolfgang and Gustav were other key players in the project. Building instruments together, those were the good days. Eventually, we had to send away the MPRu to JET, where Garry and Sergei gave us all the help we needed to get the instrument in place. Thanks.

Developing a method for neutron yield measurements Niklas and Hans gave me a head start. Thank you. Giuseppe and Jan introduced me to the work on triton burn-up; also thanks to Diego for you hard effort in the data analyses. Marco T. was the true pioneer in Control and Monitoring business and he showed me the way. Also Peter’s work in the C&M-field is acknowledged.

I want to thank my PhD co-workers Anders, Maria, Carl, and Emanuele for all interesting discussions, for the good times at JET and for all the help. For the JET experiments you need a fusion machine. To the JET team, to Kamendje and Andrea, to Kate, to the drawing office and to the JET neutron group: “Thank you for making it possible”.

Back at the department, Susanne and Inger handled the administration; Michael the management; Teresa and Ib the computers, Henrik Pettersson the recruitment; and Yngve the workshop. Ångström is an excellent workplace thanks to people like you. I also want to thank Bumpen for the challenge. I would not have been ready today without it.

At the department life is not only work. It has been real fun to share coffee-breaks and luches with Pernilla, Anni , John, Vasily, Riccardo, Peter, Björn, Ane, Nils, and Pär.

A thesis work is a lot about writing and I want to show my appreciation for the help I got from Matthias, Leif and Marco in their careful proof readings of my manuscripts.

It has been a great experience to teach new students how to use an oscilloscope together with Angelica, John, Mathias, Philip and Stephan. And "running" TRIGA reactor with the Staffan and Henrik was truly exciting.

This work has financially been supported by Uppsala University, TTA technotransfer, the Swedish Research Council and the EFDA work program, for which I am very grateful.

Vad hade livet varit utan vänner som Per, Thomas, Jenny, Magnus, Kaisa, Tobias, Eva, Anders, Jonas, and Anders. Ni har gjort att forskningsåren rusat förbi. För alla fina somrar när jag har kunnat vila upp mig, vill jag tacka Göte (postumt) och Margit.

Mina föräldrar, Lena and Ulf, vill jag tacka för den kärleksnatt när jag blev till. Utan den hade inget av det här varit möjligt. Alexandra, du är en bra syster och en fin vän. Till sist vill jag tack Anna. Ditt stöd och din kärlek är ovärderlig.

References

[1] A. Einstein 1905 *Annalen der Physik* **18** 639

[2] S. Willms 2003 “Tritium Supply Considerations” presented at the Fusion Development Paths Workshop

[3] J. Wesson 1999 “Science of JET” JET–R(99)13

[4] E. Speth 1989 *Reports on Progress in Physics* **52** 57

[5] D. Ciric et al 2007 *Fusion Engineering and Design* **82** 610

[6] T. Inoue et al 2001 *Fusion Engineering and Design* **55** 291

[7] T. H. Stix 1972 *Plasma Physics* **14** 367

[8] G. Van Oost *Transactions of fusion Science and science and technology* **41**

[9] W. M. Stacey 2007 *Fusion Engineering and Design* **82** 11

[10] F. Faghihi et al 2008 *Annals of Nuclear Energy* **35** 759

[11] J. Reijonen et al 2003 "Compact neutron generator development at LBNL" LBNL-53255

[12] H. Brysk 1973 *Plasma Physics* **15** 611

[13] L. Ballabio et al 1998 *Nuclear Fusion* **38** 1723

[14] P. Van Belle and G. Sadler 1987 *Proc. Course Workshop on Basic and Advanced Diagnostic Techniques for Fusion Plasmas* (Varenna, Italy)

[15] B. Wolle et al 1999 *Nuclear Instruments and Methods in Physics Research* **A424** 561

[16] J. Frenje et al 1998 *Plasma Physics and Controlled Fusion* **40** 1211

[17] V. Khripunov 2000 *Fusion Engineering and Design* **51-52** 281

[18] MCNP manual 1987 LA-UR-03-1987

[19] D. S. Lucas 2005 ”Comparison Of The 3-D Deterministic Neutron Transport Code Attila® To Measure Data, MCNP And MCNPX For The Advanced Test Reactor” INL/CON-05-00662

[20] L. Petrizzi et al 2007 *Fusion Engineering and Design* **82** 1308

[21] P. Antozzi et al 1995 *Review of Scientific Instruments* **66** 939

[22] K. Behringer 1986 *Review of Scientific Instruments* **57** 2000

[23] C. W. Gowers et al. 1995, *Review of Scientific Instruments* **66** 471

[24] V. Coccorese et al. 2004 *Review of Scientific Instruments* **75** 4311

[25] W. J. Youden 1962 ”Experimentation and Measurements” NIST special Publication Reprinted 1997

[26] C. Hellesen et al 2008 *Review of Scientific Instruments* **79** to be published

[27] J. Chadwick 1932 *Nature* **192** 312

[28] K. Okada 2006 *Review of Scientific Instruments* **77** 10E726

[29] O. N. Jarvis 1994 *Plasma Physics and Controlled Fusion* **36** 209

[30] M. Hoek et al 1995 *Review of Scientific Instruments* **66** 885

[31] C. W. Barnes 1990 *Review of Scientific Instruments* **61** 3190

[32] C. W. Barnes et al *Review of Scientific Instruments* **66** 888

[33] A. V. Krasilnikov et al 2005 *Nuclear Fusion* **45** 1503

[34] L. C. Johnson et al 1995 *Review of Scientific Instruments* **66** 894

[35] T. Nishitani et al 1992 *Review of Scientific Instruments* **63** 5270
[36] O. N. Jarvis et al 1990 *Review of Scientific Instruments* **61** 3172
[37] K. Asai et al 2006 *Fusion Engineering and Design* **81** 1497
[38] L. Bertalot et al 1999 *Review of Scientific Instruments* **70** 1137
[39] D. L. Jassby et al 1995 *Review of Scientific Instruments* **66** 891
[40] E. B. Nieschmidt et al 1985 *Review of Scientific Instruments* **56** 1084
[41] C. W. Barnes et al *Review of Scientific Instruments* **68** 577
[42] T. Elevant et al 1986 *Review of Scientific Instruments* **57** 1763
[43] ENDF/B-VI database
[44] M. Angelone et al 2005 *Review of Scientific Instruments* **76** 013506
[45] G. F. Knoll 2000 ”Radiation detection and measurement – third edition” p. 704
[46] A. Zimbal et al 2004 *Review of Scientific Instruments* **75** 3553
[47] E. Andersson Sundén et al 2007 “Evaluation of Spectral Unfolding Techniques for Neutron Spectroscopy” JET report EFD-C(07)04/10
[48] H. Henriksson et al 2001 *Review of Scientific Instruments* **72** 832
[49] J. Ongena 1998 *Transactions of fusion Science and science and technology* **33** 181
[50] L. Ballabio 2008 CONTROLROOM 0.3.4
[51] H. Henriksson et al 2005 *Plasma Physics and Controlled Fusion* **47** 1763
[52] G. Ericsson et al 2001 *Review of Scientific Instruments* **72** 759
[53] T. Elevant et al 1997 *Fusion technology* **32** 304
[54] G. Ericsson 2008 “Prospects for High Resolution Neutron Spectroscopy on High Power Fusion Devices in View of the Recent Diagnostic Developments at JET” EFDA–JET–CP(07)04/08
[55] O. N. Jarvis 2002 Nuclear Instruments and Methods in Physics Research A **A476** 474
[56] A. V. Krasilnikov et al. 1997 *Review of Scientific Instruments* **68** 1
[57] J. D. Strachan 1988 *Review of Scientific Instruments* **59** 1732
[58] Y. Shibata 2001 *Review of Scientific Instruments* **72** 828
[59] M. Pillon et al 2007 *Fusion Engineering and Design* **82** 1174
[60] G. J. Schmid et al 2004 *Nuclear Instruments and Methods in Physics Research* **A527** 554
[61] A. Zimbal et al 2004 *Review of Scientific Instruments* **75** 3553
[62] B. Esposito et al 2004 *Review of Scientific Instruments* **75** 3550
[63] G. Grosshög et al 1986 *Nuclear Instruments and Methods in Physics Research* **A249** 468
[64] T. Elevant et al 1991 *Nuclear Instruments and Methods in Physics Research* **A306** 331
[65] M. Gatu Johnson et al 2006 *Review of Scientific Instruments* **77** 10E702
[66] A. Hjalmarsson et al 2003 *Review of Scientific Instruments* **74** 1750
[67] N. P. Hawkes et al 1999 *Review of Scientific Instruments* **70** 1134
[68] S. Conroy et al 2008 *Review of Scientific Instruments* **79** to be published
[69] J. M. Adams et al 1993 *Nuclear Instruments and Methods in Physics Research* **A329** 277
[70] O. N. Jarvis and S. Conroy 2002 *Plasma Physics and Controlled Fusion* **44** 1651
[71] S. Popovichev et al 2004 *31st EPS Conference on Plasma Physics* **28G** 5.173 (London England)
[72] A. Hjalmarsson 1999 *“Study of signal to background ratio in fusion neutron spectroscopy measurements at JET for next step tokamak applications”* Uppsala
[73] J. Källne et al 2000 Physical Review Letters, **85** 1246
[74] A. Combo et al 2003 *Fusion Engineering and Design* **71** 151

[75] http://www.scionix.nl
[76] G. Wikström 2005 *"Performance studies of phoswich detectors in the upgraded Magnetic Proton Recoil neutron spectrometer"* Uppsala 05#01.
[77] L. Bertalot 2007 Private communication
[78] S. Conroy 1990 Ph. D. Thesis (Imperial College, London, UK)
[79] W. W. Heidbrink and G. J. Sadler 1994 *Nuclear Fusion* **34** 535
[80] M. Olsson et al 1993 *Plasma Physics and Controlled Fusion* **35** 179

Acta Universitatis Upsaliensis

Digital Comprehensive Summaries of Uppsala Dissertations from the Faculty of Science and Technology 556

Editor: The Dean of the Faculty of Science and Technology

A doctoral dissertation from the Faculty of Science and Technology, Uppsala University, is usually a summary of a number of papers. A few copies of the complete dissertation are kept at major Swedish research libraries, while the summary alone is distributed internationally through the series Digital Comprehensive Summaries of Uppsala Dissertations from the Faculty of Science and Technology. (Prior to January, 2005, the series was published under the title "Comprehensive Summaries of Uppsala Dissertations from the Faculty of Science and Technology".)

Distribution: publications.uu.se
urn:nbn:se:uu:diva-9296

ACTA
UNIVERSITATIS
UPSALIENSIS
UPPSALA
2008

Paper I

REVIEW OF SCIENTIFIC INSTRUMENTS **77**, 10E717 (2006)

New MPRu instrument for neutron emission spectroscopy at JET

H. Sjöstrand, L. Giacomelli, E. Andersson Sundén, S. Conroy, G. Ericsson,
M. Gatu Johnson, C. Hellesen, A. Hjalmarsson, J. Källne, E. Ronchi,
M. Weiszflog, and G. Wikström
INF, Uppsala University, EURATOM-VR Association, Uppsala SE-751 20, Sweden

G. Gorini and M. Tardocchi
Istituto di Fisica del Plasma, EURATOM-ENEA-CNR Association, Consorzio RFX, Padova 4–35127, Italy

A. Murari
EURATOM-ENEA-CNR Association, Consorzio RFX, Padova 4–35127, Italy

G. Kaveney and S. Popovichev
*EURATOM-UKAEA Association, JET, Culham Science Centre, Abingdon, Oxfordshire,
OX14 3EA, United Kingdom*

J. Sousa, R. C. Pereira, A. Combo, and N. Cruz
*Associação EURATOM/IST, Centro de Fusão Nuclear, Instituto Superior Técnico,
Avenida Rovisco Pais 1, 1049-001 Lisboa, Portugal*

JET-EFDA Contributors[a]

(Received 7 May 2006; presented on 9 May 2006; accepted 6 July 2006;
published online 11 October 2006)

The MPRu is an upgrade of the magnetic proton recoil (MPR) neutron spectrometer that has been used for 14 MeV DT neutron measurements at JET during the DTE1 (1997) and TTE (2003) campaigns. In this contribution the principles of the MPR and its upgrade will be presented. The MPRu allows measurements of the full range of fusion relevant neutron energies, 1.5–18 MeV, including the 14 MeV DT neutrons, now with significantly reduced background, and also new high-quality measurements of the 2.5 MeV DD neutron component. This improvement is made possible by the use of a new proton recoil detector in combination with custom-built transient recorder cards. The importance of these instrumental improvements for extending the use of the MPRu in diagnosis of D and DT plasmas will be discussed. Results from the first 2.5 MeV measurements performed with the MPRu during JET high level commissioning in April 2006 are presented. © *2006 American Institute of Physics.* [DOI: 10.1063/1.2336459]

INTRODUCTION

The ultimate goal of fusion research is to produce fusion power; hence one of the most fundamental requirements of a fusion experiment is to accurately measure the fusion power and its dependent parameters, such as the ion density and velocity distribution. Fusion experiments normally operate with pure deuterium where the $\mathrm{D}+\mathrm{D}\rightarrow\mathrm{T}+p$ and the $\mathrm{D}+\mathrm{D}\rightarrow{}^{3}\mathrm{He}+n$ (2.5 MeV) reactions take place with nearly the same probability. In more advanced experiments, such as JET and ITER, a mixture of deuterium and tritium is used; this is also the proposed fuel for a future reactor. In a 50:50 DT mixture the $\mathrm{D}+\mathrm{T}\rightarrow{}^{4}\mathrm{He}+n$ (14 MeV) reactions dominate the DD reactions.

The neutrons from the fusion reactions escape the plasma and carry a wealth of information about the core fusion process and its fuel ions; neutron emission spectroscopy (NES) can reveal this information, without perturbing the plasma. With NES one can determine the fusion power,[1] the collective motion of the main plasma, the fuel ion densities, the ion velocity distributions, and hence the effectives of the different heating modes, as well as the bulk fuel ion temperature.[2] In order to determine these parameters one needs a neutron spectrometer with high instrumental resolution, high count rate capability, high efficiency, and immunity to background.

In 1996 a magnetic proton recoil (MPR) neutron spectrometer was installed at JET[3] to perform NES for 14 MeV neutrons and it has provided important information both during the tritium campaign DTE1 in 1997 as well as in the trace tritium experiment (TTE) in 2003. However, the MPR could not perform 2.5 MeV neutron measurements due to insufficient background separation. To extend its operational range to include also the 2.5 MeV spectrum as well as improving the 14 MeV neutron spectroscopy, thus contributing valuable information in both pure D as well as in mixed DT operation, a MPR upgrade (MPRu) was completed in 2005 as part of the JET Enhanced Performance program (JET-EP1). In this article we present the principles of the MPRu and what consequences the upgrade will have on the diag-

---

[a] See the Appendix of J. Pamela *et al.*, Fusion Energy 2004 (Proc. 20th Int. Conf. Vilamoura, 2004), IAEA, Vienna.

Downloaded 22 Aug 2008 to 130.238.67.59. Redistribution subject to AIP license or copyright; see http://rsi.aip.org/rsi/copyright.jsp

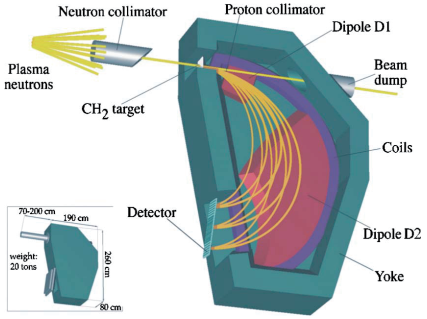

FIG. 1. (Color online) Schematic figure of the MPRu spectrometer, without its radiation shield.

nostic's performance. Some results from simulations of the MPRu will be presented as well as the first data from the high level commissioning at JET in April 2006.

THE MPR PRINCIPLE

The principle and components of the magnetic proton recoil technique are illustrated in Fig. 1. The fusion neutrons are collimated and scatter elastically on hydrogen nuclei (protons) in a thin plastic foil. The recoil protons emitted in the forward direction are allowed to enter the magnetic part of the spectrometer where they are momentum analyzed in the magnetic field and focused onto the focal plane. A focal plane detector composed of an array of plastic scintillators coupled to photomultiplier (PM) tubes register the spatial distribution of the protons. In the central detector channel, protons with an energy of 2450±20 keV will be registered. The spatial distribution of protons over the focal plane detector can be related back to the neutron energy at the foil through the spectrometer's response function.

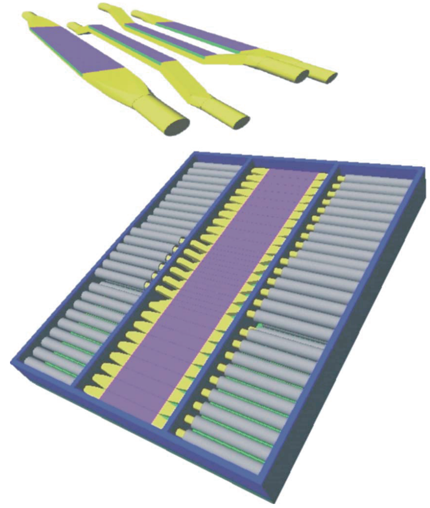

FIG. 2. (Color online) The MPRu hodoscope and its four different types of scintillators.

THE MPRU UPGRADE

To access the 2.5 MeV neutron spectrum and to develop even more detailed 14 MeV spectroscopy, an instrumental upgrade to reduce the background and noise sensitivity and to improve the calibration and the control and monitoring system has been performed. To achieve these goals, several new hardware systems have been installed, the most important being a new focal plane detector. To reduce the background sensitivity of the scintillators, each of the 32 elements of the new hodoscope consists of a two-layered phoswich detector. The top layer facing the incoming protons is the 0.3-mm-thick fast plastic scintillator (BC404, 1.8 ns decay time) in optical contact with the second thicker (2.5/3.2 mm) slow scintillator (BC444, 180 ns decay time). The distinctly different timing properties of the two layers make pulse shape discrimination (PSD) possible; 2.5 MeV protons will be completely stopped within the fast layer, hence being distinguishable from penetrating electrons and gamma induced events, which predominantly give signals in both layers. Neutron induced background will in principle scale with the fast scintillator volume, reducing the intensity of the neutron interference in both 2.5 and 14 MeV measurements. Each phoswich element has two PM tubes attached via light guides (Fig. 2), a configuration that increases the total light collection and gives more uniform longitudinal light collection efficiency. A more detailed description of the new hodoscope and its phoswich detectors are given in Ref. 4.

The PM tubes collect the emitted scintillation light and transform it to electrical signals, which are summed and amplified before being registered by new, custom-built transient recorder cards (TRCs).[5] TRCs, with their wave forms storage capability, allow a detailed PSD, hence enhancing the background separation. The PSD technique of integrating the PM-tube voltage pulse over an early (Q_{fast}) and a late (Q_{slow}) time region has been adopted for this article. The TRC modules also allow an event-by-event analysis including, e.g., base line restoration, noise reduction, and pileup rejection.

The *ab initio* energy calibration of the MPRu system requires good knowledge of the instrument's geometry. To improve the energy calibration of the instrument the relative distances between the different scintillators have been determined to 50 μm precision using a UV light-emitting diode (LED) based scanning system. By combining the results of the UV scans with the alignment and surveying of the fully assembled instrument using JET's digital photogrammetry system (V-STARS),[6] which gives the complete geometry of the MPRu installation in one common frame of reference, it was possible to determine the location of each scintillator relative to the magnetic field and the line of sight to a level of <0.1 mm. This corresponds to a calibration accuracy of about 1 keV at 14 MeV.

The MPRu control and monitoring systems have been upgraded with three new light sources. A custom-built stable LED is used to monitor the short and medium term gain stabilities of the PM tubes. To monitor the long term stability

Downloaded 22 Aug 2008 to 130.238.67.59. Redistribution subject to AIP license or copyright; see http://rsi.aip.org/rsi/copyright.jsp

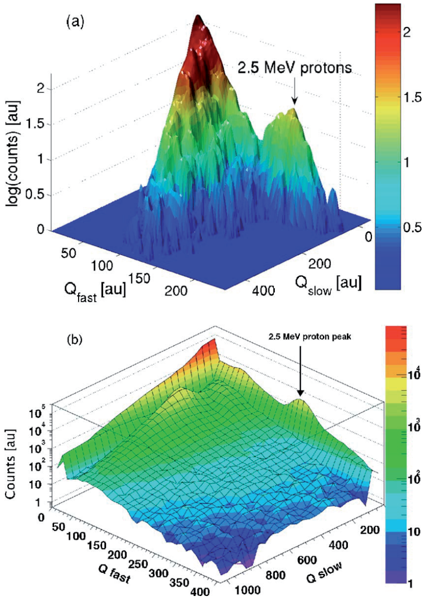

FIG. 3. (Color online) Comparison between (a) experimental data for a central hodoscope channel and (b) simulated data for a central phoswich scintillator. A standard two-gate PSD technique has been used. Q_{fast} and Q_{slow} are the integrations of the PM-tube voltage pulse over an early and a late time region, respectively.

of the LED two YAP:Ce scintillators with embedded ^{241}Am α sources are used as absolute references. In addition, a high repetition rate laser is also available.

MPRu EXPECTED PERFORMANCE

The MPR was upgraded to enable 2.5 MeV neutron spectroscopy as well as to improve the 14 MeV neutron spectroscopy. To simulate the performance of the new detector a GEANT4[7] model was developed. Simulation results indicate that the MPRu system could reach a signal-to-background (S/B) ratio of 10:1 for the 2.5 MeV measurements in D plasmas and 20000:1 for 14 MeV measurements in DT plasmas. For D plasmas the simulations indicate that the background is dominated by penetrating gammas and Compton electrons, but PSD can separate these events from the 2.5 MeV proton peak. A comparison between simulated results and the first preliminary data from the MPRu spectrometer can be seen in Fig. 3, where the background separation can be seen in both cases.

The improved S/B will enable the MPRu to determine the ion temperature and fusion power also in D operations where it was previously not feasible.

FIRST DATA

During the high level commissioning at JET in April 2006 the first 2.5 MeV neutrons were detected with the upgraded instrument. For these measurements the MPRu was set to achieve high efficiency, providing data for the characterization of the instrument and tuning of operational working points. In order to accurately determine the background the MPRu was also operated with a zero B field. Figure 4 show the first 2.5 MeV data analyzed with a traditional short gate–long gate PSD technique; the proton peak is clearly separated from the bulk of the background events and there is an absence of a "proton" peak in the $B=0$ data set. The data in Fig. 4 also give an indication of the experimental S/B situation, which seems to be in line with expectations. A detailed analysis has still to be done, but these first data indicate that the MPRu instrument works as anticipated.

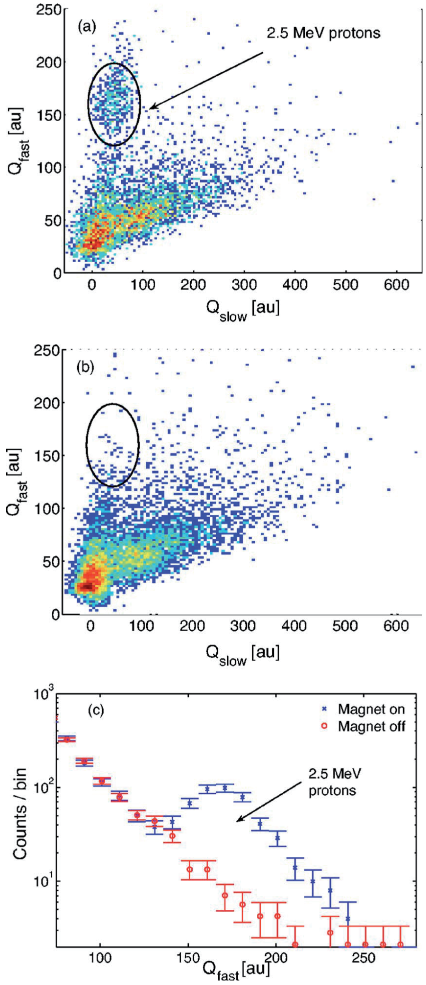

FIG. 4. (Color online) (a) Proton data for a central hodoscope channel, acquired during the commissioning of the MPRu at JET. The recoil proton peak is indicated. (b) Background data collected with a 0 T B field, with slightly better statistics than in (a). (c) The signal and the normalized background data in the 0–200 Q_{slow} region projected on to the Q_{fast} axis.

Downloaded 22 Aug 2008 to 130.238.67.59. Redistribution subject to AIP license or copyright; see http://rsi.aip.org/rsi/copyright.jsp

DISCUSSION AND OUTLOOK

NES through the MPR instrument has proven to be a reliable and accurate tool for diagnosing the core fusion process during seven years of operation at JET. In DT plasmas it has provided high quality data concerning the ion temperature, fusion power, alpha particle heating, etc. In preparation for the next step in fusion research, viz., ITER, the MPR has been upgrade to provide even more detailed information in DT plasmas as well as for the first time prove the MPR technique in pure D operations. The first MPRu results from the JET high level commissioning in April 2006 show that the new instrument performs as projected and indicates that the predicted S/B level can be achieved for 2.5 MeV measurements. The MPRu, together with the new time of flight at optimized rate (TOFOR) spectrometer,[8] represents a significant step forward of the JET NES capability.

ACKNOWLEDGMENTS

This work has been performed under the European Fusion Development Agreement (EFDA) and the Association EURATOM-VR with support from Swedish Research Council, Uppsala University, JET-EFDA.

[1] H. Sjöstrand *et al.*, 31st EPS Conference on Plasma Physics, London, UK Vol. 28G (2004), p. 5.176.
[2] L. Giacomelli *et al.*, Nucl. Fusion **45** 1191 (2005).
[3] G. Ericsson, L. Ballabio, S. Conroy, J. Frenje, H. Hendriksson, A. Hjalmarsson, J. Källne, and M. Tardocchi, Rev. Sci. Instrum. **72**, 759 (2001).
[4] L. Giacomelli *et al.*, Rev. Sci. Instrum., these proceedings.
[5] A. Combo *et al.*, 2003 Fusion Eng. Des. 71, 151 (2004).
[6] The Basics of Photogrammetry, Geodetic Services, Inc., http://www.geodetic.com/Whatis.htm
[7] S. Agostinelli *et al.*, Nucl. Instrum. Methods Phys. Res. A **506**, 250 (2003).
[8] M. Gatu Johnson, Rev. Sci. Instrum., these proceedings.

Downloaded 22 Aug 2008 to 130.238.67.59. Redistribution subject to AIP license or copyright; see http://rsi.aip.org/rsi/copyright.jsp

Paper II

EFDA–JET–PR(08)07

H. Sjöstrand, E. Andersson Sundén, S. Conroy, G. Ericsson, M. Gatu Johnson,
L. Giacomelli, G. Gorini, C. Hellesen, A. Hjalmarsson, S. Popovichev, E. Ronchi,
M. Tardocchi, M. Weiszflog and JET EFDA contributors

Control and Monitoring System of the Upgraded Magnetic Proton Recoil Neutron Spectrometer at JET

“This document is intended for publication in the open literature. It is made available on the understanding that it may not be further circulated and extracts or references may not be published prior to publication of the original when applicable, or without the consent of the Publications Officer, EFDA, Culham Science Centre, Abingdon, Oxon, OX14 3DB, UK.”

“Enquiries about Copyright and reproduction should be addressed to the Publications Officer, EFDA, Culham Science Centre, Abingdon, Oxon, OX14 3DB, UK.”

Control and Monitoring System of the Upgraded Magnetic Proton Recoil Neutron Spectrometer at JET

H. Sjöstrand[1], E. Andersson Sundén[1], S. Conroy[1], G. Ericsson[1], M. Gatu Johnson[1],
L. Giacomelli[1], G. Gorini[2], C. Hellesen[1], A. Hjalmarsson[1], S. Popovichev[3], E. Ronchi[1],
M. Tardocchi[2], M. Weiszflog[1] and JET EFDA contributors*

JET-EFDA, Culham Science Centre, OX14 3DB, Abingdon, UK

[1]*EURATOM-VR Association, Uppsala University, Department of Physics and Astronomy, 75120 Uppsala, Sweden*
[2]*EURATOM-ENEA-CNR Association, Physics Department, Milano-Bicocca University,*
and Istituto di Fisica del Plasma del CNR, Milan, Italy
[3]*EURATOM-UKAEA Fusion Association, Culham Science Centre, OX14 3DB, Abingdon, OXON, UK*
** See annex of M.L. Watkins et al, "Overview of JET Results ",*
(Proc. 21st IAEA Fusion Energy Conference, Chengdu, China (2006)).

Preprint of Paper to be submitted for publication in
Review of Scientific Instruments

ABSTRACT.

Burning plasma experiments such as ITER and DEMO require diagnostics capable of withstanding the harsh environment generated by the intense neutron flux and to maintain stable operating conditions for times longer than present day systems. For these reasons, advanced Control and Monitoring (CM) systems will be necessary for the reliable operation of diagnostics. This paper describes the CM system of the upgraded Magnetic Proton Recoil neutron spectrometer installed at the Joint European Torus focusing in particular on a technique for the stabilization of the gain of the photomultipliers coupled to the neutron detectors. The results presented here show that this technique provides good results over long time scales. The technique is of general interest for all diagnostics that employ scintillators coupled to photomultiplier tubes.

1. INTRODUCTION

The environment close to fusion plasma experiments, where most of the diagnostics are located, is characterized by strong magnetic and radiation fields as well as neutron induced activation. These conditions are expected to become worse in future experiments, such as ITER and DEMO [1]. Such a harsh environment will affect, among many other things, the stability of the operating condition of many diagnostics [2]. In addition, access to the diagnostics will be limited. Diagnostics for ITER should therefore be capable of working reliably for long times with very little intervention and maintenance. These new circumstances require the diagnostic's integrity and stability to be monitored remotely and changes in their operating conditions to be corrected for.

The Joint European Torus (JET) is today the fusion device with operating conditions most similar to those planned for ITER and it provides an excellent testbed for diagnostic research in general and for stability Control and Monitoring (CM) system development in particular. These were the reasons for the installation of the original CM system [3] for the Magnetic Proton Recoil (MPR) [4] 14MeV neutron spectrometer at JET. The MPR has been recently upgraded to extend its energy range to include also 2.5MeV neutrons [5-9]. This, in combination with the progress in data acquisition systems, motivated an upgrade of the CM system. This paper describes the main characteristics and the results of this upgraded CM system. The paper is organized as follows: section 2 describes the MPRu detection system, section 3 the CM system and the gain stabilization technique; the results are presented in section 4 and the conclusions are drawn in section 5.

2. INSTRUMENTATION

The MPR and its upgrade MPRu are described in detail in Refs 3–9 and its basic operating principles are briefly summarized here. Neutrons emitted by the DD and DT fusion reactions occurring in the JET plasma are collimated when they scatter on the hydrogen nuclei (protons) in a thin CH2 foil. The forward scattered protons are momentum analyzed and focused onto the focal plane detector by a system of magnets. The detector is composed of an array of 32 plastic phoswich scintillators that register the spatial distribution (i.e. energy) of the protons, which can be related back to the energy spectrum of the incoming neutrons. As shown in figure 1, each phoswich scintillator consists of a fast scintillator layer (with short decay-time of the scintillation light) followed by a slow scintillator layer (long decay-time); a backing is applied to some scintillators to improve light collection efficiency. Each scintillator is coupled to two Photo-Multiplier Tubes (PMT), which collect the emitted scintillation light. The voltage waveform (signal) from the two PMTs are summed and amplified in a Pulse Summing Amplifier (PSA) before being registered and stored in a Transient Recorder Card (TRC) [10]. The assembly consisting of a single scintillator, the two associated PMTs, the PSA and the TRC will in this paper be referred to as a "channel" as shown in figure 1.

Thus, the data acquisition system records and stores the voltage waveforms from all detector channels associated with an individual event where the interaction of a momentum-analyzed proton in the scintillator constitutes the sought-after signal. Together with protons, background events are present mainly due to Compton-electrons, gammas and neutrons interacting in the scintillators. Gammas and electrons normally deposit their energy in both scintillator layers while protons (of $E_p < 4.7$MeV) deposit all their energy in the fast layer, thus giving rise to the distinct different waveforms shown in figure 2.

In order to separate the protons from the background events the waveform of each event is integrated over two different time intervals indicated by the vertical lines in figure 2. This provides the charges corresponding to short and long gates (Q_S and Q_L) and from the set of Q_S and Q_L values a 2D histogram is produced. An example of such a histogram is shown in figure 3(a) for plasma discharges in which the spectrometer was operated normally except that no magnetic field was applied. Under these conditions, no protons reached the scintillator array but all background events were recorded. Figure 3(b) shows a similar histogram where the spectrometer was set to measure 2.5 MeV neutrons; here both the recoil protons and the background events were recorded. From a comparison of figures 3(a) and 3(b) the proton signature in the 2D histogram is clearly visible as an "island" of events around ($Q_S = 220$, $Q_L = 60$). A Region Of Interest (ROI) covers the region around the proton island and the number of events within this ROI is counted. The same ROI is used for counting the number of background events. Since the background and the background + proton 2D-histograms are obtained for different sets of plasma discharges, the number of background events inside the ROI of the background + proton recording is scaled to the number of background events inside the same ROI of the background-only recording. The scaling between data sets is performed either by using the total neutron yield from the JET fission chambers [11] or by using a part of the 2D-histogram unaffected by the protons (a scaling ROI). This procedure is followed for every channel.

3. THE CONTROL AND MONITORING FUNCTIONS

The system described here is focused on the control and monitoring of the overall environment (section 3.1) and of the electronics gain (section 3.2). The technique for gain correction is described in section 3.3.

3.1 ENVIRONMENTAL PARAMETER MONITORING

The following MPRu environmental parameters are monitored by the CM system: the spectrometer's magnetic field, the magnetic power supply current, the temperature, the pressure and the PMTs high voltages.

The absolute level of the magnetic field is directly related to the energy calibration of the spectrometer. Changes in the magnetic field during data taking would deteriorate the instrumental energy resolution. The field is monitored with two Hall probes at different locations in the magnet. A third Hall probe measures the magnetic field close to the PMTs where the field should be close to zero. The magnetic field is measured with a sampling frequency of 4Hz during every plasma discharge and it is found that changes during a discharge are small enough (<1 Gauss) to be ignored. The magnetic field is also verified to be stable over long periods of time, varying less than 5 Gauss over 3000 plasma discharges. The magnetic field close to the PMTs (but outside their mu-metal magnetic shield) was measured to 14 Gauss, which is sufficiently low not to affect their proper operation.

The temperature is not expected to have any direct influence on the spectrometer response, but changes can affect different subsystems or be an indication of malfunction of a subsystem. The temperature is therefore monitored at the locations of the previously mentioned Hall probes, and in additional at six different positions in and around the spectrometer by Pt100 elements.

The monitoring of the pressure inside the spectrometer is achieved with two vacuum gauges. A too high pressure contributes to a deterioration of the spectrometer's performance due to proton energy loss and straggling resulting in a poorer energy resolution. In addition, at pressures around 10^{-1} mbar arching between the PMTs electrodes could occur, which would cause over--current trips and even lead to permanent damage. Measurements of the pressure show that it is very constant at a value of 10^{-4} mbar, which is also sufficiently low to avoid the above-mentioned problems.

3.2 THE GAIN SYSTEM

As described in section 2, one of the most crucial functions of the data analysis is the separation of proton events from the background. In order to do this the total charge Q has to be linked to the amount of scintillation light produced per event and to the overall electronic "gain" G (see equation 3) by the following relation:

$$Q = eGY \tag{1}$$

where e is the electron charge and Y is the amount of light incident on the photocathode as defined by

$$Y = n_\gamma \varepsilon_{col} \tag{2}$$

where n_γ is the number of photons in the scintillator and ε_{col} is the fraction of those photons that enter the PMTs. The gain G of an individual channel is here defined as:

$$G = A_{PMT}A_{PSA}A_{TRC}t\,\frac{n_{\mathrm{PE}}}{n_\gamma} = A_{PMT}A_{PSA}A_{TRC}tq \qquad (3)$$

where A_{PMT} is the amplification of the PMT, A_{PSA} is the amplification in the summing amplifier, A_{TRC} is the amplification in the TRC, t is the fraction of the signal transmitted in the cables between the PMT and the TRC, n_{PE} is the number of photoelectrons and q is the quantum efficiency of the PMT. From this it is clear that a change in G, and thereby in Q, will lead to a corresponding change in Q_{S} and Q_{L}, requiring the ROI to move and expand accordingly. Consequently, changes in gain have to be monitored and corrected for in order to select the correct ROI in the 2D-histogram as well as to perform a proper background subtraction (see figure 3). The extra complication due to the use of two PMTs is described in section 3.3 and in Appendix A.

A limitation of the previous CM system was its lack of an absolute reference to monitor long-term trends in the gain variation. Instead, it relied on the assumption that the average gain of the system was constant over the time scales for which data needed to be accumulated for sufficient statistics. This system could monitor that the gain variations were within acceptable limits; however, it was not suitable for correcting the gain variations. Since the gain was not stable over long time periods, the proton ROI and the background correction had to be adjusted to accommodate these changes. This setup was acceptable for the previous MPR system, since it was designed to record 14MeV neutron data, where time resolution [1] was of the order 10ms and the proton-to-background ratio of the order 1000:1. The MPRu's 2.5MeV measurement has a time resolution of a couple of seconds and a proton-to-background ratio of between 1 and 10, and hence more precise gain measurements are needed. With the new system the uncertainty in the background level is reduced both in DD and DT experiments.

The preliminary design of the upgraded gain-monitoring system is described in Ref. 5. The final system consists of a custom built LED driver [12] and an Yttrium Aluminum Pervoskite (YAP) [13] scintillator with an embedded ^{241}Am α-source.

The LED light is coupled via an optical fiber to a connector which distributes the light into 38 optical fibers. Excluding 6 spares, each fiber is connected to the backplane of a scintillator. The fiber is coupled at right angle to the back of the scintillator where, after passing through the scintillator, it illuminates a dot of diffuse white paint applied centrally on the front face of the scintillator (see figure 4). In the current mode of operation the LED is used at a repetition rate of 100 Hz before and after each JET discharge for 1 to 4s giving between 100 and 400 LED events. Monitoring during the plasma discharge was done with the MPR in previous DT experiments in order to measure rate dependent gain variations [3], and such measurements can also be done in future DT experiments with the present system. However, this is not necessary in the current DD experiments due to the low count rate. The LED waveform was chosen to be easily distinguishable from other scintillator events, i.e. rectangular and 200ns wide. This is shown in figure 5.

In contrast to the LED, the YAP source provides an absolute light yield reference at a rate of

20Hz. This is one of the most important improvements compared to the previous system. The YAP source faces the PMT photo cathode and is mounted between the light guide and the PMT in the channel for lowest energies, here referred to as channel zero (see figure 4). A typical YAP waveform is shown in figure 5.

The combination of the two light sources enables the gain stability to be monitored as described in the next section. Event identification is performed by a correlation analysis, where first "typical" LED and YAP waveforms are derived by averaging over a large data set when only one type of event is present. Subsequently, the correlation coefficient between each registered waveform and the typical waveform is calculated. If the correlation is greater than a certain minimum value (here 0.8), the waveform is identified as a LED or YAP event. When the events have been identified the total charge, $Q = Q_S + Q_L$, is calculated for each individual YAP or LED event. For each JET discharge the average charge of all LED and all YAP waveforms are calculated separately and are indicated as $\overline{Q}_{\mathrm{LED}}$ and $\overline{Q}_{\mathrm{YAP}}$ respectively. Assuming a Gaussian distribution of Q the statistical uncertainty of the mean (the precision with which the mean can be determined), $\Delta\overline{Q}$, is given by:

$$\Delta\overline{Q} = \frac{\sigma}{\sqrt{N}} \tag{4}$$

where σ is the spread of the Q distribution given as the standard derivation and N is the total number of waveforms. The size of σ is dependent on the number of photoelectrons in each waveform as expressed by:

$$\frac{\sigma}{\overline{Q}} = \frac{\sqrt{n_{pe}}}{n_{pe}} \tag{5}$$

3.3 METHOD FOR GAIN MONITORING AND CORRECTION

The method for gain monitoring relies on the assumptions that the following three quantities are constant over time: (i) the YAP scintillation light yield due to the α source, (ii) the light collection efficiency (see equation 2) and (iii) the light transmission from the LED to the scintillator (see equation 10). The technique used for monitoring the gain is based on (a) a reference plasma discharge which provides the reference to which changes in the gains can be compared and (b) the plasma discharge for which changes in the gain need to be measured.

Since the α source is present only in channel zero, changes in the gain of all the other channels have to be inferred from changes of the gain of channel zero. The first step is therefore to determine the change in the gain of channel zero between the reference plasma discharge (superscript r) and the test plasma discharge (superscript k). In order to do this, the average charge per $\overline{Q}_{LED,0}$ event and per YAP event $\overline{Q}_{YAP,0}$ are measured for channel zero. Using equation (1) we can write:

$$\begin{aligned} \overline{Q}^{r}_{YAP,\,0} &= eG^{r}_{0}Y_{YAP} \\ \overline{Q}^{k}_{YAP,\,0} &= eG^{k}_{0}Y_{YAP} \end{aligned} \tag{6}$$

from which the relative change in the gain of channel zero can be obtained as:

$$\frac{G_0^k}{G_0^r} = \frac{\overline{Q}_{YAP,\,0}^k}{\overline{Q}_{YAP,\,0}^r} = \eta_{k,\,r} \tag{7}$$

Using again equation (1), it is possible to write the relation between the average charge, the gain and the collected LED light for channel zero as:

$$\begin{cases} \overline{Q}_{LED,\,0}^r = eG_0^r Y_{LED,\,0}^r \\ \overline{Q}_{LED,\,0}^k = eG_0^k Y_{LED,\,0}^k \end{cases} \tag{8}$$

from which, using relation (7) it is possible to obtain the change in the collected LED light:

$$\frac{Y_{LED,\,0}^k}{Y_{LED,\,0}^r} = \frac{1}{\eta_{k,\,r}} \frac{\overline{Q}_{LED,\,0}^k}{\overline{Q}_{LED,\,0}^r} \tag{9}$$

The absolute value of $Y_{LED,i}$ is different for every channel, *i*, and can be derived from equation 2:

$$Y_{LED,\,i} = n_{y,\,i}\varepsilon_{col,\,i} = \gamma_{LED} f_{fibre,\,i} t_{fiber,\,i} \varepsilon_{dot,\,i} \varepsilon_{col,\,i} \tag{10}$$

where γ_{LED} is the total amount of light produced by the LED, $f_{\mathrm{fibre,i}}$ is the fraction of light from the LED that via the connector enters the fiber, $t_{\mathrm{fiber,i}}$ is the transmission in the optical fiber, $\varepsilon_{\mathrm{dot,i}}$ is the reflection efficiency of the painted dot and $\varepsilon_{\mathrm{col,i}}$ is the transmission efficiency from the painted dot to the photocathode. The parameters $f_{\mathrm{fibre,i}}$, $t_{\mathrm{fiber,i}}$, $\varepsilon_{\mathrm{dot,i}}$, and $\varepsilon_{\mathrm{col,i}}$ are different for each channel, but have been assumed to be constant over time. Since all channels uses the same LED, γ_{LED} is the same for all channels. Consequently, changes $\gamma_{LED,\mathrm{i}}$ can be assumed to be the same for all channels so that it is possible to write:

$$\frac{Y_{LED,\,i}^k}{Y_{LED,\,i}^r} = \frac{\gamma_{LED}^k}{\gamma_{LED}^r} = \frac{Y_{LED,\,0}^k}{Y_{LED,\,0}^r} = \lambda_{k,\,r} \tag{11}$$

Changes in the gain for the specific channel *i* can then be determined observing that:

$$\begin{cases} \overline{Q}_{LED,\,i}^r = eG_i^r Y_{LED,\,i}^r \\ \overline{Q}_{LED,\,i}^k = eG_i^k Y_{LED,\,i}^k \end{cases} \tag{12}$$

from which follows:

$$\frac{G_i^k}{G_i^r} = \frac{1}{\lambda_{k,\,r}} \frac{\overline{Q}_{LED,\,i}^k}{\overline{Q}_{LED,\,i}^r} \tag{13}$$

The above equation is then used to correct for gain variations by normalizing the amplitude of all waveforms (proton, background, YAP and LED) using the appropriate G_i^k/G_i^r ratio.

Besides long term variations, it is also interesting to monitor if G_i and $Y_{\mathrm{LED,i}}$ are stable on short timescales such as between consecutive discharges. To test this, the relative difference, Λ, for the investigated parameter between two consecutive JET discharges can be investigated. Λ defined as:

$$\Lambda_k = 1 - \frac{X^{k-1}}{X^k} \tag{14}$$

where X is either G_i or γ_{LED} and k is the discharge number.

Another parameter useful to determine is the variation in the relative spread, $\sigma/\bar{Q}$, in Q_{LED}. Equations (1-3) show that Q_{LED} depends on the amplification (in the TRC, PSA and in the PMTs) and on the number of photoelectrons (which, in turn is affected by the quantum efficiency, photon production and photon collection). If the number of photoelectrons decreases then $\sigma/\bar{Q}$ should increase.

Since there are two PMTs coupled to each scintillator, $\sigma/\bar{Q}$ also depends on the balancing of the two PMTs. How the balancing of the PMTs affects $\sigma/\bar{Q}$ is described in Appendix 1 and is summarized as:

$$\frac{\sigma}{\bar{Q}} = \frac{\sqrt{1+\alpha\beta^2}}{\sqrt{n_{PE,\,L}}\,(1+\alpha\beta)} \tag{15}$$

with $\alpha = n_{PE,R}/n_{PE,L}$ and $\beta = A_{PMT,R}/A_{PMT,L}$, where the indices R and L represents the right and left PMT, respectively. Note that equation (15) is minimized if β is equal to 1.

4. EXPERIMENTAL RESULTS

The MPRu CM system was in operation at JET between September 2006 and April 2007 and CM data was collected for JET Discharge No's: 67672 to 70749. In this section we describe the results for the gain and LED monitoring system, obtained during this period.

4.1 YAP AND LED STABILITY

The assumption of constant light production from the YAP was assessed by measuring $\sigma(Q_{YAP})/\bar{Q}_{YAP}$, which was found constant over time. This indicates constant photoelectron production, which strongly supports the hypothesis that the YAP light production was constant. The variation of γ_{LED} over time can be seen in figure 6 together with temperature variations. A strong covariation between the LED temperature and γ_{LED} is observed.

A positive dependence of γ_{LED} on the LED temperature was also found during tests performed in the laboratory before installation at JET and it is believed to be due to the electronics driving the LED [12]. Note that the measurement of the temperature is not necessary for the gain monitoring, since the required data for the gain corrections is directly accessed from the LED light yield measurements. However, by also measuring the temperature a better understanding of the LED behavior can be achieved.

After plasma Discharge No: 69750, the number of collected LED events for each plasma discharge was increased from approximately 100 to around 400 in order to reduce the statistical spread

After Discharge No: 69750 the LED was also given more time to warm up before operation, which explains the jump in the data in figure 6. The results presented here are based on data collected after Discharge No: 69750 for a total of 800 discharges. From the statistical analysis, it is found that the relative uncertainty in the average charge per LED event $\Delta\bar{Q}_{\mathrm{LED},0}/\bar{Q}_{\mathrm{LED},0}$ is 0.21% and $\Delta\bar{Q}_{\mathrm{YAP},0}/\bar{Q}_{\mathrm{YAP},0}$ is 0.23% and hence the estimated $\Delta\gamma_{\mathrm{LED}}/\gamma_{\mathrm{LED}}$ is 0.31%. The relation below can then be derived from an error propagation of equation 14:

$$\sigma_{true}\,[\Lambda\,(X)]^2 = \sigma_{measured}\,[\Lambda\,(X)]^2 - 2\,(\Delta X)^2 \tag{16}$$

Equation 16 relates the true variation in the physical parameter X, $\sigma_{\mathrm{true}}\,[\Lambda(X)]$, to the spread in the data that has been observed: $\sigma_{\mathrm{measured}}\,[\Lambda(\mathrm{X})]$; assuming no statistical errors in the measurement, these numbers should obviously be the same. Using equation 16 $\sigma_{\mathrm{true}}\,[\Lambda(\gamma_{\mathrm{LED}})]$ is estimated to be 0.32%, where in this case $\sigma_{\mathrm{true}}\,[\Lambda(\gamma_{\mathrm{LED}})]$ is the spread in the data that cannot be ascribed to other effects than light yield variations of the LED source.

4.2 GAIN STABILITY

The relative gain variation over time of all 32 channels has been analyzed and a few selected examples are shown in figure 7.

The discharge to discharge variation parameter Λ has also been analyzed for all channels and the distributions of $\Lambda(G_1)$ and $\Lambda(G_{31})$ are shown in figure 8.

Using equation 16, $\sigma_{\mathrm{true}}\,[\Lambda(G_{\mathrm{i}})]$ has been calculated for all channels. It is found that $\sigma_{\mathrm{true}}\,[\Lambda(G_{\mathrm{i}})]$ is centered at zero for most channels except for channels 3, 7 and 31. These three channels experience a real significant gain variation also on short time scales.

If the dramatic decrease in gain observed, e.g. in channel 9 (figure 7), is as a consequence of a reduction of photoelectrons one would expect an increase in $\sigma(\bar{Q}_{\mathrm{LED},9})/\bar{Q}_{\mathrm{LED},9}$. Figure 9 shows that this is not the case, indicating that the amount of light collected by the PMT and the quantum efficiency are constant and that the reduction of the gain is due to a reduction in the amplification or transmission (see equation 3).

For most of the channels $\sigma(Q_{\mathrm{LED}})/\bar{Q}_{\mathrm{LED}}$ is constant indicating that for each LED event the number of produced photoelectrons is constant. However, for some channels there are some features in the variation of $\sigma(Q_{\mathrm{LED}})/\bar{Q}_{\mathrm{LED}}$ that need explanations.

Figure 10 shows the time variation of $\sigma(Q_{\mathrm{LED},10})/\bar{Q}_{\mathrm{LED},10}$ together with the noise level measured before the event is recorded (baseline noise). The covariation observed between the noise and the $\sigma(Q_{\mathrm{LED},10})/\bar{Q}_{\mathrm{LED},10}$ is expected since an increased level of noise should broaden the charge distribution. The sudden decrease in gain around 69500 is due to a temporary voltage trip of one of the two PMTs of channel 10. This gives the rise in $\sigma(Q_{\mathrm{LED},10})/\bar{Q}_{\mathrm{LED},10}$ as expected from equations 15 (and Appendix 1). There has been no observation of increased $\sigma(Q_{\mathrm{LED}})/\bar{Q}_{\mathrm{LED}}$ that could be coupled to a reduction in the number of photoelectrons. The observed change in Gain must thus be connected to a change in the transmission of the signal or in the amplification of the PMTs, the PSA or the TRC (see equation 3).

4.3 GAIN CORRECTIONS

An example of the gain correction with the technique described in section 3.3 is shown in figure 11 where the charge distribution for proton events is shown for two sets of JET discharges. The first set comprises Discharge No's: 68000 to 68200 and the second Discharge No's: 69000 to 70100. Comparing panels (a) and (b) of figure 11 it can be seen that the charge distribution for the second set has moved. Using the method described in section 3.3, the relative changes in the gains were calculated and a gain corrected charge distribution is shown in figure 11 panel (c). It is clearly seen that the gain correction is working properly.

CONCLUSION

In this paper, the results of the first tests with the upgraded CM system for the MPRu have been presented showing that the combination of an absolute stable YAP light source and a LED, together with a specifically designed data acquisition system, makes it possible to monitor the system's overall gain variation. The use of offline analysis enables the monitoring of a wide parameter space, such as the system's amplification, the photoelectron statistics, the noise and the LED stability. Furthermore, the CM system, together with the gain correction technique presented here, is able to compensate for gain drift over long time periods. This result is very important in consideration of possible changes to the properties of the scintillators and of the PMTs due to aging or neutron damage that can be expected to become a series problem in ITER and, later, in DEMO. Such changes can be corrected for with a similar system. This method is valid in general for any system that employs scintillators and PMTs and is not restricted to the MPRu neutron spectrometer for which the CM system presented here has been specifically designed.

ACKNOWLEDGMENTS

This work has been performed under the European Fusion Development Agreement (EFDA) and the Association EURATOM-VR with support from Swedish Research Council, Uppsala University and JET-EFDA. The views and opinions expressed herein do not necessarily reflect those of the European Commission. Marco Cecconello and Leif Nilsson are acknowledged for contributing with valuable comments.

REFERENCES

[1]. A. Donné et al., Nucl Fusion **47** (2007) S337

[2]. E. Hodgson et al. 33rd European Physical Society Conference On Controlled Fusion and Plasma Physics, Rome (2006) P1.119

[3]. M. Tardocchi et al., Nucl. Instr. and Meth. A 485 (2002) 624
[4]. G. Ericsson et al., Rev. Sci. Instrum., **72** (2001) 759
[5]. M. Tardocchi et al., Rev. Sci. Instrum. **75**, 3543 (2004)
[6]. L. Giacomelli et al., Rev. Sci. Instrum., **77** (2006) 10E708
[7]. H. Sjöstrand et al., Rev. Sci. Instrum., **77** (2006) 10E717
[8]. E. Andersson Sundén et al., 33rd European Physical Society Conference On Controlled Fusion and Plasma Physics, Rome (2006) P1.071
[9]. G. Ericsson et al., Proceedings of Science FNDA, 039 (2006)
[10]. A. Combo et al., Fusion Eng. Des., **71** (2004)151.
[11]. O.N. Jarvis, Plasma Phys. Control Fusion, **36** (1994) 209
[12]. E. Ronchi, "A bipolar approach for high performance, stability and power in the nanosecond time scale", to be published.
[13]. http://www.scionix.nl

APPENDIX 1: ON PMT BALANCING

Often more than one PMT is connected to a scintillator and the signals from the different PMTs are summed. For example, in the MPRu each scintillator is coupled to two PMTs and the PMT signals are summed in a summing amplifier. In these cases the balancing of the PMTs' amplification, A, and their photoelectron production (n) is important for the resulting distribution of the collected charged, Q. The photoelectron production, n, is given by equation A1.

$$n = n_{\gamma} \cdot \varepsilon \cdot q \tag{A1}$$

where n_{γ} is the number of photons, ε is the photon collection efficiency and q is the photocathode quantum efficiency.

This appendix describes how the PMT balancing affects the Q distribution, which is described by the one standard derivation spread, σ, and mean, $\overline{Q}$:

$$\sigma = eA\sqrt{n} \tag{A2}$$

$$\overline{Q} = eA \cdot n \tag{A3}$$

$$\frac{\sigma}{\overline{Q}} = \frac{eA\sqrt{n}}{eA \cdot n} = \frac{1}{\sqrt{n}} \tag{A4}$$

where e is the electron charge. Since the signals from the different PMTs are being summed the total mean and spread are:

$$\sigma = \sqrt{\sum_i \sigma_i^2} \tag{A5}$$

$$\overline{Q} = \sum_i \overline{Q_i} = \sum_i A_i \cdot n_i \tag{A6}$$

where the index i indicates the different PMTs.

From equation A5 and A6 we find that for multiple PMTs coupled to a single scintillator the relative spread can be expressed as:

$$\frac{\sigma}{\overline{Q}} = \frac{\sqrt{\sum_i \sigma_i^2}}{\sum_i A_i \cdot n_i} = \frac{\sqrt{n_1} \cdot A_1 \sqrt{\sum_i \alpha_i \beta_i^2}}{n_1 \cdot A_1 \sum_i \alpha_i \beta_i} = \frac{\sqrt{\sum_i \alpha_i \beta_i^2}}{\sqrt{n_1} \sum_i \alpha_i \beta_i} \tag{A7}$$

where

$$\alpha_i = \frac{n_i}{n_1} \tag{A8}$$

$$\beta_i = \frac{A_i}{A_1} \tag{A9}$$

In the special case when two PMTs are coupled to the scintillator as for the MPRu $\alpha_1 = 1$, $\beta_1 = 1$ and equation A7 simplifies to:

$$\frac{\sigma}{\overline{Q}} = \frac{\sqrt{1 + \alpha\beta^2}}{\sqrt{n_1}\,(1 + \alpha\beta)} \tag{A10}$$

When designing a PMT-scintillator system normally one wants to minimize the spread given by Equation A7 or A10. It is found that $\sigma/\overline{Q}$ is minimized by β equal to one independent of the size of α. This means that the amplification for all the PMT's should be the same. This is somewhat in contrast to common knowledge where it is normally believed that the product of α and β should be equal to one, i.e. the product of the number of the number of photoelectrons and the amplification should be the same for all PMTs (or equal pulse amplitude).

The above arguments relies on the assumption that the collection efficiency, ε, for the two PMTs are linearly positive interdependent. This is true for the LED light in the MPR (see main paper), which deposit its light on the same spot for every event. However for protons and background events which are spread over the entire scintillator ε is varying. In these cases the variation in collected charge is expressed by equation A11.

$$\frac{\Delta Q}{Q} = \frac{\sum_i n_\gamma \cdot \Delta\varepsilon_i \cdot q_i \cdot A_i + \sum_i A_i \cdot \Delta n_i}{\sum_i n_\gamma \cdot \varepsilon_i \cdot q_i \cdot A_i} = \frac{\sum_i q_i \cdot \Delta\varepsilon_i \cdot A_i}{\sum_i q_i \cdot \varepsilon_i \cdot A_i} + \frac{\sum_i A_i \cdot \Delta n_i}{\sum_i A_i \cdot n_i} \tag{A11}$$

where Δn_i is the variation due to photoelectron statistics and $\Delta\varepsilon_i$ is the variation in ε. Equation A11 is what should be minimized in any PMT-scintillator system in order to get the narrowest charge distribution. If the Δn_i term in equation A11 is dominant or if there is a linear positive correlation between the different $\Delta\varepsilon$ terms, the situation described in equations A7 to A10 is adequate. Otherwise a more complete simulation of the PMT-scintillation setup and its radiation field has to be done in order to optimize the performance. In the case when there are two PMTs and the $\Delta\varepsilon$ terms are the dominant contribution equation A11 simplifies to:

$$\frac{\Delta Q}{Q} = \frac{q_1 \cdot \Delta\varepsilon_1 \cdot A_1 + q_2 \cdot \Delta\varepsilon_2 \cdot A_2}{q_1 \cdot \varepsilon_1 \cdot A_1 + q_2 \cdot \varepsilon_2 \cdot A_2} \tag{A12}$$

If there is a linear negative proportionality between $\Delta\varepsilon_1$ and $\Delta\varepsilon_2$ (see equation A13).

$$\Delta\varepsilon_1 = -k \cdot \Delta\varepsilon_2 \tag{A13}$$

where k is a positive proportionality constant. The solution to minimize equation A11 is expressed in equation A14.

$$q_1 \cdot A_1 = k \cdot q_2 \cdot A_2 \tag{A14}$$

The condition in equation A11 does normally not hold true, which is also the case for the MPRu described in the main paper. Consequently the MPRu-system would have benefited from a full optimization in the balancing of the PMTs.

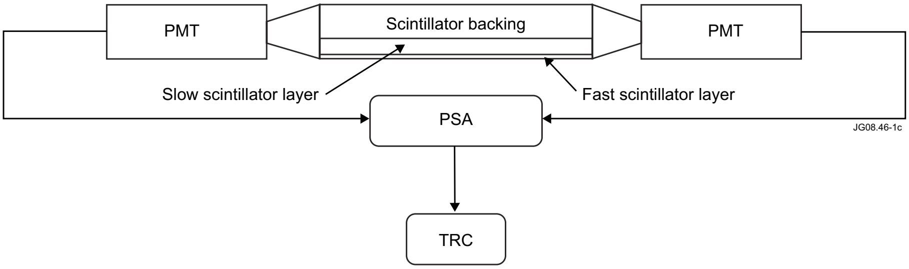

Figure 1: The different components for an MPR “channel” including the scintillator, the Photo-Multiplier Tubes (PMT), the pulse summing amplifier (PSA) and the Transient Recorder Card (TRC). The two scintillator layers and the scintillator backing are also indicated (not to scale).

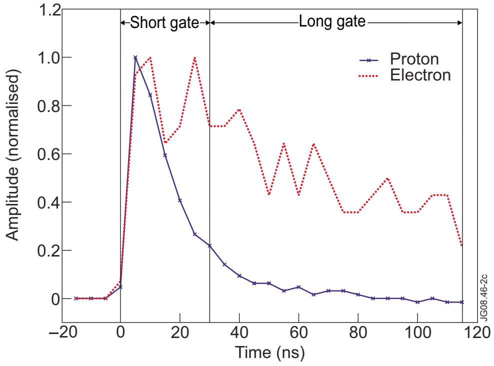

Figure 2: Waveforms normalized to the peak amplitude due to a single 2.5MeV proton (blue line with crosses) and a single background event (red broken line). The vertical lines indicate the two integration intervals used to calculate Q_S and Q_L (see text for details).

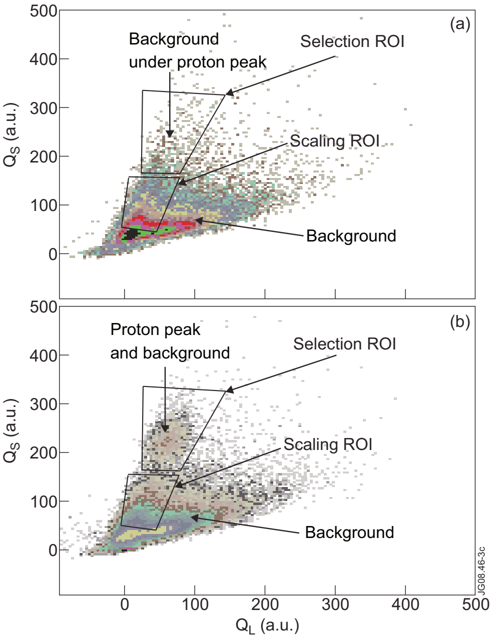

Figure 3: Example of a 2D-histogram obtained from the short vs. long gate analysis when (a) only the background is recorded and (b) also the protons are recorded. The ROIs used for proton selection, background subtraction and background scaling are also shown.

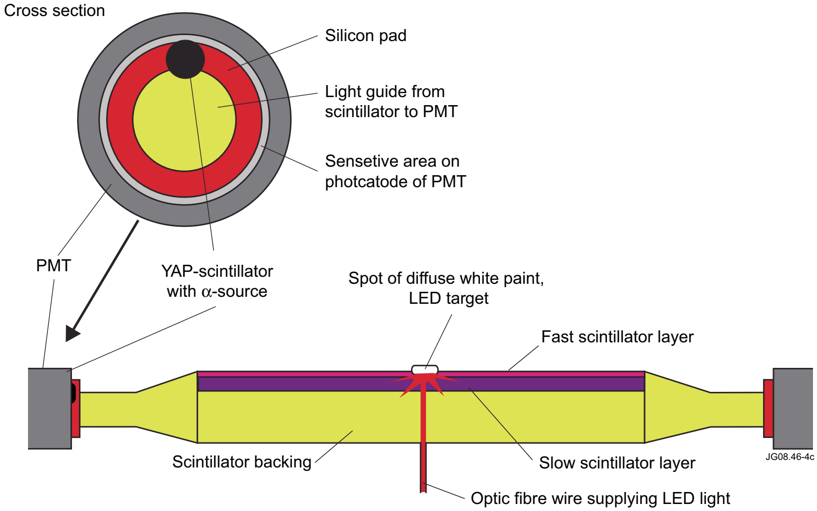
Cross section
Silicon pad
Light guide from
scintillator to PMT
Sensetive area on
photcatode of PMT
PMT
YAP-scintillator
with α-source
Spot of diffuse white paint,
LED target
Fast scintillator layer
Scintillator backing
Slow scintillator layer
Optic fibre wire supplying LED light
JG08.46-4c

Figure 4: Schematic overview of the scintillator of channel zero and its light sources. Note that the YAP light source exists only in channel zero, whereas the LED light source is coupled to all scintillators.

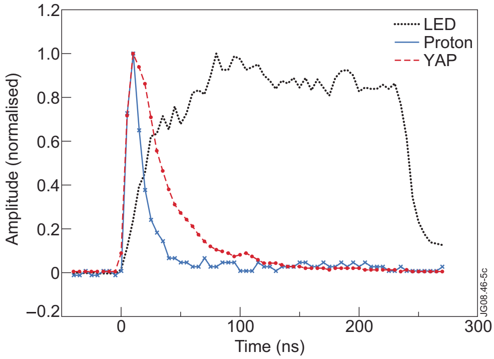

Figure 5: Waveforms normalized to peak amplitude. Proton (blue line with crosses), YAP (red broken line with dots) and LED (black broken line). The shape and amplitude of LED waveform was chosen to be easily distinguished from the YAP and background events.

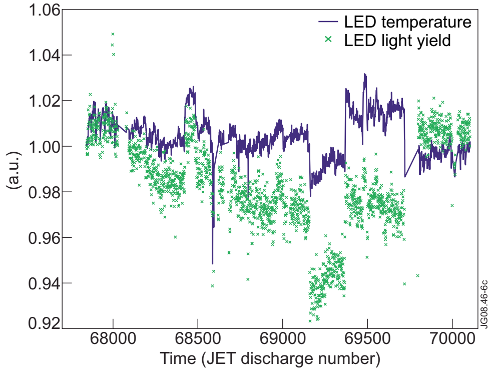

Figure 6: Time trace of the LED light yield (green crosses) and of the LED temperature (blue line) normalized to the first data point. The increase in the LED light yield from Discharge No: 69750 is due to a change in the operation of the LED. The data spans a period of about 6 months

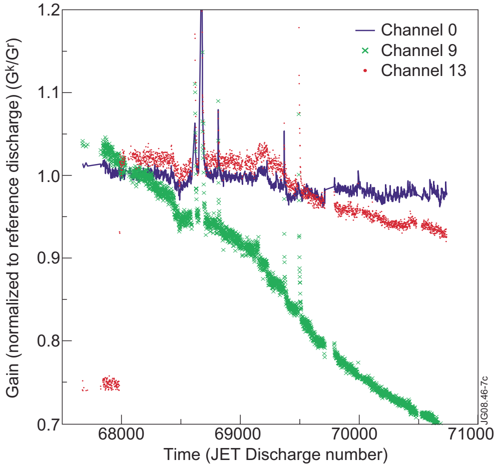

Figure 7: Time traces of G_i^k/G_i^r for channels i = 0 (blue line), 9 (green crosses) and 13 (red dots). Channel 9 shows a dramatic decrease in gain. The jump at plasma Discharge No: 67984 visible in channel 13 is due to an increase in the high voltage supplied to the PMTs of this channel. The spikes in the data are due to PMT over-current trips and subsequent reapplication of the PMT high-voltage.

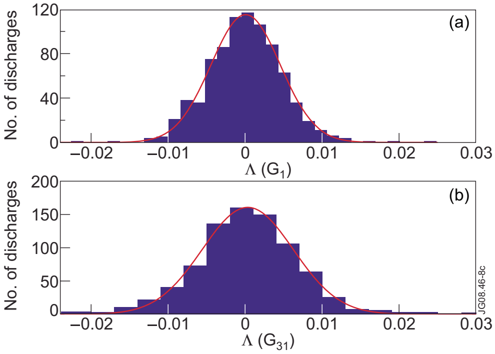

Figure 8: Example of frequency distributions for (a) $\Lambda(G_1)$ and (b) $\Lambda(G_{31})$. The red curves indicate Gaussian fits to the data.

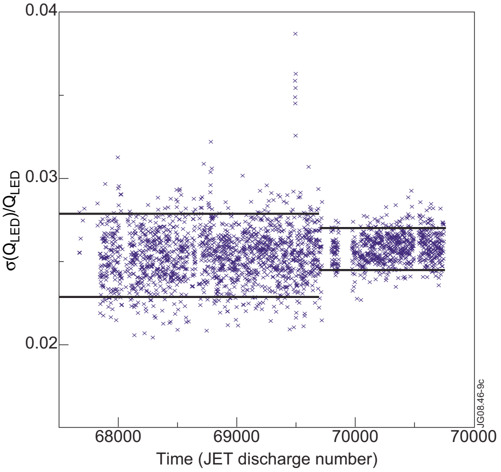

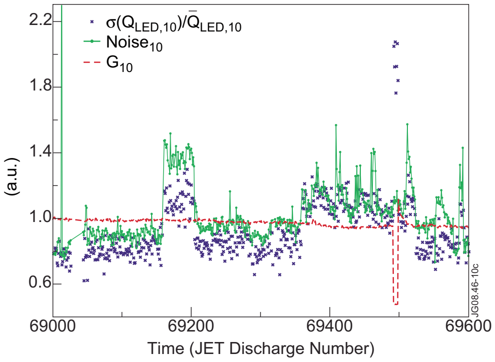

Figure 9: Time trace of $\sigma(Q_{LED}/\bar{Q}_{LED})$: the horizontal lines indicated the one standard deviation limits in $\sigma(Q_{LED,10})$. After plasma discharge 69750, the number of recorded LED waveforms was increased resulting in a reduced statistical uncertainty. This behavior is representative for most of the channels.

Figure 10: Channel $i = 10$ is an example of a channel that experience variations of $\sigma(Q_{LED,10})/\bar{Q}_{LED,10}$ (blue crosses). Time trace of G^k_{10}/G^r_{10} is also shown (red broken line) together with the baseline noise (green line with dots).

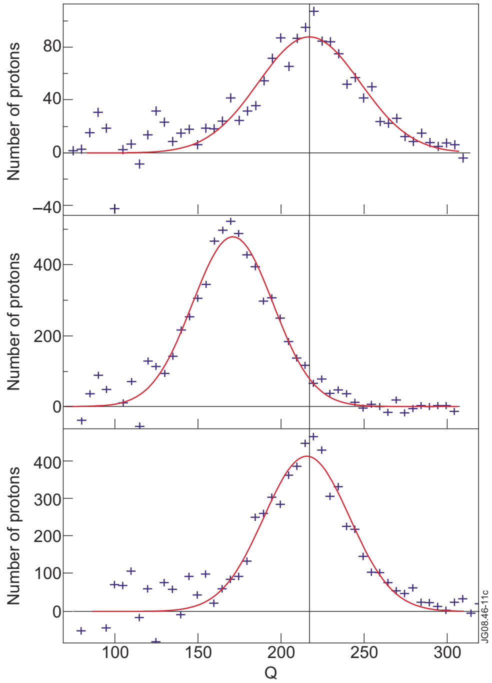

Figure 11: Example of gain correction applied to proton events. The top and middle panels show the distribution of the total collected charge per proton event, Q, for two different sets of JET plasma discharges. The top panel comprises discharges 68000 to 68200, while the middle panel includes discharges 69000-70100. The bottom panel shows the gain corrected proton charge distribution for discharges 69000-70100. The red continues lines are Gaussian fits to the data.

Paper III

UU-NF 08#05

(September 2008)

UPPSALA UNIVERSITY NEUTRON PHYSICS REPORT

ISSN 1401-6269

UPPSALA
UNIVERSITET

THE THIN FOIL MAGNETIC PROTON RECOIL NEUTRON SPECTROMETER MPRU

E.Andersson Sundén, H.Sjöstrand, S.Conroy, G.Ericsson, M.Gatu Johnson, L.Giacomelli, C.Hellesen, A.Hjalmarsson, E.Ronchi, M.Weiszflog, J.Källne, G.Gorini, M.Tardocchi, A.Combo, N.Cruz, A.Batista, R.Pereira, R.Fortuna, J.Sousa, S.Popovichev and JET-EFDA contributors

---

UPPSALA UNIVERSITY
DEPARTMENT OF PHYSICS AND ASTRONOMY
PROGRAM OF APPLIED NUCLEAR PHYSICS
UPPSALA, SWEDEN

THE THIN FOIL MAGNETIC PROTON RECOIL NEUTRON SPECTROMETER MPRU

E.ANDERSSON SUNDÉN, H.SJÖSTRAND, S.CONROY, G.ERICSSON,
M.GATU JOHNSON, L.GIACOMELLI, C.HELLESEN, A.HJALMARSSON,
E.RONCHI, M.WEISZFLOG, J.KÄLLNE[1], G.GORINI[2], M.TARDOCCHI[2],
A.COMBO[3], N.CRUZ[3], A.BATISTA[3], R.PEREIRA[3], R.FORTUNA[3], J.SOUSA[3],
S.POPOVICHEV[4] AND JET-EFDA CONTRIBUTORS*

Uppsala University, Department of Physics and Astronomy, 751 20 Uppsala, Sweden

1Uppsala University, Department of Engineering Sciences, 751 21 Uppsala, Sweden

2 Physics Department, Milano-Bicocca University, and Istituto di Fisica del Plasma del CNR, Milan, Italy 3Centro de Fusão Nuclear, Instituto Superior Técnico, Av. Rovisco Pais 1, 1049-001 Lisboa, Portugal 4 JET-EFDA, Culham Science Centre, OX14 3DB, Abingdon, UK See the Appendix of *M.L.Watkins et al., Fusion Energy 2006 (Proc. 21st Int. Conf. Chengdu, 2006) IAEA, (2006)*

Neutrons are produced in fusion energy experiments with both deuterium (D) and deuterium - tritium (DT) plasmas. Neutron spectroscopy is a valuable tool in the study of the underlying fuel ion populations. The Magnetic Proton Recoil neutron spectrometer, originally installed at JET in 1996 for 14-MeV neutron measurements, has been upgraded, with the main aim to improve its signal to background ratio (S/B), making measurements of the 2.5-MeV neutron emission in D plasmas possible. The upgrade includes a new focal plane detector, based on the phoswich technique and consequently less sensitive to background, and a new custom designed digital data acquisition system based on transient recorder cards. Results from JET show that the upgraded MPRu can measure 2.5-MeV neutrons with a S/B = 5, an improvement with a factor of 50 compared to the original MPR. From this, together with simulation, a S/B of $2 \cdot 10^4$ in future DT experiments are predicted. The performance of the MPRu is exemplified with results from recent D plasma operations at JET, both concerning the new 2.5-MeV measurements with Ohmic, RF and NB heating, as well as 14-MeV measurements of tritium burn-up neutrons. The upgraded instrument allows for 2.5-MeV neutron emission and deuterium ion temperature measurements in plasmas with low levels of tritium, a feature necessary for the ITER experiment.

UPPSALA UNIVERSITY
DEPARTMENT OF PHYSICS AND ASTRONOMY
PROGRAM OF APPLIED NUCLEAR PHYSICS
UPPSALA, SWEDEN

1 Introduction

Neutrons are produced in fusion energy experiments in deuterium (D) plasmas through the reaction $d+d\rightarrow{}^3He+n$ (E_n=2.5 MeV) and in deuterium - tritium (DT) plasmas through $d+t\rightarrow\alpha+n$ (E_n=14 MeV). Neutron emission spectroscopy (NES) is a valuable tool in fusion energy research, since the neutrons leave the fusion plasma undisturbed and can give information on the state of the fuel ions and thereby on important plasma parameters. NES often focuses on measurements of the dominant 2.5-MeV or 14-MeV neutron emission and phenomena such as ion kinematics, alpha knock-on(1) and plasma heating (2)(3) are studied. However, measurements of the minority-energy emission are also of interest, e.g., the 14-MeV neutrons from tritium burn up in D plasmas (4) and 2.5-MeV neutrons in DT plasma operations; the latter being of particular significance as it would allow an estimate of the density ration, n_d/n_t. Measurements of the 2.5-MeV neutron flux in a substantial 14-MeV neutron background is a requirement for ITER D operations. The high power of the ITER pulses in combination with long particle confinement times will lead to the build-up of a tritium inventory from $d+d\rightarrow t+p$ reactions. DT reactions involving this accumulated tritium will contribute to a strong 14-MeV neutron source.

The measurement conditions close to a fusion reactor are harsh. High levels of background radiation of neutrons and gammas are often present and the stray magnetic field from the fusion machine (tokamak) is an additional complication. In addition, for machines like ITER, temperatures close to the vessel are predicted to be high. Ideally, a fusion neutron spectrometer should be able to handle both a high variability in count rate, reflecting transients in the underlying plasma conditions, a high level of background radiation as well as the other adverse environmental conditions. In the design of a spectrometer for plasma neutron measurements a number of performance indicators need to be taken into account; which depends on the intended application. These performance indicators include: the instrument's sensitivity, i.e., the ability to measure weak components in the neutron emission; the rate capability of useful counts in the spectrum; the energy bite, i.e., the energy range covered by the instrument; the operational and calibration stability; the energy resolution (5); and the efficiency. Furthermore, the system should possess a flexibility (or inherent capability) to cope with neutrons in a broad band of energies, specifically around 2.5 and 14 MeV, and in a wide range of neutron emission intensities (dynamic range). In addition, interfacing issues might be a concern, especially for instruments of considerable size and/or with particular installation requirements.

JET has explored and developed NES since the early 1980's (6). The Magnetic Proton Recoil spectrometer (MPR) concept was conceived in the early 1990's (7) and a first spectrometer of this type was installed at JET in 1996 and has been in operation in all subsequent campaigns (4)(8)(9)(10). The original MPR was optimised for measurements of the 14-MeV neutron emission in high power DT plasmas and designed to provide efficient background rejection in order to discern and determine the weak components of the spectrum. The design was also flexible enough to allow for measurements of the 2.5-MeV neutron emission, although these measurements were severely hampered by a high background level (11). In the 14-MeV case, the MPR has been operated at a maximum signal count rate of 0.61 MHz with a signal-to-background ratio (S/B) of $2\cdot10^3$ (3). The 2.5-MeV neutrons emitted from D plasmas were measured with an $S/B=10^{-1}$.(11)

The MPR has been upgraded (12)(13) as part of the JET enhanced performance programme, JET-EP1 (14). The emphasis of the upgrade has been on the spectrometer's focal plane detector, the associated data acquisition and the control and monitoring system. Some subsystems like the conversion foils and the vacuum system have also seen substantial changes. However, the upgraded spectrometer also retains many of the original components, e.g., the neutron collimator, magnetic system, proton collimator and radiation shielding. The aim of the MPR upgrade project was to improve the S/B for 2.5-MeV neutron measurements in D plasmas by a factor 100 and a factor of 10 in 14-MeV DT plasmas, while retaining the high count rate capability of the system.

The MPR upgrade (MPRu) instrument is described in this paper. Section 2 introduces the measurement principles of the device and the requirements that have to be met for measurements of both 2.5-MeV and 14-MeV neutrons. Section 3 reviews the technical and mechanical solutions adopted for the different subsystems of the device and section 4 describes their operational working points. Section 5 gives a brief description of the installation of the MPRu at JET, both physically and in terms of data acquisition and data transfer. Section 6 presents some results on calibration and performance. Finally, discussion, outlook and conclusions are given in Sections 7, 8 and 9.

2 Measurement principles and requirements

The MPRu is based on the thin-foil proton recoil technique employing a magnetic field for the momentum (energy) separation of the recoil protons. Collimated neutrons impinge on a thin foil, where a small fraction of the neutrons undergo elastic nuclear scattering on hydrogen nuclei (protons). The energies of the recoil protons are

$$E_\mathrm{p} = E_\mathrm{n} \cos^2 \theta_\mathrm{np} \qquad (1)$$

where E_p is the proton energy, E_n is the incoming neutron energy, and θ_np is the scattering angle in the lab system. A circular aperture selects forward scattered protons. By selecting protons in the forward direction the (n,p) cross section is maximised as is the recoil proton energy and improve S/B of the detector. The selected protons enter a magnetic system where they are momentum analysed. Finally, the positions of the protons are actively measured in a position sensitive scintillator array placed in the curved focal plane of the magnet. The application of particle transport in a magnetic field makes it possible to avoid some of the problems associated with placing energy-resolving detectors in or close to the collimated neutron flux.

As mentioned above, the requirements on a high-resolution neutron spectrometer for fusion applications depend partly on the intended application, i.e., on the plasma parameters that one wants to study. It has been the ambition of the MPRu development to design an instrument to explore the full potential of neutron spectroscopic measurements in high power fusion plasmas of both D and DT fuel.

3 Components of the MPRu system

The original MPR design and installation has been described in some detail before (7)(8). Since the measurement principle of the system has not changed, we give only a brief summary here. A schematic overview of the MPRu system is shown in Figure 1. Plasma neutrons pass through a neutron collimator forming a neutron "beam" into the spectrometer. At the end of the collimator, neutrons scatter elastically on the protons of a thin polyethylene (CH_2) foil target. A circular aperture, serving as proton collimator, selects the forward scattered protons, which then enter the magnetic system where they are spatially separated according to their momentum.

The magnetic system consists of three main parts; the coils energising the magnet; the magnetic pole pieces shaping the magnetic field to its desired topology; and finally the yoke, which also serves as vacuum vessel and magnetic shield against JET's strong stray field.

A detector array of scintillators is placed at the curved focal plane of the spectrometer, detecting the positions of the momentum-separated protons. The MPRu scintillators are of phoswich type(15).

The spectrometer is surrounded by a concrete radiation shield weighing more than 60 tonnes further complemented with about 2 tonnes of lead closest to the focal plane detector. Neutrons that pass through the thin target foil are stopped in a beam dump located in the far wall of the radiation shield to avoid scattering of neutrons into the spectrometer and towards the detector.

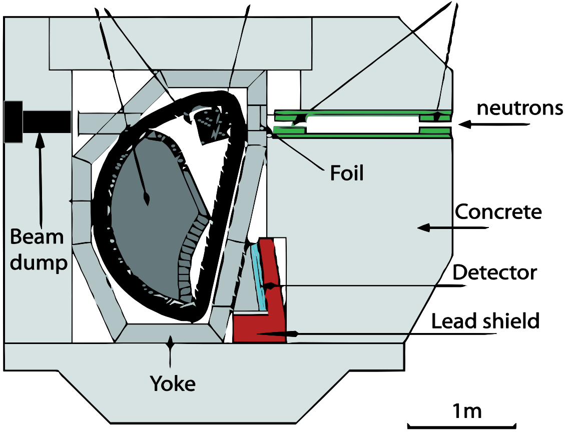

Figure 1. Vertical cut through the MPRu with its radiation shield. Five of the seven concrete blocks (grey) enclosing the spectrometer are shown; only the two side walls are not visible in this projection.

The MPRu's ion optical system is designed for the neutron "beam" to be aligned along a specific axis through the instrument, here referred to as the optical axis (straight line through the neutron collimator in Figure 1). For optimal performance, all physical components have to be accurately aligned and positioned with respect to this axis. Specifically, this concerns the neutron collimator, the conversion foil, the proton collimator and the focal plane detector. The extended optical axis towards the JET machine defines the centre of the field of view, i.e. the line of sight (LOS), of the instrument.

3.1 Neutron Collimator

The neutron collimator defines the neutron "beam" entering the MPRu and the field of view into the plasma. The collimator is partly integrated within the concrete radiation shield facing the torus (Figure 1). It consists of two steel cylinders, each of the length 350 mm, outer diameter 150 mm and with a concentric bore of 10 cm^2. Both cylinder bores are aligned to the optical axis by optical surveying, by the use of a theodolite. The inner cylinder is fixed to the spectrometer yoke, at a distance of 0.17 m from the foil, while the plasma-facing outer cylinder can move relative to the inner one to a position 1.3 m towards the plasma, allowing for a flexible effective collimator length in the range 0.87 m to 2.17 m.

The position of the movable, outer cylinder is set by a remotely controlled motor. The number of revolutions made by the motor is monitored to give the cylinder position and thereby the collimator length. Micro-switches are installed at the extreme cylinder positions to prevent the motor from driving the system beyond its limits.

3.2 Conversion Foils

A neutron-to-proton (n,p) conversion foil is placed at the end of the neutron collimator, inside the MPRu vacuum chamber and aligned to the optical axis. Six different circular foils are installed in a special foil-holder arrangement. The foils are 10 cm^2, chemically pure, self-supporting CH_2 targets[1] with different thicknesses to accommodate different operating scenarios in both 2.5 and 14-MeV neutron measurements (Table 1). The foil holder is a wheel-like construction (Figure 2) made mostly of aluminium but with the parts closest to the neutron beam, facing the spectrometer, made of graphite in order to reduce the risk for undesired (n,p) scattering events in the holder mechanics[2]. The assembly is about 150 mm across.

Table 1. The thickness of the six conversion foils presently installed in the MPRu. All foils have a 10 cm^2 active area.

Foil	1	2	3	4	5	6
Thickness (mg/cm^2)	1.583	2.756	3.67	8.09	13.56	22.11

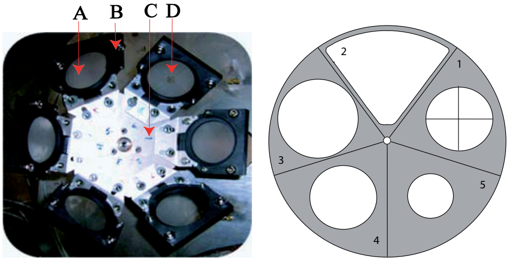

Figure 2. Conversion foil and proton aperture arrangements. Left panel: Photograph of the conversion foil holder, made from graphite and aluminium. "A" points to one of the CH_2 foils, "B" to a graphite holder and "C" to the Al base plate. "D" to the crosshair and central hole in position 6, to the right of foil "A". Right panel: Schematic drawing of the five available apertures of the proton collimator. Note the cross hair in proton collimator position 1.

The thickest conversion foil has a small central circular cut-out and a cross-hair installed (on the plasma-facing side) for alignment purposes. A motor placed outside the vacuum chamber controls the selection of conversion foil; the motor is stopped by micro switches at the six positions that place the conversion foils in positions aligned to the optical axis (neutron beam). A long straight shaft with a vacuum tight feed-through connects the motor to the centre of the foil wheel.

---

[1] Provided by Goodfellow, Huntingdon, Cambridgeshire, England, and Borealis AS, Stathelle, Norway.

[2] The threshold for (n,p) reactions in Carbon is high, about 12 MeV, while it is only 1.8 MeV in Aluminum.

3.3 Proton Collimator

The proton collimator is aligned with the optical axis and selects forward scattered protons from the conversion foil for further analysis in the spectrometer's magnetic field. It is tilted with 15 degrees with respect to the target foil as required by the bending of the proton trajectories at this point. The proton collimator arrangement consists of two components, namely, a 2-mm thick collimator "wheel" (Figure 2) attached to a 3 mm thick screening plate. The collimator wheel has five triangular holes onto which up to five 3 mm thick "pie" pieces, defining more restrictive circular apertures, can be attached. The sizes and shapes of the presently installed apertures are given in Table 2. The collimator wheel is 230 mm in diameter.

The wheel is controlled by a motor, placed outside the vacuum chamber, and stopped by micro switches at the five aligned positions. The motor turns the wheel so that the desired aperture is placed in front of a hole in the screening plate. The screening plate is attached to the front of the D1 poles and has a single fixed opening corresponding to the largest opening in the collimator wheel, i.e., the triangular one of position 2 (Figure 2). The screening plate allows only protons with trajectories through the selected aperture to reach the magnetic part of the system. One of the apertures has a cross hair installed, used in the alignment of the collimator.

Table 2. The five different proton collimator apertures of the MPRu. An approximate solid angle is given, as seen from the centre of the conversion foil. The triangular opening is used for calibration and tuning of the instrument.

Position	Type	Radius (mm)	Solid Angle (msr)
1	Circular with cross hair	34.9	39.5
2	Triangular	Special	Special
3	Circular	40.0	51.9
4	Circular	34.9	39.5
5	Circular	18.0	10.5

3.4 Electromagnet and integrated parts

The momentum (energy) separation of the protons is performed passively in the spectrometer's magnetic field. The MPRu electromagnet system consists of the yoke, the coils, the pole pieces and the integrated monitoring equipment. The magnetic return yoke is an irregularly shaped steel box (Figure 1) with approximate outer dimensions (L×H×W) 1.50 m×2.25 m×0.80 m and a wall thickness of 0.20 m. It surrounds the magnetic volume, thereby preventing all but a small (a few Gauss just outside the yoke) stray field to leak out into the surrounding area even at the highest magnetic excitation levels. The yoke also serves as magnetic shield against the strong stray field produced by the tokamak, which can reach several hundred Gauss at the spectrometer's position on JET. Larger penetrations in the yoke are provided for neutron beam entrance and exit, for protons exiting to the focal plane detector and for cooling water and power services to the coils. Two smaller penetrations are provided for the motor driving shafts of the foil and collimator wheels.

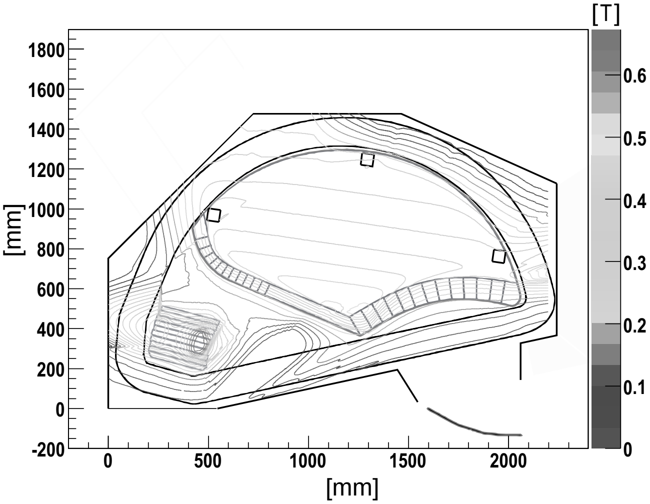

Figure 3. Interpolated magnetic field map of the MPRu for a 2.5-MeV setting in the magnetic symmetry plane. The x and y axes are both in mm and the contour lines give the magnetic field strength. Indicated in the figure are the positions of the inner wall of the yoke and the outline of the coils (black), the magnetic poles (grey) and the curved focal plane (red). Three distance blocks (black squares) in the D2 pole are also indicated; these were used as reference points in the surveying of the instrument.

The electromagnet is energised by two sets of D-shaped coils, which are manufactured from about 1 km of insulated rectangular copper pipes with centred circular holes for water cooling. The coils are powered by a magnetic power supply (MPS) providing a maximum current of 560 A at 105 V voltage drop. The MPS is placed in the JET basement below the spectrometer and is remotely controlled and monitored.

The magnetic field (Figure 3) is given its shape from two separate poles, one multi pole, D1, and one pole of clamshell design, D2. The two parts of the D1 pole are each built up from 11 plates of individual profiles while the two pieces of the D2 pole are manufactured from single blocks of metal. The D1 produces a field with strong multi-pole components. These components, mainly of quadru- and sextupole type, give focusing of the protons in the momentum-dispersive direction of the magnet and provide higher-order ion-optical corrections. The D1 bends the protons by about 30 degrees and produces a field with strong multi-pole components. The D2 bends the protons an additional 120 degrees while also assisting in the focusing. The curved entrance and u-shaped exit boundaries of the D2 provide further ion optical corrections.

Three magnetic field probes (Hall probes) are placed in the spectrometer for monitoring of the magnetic field; one in each magnetic pole and one at the focal plane detector. Together with the measured field maps (see Section 6), these monitors provide the information needed to determine the magnetic field topology for any excitation level. The Hall probes are also used to monitor the stability of the B-field and the temperature at their locations; they are read out at a frequency of 4 Hz during plasma operation. Additional temperature probes (Pt100) are placed on the cooling water pipes for the coils to monitor any temperature fluctuations. Water flow guards are also installed on the cooling water pipes both on the electro-magnet and on the MPS; in the event of too low water pressure or complete water loss these units switch off the MPS.

The spectrometer is equipped with a local vacuum system, serving the one cubic meter volume contained by the yoke and the extension box housing the focal plane detector. The pressure is kept at a level of typically 10^{-4} mbar, which is low enough to prevent energy loss and scattering of the recoil protons to significantly affect the measurements. The vacuum components consist of a turbo and a backing pump, connected via a remotely controlled valve, and two vacuum gauge heads with associated read out electronics, also controlled remotely. The turbo pump is directly attached to the spectrometer's vacuum vessel in the beam dump region, well removed from the neutron beam. It connects to the backing pump via a flexible tube pulled through a curved channel in the back wall of the radiation shield. In addition, a sliding 50 μm thick steel vacuum window is installed at the spectrometer entrance, remotely controlled by compressed air. This seal can be opened for LOS surveying. The vacuum flange at the exit of the neutron beam is also accessible from the outside, by removing the beam dump plug in the shielding back wall.

3.5 Focal Plane Detector

The MPRu implements a focal plane detector with phoswich detectors onto which two photomultiplier tubes (PMTs) are attached at each end. The focal plane detector is placed at the curved focal plane of the spectrometer. It can be divided into three parts; the detector mechanics, the scintillator array and the PMT assemblies. The detector mechanics serves as the mounting frame for both the PMTs and the phoswich detectors as well as magnetic shielding of the PMTs and to assist in the heat dissipation of the PMT bases. The focal plane of the magnetic system is curved in space (see Figure 3). For simplicity, the focal plane detector has been constructed as a single straight plane.

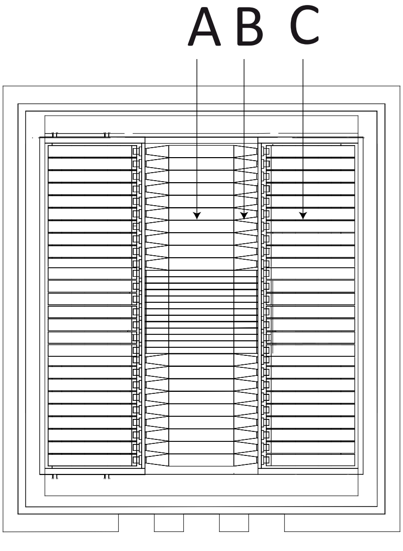

Figure 4. The layout of the detector array and mechanics, with phoswich scintillators in the centre (red outlines; A), light guides (black; B), PMTs (blue; C), and the surrounding frame (green).

3.5.1 Phoswich detectors

The phoswich scintillators[3] consist of two scintillating layers in optical contact, each with its characteristic light-pulse decay-time. A thin (0.3 mm) layer with a short decay time (t_{decay}=1.8 ns, material Bicron BC404) faces the incoming protons, followed by a thick (2.3-3.2 mm) layer with a long decay time (t_{decay}=180 ns, Bicron BC444) and finally a backing layer (0 - 5 mm) of the same material as the light guides (Bicron BC800). The range of 2.5-MeV and 14-MeV protons in scintillator plastic is about 0.1 mm and 2.2 mm, respectively. Hence, a 2.5-MeV proton is stopped in the thin layer whereas a 14-MeV proton deposits its energy in both scintillator layers. This results in different pulse shapes depending on proton energy (and particle type), a property of the phoswich detectors that is exploited here to improve the background reduction.

Phoswich scintillators of four different types are mounted in the focal plane detector, labelled III, IV, V and VI for historical reasons. Types III and VI are 20 mm wide, used in the low and high energy sections of the detector plane, and have straight light guides. Types IV and V are narrower (10 mm), have bent light guides, and are placed in the central section. Types IV and V differ only in the bending direction of the light guides, being bent either towards or away from the electromagnet. (See Table 3 and Figure 4) (12).

The light guides transform the rectangular shaped phoswich (and backing) cross section to a circular one suitable to couple to the PMT.

Table 3. Specifications for the four types of phoswich scintillators and their nominal dimensions. The second column gives the number of items of each scintillator type present in the detector array. The light guide shapes are either straight or bent. The bent light guides are bent either away from or towards the electromagnet.

				Thickness of layer				
Type	**#**	**Position**	**Light Guide Shape**	**Fast BC404 (mm)**	**Slow BC444 (mm)**	**Backing BC800 (mm)**	**Width (mm)**	**Length (mm)**
III	9	Low Energy	Straight	0.3	2.3	1.3	20	100
IV	7	Mid Energy	Bent (against)	0.3	2.5	5.0	10	100
V	6	Mid Energy	Bent (from)	0.3	2.5	5.0	10	100
VI	10	High Energy	Straight	0.3	3.2	0.0	20	100

The thickness of the thin layer is purposely chosen to be substantially larger than the range of 2.5-MeV protons in plastic. This is to ensure sufficient energy deposition for penetrating 14-MeV protons in this layer; there are manufacturing advantages as well.

To give good optical coupling the light guides at each end of the phoswich scintillators are connected to the PMTs via 3 mm thick cylindrical silicon pads to which a thin film of optical grease have been applied.

The available space in the detector location is restricted. The use of two PMTs per scintillator therefore required some changes of the system. Such changes included the increase of the width of the central channels (from 8 mm to 10 mm), the bending of the light guides of the central channels, and the reduction in the number of detectors in the detector array (from 37 to 32).

---

[3] Provided by St. Gobain (Bicron), Newbury, Ohio, US.

3.5.2 PM-tube assemblies

Each phoswich detector is attached to two PMTs[4] for a total of 64 installed. The PMTs have an outer diameter of 19 mm and a length of 127 mm as measured from the photocathode to the back. The bare glass PMT is coated with a conductive layer, sleeved with an insulator, and fitted within a 0.2 mm μ-metal cylinder for magnetic shielding. The photocathodes have an active area with diameters in the range 14.7-17.6 mm and quantum efficiencies between 24.6% and 34.0%. For typical 14-MeV proton induced pulses, the PMT resistor chain is designed to give a maximum gain shift of 6% at a count rate of 100 kHz. Such rates are a concern only in high power DT operations; in D operation rates are expected to be sufficiently low to avoid any rate-dependent effects. The PMTs are long-term vacuum compatible and designed to each generate less than 1 W of heat at nominal high voltage (-1500 V). Two remotely controlled high voltage (HV) power supplies[5] provide the necessary high voltage for the PMTs, in the range -1000 V to -1600 V.

The temperature in the surroundings of the PMTs is measured by two Pt100 elements, one in each PMT box (see below).

3.5.3 Magnetic shielding and mechanics

The MPRu system is sensitive to magnetic field disturbances. This concerns, firstly, the ion optical properties of the spectrometer, which are determined by the magnetic field topology as provided by the D1 and D2 poles. Consequently, the magnetic volume must be shielded from any external magnetic field; this is provided by the thick walls of the electromagnet's return yoke. Secondly, the PMTs must be shielded to sub-Gauss levels to function properly. Therefore, the PMT magnetic shield consists of three layers. The outermost layer is a 20 mm thick soft iron cap surrounding all sides of the detector installation volume except the side facing the electromagnet and an opening below the detector installation for feed-through of signal and HV cables. The next layer, the PMT mounting boxes of the detector mechanics (Figure 5), is manufactured from 4 mm thick soft iron and, finally, each PMT is enclosed in a 0.2 mm thick μ-metal cylinder.

A Hall probe for magnetic field measurements is placed in one of the PMT boxes. The field is monitored during plasma operations and has been shown to be unaffected (within 0.1 Gauss) by the operations of the tokamak magnetic field for all JET operational scenarios as well as by the operations of the spectrometer's electromagnet up to its maximum excitation. The remaining magnetic field in this area is at a sufficiently low level to be safely handled by the PMT's μ-metal shielding.

The position of the assembled focal plane mechanics relative to the components of the magnetic system has been measured by 3D photogrammetry with an uncertainty of 0.05 mm (16). The width and position of each scintillator in the MPRu detector array were measured by illuminating the scintillators of the fully assembled hodoscope with light from a pulsed ultraviolet LED light source. The relative positions of the scintillators were determined with an uncertainty of 0.05 mm (17).

---

[4] Provided by Electron Tubes Ltd, Ruislip, UK. Assembly type P19VN-06.

[5] Provided by CAEN, Viareggio, Italy.

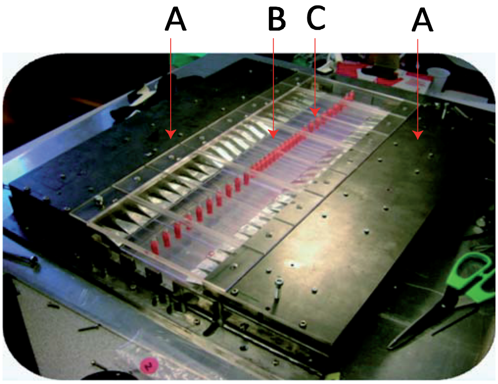

Figure 5. Overview of detector mechanics, with the PMTs mounted inside their magnetic shielding boxes (A). The plastic roof (B) and the fibre guides pieces (C) are also visible.

The PMTs are placed in aluminium holders to improve the heat dissipation from their voltage divider bases. Still, temperatures during assembly (room temperature around 20ºC) are quite different from those at full operation of the magnet and detector (up to 60ºC). Therefore, two robust plastic bars and a plastic "roof", with the same heat expansion coefficient as the scintillators, have been inserted between the two PMT boxes (see Figure 5). One PMT box is free to move relative to the other one. With this arrangement, temperature variation causes the plastic to expand or contract at the same rate as the scintillators, thereby relaxing any stress on the scintillators.

For each phoswich detector, a light fibre is guided through a penetration in the plastic roof and directed perpendicularly to the back of the scintillator surface. Light emerging from the fibre is aimed at a spot (d~2 mm) of diffuse white paint applied on the opposite surface of the scintillator. This scatters the incident LED light randomly within the scintillator, and hence partly also towards the PMTs.

3.6 Radiation shielding

Being placed in the JET torus hall, the MPRu is exposed to high levels of both direct and ambient gamma ray and neutron background radiation. The primary background source is the fusion plasma, emitting neutrons at predominantly 2.5 MeV and/or 14 MeV energies in all directions. The energy distribution of the background is smeared out and shifted toward lower energies due to scattering in surrounding materials. The gamma rays are mainly due to capture of thermal neutrons in construction materials, for the MPRu mainly in its own radiation shielding.

The shielding consists of seven large concrete blocks, weighing between 4 and 16 tons, with an additional lead block around the focal plane detector for enhanced gamma suppression. Furthermore, the plastic roof in the focal plane mechanics shields from Compton electrons. The concrete shielding wall that faces the plasma is 1.5 m thick and the other walls are 0.50-0.76 m. The larger voids between the magnet yoke and the concrete shield are filled with bags of polythene pellets for additional shielding. The same type of pellets is inserted into the void between the neutron collimator housing and the concrete. The concrete pieces were cast sequentially "in situ" from the bottom up, so that all joining horizontal surfaces were individually matched to each other.

Thus, the shielding gaps normally associated with the tolerances required by more traditional labyrinth-type joints were largely avoided and a practically seamless shield was obtained.

Signal and control cables are pulled out from the spectrometer past the shielding through a hole in the lower back wall. The same hole is also used for the water and current cables for the electromagnet. A separate penetration in the upper back wall allows for the exhaust of the turbo pump (placed inside the concrete shield) to be connected to the backing pump (outside). The present shielding configuration was designed and evaluated using a MCNP (18) model for the MPR and the JET torus hall.

3.7 Beam dump

The neutron beam exiting the yoke is made to intersect with a hydrogen-rich plastic cylinder placed in a cut-out hole in the back concrete wall of the MPR. This beam dump is there to prevent the exiting neutrons from scattering back into the spectrometer where they could contribute to the background in the focal plane detector. The plastic plug is removable from the outside making access to the back exit vacuum flange of the spectrometer possible.

3.8 Data acquisition electronics and Control and Monitoring

The recoil protons interacting in the phoswich detector elements provide the primary signals on which the physics analysis in terms of neutron energy spectra is based. The MPRu signal processing chain, from phoswich scintillators to data storage in the system's intermediate data acquisition computers is shown in Figure 6. For each phoswich detector, it consists of two PMTs, a pulse-summing amplifier (PSA), a channel in a transient recorder card (TRC)(19) and associated cables. The phoswich scintillator placed at the very low energy end of the detector array (channel 0) serves some further functions in the control and monitoring (C&M) system and therefore has some additional components included in its signal processing chain; this is the situation depicted in Figure 6.

The signals from the two PMTs connected to a phoswich detector are summed and amplified in the custom-built PSA. An amplification of about a factor of six is provided in order to match the input range of the TRCs. The TRCs digitize and store the full pulse shape of the summed PMT signals. The input voltage range of the TRCs is 0 to -1 V over 50 Ω and the digitization is done with 8 bit resolution at 200 MHz sampling frequency. Each TRC has four input channels. The TRCs allow for individual settings for each channel regarding, e.g., voltage offset, trigger level, and the number of pre- and post trigger samples.

The C&M system consists of a number of artificial, controlled light sources (CLS) and in addition two scintillators with embedded sources for absolute reference. These latter light sources employ scintillators of the type Yttrium Aluminium Perovskite doped with Cerium (YAP:Ce) with embedded 5.5 MeV α-emitting ^{241}Am sources [6]. The YAP sources illuminate the photocathode of the two PMTs of the system's monitoring channel (channel 0). The light from a CLS is optically connected to the centre of every scintillator via light fibres. Two CLSs are installed with the MPRu, namely, a laser emitting green light (20) and a LED emitting blue light (21). To relate the time trace of the data from the spectrometer to that of JET, a 1Hz standard NIM clock pulse is provided by JET and has been added to the signal chain of the monitoring channel via a fan in/fan out (FIFO) unit.

---

[6] Provided by Scionix, Bunnik, The Netherlands,

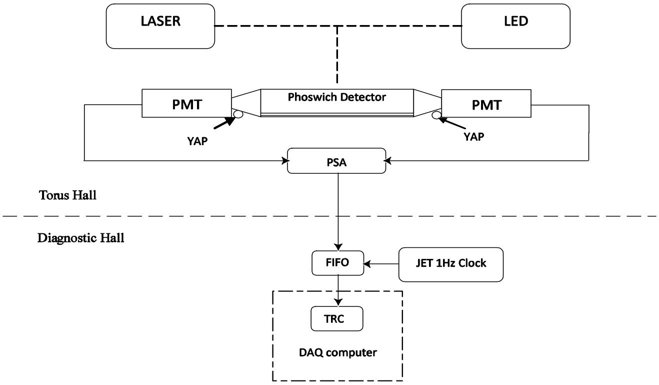

Figure 6. Overview of signal chain for channel 0, where dashed lines and whole lines are optical and electrical connections, respectively. All other channels have the same signal chain, but do not include the YAP sources, the FIFO and the JET 1 Hz clock.

Pulses due to the YAP, the CLS and the clock have distinct shapes and, in some cases, fixed repetition frequencies, making them easily distinguishable from each other and from pulses due to particles interacting in the scintillators. The recording of the full pulse shape for each event with the TRCs gives the possibility to perform off-line pulse shape discrimination and data reduction, as is discussed below.

4 Settings of operational points

Different spectrometer working points are used to measure the 2.5-MeV or 14-MeV neutrons. Each working point is built up of the individual settings of the different spectrometer sub-systems. These include the length of the neutron collimator, the thickness of the (n,p) conversion foil, the aperture of the proton collimator, the magnetic field, the focal plane detector settings, and the data acquisition parameters employed.

4.1 Optimisation

A characteristic of the thin-foil method is a reciprocal relation between energy resolution and efficiency. While the best resolution of the system is obtained when a thin conversion foil and a restrictive proton collimator aperture are used, the best efficiency requires the opposite choices.

The separation of tasks with the MPR technique offers the possibility to maximise the efficiency for a specific resolution by varying the settings of proton collimator aperture and conversion foil thickness. The two contour plots in Figure 7 show the results of a study to find the optimal working point for mono-energetic 14-MeV neutrons. The figures show contours of efficiency and resolution (σ/E_n)[7] as a function of the foil thickness and the proton collimator radius. For a specific "choice" of resolution there is one combination of conversion foil thickness and proton collimator radius that maximises the efficiency. The set of optimised combinations is indicated by the thick red curve in the two panels of Figure 7. The neutron collimator length, the foil area, and possibly other parameters, can be included in this optimisation; here the foil area is 10 cm^2 and the neutron collimator length is 870 mm. The B-field is 1.091 T.

---

[7] The standard deviation (σ) is used since it is a function of the entire proton distribution. In contrast, the more frequently used Full Width Half Maximum excludes possible tail effects of the proton distribution.

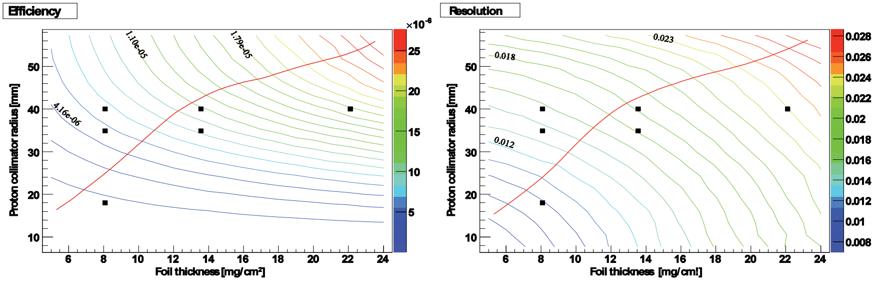

Figure 7. Optimisation of spectrometer settings for 14-MeV operations. Left frame: The efficiency of the MPRu as a function of proton collimator radius and foil thickness. Right frame: The resolution (σ/E_n) of the MPRu as a function of proton collimator radius and foil thickness. Black squares in the figures refer to the possible MPRu settings for the proton collimator and the foil target.

In practice, the MPRu is limited to three proton collimator radii and six conversion foil thicknesses. As can be seen in Figure 7, the setting actually installed is close to optimised for the 13.56 mg/cm^2 foil while the situation for the 8.09 mg/cm^2 is a bit less optimal. The configuration 8.09 mg/cm^2 foil and proton collimator radius 34.9 mm was the reference setting for high resolution operations in 14 MeV of the original MPR. This setting was kept for backwards compatibility even though the optimisation calculation of Figure 7 indicates that a choice of ~10.0 mg/cm^2 and 32 mm would have been better for this particular choice of resolution.

The same optimisation is presented for the 2.5-MeV case in Figure 8. Two of the installed foils are suitable for operations in the 2.5-MeV energy region. The B-field is 0.4293 T. As can be seen, the best operational points available, employing the largest installed proton aperture, of 40-mm radius, are not very close to the optimal values. However, a proton aperture of R = 55 mm, as suggested by this study, was not possible within the constraints given by the overall proton collimator mechanics.

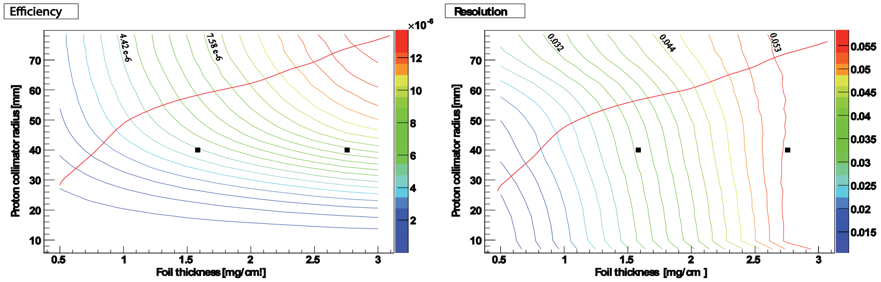

Figure 8. Same as for Figure 7, but for mono-energetic 2.5-MeV neutrons.

Table 4. The combinations of proton collimator radius and foil thickness closest to the simulated optimal combination for 14-MeV (DT) and 2.5-MeV (D) measurements. Efficiency and resolution values are given for mono-energetic neutrons of 2.5 MeV and 14.0 MeV, respectively.

Neutron energy [MeV]	Proton Collimator radius [mm]	Foil thickness [mg/cm^2]	Efficiency [10^{-6}]	Resolution (σ/E_n) [%]
14	18.0	3.67	0.51	0.83
	18.0	8.09	1.13	1.01
	34.9	8.09	5.19	1.42
	34.9	13.56	8.69	1.68
	40.0	8.09	6.54	1.55
	40.0	13.56	11.3	1.80
2.5	40.0	1.584	4.35	3.30
	40.0	2.756	7.57	5.44

4.2 Selection of other settings

The neutron collimator is typically set to the minimum length, 870 mm, to get the maximum number of neutrons impinging on the target. A longer collimator (resulting in a narrower viewing cone into the plasma) gives a somewhat improved energy resolution at the expense of reduced count rate.

The magnetic field of the MPRu for 2.5-MeV and 14-MeV neutron measurements is about 0.4T and 1.0T, respectively, but the field can in principle be set to accept any neutron (proton) energy in the range 0-18 MeV. To achieve good reproducibility in the magnetic field setting the current is “cycled” to the desired value. This is done by slowly oscillating the current delivered by the MPS around the final value and decreasing the amplitude of the oscillation, until the desired setting is reached.

The only detector settings are the high voltage (HV) settings of the PMTs. The main issue of the HV settings is to provide the largest possible pulse height considering the HV limits of the PMTs and the -1V input maximum of the TRCs. A HV of a PMT also needs to be balanced with its partner tube on the same detector (22).

The CLS of the C&M system can also be set to different working points; in particular the LED can be set in numerous ways. For example, the operating frequency of the LED driver can be set between 20 Hz and 20 MHz and the width of the LED pulse can be adjusted in a wide range, from a few ns up to several hundred ns (21). Each TRC channel has a number of parameters that can be set to suit the application.

5 Installation at JET

The installation of the MPRu in the JET torus hall is schematically depicted in Figure 9. The MPRu views the plasma through a diagnostic port at about 4 m distance from the conversion foil. The LOS is semi-tangential passing through the plasma centre twice and making an angle of 47° to the toroidal B-field at the plasma centre. To achieve the best possible coverage of the plasma, the LOS inclination is 4.8° with respect to the equatorial plane of the tokamak (23).

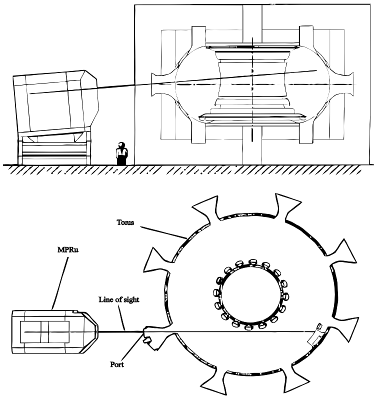

Figure 9. Illustration of the semi-tangential LOS of the MPRu.

5.1 Data handling, storage and reduction

5.1.1 Data acquisition

The TRCs and other data collecting devices are connected to two data acquisition (DAQ) PCs. Both PCs are running a custom-built server program, which uses HTTP 1.1 as protocol. During plasma operation, the server programs collect data from the different devices described in the previous sections and stores it temporarily. In between shots, JET's central Control and Data Acquisition System (CODAS) connects to the server via an internal JET Ethernet connection and initiates a transfer of the data to a central database where it is stored in a Late Pulse File (LPF). The data acquisition is normally initialised by CODAS before each JET shot. However, an acquisition sequence can also be started from the DAQ PCs if desired.

The server programs handle the internal communication between the two DAQ PCs of the MPRu as well as the external communication with CODAS. The MPRu servers can be inquired by CODAS if they are ready to take data and what settings are used.

5.1.2 Data reduction

The acquisition and storage of the full pulse shape for each registered TRC event allows post discharge processing. The MPRu data reduction chain consists of baseline restoration, gain correction, event separation and selection as well as background correction. The result is a time-resolved proton position histogram. The baseline restoration removes the effects of the applied voltage offset as well as any high and low frequency noise pickup from the individual pulse shapes. Since the different detector channels are affected by noise pick-up to a quite varying degree, each TRC data channel is analysed separately, and customised baseline restoration methods are selected for each channel individually. These methods include treating the baseline off-set as a constant, a linear or a sinusoidal function. The gain correction takes into account changes in signal amplification in the PMTs, PSAs and TRCs. It is based on a method using the YAP and LED light sources (22).

For event separation and selection, a two-gate pulse shape discrimination (PSD) technique is used. Each waveform registered by the TRCs is divided into two parts ("gates"). The integrated charge, Q, is calculated for each part separately, i.e., for an early, "fast" part of the pulse, and a longer “slow” part after the fast gate. These sums of sampled voltage values are referred to as Q_{short} and Q_{long}, respectively, and constitute the basis for further event selection and separation as described below. The storage of the full pulse shape gives the possibility to apply more advanced PSD techniques in the future.

Waveforms due to the CLS of the C&M system can be identified both by their timing within the plasma discharge, since these light sources are (in low rate operations) only activated before or after the main plasma pulse, and by their fixed repetition frequencies and characteristic pulse shapes. These latter properties make it possible to separate them also in situations where they are mixed with the normal scintillator events, such as would be the case if they were used to follow gain variations due to rate transients during a plasma pulse. This option will be studied in future high rate operations.

6 Performance of the installed MPRu system

6.1 Calibration

The calibration (in energy and efficiency) of the MPRu depends on two sets of quantities. The first set is a number of physical relations and constants, namely, 2-body kinematics, nuclear masses(24), charged particle energy loss in matter(25), the Lorentz force and the double differential cross-sections (over energy and angle) for the H(n,p)n’ reaction(26); these determine the physical process occurring in the spectrometer. The second set of quantities is that of the spectrometer, in terms of geometry, and magnetic field; these determine the response of the instrument to the physical process. All quantities are assembled into a response function calculation (see Section 6.2.1.), giving an *ab initio* (from first principles) calibration of the instrument.

The geometry of the magnetic system was measured by hand during assembly of the MPR in 1994-1995. The uncertainties of these measurements were estimated to <0.5 mm. The internal geometry of the subsystems (conversions foils, proton collimator and neutron collimator) were determined with an uncertainty of 0.1-0.25 mm. These uncertainties are the same for the MPRu. The magnetic field mapping was done at four different settings of the electromagnet, two close to the 2.5-MeV setting and two for the 14-MeV setting. Each magnetic setting was measured by Hall probes at more than 6000 points in the magnetic mid-plane. These measurements combined with the reference Hall probe measurements in the D1 and D2 poles are used to determine the magnetic field map for a specific magnetic setting. This determination involves an interpolation between the measured field maps, resulting in an interpolated field map. One such interpolated map corresponding to a setting for 2.5-MeV neutron measurements is shown in Figure 3.

The geometry and alignment of the new components of the MPRu were surveyed during the assembly and installation in 2004-2005 using JET’s digital photogrammetry system (16). The accumulated precision in the determination of the position of the focal plane detector with respect to the optical axis is about 0.1 mm. Based on the dispersion (see Table 5 below), this contributes a systematic uncertainty of about 0.2 keV in the energy determination in 2.5-MeV operations, i.e., a $dE/E \approx 1\cdot 10^{-4}$.

The total energy dependent neutron to proton conversion efficiency (ε) is given by $\varepsilon_i = \Psi_{n,p,I} \cdot f_i \cdot d_i$. The index i denotes a specific setting of the MPR spectrometer, $\Psi_{n,p,i}$ is the total emission probability for recoil protons from (n,p) scattering to enter the proton collimator and f_i is their transmission from the proton collimator to the focal plane detector. Finally, d_i is the detector efficiency for protons of the scintillator array. Standard differential cross-sections for elastic H(n,p)n' scattering (26) are used for calculating $\Psi_{n,p}$ for the different energies and angles.

The error in the response function code, which is used to calculate the transmission, stems mainly from the uncertainty in the geometry of the instrument and how it is implemented in the code. The transmission has previously been calculated with another independent code giving consistent results; it is about 83% and 90% for 2.5 and 14-MeV protons, respectively (see Table 5). The systematic error in the transmission results is estimated to be k_{trans}~2%. The number of particles in the simulation calculation is high enough to avoid a significant statistical contribution to the error.

The error in $\Psi_{n,p}$ comes from the uncertainty in the geometry of the target and the proton collimator and the uncertainty in the cross section. The uncertainty in the geometry stems from a 0.1 mm uncertainty in the measurement of the target and the collimator diameters. This gives the following estimated errors: the target area k_{area}~1.1%, the size of the solid angle of the proton collimator k_{pcol}~0.5% and the uncertainty in the thickness of the target k_{target}~0.5%. The uncertainty in the cross-section is $k_{c\text{-}s}$~1.4%. Assuming all errors to be Gaussian distributed and uncorrelated, the total error for the efficiency is:

$$\frac{\partial\varepsilon}{\varepsilon} = \sqrt{k_{\text{trans}}^2 + k_{\text{area}}^2 + k_{\text{pcol}}^2 + k_{\text{target}}^2 + k_{\text{c-s}}^2} = 2.6\% \qquad (2)$$

The stability of the energy calibration depends on the stability of the spectrometer's magnetic field; this is monitored at a rate of 4 Hz during plasma operation. The short- and long-term stability was verified at a reference setting for 2.5-MeV neutron measurements where only small (sub Gauss) variations in the B-field were observed, both during the evolution of a pulse and over longer periods of operation. Over an 8 week period of JET operations in 2006 (500 plasma discharges), one of the reference Hall probes showed a one-sigma spread of ±0.3 G on a level of 3300 G (the other was stable on a level of 4300 G). This corresponds to an energy uncertainty of at most ±0.4 keV, which is of the same order as the estimated uncertainty due to the positioning of the focal plane detector elements, and small compared to the mean neutron energy (of order 2450 keV); it contributes a (random) uncertainty in the energy calibration of the order $dE/E \approx 2\cdot10^{-4}$.

6.2 Simulated spectrometer performance

Simulation codes were used for two main purposes. One was to include all the relevant knowledge about the full spectrometer system into a simulation code that could provide the spectrometer response functions. The second was to assist in the design and analysis of the new phoswich-based focal plane detector. The codes used for these two tasks are described in the following two sub sections.

6.2.1 Spectrometer response functions

All the inputs needed to assess the performance of the spectrometer were assembled into a Monte Carlo code used for calculating the instrumental response function. Protons are tracked from the conversion foil, to the proton collimator and through the interpolated measured magnetic field using a fourth order Runge-Kutta technique. Validation of the response function was obtained from measurements with a point ^{241}Am source placed in the target position (8) and from fusion neutron measurements under specific conditions, in particular for ohmic plasmas (see Section 6.3.2). The response function is used both in the analysis of plasma neutron data and to provide information on spectrometer performance.

The response function of the spectrometer can be approximated by a number of (energy dependent) parameters. These include the dispersion along the detector array; the resolution of mono-energetic neutrons; the line shape, i.e. the proton position distribution at the detector array for one specific neutron energy (cf. line shapes of gamma spectrometers); the transmission fraction from proton collimator to detector array; and the overall efficiency.

The dispersion, resolution and line shape are illustrated in Figure 10 for typical 2.5-MeV and 14-MeV neutron measurement settings, where each proton position distribution over the detector plane is the result of a separate simulation calculation of mono-energetic neutrons that have been "forced" to scatter in the conversion foil. Table 5 gives a summary of some of the performance parameters. The dispersion is the differential separation of proton energies over the length of the hodoscope, i.e., $\mathrm{d}E_{\mathrm{p}}/\mathrm{dL}$. The transmission is the fraction of protons selected by the proton collimator that reach the detector array, which is about 97% efficient in registering protons(17). For a 2.5-MeV operational point (foil of 1.583 mg/cm^2, proton aperture 52.5 msr and B-field 0.4297 T), the resolution (σ/E_n) of the spectrometer is 3.2% for mono-energetic protons of 2450 keV. For 14-MeV neutrons, the operational point (8.09 mg/cm^2, 40 msr and 1.091 T) allows a resolution of 1.4% at 14.0 MeV. The effective neutron collimator length is 870 mm in both cases.

Table 5. Simulation results for one 2.5-MeV and one 14-MeV operational point. The spectrometer settings are described in the text.

	2.5-MeV operational point				14-MeV operational point			
Neutron energy (E_n) [keV]	2 250	2 450	2 750	2 950	12 600	14 000	15 400	16 800
Median position [mm]	89.5	198.6	355.2	450.8	128.6	261.2	383.2	494.5
Dispersion [keV/mm]	3.27	1.82	1.99	2.13	10.2	10.9	11.9	13.1
σ [keV]	99.1	79.1	76.1	75.8	194.7	199.5	218.2	241.6
Resolution (σ/E_n) [%]	4.4	3.2	2.8	2.6	1.5	1.4	1.4	1.4
Transmission [%]	81.5	83.1	81.2	78.4	91.3	90.3	87.6	83.1

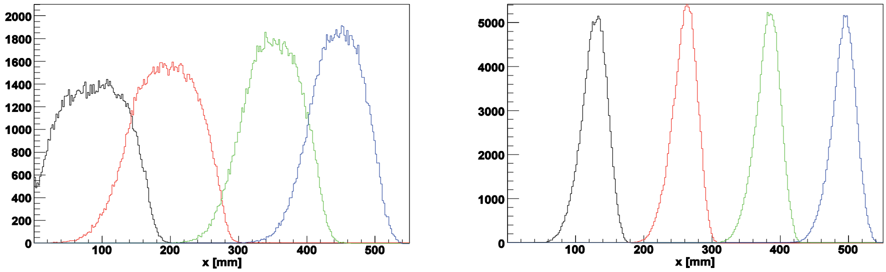

Figure 10. Simulated proton position distributions at the focal plane detector. The left frame shows results for four cases of mono-energetic neutron emission for the 2.5-MeV operational point of Table 5, namely, 2.25 MeV (black), 2.45 MeV (red), 2.75 MeV (green) and 2.95 MeV (blue). The right frame shows results for four mono-energetic cases for the 14-MeV operational point of Table 5, namely, 12.6 MeV (black), 14.0 MeV (red), 15.4 MeV (green) and 16.8 MeV (blue).

6.2.2 Simulations of phoswich performance

To assist in the design of the instrument, interpretation of results and the evaluation of its performance, a separate Monte Carlo model has been set up specifically to study the performance of the phoswich scintillators of the detector array (27). The model is based on the GEANT4 code package (28) and includes the full geometry of the installed focal plane detector describing the detector assemblies as well as the mechanical support structures. The simulation calculates the response to signal protons as well as to the different background components like neutrons, gammas and electrons. The intensities and shapes of the background components were modelled using input from an analysis of the main 14-MeV as well as the preliminary 2.5-MeV measurements with the original MPR. The calculations can be done for any detector element of the hodoscope; here we report results for a central hodoscope channel. For the original MPR, 14-MeV measurements in DT, the simulations gave a $S/B = 2.5\cdot10^3$ while the experimental value was $2\cdot10^3$; for 2.5-MeV measurements in D plasmas the simulations gave a $S/B = 2.5\cdot10^{-1}$ while the experimental S/B was 10^{-1}. For the MPRu, the phoswich response was modelled with input from prototype tests using radioactive sources. In this case, the simulation predicts a 2.5-MeV proton $S/B_{2.5} \sim 10$; in the 14-MeV case the simulations predict a $S/B_{14} \sim 2.5\cdot10^4$.

6.3 Measured spectrometer performance

6.3.1 Signal to background determination

To evaluate the S/B of the MPRu experimentally, we have combined data from several hundred JET D plasma pulses where the spectrometer was operated at the 2.5-MeV setting described in Table 5. This resulted in a data set containing both signal and background events; we call this the "signal+background" data set. The background component was determined from a separate data set where the magnet was turned off or set to 14-MeV measurements; both these settings prevent 2.5-MeV protons from reaching the detector array. It was tested if the background component seen by the MPRu in D plasma operations is affected by the level of the spectrometer's magnetic field, but no such effects were found.

The left frame of Figure 11 shows the Q_{short} versus Q_{long} distribution of a central detector channel for the signal+background data set. The black line in the figure indicates a "linear cut" applied to the (Q_{long}, Q_{short}) distribution. All events to the right of the cut are discarded and $Q_{tot}=Q_{short}+Q_{long}$ is calculated for the remaining events, resulting in the distribution shown in the right frame of Figure 11. In this Q_{tot} distribution two regions are selected, namely, a normalisation region (between blue lines) and a signal region (between green lines). The normalisation region is assumed free from proton signal events. Data from the acquisition of background-only data (red points) are normalised to the signal+background data (black points) in the normalisation region. By subtracting the normalised background from the signal+ background data in the signal region, the total number of proton events in that region can be determined. For the central hodoscope detector shown here a S/B=4.8 is obtained.

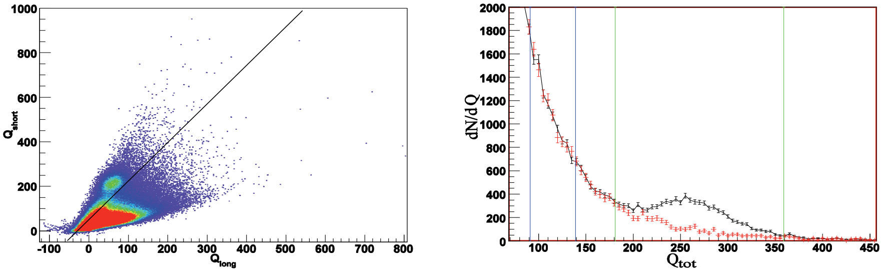

Figure 11. Left frame: The 2.5-MeV signal+background data for a typical central hodoscope channel as a function of Q_{long} (x-axis) and Q_{short} (y-axis). The black line indicates the linear cut mentioned in the text. Right frame: Signal+background (black points and line) and scaled background (red points) of a central channel. The graph shows the number of counts in a central channel as a function of Q_{tot}. The two blue (two left-most vertical) and two green (two right-most vertical) lines enclose the normalisation and signal regions, respectively.

6.3.2 Measurements

Data on the 14-MeV neutron emission from Ohmically heated discharges in the DTE1 campaigns were used previously to validate the energy calibration of the MPR system(29). The new MPRu system is in this respect quite similar to the original MPR.

MPR Ohmic data for three different 14-MeV settings have been analysed using a model with a single thermal (Gaussian) neutron emission spectrum corresponding to a fuel ion temperature of T_i=2-3 keV. No significant plasma rotation is expected in Ohmic operations. The combined results from the three data sets give a deviation of +0.8 keV from the expected mean neutron energy of 14041 keV[8], well within the estimated systematic uncertainty of the energy calibration. At the time the systematic uncertainty was estimated to be ±20 keV mainly from surveying (30). The surveying accuracy has been improved considerably in the MPRu installation and the uncertainty is now only a few keV.

To validate the MPRu instrument in measurements of 2.5-MeV neutrons in D plasmas, data were summed for (parts of) about 1500 JET Pulses from campaigns C15-C19 (2006-2007), when only Ohmic heating was applied. Due to the lower neutron fluxes and somewhat lower efficiency of the system in D operations, the statistics is much reduced compared to the case with DT plasmas. The deduced mean neutron emission energy is 2465 ±9 keV, which is consistent with the expected neutron energy of 2458 keV[9]. For this analysis, the thermal temperature was fixed at 2 keV, based on the experience of Ohmic data from DTE1. The resulting fit gave a reduced chi-squared of 0.86.

To illustrate the differences between MPRu data for different heating scenarios, we present data from JET pulse 68379 subjected to both neutral beam injection (NBI) and ion cyclotron resonance heating (ICRH) data and from pulse 68569 heated with NBI only. The total neutron yield was $3.5\cdot10^{16}$ and $6.0\cdot10^{16}$, for the mixed heating and NBI-only pulse, respectively.

The extracted proton position histograms are shown in Figure 12 together with the result of a preliminary analysis. Gaussian neutron energy spectra are convoluted with the response function and fitted to the two data sets for demonstration purposes. The intensity, width and mean energy are free parameters of the fit. The fits to the data give a reduced chi-square of 1.1 and 1.5 in the mixed and NBI-only cases, respectively. The best fit to the mixed heating pulse gives a broader neutron energy distribution than the NBI-only case (Figure 12c), namely, FWHM = 476 keV compared to 357 keV. The broader neutron energy distribution in the mixed heating pulse reflects the fact that ICRH heating can accelerate the deuterium fuel ions up to several hundred keV of energy, while in the NBI case the maximum ion energy is given by the injection energy of the beams, here 130 keV. The analysis also indicates a common energy shift (beyond the kinematical shift discussed above) of about 40 keV for both data sets.

---

[8] For a “cold” DT plasma, E_n = 14028 keV, to which is added a kinematical shift dependent on the plasma temperature. For a 2.5 keV thermal DT plasma the shift is about 13 keV.

[9] For a “cold” D plasma, E_n = 2449 keV, to which is added a kinematical shift dependent on the plasma temperature. For a 2 keV thermal D plasma the shift is about 9 keV.

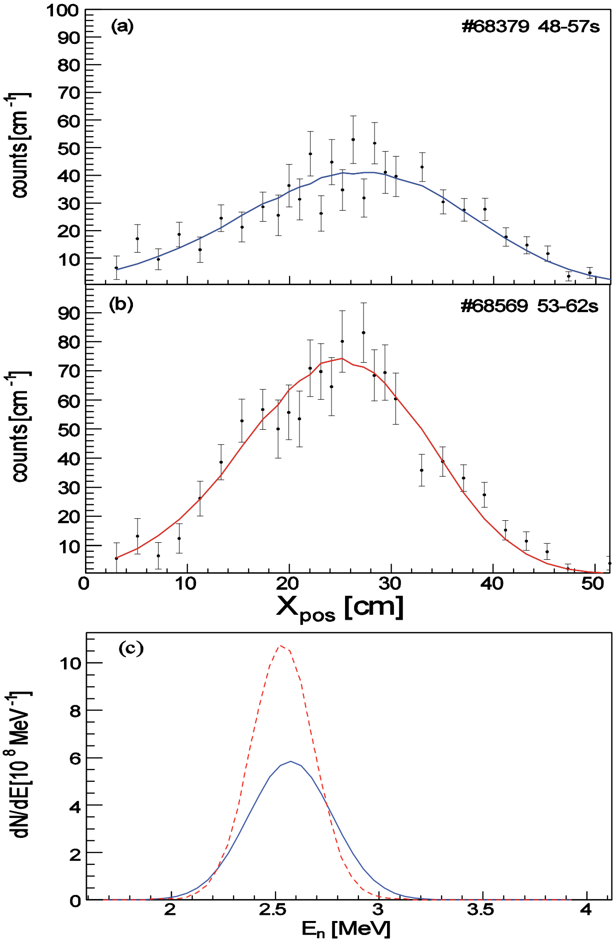

Figure 12. (a) Proton position histogram for pulse 68379, which was heated with both NB and ICRH, including the result of a preliminary analysis (blue solid line). (b) Proton position histogram for pulse 68569, which was heated with NB only, including the analysis result (red solid line). (c) Energy spectra (Gaussian) corresponding to the best-fit parameters for 68379 (NBI+ICRH, blue solid line) and 68569 (NB, red broken line).

Even in D plasma operations tritium is present in the fusion device through the breeding reaction $(d+d \rightarrow t+p)$. In a secondary reaction, these tritons can fuse with the bulk deuterium ions and thereby contribute a triton burn-up neutron (TBN) emission. The intensity of the TBN emission in such plasmas is much lower (about 1% relative intensity) than the 2.5-MeV neutron emission, but the TBN can clearly be seen when the MPRu is set to a 14-MeV operational point during D operation. Data from a set of about 230 pulses when the MPRu was tuned to 14-MeV measurements was combined to investigate the TBN component. Looking at the data for a single phoswich detector (Figure 13a), a concentration of events around $(Q_{\text{long}}, Q_{\text{short}}) = (600, 600)$ is evident in the 14-MeV data, but is absent when the system is tuned for 2.5-MeV measurements (Figure 11a). This group of TBN recoiled protons is highlighted in the rectangular region indicated in Figure 13a (red line). Figure 13b shows the extracted proton position histogram, containing 3139 events, and the results of a preliminary analysis. The analysis used two spectral components, namely, a TBN component (blue) of known shape (31), and a thermal component due to a population of residual tritium (4) (red broken line) with a temperature fixed at 20 keV. A fit to the data has been performed with three free parameters, namely, the intensity of the TBN component, and the intensity and mean energy of the thermal component. The best fit to the data (with a reduced chi-squared = 1.6) is shown as lines in Figure 13b and the corresponding neutron energy spectrum is given in Figure 13c. The intensity of the residual tritium component is 9% of the total flux at the target, which is in fair agreement with previous results (4). Clearly, the TBN component alone would not give an acceptable fit to the data, illustrating the ability of the MPRu to discern multiple components even in situations of quite weak neutron emission.

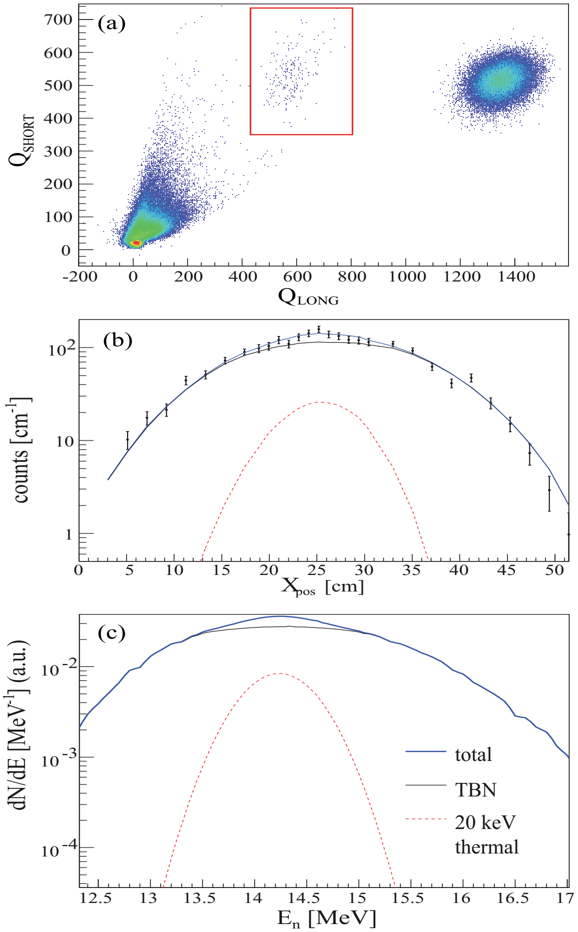

Figure 13. Illustration of 14-MeV measurements during D plasma operation (data from JET pulses 69481-69718). (a) Q_{short} versus Q_{long} distribution in a single central phoswich detector channel; the rectangle encloses the selected "14-MeV" proton events. (b) Position distribution of selected proton events from all detector channels (except channel 21), with the best-fit result drawn as full and dashed lines (see text for details). (c) The neutron energy spectrum corresponding to the best-fit case shown in b).

The MPR is absolutely calibrated in flux efficiency, as discussed above. The measured MPRu 2.5-MeV counts (integrated over full JET discharges) together with the absolute flux calibration of the instrument, can be used to estimate the total JET neutron yield, Y. A separate estimate of the neutron emission profile is required, which can be obtained from an analysis of the JET neutron camera data. A preliminary comparison between the neutron yield of the MPRu, Y_{MPRu}, and that of the JET fission chambers (FC), Y_{FC}, has been performed for 311 JET discharges. The results are presented in Figure 14. A proportionality fit to the data gives $Y_{MPRu}=1.06 \cdot Y_{FC}$. This is consistent within the systematic uncertainty of the two systems. However, for the time period studied here, no processed neutron camera data was available and instead a fixed reference neutron emission profile obtained from previous tritium campaigns was used for this preliminary analysis effort (32). The random uncertainties are dominated by the counting statistic in the MPR.

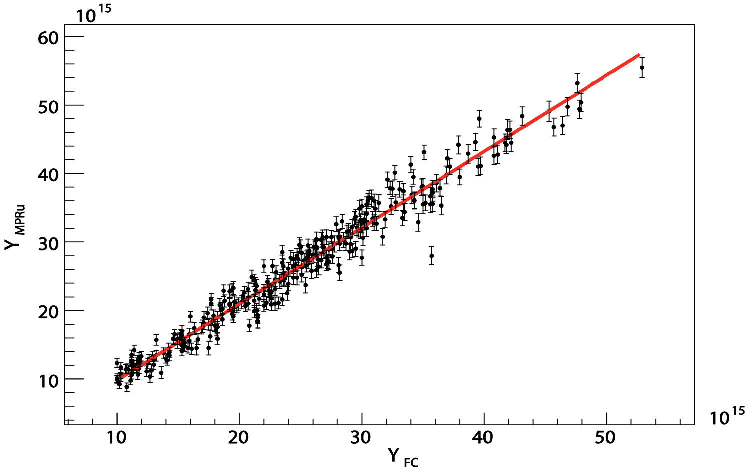

Figure 14. The neutron yield estimated with the MPRu compared to the result of the calibrated fission chambers.

A full analysis of the neutron yield monitoring using the MPRu, including data from the JET neutron camera for each individual pulse will be presented in a separate paper.

The highest count rate registered by the MPRu in JET D plasmas so far has been for pulse 70232 with 800 Hz during a period having a total JET neutron rate of $1.8 \cdot 10^{16}$ n/s.

7 Discussion

The limited range of JET operational scenarios offered since the installation of the MPRu in 2005 has not allowed experimental tests of all the relevant performance indicators of the spectrometer. Here we review some of these important aspects in view of the available experimental results using the simulations as an additional guide, with the aim to estimate the operational limits of the MPRu and identify possible areas for improvements.

The sensitivity of the MPRu has so far been tested in its ability to resolve the weak TBN component in D plasma operations. However, the data are still too scarce to make any detailed statements on the S/B in this measurement situation. In general, a high sensitivity is necessary in order to measure any weak components in the neutron emission. The sensitivity of the instrument is closely related to the S/B of the individual phoswich detectors and can be further improved by background corrections, within the limitations given by the counting statistics. The original MPR had a S/B of about $2 \cdot 10^3$ in 14-MeV (full DT) and 10^{-1} in 2.5-MeV (full D) measurements. With phoswich detectors, double PMT read-out and event-based, digital TR electronics, simulations predict a S/B increase to $2.5 \cdot 10^4$ and 10 for the 14-MeV and 2.5-MeV cases, respectively. It is in this context interesting to mention that the GEANT4 simulations actually predict an improvement of a factor 40 in the 2.5-MeV D plasma situation. The analysis presented above gave a MPRu $S/B_{2.5} = 5$ in 2.5-MeV measurements, which is an improvement of a factor 50 with respect to the original MPR, consistent with the improvement factor predicted by the GEANT4 simulation. We take these results as an indication that the improvement factor follows the simulation results. We can then estimate the S/B in other measurement situations for the MPRu: we would for example expect a S/B_{14} in 14-MeV measurements in high power DT plasmas of $S/B_{14} = 2\cdot10^4$, i.e., the improvement factor of 10 as given by the simulations. The original MPR could distinguish weak components down to the 10^{-4} level of the main emission(1); consequently, the MPRu should be able to push the sensitivity to 10^{-5}, statistics permitting.

We estimate that the main rate capability limitation with the system still lays with the individual detector channels, in particular the performance variations of the PMTs associated with high and variable event rates. However, with the performance monitoring offered by the C&M system of the MPRu, making tracking of transients during a plasma pulse possible, we estimate that individual detector channels should be able to sustain rates of several hundred kHz with preserved data quality. This would indicate a maximum useful count rate in the full spectrometer of several MHz.

The energy bite of the present MPRu is restricted to E_0 ±20% by the physical dimensions of the focal plane detector and the properties of the spectrometer's magnetic field. In principle, the tunable B-field makes it possible to measure neutrons in a broad range of energies, not only around the dominant 2.5 and 14-MeV neutron emission bands, but actually at any energy from 0 to 20 MeV. In practice, the more severe background situation encountered at lower neutron energies would restrict the possibilities to $E_n > 1$ MeV.

The dynamic range of the MPRu in terms of plasma fusion neutron rate varies depending on the plasma conditions. Under certain conditions, a relatively modest instrumental resolution is sufficient, in which case the efficiency of the system can be increased and consequently the operating range can be pushed towards lower neutron rates. In other cases, time-resolved results with good energy resolution are needed, requiring higher neutron rates. For the sake of illustration, as a miniumum requirement we consider the determination of a 20 keV ion temperature with 10% precision and 1 second time resolution using the MPRu with a 1.8% and 3.3% energy resolution setting (for 14-MeV and 2.5-MeV measurements respectively). To achieve this(33), 400 protons per second are required in 14-MeV operations, which implies a minimum JET neutron rate of about $4\cdot10^{15}$ neutrons per second. For 2.5-MeV operations, 300 protons are required and the minimum rate is about 10^{16} neutrons per second. The high end rate is set by the individual detector channels' abilities to cope with high count rates. For the present phoswich assemblies this is about 200 kHz per detector, which translates to about 2 MHz for the full array and further to a total JET flux of 10^{22} 14-MeV neutrons per second (employing the thinnest conversion foil, the longest neutron collimator and the most restrictive proton aperture presently available, i.e., the lowest possible efficiency). Thus, for the present MPRu in 14-MeV measurements, the dynamic range is about $2\cdot10^6$ ($4\cdot10^{15} < R_n < 10^{22}$), with an estimated $S/B = 2\cdot10^4$ at the low-rate end.

8 Outlook

An important aspect of the modular structure of the MPRu concept is that it allows for improvements of specific sub-systems, without a complete re-build of the entire instrument. For example, the focal plane detector is easily removed and replaced, allowing for improvements based on progress in detector techniques. The present selection of a phoswich hodoscope offers good performance in a broad range of neutron (proton) energies; however, a selection of detectors that are more optimized for a more restricted energy range is always a possibility (as was indeed the case in the original MPR). Furthermore, the present restriction to 6 conversion foils and 5 proton apertures could be removed in a different design.

The slightly lower measured S/B is within errors of the simulations. It can, however, partly be attributed to a poorer light collection efficiency, more severe pick-up noise and a generally larger background intensity than anticipated. The light collection efficiency of the phoswich detectors could be improved, partly by selecting scintillating materials for the thin and thick layers that are more optimally matched, partly by improving the quality of material interfaces (32). Based on initial measurements on a prototype detector, we conclude that an improvement of about a factor of 2 is possible (34). The electronic and pick-up noise seen by the individual TR channels at JET is more severe than was observed in laboratory tests, in terms of both magnitude and structure, and the correction for this introduces a slight deterioration of the S/B. To reduce the impact of the noise, PMTs with higher gains can be employed or the amplitude of the signals can be increased by adding new amplifiers. This would simplify the analysis and reduce the errors introduced in the baseline restoration. Finally, by increasing the width of the neutron collimator, it would be possible to increase the flux at the foil and hence reduce the minimum requirement of neutron yield to perform neutron spectroscopy; a wider neutron collimator would also increase the S/B ratio and reduce the errors in the yield determination.

Refinements in the topology of the B-field could be made using modern magnetic simulation codes, thereby increasing the energy bite to some extent; the corresponding modifications of the detector array would be a comparatively trivial task.

Since the neutron yield measurements of the MPRu is absolutely calibrated, it can be used to compare the data with other instruments and simulation from, e.g., TRANSP(35).

9 Conclusion

The MPR neutron spectrometer has been upgraded with the performance improvement in signal to background are in line with project goals and expectations from simulations. With the upgrade, the instrument can perform neutron spectroscopy in both pure D and DT plasmas and thereby provide valuable information on the physics of the fusion plasma in all experimental scenarios.

The MPRu can benchmark codes and fine-tune experimental settings in a D phase. Hence, the instrument is ready to deliver high quality data from day one of the next JET DT experiment. This feature is also important for the ITER experiment since reliable neutron data is essential from the start of ITER DT experiments.

From the results in D plasmas (S/B = 5) one can project the instrument performance in DT operation: a $S/B = 2\cdot10^4$ and a rate capability in excess of 1 MHz. Hence the fast ion population from RF heating, NB heating and alpha knock-on reactions can be studied in even more detail. In JET D operation the instrument can provide complementary spectroscopic information (36) together with other spectrometers, e.g. TOFOR (37).

The original MPR showed that the technique could provide an estimate of the total JET 14-MeV neutron yield with low systematic uncertainties (38), and with the MPRu these measurements are further improved. The results of the MPRu achieved on JET shows that the instrument can also measure the 2.5-MeV neutron yield. The ability to distinguish between the D and the DT neutron emission makes the instrument an excellent candidate for detailed studies of the two species in scenarios where they are both present, such as in trace tritium experiments[10] and during the advanced ITER D phase.

10 Acknowledgments

This work has been performed under the European Fusion Development Agreement (EFDA) and the Association EURATOM-VR with support from Swedish Research Council, Uppsala University and JET-EFDA. The views and opinions expressed herein do not necessarily reflect those of the European Commission. A special thanks to Olle Byström for providing drawings and to Garry Kaveney for all the help with installing the MPRu at JET.

11 References

1. *Observation of the Alpha Particle "Knock-On" Neutron Emission from Magnetically Confined DT Fusion Plasmas.* **Källne, J. et al.** 2000, Phys. Rev. Lett., pp. 1246-1249.
2. *Systematic spectral features in the neutron emission from NB heated JET DT plasmas.* **Henriksson, H. et al.** 2005, Plasma Phys. Control. Fusion, Vol. 47, pp. 1763–1785.
3. *Synergetic RF and NB heating effects in JET DT plasmas studied with neutron emission spectroscopy.* **Henriksson, H. et al.** 2006, Nucl. Fusion, Vol. 46, pp. 244–253.
4. *Triton burn-up neutron emission in JET low current plasmas.* **Sjöstrand, H et al.** 2008, J. Phys. D: Appl. Phys, Vol. 41, p. 115208.
5. *Prospects for High Resolution Neutron Spectroscopy on high power fusion devices in view of the recent diagnostic developments at JET.* **Ericsson, G. et al.** 2007. Burning Plasma Diagnostics.
6. *Neutron Spectrometry at JET (1983-1999).* **Jarvis, O N.** 2002, Nucl. Inst. and Meth., Vol. A476, pp. 474-484(11).
7. *Magnetic proton recoil spectrometer for fusion plasma neutrons.* **Källne, J. and Enge, H.** 1992, Nucl. Instr. and Meth. A311, pp. 595-602.
8. *Neutron emission spectroscopy at JET—Results from the magnetic proton recoil spectrometer.* **Ericsson, G., et al.** 2001, Rev. Sci. Instr., Vol. 72.
9. *New neutron diagnostics with the magnetic proton recoil spectrometer.* **Källne, J. et al.** 1999, Rev. Sci. Instr., Vol. 70, p. 1181.
10. *The monitoring system of a high performance fusion neutron spectrometer.* **Tardocchi, M. et al.** 2002, Nucl. Instr. and Meth., Vol. A485, pp. 624–639.
11. *Study of signal to background ratio in fusion neutron spectroscopy measurements at JET for next step tokamak applications.* **Hjalmarsson, A.** 1999. UU-NF 99/#7.
12. *Upgrade of the Magnetic Proton Recoil (MPRu) spectrometer for 1.5-18 MeV neutrons for JET and the next step.* **Ericsson, G. et al.** 2006. Proceedings of Science FNDA.
13. *New MPRu instrument for neutron emission spectroscopy at JET.* **Sjöstrand, H. et al.** 2006, Rev. Sci. Instr., Vol. 77, p. 10E717.
14. *Annual Report of the EURATOM/UKAEA Fusion Programme 2004/05.*
15. *Radiation detection and measurements.* **Knoll, G.F.** New York : Wiley, 1999.

---

[10] Experiments where the tritium levels are below 10%.

16. The basics of photogrammetry. *Geodetic Services Inc.* [Online] 29 9 2005. [Cited: 14 01 2008.] http://www.geodetic.com/Whatis.htm.
17. **Glasser, W.** *Determination of the hodoscope geometry of the MPRu neutron spectrometer.* 2005. http://www.inf.uu.se/Reports/UU-NF05-11.html.
18. MCNP home page. [Online] http://mcnp-green.lanl.gov/.
19. *A PCI transient recorder module for the JET magnetic proton recoil neutron spectrometer.* **Combo, A. et al.** 2004, Fusion Engineering and Design, Vol. 71, pp. 151-157.
20. *Control and monitoring system for fusion neutron spectroscopy on the Joint European Torus.* **Tardocchi, M. et al.** 2004, Rev. Sci. Instrum., Vol. 75.
21. *A Bipolar LED drive technique for high performance stability and power in the nanosecond time scale.* **Ronchi, E. et al.** 2008. EFDA–JET–PR(08)14.
22. *Control and Monitoring System of the Upgraded Magnetic Proton Recoil Neutron Spectrometer at JET.* **Sjöstrand, H., et al.** 2008, ? EFDA-JET-Preprint(08)07.
23. *Ion temperature and plasma rotation profile effects in the neutron emission spectrum.* **Tardocchi, M. et al.** 2004, Rev. Sci. Instr., Vol. 75, pp. 661-668.
24. [Online] http://nucleardata.nuclear.lu.se/database/masses.
25. [Online] http://physics.nist.gov/PhysRefData/Star/Text/PSTAR.html.
26. CNS Data Analysis Center. [Online] [Cited: 20 2 2008.] http://gwdac.phys.gwu.edu/.
27. *Performance studies of phoswich detectors in the upgraded Magnetic Proton Recoil neutron spectrometer.* **Wikström, G.** 2005. http://www.inf.uu.se/Reports/UU-NF05-01.html.
28. Geant4: A toolkit for the simulation of the passage of particles thorugh matter. [Online] [Cited: 20 2 2008.] http://geant4.web.cern.ch/geant4/.
29. **Henriksson, H.** *Neutron Spectroscopy Studies of Heating Effects in Fusion Plasma.* Uppsala : s.n., 2003. PhD thesis. ISSN: 1104-232X ISBN: 91-554-5678-2.
30. *Neutron emission study of DT plasmas heated with tritium neutral beams.* **Henriksson, H. et al.** 2001, Rev. Sci. Instr., Vol. 75, p. 832.
31. *Measurement and Interpretation of the Spectrum of the Triton Burn-Up Neutron Emission from Deuterium Tokamak Plasmas.* **Ballabio, L. et al.** 1, 2000, Nucl. Fus., Vol. 40, p. 21.
32. *Test Of Phoswich Scintillators For The MPRu Neutron Spectrometer.* **Hellesen, C.** 2005. http://www.inf.uu.se/Reports/UU-NF05-03.html.
33. *Neutron measurement techniques for tokamak plasmas.* **Jarvis, O.N.** 1994, Plasma Phys. Control. Fusion, Vol. 36, p. 209.
34. *Development and characterization of the proton recoil detector for the MPRu neutron spectrometer.* **Giacomelli, L. et al.** 2006, Rev. Sci. Instr., Vol. 77, p. 10E708.
35. **Ongena, J.** 1998, Trans. Fusion Technol. , Vol. 33, p. 181.
36. *Validating TRANSP simulations using neutron emission spectroscopy with dual sight lines.* **Hellesen, C. et al.** Rev. sci. Instr., Vol. 79. In print.
37. *The 2.5-MeV neutron time-of-flight spectrometer TOFOR for experiments at JET.* **Gatu Johson, M. et al.** 2008, Nucl. Instr. and Meth., Vol. A591, pp. 417-430.
38. *Fusion power measurements using a combined spectrometer-camera system at JET.* **Sjöstrand, H., et al.** s.l. : To be bublished, 2007.

Paper IV

REVIEW OF SCIENTIFIC INSTRUMENTS **77**, 10E708 (2006)

Development and characterization of the proton recoil detector for the MPRu neutron spectrometer

L. Giacomelli,[a] E. Andersson Sundén, S. Conroy, G. Ericsson, M. Gatu Johnson, C. Hellesen, A. Hjalmarsson, J. Källne, E. Ronchi, H. Sjöstrand, and M. Weiszflog
EURATOM-VR Association, INF, Uppsala University, SE-751 05 Uppsala, Sweden

G. Gorini and M. Tardocchi
EURATOM-ENEA-CNR Association, Istituto di Fisica del Plasma, Milan 20125, Italy

A. Murari
EURATOM-ENEA-CNR Association, Consorzio RFX, Padova 4-35127, Italy

S. Popovichev
EURATOM-UKAEA Association, JET, Culham Science Centre, Abingdon, Oxfordshire OX14 3EA, United Kingdom

J. Sousa, R. C. Pereira, A. Combo, and N. Cruz
Associação EURATOM/Instituto Superior Técnico (IST), Centro de Fusão Nuclear, Avenida Rovisco Pais 1, 1049-001 Lisboa, Portugal

JET EFDA contributors
EURATOM-UKAEA Association, JET Culham Science Centre, Abingdon, Oxfordshire OX14 3EA, United Kingdom

(Received 5 May 2006; presented on 9 May 2006; accepted 28 May 2006; published online 29 September 2006)

The magnetic proton recoil neutron spectrometer has been upgraded (MPRu) with a new focal plane hodoscope detector as a major part to improve the immunity to background and to extend the measuring range from 18 down to 1.5 MeV. The MPRu detector project has entailed the development of the phoswich technique for this application. This was done through tests of prototype scintillators to reach the final design. The article reports on the tests conducted, the projected specification, and demonstrated performance through the first MPRu results obtained at JET. © *2006 American Institute of Physics.* [DOI: 10.1063/1.2219974]

INTRODUCTION

The magnetic proton recoil (MPR) spectrometer at JET works on the principle of converting the incoming neutron flux from the plasma into an energy distribution of spatially dispersed proton flux[1] impinging on the focal plane detector, an array of plastic scintillators. The proton count rate depends on the plasma conditions and reached 0.7 MHz during the JET DT experiment (DTE1) in 1997, well below the MPR maximum capability, with single detector rates up to 50 kHz. In principle, the MPR spectrometer can be set to record fusion neutrons from 1.5 to 18 MeV (over a range of ±20%). In practice, there is a limitation in the capability of the focal plane detector to record (count) protons at a reasonable ratio of signal to background (S/B). The previous array (hodoscope) of plastic scintillation detectors had sufficient S/B value to measure details of the 14 MeV neutron $d+t \rightarrow \alpha+n$ emission from DT plasmas down to the 10^{-5} level of the neutron spectrum. However, the immunity to background, especially to electrons, has been found insufficient to measure the 2.5 MeV $d+d \rightarrow {}^3\text{He}+n$ emission from D plasmas.[2] A detector with enhanced background immunity has therefore been developed and built as the principal part of the MPR upgrade (MPRu) project (Refs. 3 and 4 contribution to this article). The main difference is that the monolithic scintillators of the MPR have been replaced with laminated ones using the so-called phoswich technique. It affords selection of the desired fraction of recorded events based on pulse height and also the range in matter of ionizing radiation.

In the present phoswich application, the thickness of the first layer was chosen to correspond to the range of proton recoils of *dd* neutrons (i.e., 0.3 mm for $E_p < 5$ MeV) and the total thickness covers the range of *dt* neutron recoils (<3.5 mm). Scintillators 1 and 2 have different (fast and slow) response times to radiation and their contribution to the pulse height sum $P=P1+P2$ is determined through the wave form, $P(t)$. The wave form was recorded with an oscilloscope in the tests and with fast data acquisition electronics with analysis/storage capability (DAAC), custom built for MPRu.[5] This article describes the development of the phoswich technique for the hodoscope through the test of prototypes to reach the final design for MPRu. The performance specifications based on the test results are presented and are compared with the first results on the wave forms

---

[a] Electronic mail: luca@tsl.uu.se

Downloaded 22 Aug 2008 to 130.238.67.59. Redistribution subject to AIP license or copyright; see http://rsi.aip.org/rsi/copyright.jsp

recorded for signal proton recoils from *dd* fusion neutrons at JET as well as with those of background radiation.

PRINCIPLE OF THE PHOSWICH SCINTILLATORS IN A HODOSCOPE

The phoswich method is rather common in various applications for low energy radiation detection. The present application requires the use of bars of scintillators where the total thickness as well as that of the thin layer are both used as a means to discriminate against background. Moreover, to fit into a hodoscope, the light is collected with photomultiplier (PM) tubes attached to the scintillator ends. This means that special care must be paid to the bonding of the two active layers plus the backing where that is used. Finally, the MPRu hodoscope must be able to handle recoil protons in the range of 1.5–18 MeV. The material chosen for the thin layer was the same as for MPR monolithic scintillators, i.e., Bicron BC-404 with a fast decay time of 1.8 ns and Bicron BC-444 for the second layer with a slow (180 ns) decay time; different thicknesses of the latter were used depending on hodoscope position to correspond to the varying range (2.5–3.5 mm) of protons about ±20% in energy with the MPR set to $E_n=16$ MeV in the middle to record the extreme high energy tail of *dt* neutrons.

The signals from the PM tubes have the wave form characteristics of the superposition of light emitted from the fast and slow layers. The wave forms were recorded with an oscilloscope for low data rates offering very high precision with sampling rates of 1 GHz. In the MPRu, the PM tubes are read out up to high (100 kHz) event rates at a 5 ns sampling time; the covered ranges are $t=-200-800$ ns and $t=-110-390$ ns, respectively, with triggering at $t=0$ ns.

THE SCINTILLATION DETECTORS AND RADIATION TESTS

The MPRu phoswich detectors were designed based on tests of prototypes[6] of similar geometries. The tests used sources of 5.5 MeV alpha particles and variable energy protons (both stopping in the scintillator), penetrating (minimum ionizing, $E_e \leqslant 3.5$ MeV) electrons and pulsed light sources of controllable amplitude, width, and rate (not reported here). These different sources were chosen because they simulate the radiations that are anticipated to be detected with the hodoscope when it is deployed at JET. The MPRu hodoscope is made of 32 plastic scintillator strips 100 mm long of widths 10 or 20 mm consisting of 0.3 mm fast and 2.5/3.2 mm slow scintillators. The scintillator ends have cross section areas of between 38 and 76 mm^2 which coupled to PM tubes with photocathodes of 12 mm diameter and can receive light distributed over an area of up to 110 mm^2. To utilize this limit, a backing layer of acrylic plastic (Bicron BC-800) was used in some cases. The tests were performed on phoswich prototypes 10 mm wide with and without backing.

The backing has a considerable effect on the fraction of light collected by the PM tubes as demonstrated in the measurement with a collimated alpha source used to irradiate the fast side of the prototypes [Fig. 1(a)]. The backing improves the fraction of the produced light received at the PM tube by more than a factor of 2. These data represent the average wave form for an ensemble of events. For individual events it is convenient to use two amplitudes, A1 and A2. These are defined as the integrals of the wave form over periods $t=0-60$ ns and $t=60-460$ ns with the trigger set at $t=0$ [Fig. 1(a)]; the amplitude in the region $t=-20$ to -2 ns is used to determine the offset level that is subtracted to obtain A1 and A2.

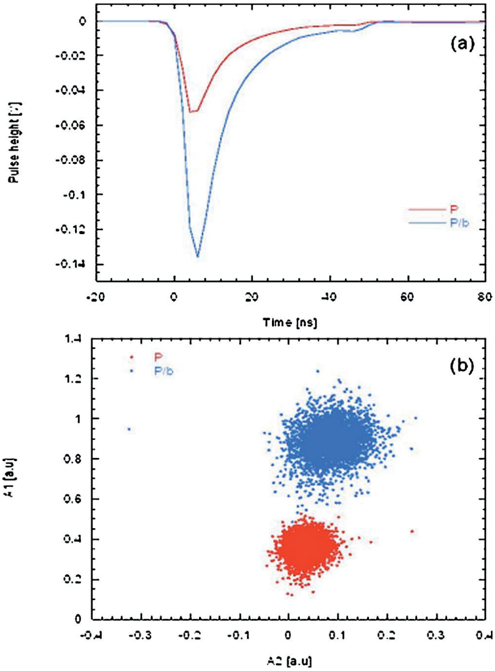

FIG. 1. (Color online) The response of the fast layer of the phoswich scintillator with and without backing to 5.5 MeV alpha particles with results on the average wave forms (a) and presentation of the individual event distributions A1 vs A2 (b).

The results on the event distributions A1 versus A2 for the two scintillators [Fig. 1(b)] are individually well clustered with their centers lying on a line of fixed A1/A2 ratio as expected for the same kind of radiation. The spreading area of the event groups depends on the fraction of the generated light in the scintillator that is collected. In other words, this spread represents the pulse height resolution which varies in proportion to the square root of the collected light in terms of the Poisson statistics of the number of photoelectrons generated in the PM tube cathode. This expresses the underlying quality of the pulse information contained in A1 and A2. The pulse height resolution results for the cases described above showed that it improves from 36% to 25% [full width at half maximum (FWHM)] with backing for A1+A2. This is about the factor of 1.5 expected from the pulse height difference taking the square root of the summed A1+A2 ratio for the two cases. For the amplitude A1 one

Downloaded 22 Aug 2008 to 130.238.67.59. Redistribution subject to AIP license or copyright; see http://rsi.aip.org/rsi/copyright.jsp

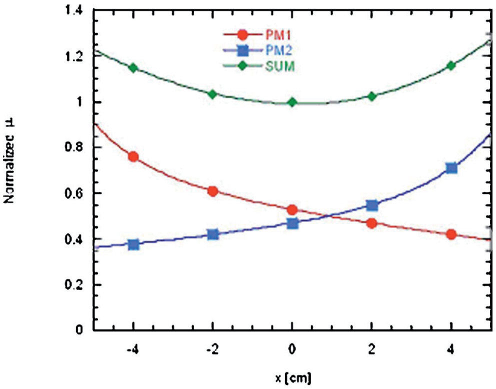

FIG. 2. (Color online) The response of the phoswich scintillator with backing in response to the flux of minimum ionizing electrons localized to different longitudinal positions x. The mean value μ of the event distributions A1+A2 from individual PM tubes compared to fitted double exponential curves and the sum (normalized to 1 for x=0 mm).

obtains 33%–22% which gives approximately the same ratio. The A1 values are slightly better which can be ascribed to the fact that the alphas stop in the thin layer. Adding A2 deteriorates resolution from the increase in the error coming from base line subtraction; in fact, the latter aspect makes the results on A2 unsuitable to extract a meaningful pulse height resolution.

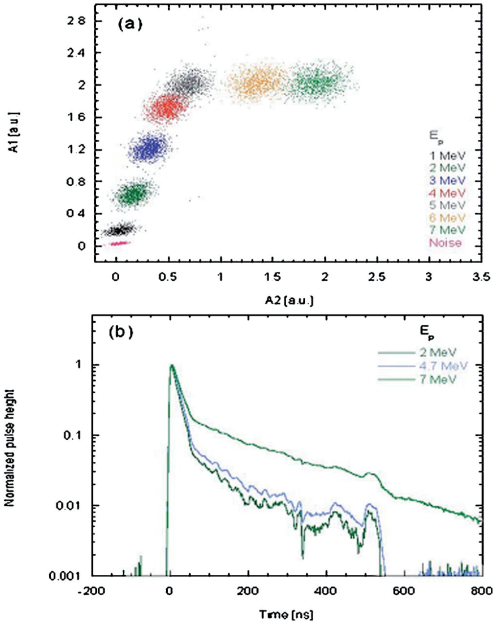

FIG. 3. (Color online) The response of the phoswich detector with backing presented as function of the event distributions A1 vs A2 for a protons of fixed energies (a) and average wave forms for E_n=2, 4.7, and 7 MeV (b).

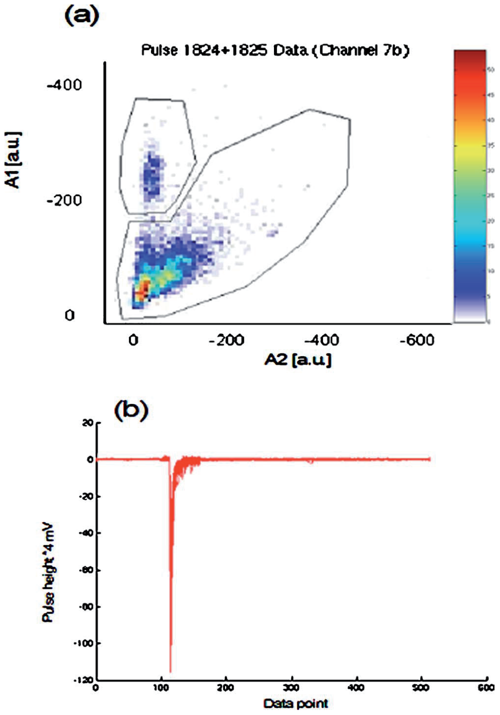

FIG. 4. (Color online) Data from the MPRu phoswich detector taken at JET for D plasmas with example of A1 vs A2 event distribution showing groups of recoil protons and background radiation (a) and wave forms for protons recorded with DAAC system (b). The MPRu was set at 2.5 MeV to record $d+d \rightarrow {}^3\text{He}+n$ neutron emission.

The above result for the alphas can be compared with that for electrons depositing energy in both layers in proportion to their thickness. Here we determine the pulse height resolution for the scintillator with backing to be 54% and 45% (FWHM) for A1 and A1+A2, respectively, and 54% for A2 only; the interpretation of these results is complicated by the presence of straggling. It can be mentioned in this context that the monolithic MPR scintillators performed better than the phoswich type which is the price to pay for the added range information. Another source of imprecision in pulse height is the variation that comes from longitudinally different interaction positions (x), i.e., the light transport distances to a PM tube. Such pulse response studies were performed with a collimated electron flux from a beta sources penetrating the prototype scintillator and detected with a small coincidence detector on the opposite side. The results obtained for a scintillator with backing (Fig. 2) show that the pulse height from the individual PM tubes changes more than a factor of 2 end to end with an x dependence of a double exponential. The summed pulse from the two PM tubes has a total variation span of about 20% from either scintillator end to the minimum in the middle and is a factor of almost 2 higher than the pulse of a single PM tube. As the summed pulse height is always used from the MPRu detec-

Downloaded 22 Aug 2008 to 130.238.67.59. Redistribution subject to AIP license or copyright; see http://rsi.aip.org/rsi/copyright.jsp

tor, the longitudinal variation is negligible compared to the pulse height resolution connected to the fraction of light that is emitted in the direction of the cone of total reflection transportation to the PM tubes. The MPRu scintillators have backing to approach the area limit set by the PM tubes.

A Tandem accelerator was used to expose a phoswich detector to a collimated beam of protons of fixed but changeable energy in the range $E_p=1-7$ MeV. With the protons impinging into the thin layer one finds a response in terms of the A1 versus A2 event distribution, as presented in Fig. 3(a). For each energy, the events are well clustered with centers following a curve close to that of a fixed A1/A2 ratio up to $E_p=5$ MeV. Beyond this point, there is no further increase in A1 but only A2. The abrupt change in the A1/A2 ratio indicates that the range of the impinging protons exceeds the 0.3 mm thick plastic scintillator, just below 5 MeV, the nominal value being 4.7 MeV.

The above range information were derived from the change in the measured wave forms produced by protons as exemplified by the data presented in Fig. 3(b). Here one can see that the wave forms stay steady from $E_p=1-4.7$ MeV while that of $E_p=7$ MeV shows the same leading edge shape but a broad tail setting at $t\approx 30$ ns. At JET, the scintillators of the MPRu spectrometer will be irradiated with practically monoenergetic recoil protons, so they will show A1 versus A2 event distributions of the type shown in Fig. 3(a).

SCINTILLATOR RESPONSE TO FUSION NEUTRONS AND BACKGROUND AT JET

The phoswich hodoscope has been put to the first test under realistic measuring conditions at JET operating with deuterium plasmas and the MPRu set to measure the 2.5 MeV *dd* neutron emission. An example of the results on the A1 versus A2 event distribution [Fig. 4(a)] shows a close clustering of the proton recoil events well separated from the ones due to the detector exposure to background radiation. Underlying these results are the measured wave forms. Those for protons are presented in Fig. 4(b) which are found to be similar to those projected from the prototype results [Fig. 3(b)].

DISCUSSION

In this article we have described the application of the phoswich scintillator technique to the focal plane detector hodoscope of the MPR spectrometer in its upgraded version (MPRu). The MPRu hodoscope was developed on the basis of the prototype tests described in the article to assess the required performance with regard to the ability to identify recoil protons against background. The MPRu hodoscope is performing as expected based on the first results of the MPRu under realistic measuring conditions at JET.

ACKNOWLEDGMENTS

This work has been performed under the European Fusion Development Agreement (EFDA) and the Association EURATOM-VR with support from Swedish Research Council, Uppsala University, JET-EFDA.

[1] J. Källne, *Proceedings of the Workshop on Diagnostics for ITER, Varenna, September 1997* (Plenum, New York, 1998); J. Källne, L. Ballabio, S. Conroy, G. Ericsson, J. Frenje, G. Gorini, M. Tardocchi, and E. Tranues, Rev. Sci. Instrum. **70**, 1181 (1990).

[2] A. Hjalmarsson, Uppsala University Neutron Physics Report No. UU-NF 99/7, 1999 http://www.inf.uu.se/Reports/Theses.html@1999 (unpublished); MS thesis.

[3] G. Ericsson, S. Conroy, G. Gorini, H. Henriksson, A. Hjalmarsson, J. Källne, and M. Tardocchi, *Advanced Diagnostics for Magnetic and Inertial Fusion* (Kluwer Academic, Dordrecht/Plenum, New York, 2002), pp. 121–124.

[4] H. Sjöstrand *et al.*, Rev. Sci. Instrum., these proceedings.

[5] A. Combo *et al.*, Fusion Eng. Des. **71**, 151 (2004).

[6] L. Giacomelli *et al.*, Uppsala University Neutron Physics Report No. UU-NF 06/8, 2006 (to be published).

Downloaded 22 Aug 2008 to 130.238.67.59. Redistribution subject to AIP license or copyright; see http://rsi.aip.org/rsi/copyright.jsp

Paper V

EFDA–JET–PR(08)02

H. Sjöstrand, E. Andersson Sundén, L. Bertalot, S. Conroy, G. Ericsson,
M. Gatu Johnson, L. Giacomelli, G. Gorini, C. Hellesen, A. Hjalmarsson,
J. Källne, S. Popovichev, E. Ronchi, M. Weiszflog, M. Tardocchi
and JET EFDA contributors

Fusion Power Measurement using a Combined Neutron Spectrometer-Camera System at JET

“This document is intended for publication in the open literature. It is made available on the understanding that it may not be further circulated and extracts or references may not be published prior to publication of the original when applicable, or without the consent of the Publications Officer, EFDA, Culham Science Centre, Abingdon, Oxon, OX14 3DB, UK.”

“Enquiries about Copyright and reproduction should be addressed to the Publications Officer, EFDA, Culham Science Centre, Abingdon, Oxon, OX14 3DB, UK.”

Fusion Power Measurement using a Combined Neutron Spectrometer-Camera System at JET

H. Sjöstrand[1], E. Andersson Sundén[1], L. Bertalot[2], S. Conroy[1], G. Ericsson[1], M. Gatu Johnson[1],
L. Giacomelli[1], G. Gorini[3], C. Hellesen[1], A. Hjalmarsson[1], J. Källne[1], S. Popovichev[4],
E. Ronchi[1], M. Weiszflog[1], M. Tardocchi[3] and JET EFDA contributors*

JET-EFDA, Culham Science Centre, OX14 3DB, Abingdon, UK

[1]*Uppsala University, Department of Physics and Astronomy, Division of Applied Nuclear Physics,*
75120 Uppsala, Sweden (EURATOM-VR Association)
[2]*ITER Diagnostic Division, ITER, Cadarache Centre, 13108 St. Paul lez Durance, France*
[3]*Physics Department, Milano-Bicocca University, and Istituto di Fisica del Plasma del CNR, Milan, Italy*
(EURATOM-ENEA-CNR Association)
[4]*EURATOM-UKAEA Fusion Association, Culham Science Centre, OX14 3DB, Abingdon, OXON, UK*
** See annex of M.L. Watkins et al, "Overview of JET Results ",*
(Proc. 21st IAEA Fusion Energy Conference, Chengdu, China (2006)).

Preprint of Paper to be submitted for publication in
Nuclear Instruments and Methods in Physics Research Section A

ABSTRACT.

Fusion power production is the ultimate goal of fusion research and its determination is crucial in any fusion energy application. In this paper the principles of collimated neutron flux measurements for fusion plasma power determination are described. In this method, a high-resolution neutron spectrometer provides an absolutely calibrated neutron flux and a neutron profile monitor ('camera') gives information on the neutron emission profile of the plasma. The total neutron flux seen by the spectrometer is discussed in terms of direct and scattered flux and a model is set up to evaluate the magnitude of these different components. Particular care is taken to estimate the uncertainties involved, both in the model and the measurements. The method is put to practical use at JET where a Magnetic Proton Recoil spectrometer and a neutron profile monitor are available. Results from JET's Trace Tritium experimental campaign in 2003 are presented, which shows that the systematic uncertainties in fusion power measurements is reduced in comparison to what has been presented for foil activation systems. A systematic error of 6% is reported here. For ITER these results imply that the fusion power can be redundantly measured and with better accuracies than for traditional methods. Furthermore the need for source calibration is reduced.

1. INTRODUCTION

Fusion power determination is one of the most fundamental requirements in a fusion energy application. Power control is essential for reactor control and safety, adherence to regulatory demands, control of material radiation effects, etc. Today's fusion power experiments utilize fuels of the hydrogen isotopes Deuterium (D) and Tritium (T). Energy is released in the neutron-emitting reactions $d + d \rightarrow {}^3He + n$ ($E_n = 2.5MeV$) or $d + t \rightarrow \alpha + n$ ($E_n = 14MeV$). The fusion power can be determined by separately measuring the 2.5 and 14MeV neutron emission rate.

At large fusion machines, such as TFTR, JET, JT-60U and ITER, fusion power measurements constitute an essential part of the diagnostic systems. At JET, the only fusion machine that at present can handle tritium, a combined system of activation foils and fission chambers is used for this purpose; for the next step machine, ITER, a similar system is proposed [1]. Possessing no intrinsic energy resolution the fission chambers serve as neutron monitors providing an integral measurement of all components of the total neutron emission [2]. The calibration accuracy achieved in such activation-foil based systems is has been reported to be 10% with about equal contributions (about 4-5%) from detector efficiency, measurement reproducibility, cross sections, neutron transport modeling statistics and systematics [3], the latter in some cases reaching 15% [4]. At JET the neutron camera has also been absolutely calibrated [5] with quoted accuracy of 15% [6]. The ITER design team calls for 10% accuracy in the fusion power determination [1]. However, due to concerns of the ITER tritium inventory an accuracy of 5% is desirable.

The present calibration methods are associated with inherent problems, both regarding calibration of the detectors themselves and the reliability of neutron transport model calculations [2, 7]. The estimates provided for the systematic uncertainties in the transport calculations often seem based on rather subjective comparisons of results from different models [8], hence the error in the uncertainty might be large. With larger machines the modeling uncertainties are likely to increase rather than decrease.

In this paper we discuss the principles of fusion power determination from collimated neutron measurements with a high-resolution [1] and well-characterized [2] neutron spectrometer, combined with plasma profile information provided by a neutron emission profile system. The possibilities offered are illustrated with results from JET using the magnetic proton recoil spectrometer, MPR [9], in combination with the neutron camera [10] system installed there. This is achieved by associating the MPR spectrometer count rate with the total rate and hence fusion power and internal heating. As a prerequisite the instrumental response, as well as the characteristics of the JET neutron flux, have to be well understood. This method has the potential of meeting the demands of high-accuracy measurements of the fusion power for future fusion experiments such as ITER.

2. CHARACTERISTICS OF THE JET NEUTRON FLUX

The neutron flux in and around a fusion device has two components, a direct flux and an indirect, scattered flux. These two components can be registered and distinguished by a neutron spectrometer.

The direct flux is composed of neutrons that have not undergone any interactions from their release in a fusion reaction to their detection; hence they retain their birth energy. From the plasma to the detection device (spectrometer), the direct flux may be reduced by different machine structures, by the machine-spectrometer interface and by the neutron collimator of the spectrometer. In magnetic confinement experiments the plasma is of low density, consequently the neutron flight path is not affected by the plasma itself.

The source of the scattered flux is also fusion neutrons; in this case those that have been scattered on their way from the fusion plasma to the spectrometer. Therefore, all scattered neutrons are, to some degree, energy degraded. The scattered flux can be further separated into two components: a high-energy component where the neutrons have lost so little energy (<200keV) that they are inseparable from the direct flux and a low energy component; the later can be separated from the direct flux. From a purely diagnostic point of view, scattered neutrons can come from three different sources:

- Machine structures, such as the back wall, the central column and other integral parts of the machine.
- Machine-spectrometer interface structures, such as the port and its components.
- Instrumental structures, such as the spectrometer's neutron collimator and radiation shield.

In the evaluation of the neutron flux some assumptions have to be made; in this work the is assumed to be toroidally symmetric and isotropic. The isotropic assumption is tested for different JET plasmas using the Fusion Product Spectra (FPS) code [11], which calculates the fusion product spectrum and the neutron flux distribution using the ion velocity distribution as input. It is found that the anisotropy, i.e., the ratio between the radial and the toroidal neutron emission, could, in principle, be as high as

---

[1] *A high-resolution neutron spectrometer has a peaked response function and a narrow (<10%) instrumental line width.*
[2] *The uncertainties in the response function are quantified.*

3%. In practice, the anisotropy of the emission is sufficiently low (<1% for JET plasmas) to be ignored.

2.1 DETERMINATION OF THE DIRECT FLUX

The calculation of the direct flux proceeds in two steps. First, an optical model for the direct neutron flux is applied. This model considers all mechanical structures of the fusion machine and the spectrometer to be either opaque or transparent. In a second step, modifications to the optical model are introduced. These take into account the attenuation of direct flux in structures initially considered transparent and transmission through structures that are initially considered opaque; an attenuation factor, a, and a transmission factor, st, are calculated. To determine these factors, neutron transport codes such as MCNP [12] are used. Thus, a removes part of the direct flux while the st factor restores some flux initially lost in the simplified optical model.

For a fusion plasma the neutron emission profile varies depending on the plasma conditions. Plasma conditions affecting the neutron emission, such as the plasma temperature and density profiles, are normally peaked, hence the neutron emission profile is also peaked. Consequently, the shape and location of the neutron emission profile can be parameterized. Using the optical model with a standard neutron emission profile as reference the ratio, p_{ref}, between the optical flux at the spectrometer, $F_{\mathrm{n,optical}}$, and the total neutron yield from the plasma, Y_{n}, can be calculated:

$$F_{\mathrm{n,optical}} \cdot A = Y_{\mathrm{n}} \cdot p_{\mathrm{ref}} \tag{1}$$

where A is the active area of the spectrometer. Deviations from the reference neutron emission profile are included as a profile factor Δp:

$$F_{\mathrm{n,optical}} \cdot A = Y_{\mathrm{n}} \cdot p_{\mathrm{ref}}\,(1+\Delta p) \tag{2}$$

The magnitudes of the attenuation and transmission factors depend on the profile, so profile factors have to be included also for these factors:$\Delta p, \Delta st$. Using the attenuation and transmission factors in the flux expression, the direct flux, $F_{\mathrm{n,direct}}$, can be calculated[3]:

$$F_{\mathrm{n,direct}} \cdot A = Y_{\mathrm{n}} \cdot \big(p_{\mathrm{ref}}\,(1 + \Delta p) + st\,(1 + \Delta st)\big) \cdot (1 - a)(1 + \Delta a)\big) \tag{3}$$

Δa is normally very small and has therefore been left out in this report and in the following equations.

2.2. DETERMINATION OF THE SCATTERED FLUX

The scattered flux can be divided into two components, a high-energy component, $F_{\mathrm{nS(HE)}}$, which is indistinguishable from the full-energy peak and a low energy component that can be separated from the full-energy peak. Using neutron transport models and a standard neutron emission profile the ratio, S_{HE}, between $F_{\mathrm{nS(HE)}}$ and Y_{n} can be calculated. In analogy with the direct flux case, deviations from the standard neutron emission profile are included in a profile factor ΔS_{HE}:

---

[3] *The signs used here are to give the actual factors/terms positive values.*

$$F_{\mathrm{nS(HE)}} \cdot A = Y_{\mathrm{n}} \cdot S_{\mathrm{HE}} \, (1 + \Delta S_{\mathrm{HE}}) \; (1 - a) \tag{4}$$

Experience with spectroscopic measurements at JET has shown that the low-energy flux is hard to predict by model calculations; its intensity is often underestimated [13]. The use of a high-resolution spectrometer allows the intensity and shape of this contribution to be determined experimentally. This information is used to correct the measured flux for the fraction of the low-energy scattered flux that is hidden under the full-energy direct peak. Thus, only the high energy scattered flux remains to be handled in the neutron transport model.

Contributions to the high-energy scattered flux come from small-angle scattering in the spectrometer's neutron collimator, the plasma vessel port plate and other internal port structures. The extent of the neutron source for this contribution depends on the location of the scattering point; for example, a vessel port "views" a much larger part of the plasma than the neutron collimator of the spectrometer (see Figure 1). Contributions to the low-energy scattered flux come from large-angle or multiple scattering and include the machine back wall, and other machine structures; the source of this component is in principle the entire plasma.

In summary, taking all the different factors and terms of this model into account, and experimentally excluding the low energy flux, one can write the expression for the total neutron yield as a function of the measured full energy flux, $F_{n,}$ at the spectrometer:

$$Y_{\mathrm{n}} = F_{\mathrm{n}} \cdot A \cdot \left[\left(p_{\mathrm{ref}} \, (1 + \Delta p) + st \, (1 + \Delta st) + S_{\mathrm{HE}} \, (1 + \Delta S_{\mathrm{HE}}) \right) \cdot (1 - a) \right]^{-1} \tag{5}$$

2.3 INSTRUMENTAL REQUIREMENTS

In order to determine the neutron flux in a collimated Line Of Sight (LOS) with good accuracy the diagnostic system must include a well characterized, high-resolution neutron spectrometer in combination with a neutron emission profile monitor. To minimize the dependence on modeling and transport calculations and make efficient use of the direct neutron flux the spectrometer should have a narrow instrumental line width. This makes it possible to retain most of the neutron spectrum dominated by the direct full-energy flux, while excluding most of the low-energy scattered flux. The spectrometer should have an energy bite [4] that allows simultaneous experimental determination of the intensity and shape of the low-energy scattered flux and the full-energy emission peak. This allows the fraction of low-energy scattered flux still remaining under the full-energy peak to be corrected for. Furthermore, such measurements can serve as important input for benchmarking of transport calculations. To determine the incident neutron flux, F_{n}, from the instrumental count rate, *c*, the instrumental response function has to be known. The response of the instrument is a function of the incident normalized neutron spectrum, $I(E_{\mathrm{n}})$, the neutron flux F_{n} and the spectrometer's energy-dependent efficiency (response) function, $e(E_{\mathrm{n}})$, which relates *c* to F_{n}:

[4] *Energy range covered for a specific setting of the spectrometer*

$$c = F_n \cdot A \cdot \int I(E_n) \cdot e(E_n) \cdot dE_n \tag{6}$$

$$c = F_n \cdot A \cdot e_{ref} \rightarrow F_n = \frac{c}{e_{ref} \cdot A} \tag{7}$$

where e_{ref} is the efficiency for a reference neutron spectrum, $I(E_n)_{ref}$. The uncertainty in $e(E_n)$ introduces systematic uncertainties in c and accordingly in Y_n. To be independent from other neutron flux measurements, the spectrometer must be absolutely calibrated in efficiency and energy.

In order to minimize statistical uncertainties high count rates are desirable. Consequently the instrumental efficiency and neutron flux, F_n, should be maximized. In order to maximize F_n the spectrometer should be placed close to the fusion machine. This puts great demands on the robustness and reliability of the instrument; it must be able to cope with harsh radiation and magnetic conditions. This also requires the instrument to possess an immunity to background, as given by the following characteristics:

- The instrument should be physically shielded from background radiation, so that only few background events are registered. Normally concrete, preferably borated, is used for neutrons, high Z materials are used for gammas and low Z material are used for Compton electrons.
- Even if detected, background events should be well separated from signal events.
- The background that remains indistinguishable from the signal should be possible to determine, so that the observed signal can be corrected.

Furthermore, a matching count-rate capability is necessary for the spectrometer not to saturate. Finally, for any instrument used in a fusion application the instrumental stability must be measured. The effects of instrumental transients and long-term variations in the measured results should be quantifiable and possible to correct for. This is particularly important in tritium experiments where access to the instrument is limited for safety reasons and the possibilities for service interventions can be years apart.

The neutron emission profile measurement is only used to determine the shape of the neutron emission profile and not the absolute intensity. The neutron emission profile can be determined directly by measuring the neutron emission from different parts of the plasma, or indirectly by recording the spatial distribution of important reactivity parameters, such as ion temperature and density. For the direct measurement, which is normally preferred, well calibrated detectors, a good understanding of the scattering situation and a correct model for the neutron emission profile are the most important prerequisites. A well-chosen LOS for the spectrometer can also minimize the propagation of the uncertainty of the neutron emission profile to the neutron yield.

3. FUSION POWER MEASUREMENTS AT JET

At JET a MPR neutron spectrometer and a neutron camera are present. These instruments meet many of the requirements posed above and have thus been put to use in an application of the neutron yield measurement method outlined here. The schematics of this system are illustrated in Figure 2.

The measured neutron flux at the spectrometer can be calculated using Equation 7. Combined with Equation 5, which relates the measured flux to the neutron yield, this gives the full expression for determining the neutron yield from the MPR count rate:

$$Y_n = \frac{c}{e_{ref}} \cdot \left[\left(p_{ref}(1+\Delta p) + st(1+\Delta st) + S_{HE}(1+\Delta S_{HE})\right)(1-a)\right]^{-1} \quad (8)$$

Based on this expression the fusion power can be derived. The original MPR-camera system at JET could only measure the 14MeV neutron yield and hence only the DT fusion power. To determine also the DD fusion power, a separate 2.5MeV spectrometer with similar characteristics to the MPR is needed. This is a requirement that has to be met for future fusion machines and a recent upgrade of the MPR [14-17] will allow for such measurements.

3.1 MODELLING AND CALCULATIONS

In order to relate'Y_n to'F_n as shown in Equation 2 and to determine the direct and scattered fluxes seen by the MPR at JET, two different computer models have been used. One code (LINE1) is based on an optical model and evaluates the direct flux by numerical volume integration. In this integration, the relevant plasma volume is divided into about 300 000 volume elements ("voxels"). The emissivity of each voxel and the solid angle of the spectrometer's active area from each voxel are determined. In this way one can establish a relation between the optical neutron flux and the total neutron emission given by Equations 9-12.

$$F_{n,optical} \cdot A = \int_{V_{plasma}} y \cdot \lambda(R,Z,\phi) \cdot \frac{\Delta\Omega(R,Z,\phi)}{4\pi}\, dV \quad (9)$$

where $\lambda(R,Z,\phi)$ is the normalized neutron emission profile and y is a scaling parameter to scale to the camera data, R is the major radius, Z is the height above the midplane and ϕ is the toroidal location. $\Delta\Omega(R,Z,\phi)$ is the solid angle of the spectrometer's active area as seen from location (R,Z,ϕ).

$$Y_n = \int_{V_{plasma}} y \cdot \lambda(R,Z,\phi)\, dV \quad (10)$$

$$\int_{V_{plasma}} \lambda(R,Z,\phi)\, dV = 1 \quad (11)$$

From Equation 2 one can identify:

$$p_{ref}(1+\Delta p) = \frac{\int_{V_{plasma}} \lambda(R,Z,\phi) \cdot \frac{\Delta\Omega(R,Z,\phi)}{4\pi}\, dV}{\int_{V_{plasma}} y \cdot \lambda(R,Z,\phi)\, dV} \quad (12)$$

Since $\lambda(R,Z,\phi)$ is assumed to be toroidally symmetric it can be projected onto a poloidal plane without loss of information.

$$\lambda\,(R,Z) = \int \lambda\,(R,Z,\phi)\,d\phi \tag{13}$$

In the present JET model the structures that cover the entire LOS, such as the port plate and the air gap between the port plate and the MPR, were initially treated as transparent, while structures that only partly restrict the LOS were considered opaque (beam scrapers, for example). The $y\cdot\lambda\,(R,Z,\phi)$ is calculated from camera data using the fitting code YAPAN [18].

A MCNP model of JET has been set up to calculate the deviation from the optical model in the direct flux case, providing the attenuation and the transmission factors. The same MCNP model is also used to calculate the scattered flux, and its energy distribution. In addition, the model is used to validate the optical flux calculations from LINE1. Horizontal and vertical cuts of the model are shown in Figure 3.

The JET neutron source, i.e., the plasma, has been modeled using toroidal rings at different poloidal positions with spatial-isotropic 14MeV mono-energetic neutron emission. To calculate the scattered flux 30×19 (vertical x radial) rings have been used. For the transmission and optical calculations 70×22 rings have been used. The size of the rings were (10×10) cm^2 for the scattering calculations and (2×10) cm^2 for the transmission calculations. These rings mapped the neutron emission region of the plasma, providing the MCNP corrections associated with the varying $\lambda\,(R,Z)$. Examples of the variation of model parameters depending on the location of the rings are displayed in Figure 4.

There are four features that needs to be accentuated in Figure 4: Firstly, in (a) and (b) one sees how the LOS enters the plasma at Z = 18cm and exits the plasma at Z = 70cm, which is due to the tilt of the LOS; secondly, there is a negative correlation with R for $\psi\,(R,Z)_{optical}$ and $\psi\,(R,Z)_{st}$. This can be understood from the fact that a larger fraction of the volume of the inner toroidal rings is covered by the LOS; thirdly, the ridges observed in (b) are located at the edge of the LOS where transmission through the collimator is most likely; and finally the broad shape of the scattered distribution seen in (c) is explained by the scattering surfaces (port structures and the central column) being illuminated by a large part of the plasma.

The 2D surfaces in Figure 4 are the flux response functions of the spectrometer, which have to be multiplied with the $\lambda\,(R,Z)$ (shown in Figure 5) and added in order to get the total number of neutrons seen by the spectrometer. In principle the flux response functions also have a toroidal dimension; however, since the neutron emission profile is toroidally symmetric the flux response functions is projected onto the poloidal plane.

From the flux response functions and the neutron emission profile the different flux components can be calculated (see Equation 14 -16).

$$p_{\mathrm{ref}}\,(1+\Delta p) = \frac{F_{n,optical}\cdot A}{Y_n} = \int \lambda\,(R,Z)\cdot\,\Psi\,(R,Z)_{\mathrm{optical}}\,dR\,dZ \tag{14}$$

$$S_{HE}\,(1 + \Delta S_{HE}) = \frac{F_{nS(HE)} \cdot A}{Y_n} = \int \lambda\,(R,Z) \cdot \Psi\,(R,Z)_{scatter}\,\mathrm{d}R\mathrm{d}Z \tag{15}$$

$$st\,(1 + \Delta st) = \frac{F_{st} \cdot A}{Y_n} = \int \lambda\,(R,Z) \cdot \Psi\,(R,Z)_{st}\,\mathrm{d}R\mathrm{d}Z \tag{16}$$

where F_{st}, is the flux due to transmission.

Equation 14 gives an estimate of the same quantity as Equation 12 (using the optical LINE1 model), by using an MCNP model where the transmission and scattering has been suppressed. The optical LINE1 model has been used in the data analysis. It has the correct geometry for the spectrometer's active area and hence models the optical flux with better accuracy than the MCNP model, for which a point approximation is used. The difference between the direct flux in the LINE1 model and the MCNP model gives an indication of the magnitude of the uncertainties introduced in S_{HE} and st due to the point approximation. When using the point approximation in the LINE1 model the results from the MCNP model and LINE1 model should be consistent given a correct implementation of the geometry in the two models.

A complicated JET model such as shown in Figure 3 is computationally very "expensive". Consequently, the contribution from unlikely events such as neutrons scattering deep inside the spectrometer's neutron collimator is not very well determined. Therefore, a second simpler MCNP model is set up to calculate the scattered flux in the neutron collimator and to validate the backscattering flux calculated with the JET model. This model uses a mono-energetic isotropic neutron source with the assumption that direct neutrons dominate the neutron flux (in the 10-14MeV region) in the neutron collimator. This assumption is supported by results from the more complete JET MCNP model.

Using these two MCNP models, both the origin of the scattered flux (see Figure 4) and its energy distribution is calculated. The scattered-neutron energy spectrum at the MPR spectrometer for a mono-energetic 14MeV flux is the sum of the two spectra seen in Figure 6.

In Figure 6 the low energy scattering component constitutes the relatively flat contribution from 10−13.8MeV. The high energy scattering component is restricted to the highest energy bin (13.8−14MeV).

A further complication is the fact that JET is operated at elevated temperatures of 200^o−300^oC, while mechanical drawings of the vessel and its parts normally are given at room temperature. The thermal expansion is monitored to evaluate the position of JET's system of magnetic probes. From this data it can be seen that the thermal expansion causes a shift in the port position by 9mm in the radial direction. In the port the angle between the machine radius and the MPR LOS is 25^o, consequently the port structures move by 3.8mm in the perpendicular direction to the MPR LOS and by 8.2mm towards the MPR spectrometer. This radial thermal expansion of the JET vessel has been included in the geometry in the different models.

3.2 THE MAGNITUDE OF THE DIFFERENT COMPONENTS

The magnitudes of the different components in Equation 8 are summarized below. Percentage values indicate the relative contribution to the full flux measured by the spectrometer for the case of the reference plasma. The size of p_{ref} is $8.97 \cdot 10^{-9}$, which means 1 out of $1.11 \cdot 10^{-9}$ neutrons from the reference plasma are reaching the spectrometer assuming an optical model.

There are four different structures that contribute to the attenuation factor, a: The port plate (14%), the thermal insulation of the port (1%) and the air between the port and the MPR (3%). In addition, a removable cross hair, accidentally left behind from the surveying of the instrument, also makes a significant contribution (22%) for data before 2004. The correction coefficients associated with these structures and components are understood. These factors have also been verified with simple exponential attenuation models.

There are two contributions to the transmission factor, st: structures in the port (8%), such as the beam scrapers, and the spectrometer's neutron collimator (10%). The central column is also included, but its contribution is negligible.

The high-energy scattering, $F_{\text{n}}(S_{\text{HE}})$, have three main contributions: the neutron collimator (3%), the port plate (1%), and other port structures (1%). The port contributions have been calculated using the JET model and the neutron collimator contribution has been calculated using the neutron collimator model. The sizes of the profile dependent components (ΔS_{HE}, Δst and Δp) are different for each particular experiment. The spread of these components for the analyzed data set are given in the results section.

Besides the signal protons there is also a Low-Energy Component (LEC) in the measured proton distribution (see Figure 7). The ±20% energy bite of the MPR allows for a determination of the intensity and shape of the LEC below the main emission peak. It turns out to be a flat distribution, with amplitude of a few percent of the main emission peak and extending from the main peak all the way down to the spectrometer's low-energy cut-off at 11MeV.

Besides the fitting of the amplitude of the LEC at low energies, $I(10MeV)_{LEC}$, the LEC spectral shape $I(E_{\text{n}})_{LEC}$ is given by the available signal spectrum, $I(E_{\text{n}})_{Signal}$, with higher energies as shown in Equation 17.

$$I(E_{\text{n}})_{\text{LEC}} = I(10MeV)_{\text{LEC}} \cdot \frac{\int_{E_n+\Delta E_n}^{+\infty} I(E_{\text{n}})_{\text{Signal}}}{\int_{0}^{\infty} I(E_{\text{n}})_{\text{Signal}}} \tag{17}$$

where ΔE_n is the energy shift of the LEC. ΔE_n is assumed to be zero. The LEC, including the part obscured by the main emission peak, is "removed" from the data in the fitting procedure. Most neutron spectrometers suffer from a low energy component in their measured spectra. For the MPR, the origin of LEC has been investigated, though it has still not been completely understood. The intensity of the LEC integrated from 10MeV to 18MeV is (7±2) % of the full energy peak [19]. The results from MCNP calculations (shown in Figure 6) estimates the low-energy scattering component to be only 0.5% for a metallic vessel back wall and up to 1% for a carbon back wall; obviously another source of the LEC has to be found. One possibility could be neutrons scattered at the end of the neutron collimator, which lose little energy, although the recoil-proton energy distribution would be downshifted in energy (a so called kinematical shift) due to larger *np* scattering angles. However, the maximum shift of such protons is about 700keV and the average shift only 300keV, so this process could not contribute to the LEC seen in Figure 7. Attempts have been made to associate the low energy component with *np* reactions in the aluminum structures. However, since the majority of such protons have energies in the 3-8MeV region, these events do not significantly contribute to the LEC in the 11 to 18MeV range [20].

Hopefully, new investigations using the upgraded MPR will shed further light on this issue. Since the origin of the low energy component cannot be fully explained, it is important to use a high-resolution spectrometer that allows for the low energy tail to be determined experimentally.

3.3 ERROR ANALYSIS

In this section the different contributions to the random and systematic uncertainties of the derived neutron yield given by Equation 8 are presented. The statistics of the instrumental count rate introduces a random uncertainty as presented in Equation 18.

$$\frac{\Delta c_{\mathrm{random}}}{\mathrm{c}} = \frac{\sqrt{c + 2b}}{\mathrm{c}} \tag{18}$$

where c is the number of protons and b is the number of background events registered in the hodoscope. Δc has also a systematic component due to errors in the separation of the signal protons from the background. In DT operation with an admixture of tritium of >5%, this systematic contribution is small (<1%); for trace tritium experiments, this contribution can be significantly higher, up to 3%. The subtraction of the LEC also contributes to the total error. The shape of the LEC is not fully known and partly covered by the signal peak, which introduces a systematic uncertainty. The number of LEC protons hidden under the signal peak amounts to 3%. An error propagation has been performed by varying ΔE_{n} (see Equation 17) and it was found that an error in the assumed shape contributes to a 1% systematic uncertainty in Y_{n}. The determination of the level of the LEC also introduces a random uncertainty. How well the LEC is determined is dependent on the statistics and the spectral shape. For pulses with insufficient statistics to determine the LEC the random uncertainty amounts to 2% due to the variations in the LEC [19].

The contributions to the uncertainty in the efficiency of the MPR instrument are reported here for completeness: the proton transmission (2%), the foil area (1.1%), the solid angle of the proton collimator (0.5%), the foil thickness (0.5%) and the *np* scattering cross section (0.2-1.0%). Summing the contributions in quadrature gives a total efficiency uncertainty of 2.6%. For a more detailed description of the instrument and the efficiency uncertainty calculations see Refs. [9] and [21].

The uncertainty in the profile correction factor, Δp, is estimated using a sensitivity analysis of the LINE1 results, using the uncertainties in the extracted λ (R,Z) parameters. The retrieved uncertainties are used as the standard deviation and the extracted parameters are used as the mean in a Poisson random number generator. The parameters with the added Poisson errors are fed into the LINE1 code and a new randomized Δp value is obtained. This procedure is repeated 300 times for each pulse and the mean and the standard deviation of the Δp distribution are calculated. From these studies it is found that the random uncertainty of Δp is between 0.01 and 0.04 (see Figure 8). There is an anti-correlation between the uncertainty in Δp and the neutron yield. This is expected, since higher neutron yields gives better statistics in the neutron camera and hence reduce the uncertainty in λ (R,Z).

The systematic uncertainties in the reference profile ratio, p_{ref}, are determined by the uncertainty in the geometry of the LOS and the JET torus. The flux calculations using the point approximation in the LINE1 model and the MCNP model agrees within 1%. Consequently it is reasonable to believe that the surveyed geometry has been correctly included in the models (attributing to an error < 1%). The systematic uncertainties in the camera data contributes to a systematic uncertainty in λ (R,Z), which propagates to a systematic uncertainty in p_{ref} (2.7%). The modeling of the λ (R,Z) also introduces a systematic uncertainty in p_{ref}. By changing the modeling assumptions it is found that p_{ref} is distorted with < 1%.

There are also systematic uncertainties associated with the parameters derived from the two MCNP models, such as the attenuation, transmission and high-energy scattering. The minimum achievable uncertainty in these parameters is given by the uncertainty in the cross sections used in the different models. Both the surveying of the JET geometry and the LOS contribute to uncertainties as do the actual modeling of the JET and MPR geometry and the physics included in the MCNP code. It is found that the point approximation in the MCNP model gives a 15 % difference between Equation 12 and Equation 14. This difference has no impact on the estimation of the optical flux (since the LINE1 model is used for that calculation). However, the magnitude of this difference gives an estimate of the uncertainty in the scattering and the shine-through calculations. The point approximation is the dominant uncertainty in these calculations.

For the attenuation calculations the accuracy of the surveying will dominate the uncertainty. The main uncertainty in the MCNP physics is the uncertainty of the cross-sections. However, in the present study this uncertainty is small compared to the factors mentioned above.

The different contributions to the systematic uncertainty are listed in Table 2. Summing the different contributions in quadrature gives a total systematic uncertainty of 6%.

4. RESULTS

The results presented here are from the JET Trace Tritium Experiment (TTE) in 2003 where around 1% of tritium was introduced to the plasma. During the TTE JET was operated under a variety of plasma and heating scenarios. The campaign had an emphasis on neutron diagnostic development and the MPR-camera system was operated independently of other neutron diagnostics and could provide data with a turnaround time of a couple of minutes. During the TTE, the JET reference method for determining the 14MeV neutron yield was the silicon diode detectors cross-calibrated with activation foils. A comparison between the results obtained with the MPR-camera system and the JET silicon diodes can be seen in Figure 9, where also the random uncertainties for the MPR-camera system are shown. The overall agreement between the two systems is good over the three orders of magnitude of data presented in the figure. A preliminary analysis of these data is reported in Ref. [22]; since then there have been several improvements in the models. These changes include a more complete treatment of the scattering and transmission effects, a more detailed surveying of the LOS, the addition of the aluminum cross hair accidentally left behind from the surveying of the instrument and the use of more accurate conversion foil thickness values (new measurements showed that their thickness differed by a percent from the design value).

The selection criteria for the data plotted is a 14MeV neutron yield $>10^{14}$ and a chi-square for the $\lambda\,(R,Z)$ fit < 5. The total systematic uncertainty for the MPR data is 6% and reported to be 10% [3] for the silicon diodes system, so the agreement between the two data sets is within the uncertainties.

For the TTE campaign the one-sigma-spread of the different profile components in Equation 8 has been calculated and can be seen in Table 3 were all the numerical values are summarized. Table 3 also summarizes the different contributions to the random uncertainties and their magnitudes for data from the TTE campaign.

The variations in the Δ parameters are not independent; Δp and Δst have a strong linear dependence whereas for ΔS_{HE} and Δp the correlation is weaker. A histogram of the variation of Δp can be seen in Figure 10.

5. DISCUSSION

There are several advantages in using a neutron spectrometer-camera system as described here for neutron yield determination. One is that practically all full-energy (14MeV) events counted by the spectrometer are used in the determination; a second advantage is that the low energy scattered component can be studied and excluded experimentally. A neutron spectrometer determines the neutron spectrum, so if there is an energy dependence in the flux detection efficiency (as there normally is) this can be accounted for as outlined in Equation 6. It has been reported that if not corrected for this can contributed to errors of up to 5% [23]. Furthermore, using a collimated neutron flux decreases the influence of the scattered flux at the detector, which is difficult to model. This method allows using optical models as the main tool and neutron transport models are only used to calculate corrections to the optical model. Since neutron transport models such as MCNP have systematic uncertainties whose magnitudes are hard to estimate, the use of optical models can reduce the systematic uncertainties.

Using a thin foil spectrometer like the MPR has some added advantages. The MPR efficiency is only dependent on well-known quantities, such as the *np* scattering cross section and the spectrometer geometry, thereby limiting the uncertainty in the flux measurement. Hence, the MPR is *ab initio* absolutely calibrated both in flux and in energy, and no *in situ* calibration of the instrument is needed. *In situ* calibration of neutron spectrometers have previously been attempted at TFTR where accuracies of 20% were achieved, mainly dependent on the uncertainty in the neutron generators [24]. *In situ* calibrations have also been performed at JET for fission chamber calibration were accuracies of 10% were achieved [25]. However the method has been abandoned, since new calibrations were needed after modifications to the JET hardware [26]. The calibration is also time consuming, delaying the physics experiments.

Since the present system has not been optimized for this application, modifications based on neutron transport calculations of the order of 20% have to be applied, which contributes significantly to the total uncertainty. Even so, this first application of the Spectrometer-camera method has provided good results with uncertainties smaller than what has been reported for traditional methods. Valuable experience has been gained and uncertainties could be substantially reduced in a dedicated yield measurement system, for example for ITER. In such a system the LOS should be chosen to minimize the absolute uncertainties in the attenuation and transmission factors, the scattered flux, the variations in the profile factors and the signal to background. To achieve good counting statistics, the neutron flux F_n should always be maximized. This is achieved by placing the spectrometer as close as possible to the torus, minimizing the intervening material and designing the collimator to make full use of the available neutron flux. A LOS for a dedicated yield/rate application would involve a better defined viewing cone, with a longer, but broader neutron collimator, although the influence of scattering in the collimator would have to be studied carefully. The systematic uncertainties of the MCNP model and in p_{ref} can also be reduced by a more careful surveying of the spectrometers geometry, the LOS as well as the torus geometry.

CONCLUSION AND OUTLOOK

The neutron yield/rate results from the spectrometer-camera system described here have shown that the systematic error in fusion power measurements is reduced in comparison to standard methods using foil activation systems. A systematic error of 6% is reported here for the 14MeV yield from fusion plasmas with trace amounts of tritium in the fuel. The new method has been compared to the 14MeV yield determined by the traditional Si diode system (calibrated by activation foil measurements) using data from JET's Trace Tritium experimental campaign in 2003; the agreement between the two methods is good. The availability of this new method has great implications for future fusion power measurements in both DD and DT operation. For ITER in particular these results imply that the fusion power can be redundantly measured and that the need for source calibration is reduced. Moreover, the high accuracy of the system is desirable due to concerns of the determination of the ITER tritium inventory. The method described here has been developed for 14MeV neutron measurements at JET; however with the new upgraded MPR spectrometer it should also be possible to measure the 2.5MeV neutron yield. In conclusion, this work highlights the important role that can be played by a high-resolution, well-calibrated neutron spectrometer when the fusion process is studied.

ACKNOWLEDGMENT

This work has been performed under the European Fusion Development Agreement (EFDA) and the Association EURATOM-VR with support from Swedish Research Council (VR), Uppsala University and JET-EFDA. The views and opinions expressed herein do not necessarily reflect those of the European Commission.

REFERENCES

[1]. A. Krasilnikov et al. 2005 *Nuclear Fusion* **45** 1503

[2]. O.N. Jarvis 1994 Plasma Phys. Control Fusion **36** 2

[3]. L. Bertalot, A. L. Roquemore, M. Loughlin, and B. Esposito 1999 *Rev. Sci. Instrum.* **70** 1137

[4]. M. Pillon, K.A. Verschuur, O.N.Jarvis, J.Källne and M.Martone 1989 *Fus. Eng. Des.* **9** 347

[5]. S. Popovichev et al. 2004 31st EPS Conference on Plasma Physics **28**G 5.173

[6]. JET DATA HANDBOOK: http://users.jet.efda.org/pages/data-dmsd/jetdatahandbook/web/php/ViewEntry_Results.php?type=1&name=DTN3&view=0

[7]. G. Sadler at al. in: P.E. Stott et al. (Eds) 1998 *Proceedings of the International School of Plasma Physics* Varenna, Italy, Plenum Press **2** 501

[8]. P. van Belle, O.N. Jarvis, and G. Sadler 1990 *Rev. Sci. Instrum.* **61** 3178

[9]. G. Ericsson, L. Ballabio, S. Conroy, J. Frenje, H. Henriksson, A. Hjalmarsson, J. Källne, and M. Tardocchi 2001 *Rev. Sci. Instrum.* **72** 759

[10]. J.M. Adams, O.N. Jarvis, G.J Sadler, D.B.Syme and N. Watkins 1993 *Nuclear Instruments and Methods in Physics Research* **A329** 277

[11]. P.van Belle and G.Sadler 1986 *Basic, Advanced Fusion Plasma Diagnostic Techniques* Varenna, Italy **3** EUR 10797 EN 764

[12]. MCNP manual, LA-UR-03-1987, Los Alamos

[13]. O.N. Jarvis 2002 Nucl. Instr. and Meth. in Physics Research **A476** 474

[14]. L. Gicomelli et al. 2006 *Rev. Sci. Instrum.* **77** 10E708

[15]. H. Sjöstrand et al. 2006 *Rev. Sci. Instrum.* **77** 10E717

[16]. E. Andersson SundÈn et al. 2006 *33rd EPS Conference on Plasma Phys. ECA* **30I** 1.071

[17]. G. Ericsson et al. 2006 Proceedings of Science FNDA, 039

[18]. O.N. Jarvis and S Conroy 2002 *Plasma Phys. Control. Fusion* **44** 1651

[19]. M. Johansson 2004 Uppsala Univ. Neutron Physics Report 04 02 UU-NF ISSN 1401-6269: http://www.inf.uu.se/Reports/UUNF04-02.pdf

[20]. K. Debertin 1965 *Rept. Inst.fuer Kernphysik, Frankfurt Reports* 11, exfor: http://www.nea.fr/dbforms/x4swdisp.cgi?21099.002

[21]. H. Sjöstrand 2003 Uppsala Univ. Neutron Physics Report 03 01 UU-NF ISSN 1401-6269: http://www.inf.uu.se/Reports/UU-NF03-01.pdf
[22]. H. Sjöstrand et al. 2004 31st EPS Conference on Plasma Physics **28**G 5.176
[23]. F.B. Marcus et al. 1991 *Plasma Phys. Control Fusion* **33** 4
[24]. C.W. Barnes and J.D.Strachan 1990 *Rev. Sci. Instrum.* **61** 9
[25]. O.N. Jarvis, G.Sadler, P.van Belle and T.Elevant 1990 *Rev. Sci. Instrum.* **61** 10
[26]. O.N. Jarvis et al. 1991 *Fusion Technology* **20** 265.

Table 1 Contributions to the uncertainty in p_{ref}. *and their propagation to the uncertainty in* Y_n.

Contributor	Nominal value	Uncertainty	Uncertainty Y_n
Collimator length	870mm	5mm	1%
Point of closest approach (LOS – JET center)	2048.5mm	10mm	0.4%
2 Beam scrapers	–	1mm	1.4%
Thermal expansion	6mm	3mm	1.2%
Collimator width	36mm	0.25mm	0.5%
LINE1 modeling	–	–	<1%
Camera data	–	–	2.7%
Modeling assumptions	–	–	<1%
Sum p_{ref}	**–**	**–**	**3.8%**

Table 2 The different contributions to the systematic uncertainty in the determination

Contributor	Nominal value	Uncertainty	Uncertainty Y_n
c	–	1–3%	1–3 %
e	$1.44 \cdot 10^{-5}$	2.6%	2.6%
p_{ref}	$8.97 \cdot 10^{-9}$	3.8%	3.8%
S_{HE}	$0.05 \cdot p_{ref}$	15%	0.2%
st	$0.18 \cdot p_{ref}$	15%	2.7%
a	0.33	5%	1.6%
Sum	**–**	**–**	**6%**

Table 3 The contributions to the random uncertainties and their magnitudes.

Contributor	σ	Uncertainty	Uncertainty Y_n
c(LEC)	–	1–2%	1–2%
c(statistics)	–	2–10%	2–15%
Δp	0.12	8–16%	1–2%
ΔS_{HE}	0.036	8–16%	<0.03%
Δst	0.12	8–16%	0.4%
Thermal expansion	2mm	2mm	0.8%

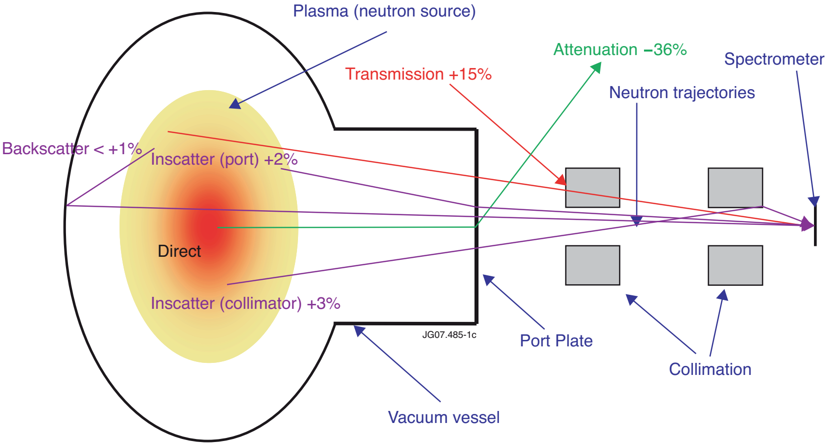
Plasma (neutron source)
Attenuation –36%
Spectrometer
Transmission +15%
Neutron trajectories
Backscatter < +1%
Inscatter (port) +2%
Direct
Inscatter (collimator) +3%
JG07.485-1c
Port Plate
Collimation
Vacuum vessel

Figure 1: Schematic view of the most important structures of JET and the MPR spectrometer affecting the magnitude of the neutron flux at the spectrometer. Different components of the neutron flux calculation model are identified and their influence on the flux for a reference neutron emission profile is shown.

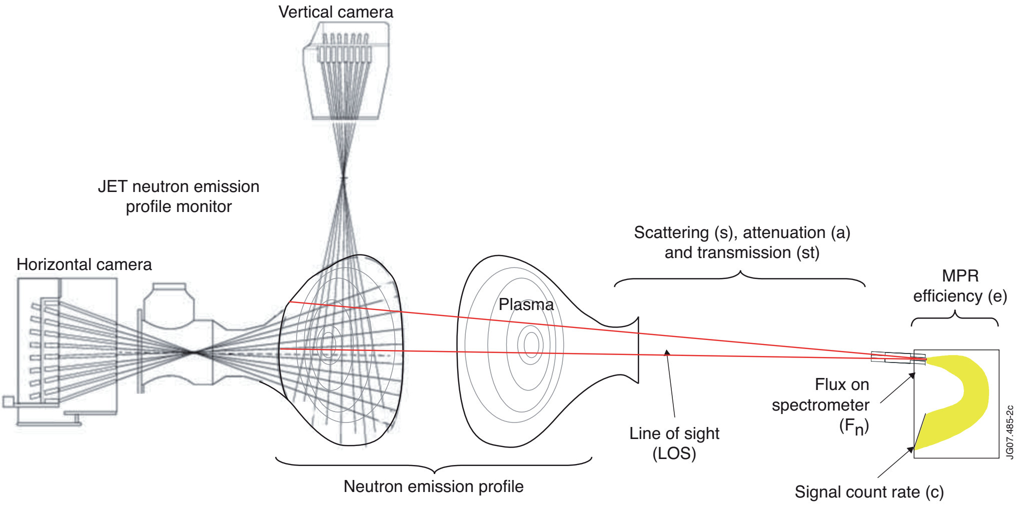
Vertical camera
JET neutron emission profile monitor
Horizontal camera
Plasma
Scattering (s), attenuation (a) and transmission (st)
MPR efficiency (e)
Flux on spectrometer (F_n)
Line of sight (LOS)
Signal count rate (c)
Neutron emission profile
JG07.485-2c

Figure 2: Schematic picture showing the positions and lines-of-sight of the MPR spectrometer and the neutron camera at JET. The different factors influencing the yield determination are also indicated in the figure.

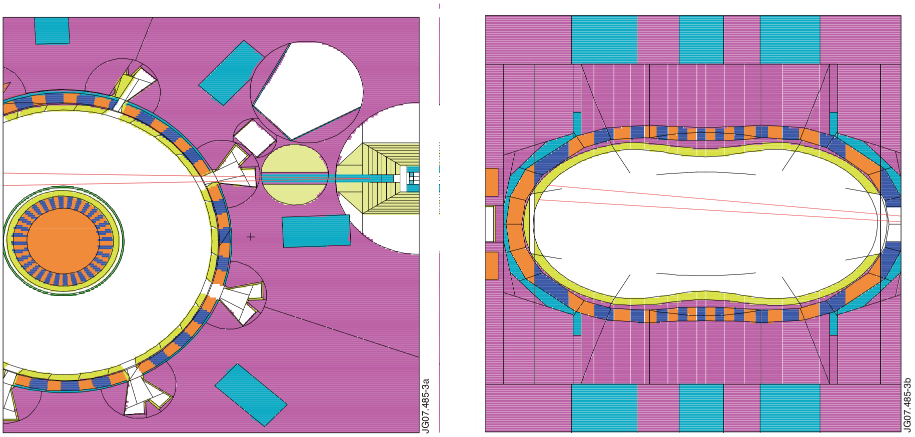
JG07.485-3a
JG07.485-3b

Figure 3: Illustration of the geometry used in the MCNP model of JET, the MPR spectrometer and surrounding structures. A horizontal cut to the left and vertical cut to the right. The MPR LOS is indicated with red lines.

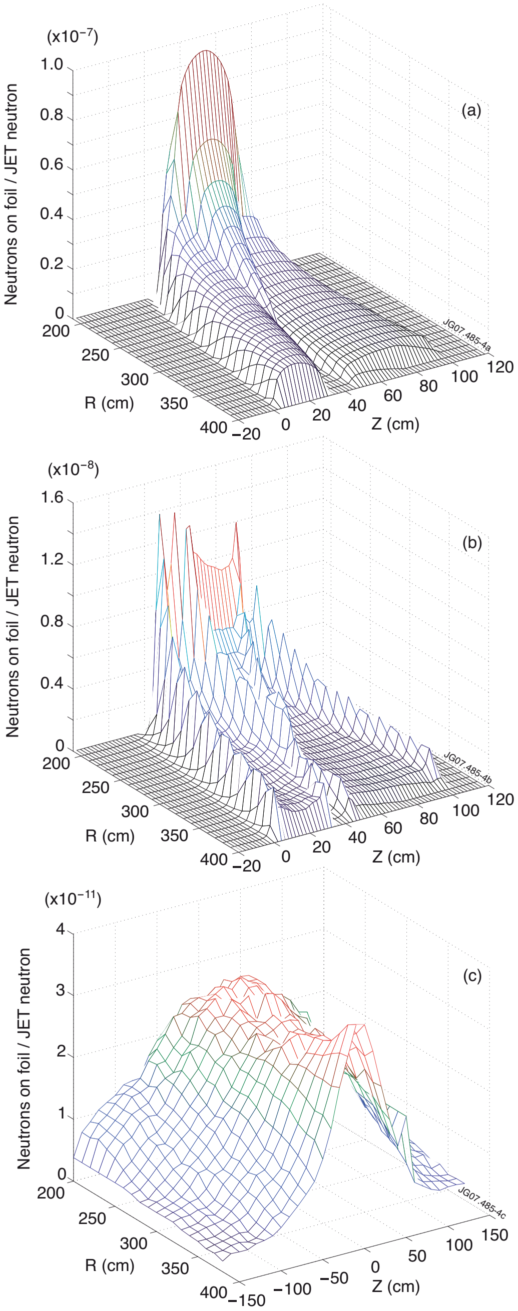

Figure 4 The optical flux response function $\psi\ (R,Z)_{optical}$ in (a), transmission flux response function $\psi\ (R,Z)_{st}$ in (b) and scattered flux response function $\psi\ (R,Z)_{scatter}$ in (c) as functions of the poloidal location of the emission ring. These flux response functions of the LOS expresses the relation between the number of neutrons emitted from the plasma and the number of neutrons on the spectrometer hence these functions have to be multiplied with the neutron emission profile to get the number of neutrons on the spectrometer. Note the different orders of magnitude in the three panels.

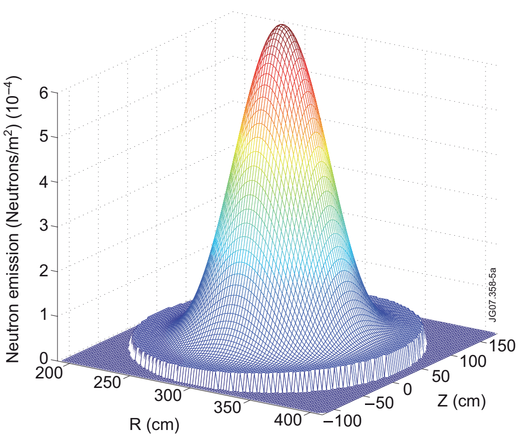

Figure 5: The normalized reference neutron emission profile, ψ (R,Z).

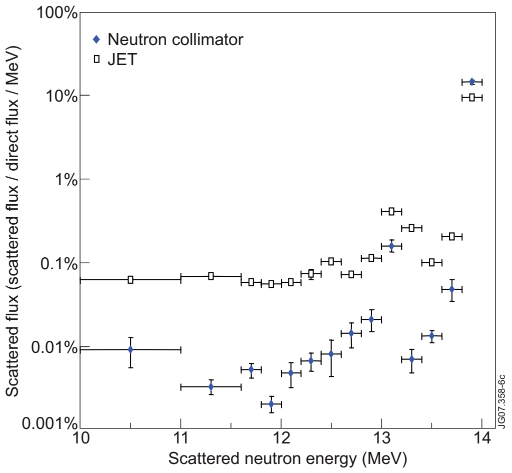

Figure 6: The MCNP-calculated relative flux intensity of scattered neutrons as a function of neutron energy. The contribution from the neutron collimator (diamonds) and from the rest of JET (squares) is shown. Horizontal bars indicate bin width. Note that the y-axis is in scattered†flux/ direct flux/MeV.

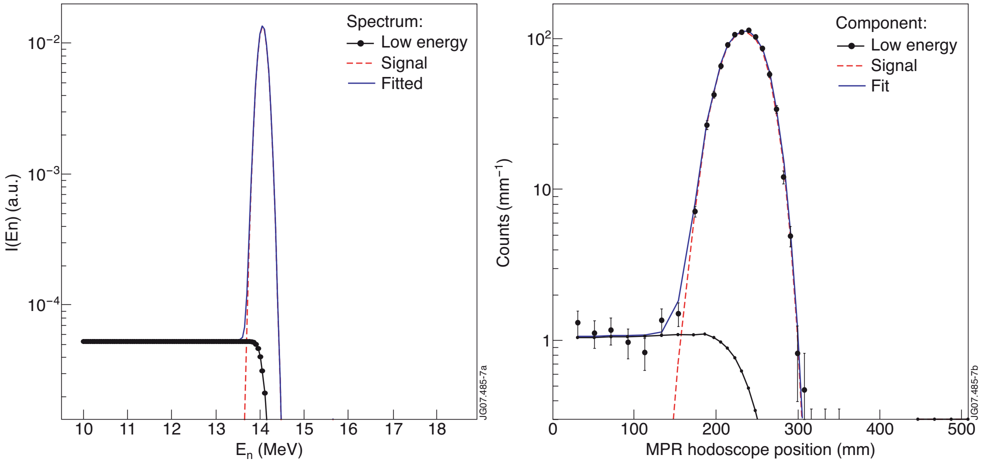

Figure 7: Left: The fitted neutron energy spectrum. Right: Example of a MPR proton position histogram with two fitted components: the low-energy component (black full line, dots, from 0 mm and up) and the main "14 MeV" signal peak (red broken line, peaking at 250 mm). The data (black diamonds) with error bars and the resulting fit (blue line) are also shown.

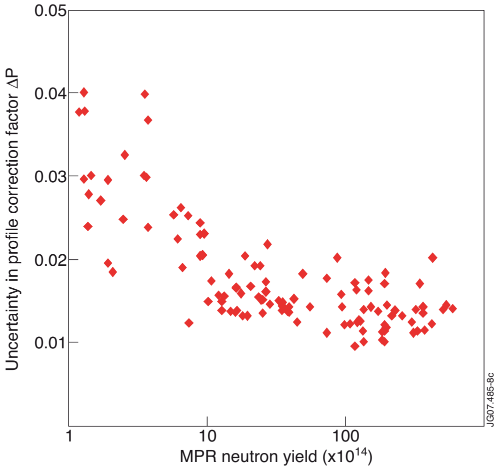

Figure 8: The random uncertainty in the profile correction factor, λ (R,Z), due to uncertainties in the Δp obtained in a sensitivity analysis (see text for details).

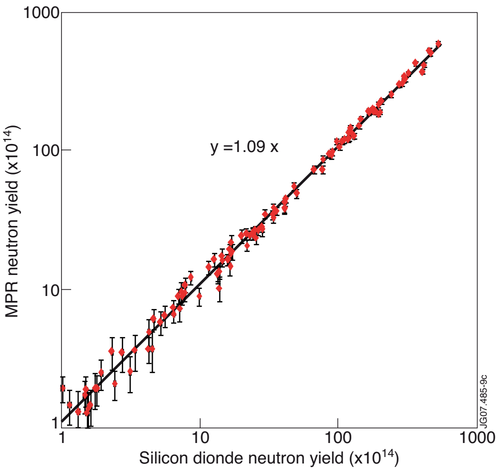

Figure 9: Comparison of pulse-integrated neutron yield data from the MPR-camera and silicon diode systems for 110 TTE pulses. The random uncertainties for the MPR-camera data are also shown. The silicon diode and MPR data sets are independent and ***no*** *cross-calibration has been done.*

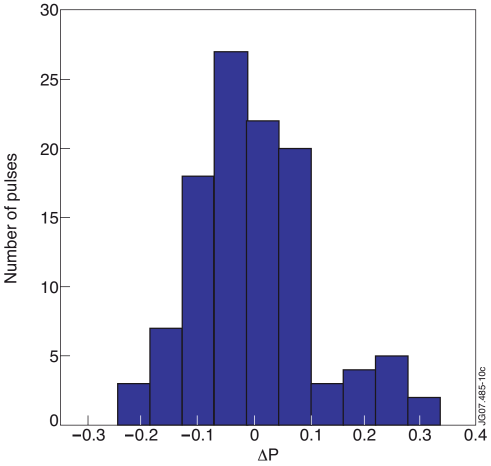

Figure 10: The distribution of Δp for the TTE campaign.

Paper VI

Fusion Power Measurement Using a Combined Neutron Spectrometer-Camera System at ITER

Henrik Sjöstrand[1], E.Andersson Sundén[1], S.Conroy[1], G.Ericsson[1], M.Gatu Johnson[1], L.Giacomelli[1], C.Hellesen[1], A.Hjalmarsson[1], J.Källne[2], E.Ronchi[1], M.Weiszflog[1] and JET EFDA contributors*.

JET-EFDA, Culham Science Centre, OX14 3DB, Abingdon, UK
1) INF, Uppsala University, EURATOM-VR Association, Uppsala, Sweden
2) Engineering Sciences, Uppsala University, Uppsala, Sweden
(Proc. 21st Int. Conf. Chengdu, 2006) IAEA, (2006)
** See the Appendix of M.L.Watkins et al., Fusion Energy 2006 See the Appendix of M.L.Watkins et al., Fusion Energy 2006 (Proc. 21st Int. Conf. Chengdu, 2006) IAEA, (2006)*

Abstract. A central task for fusion plasma diagnostics is to measure the 2.5 and 14 MeV neutron emission rate in order to determine the fusion power. A new method for determining the neutron yield has been developed at JET. It makes use of the magnetic proton recoil neutron spectrometer and a neutron camera and provides the neutron yield with small systematic errors. At ITER a similar system could operate if a high-resolution, high-performance neutron spectrometer similar to the MPR was installed. In this paper, we present how such system could be implemented and how well it would perform under different assumption of plasma scenarios and diagnostic capabilities. It is found that the systematic uncertainty for using such a system as an absolute calibration reference is as low as 3 % and hence it would be an excellent candidate for the calibration of neutron monitors such as fission chambers. It is also shown that the system could provide a 1 ms time resolved estimation of the neutron rate with a total uncertainty of 5 %.

Keywords: Fusion, diagnostics, neutron spectroscopy
PACS: 52.70.–m 29.30.Hs 89.30.Jj 29.40.– n

INTRODUCTION

The ultimate goal of fusion research is to produce fusion power and hence its determination will be an essential requirement at ITER. By separately measuring the 2.5 and 14 MeV neutron yield (Y) and neutron rate (R) at ITER the fusion energy and power can be determined. The fusion power measurement requirement for ITER is set to 10 % accuracy with 1 ms time resolution [1]. At JET a system consisting of a Magnetic Proton Recoil (MPR) High Resolution Neutron Spectrometer (HRNS) and a neutron camera has been used to measure the 14 MeV neutron yield independent of other neutron diagnostics [2] and this paper describes how a similar system could be used at ITER. The paper will concentrate on the ability to measure Y and the magnitudes of the systematic relative uncertainties that are associated to such measurements. The measured Y provides an absolute calibration for time resolved diagnostics such as fission chambers. The paper also investigates the accuracy of which R can be determined directly with the spectrometer-camera-system.

CP988, *Burning Plasma Diagnostics*, edited by F. P. Orsitto, G. Gorini, E. Sindoni, and M. Tardocchi
2008 American Institute of Physics 978-0-7354-0507-3/08/$23.00

Downloaded 01 Sep 2008 to 130.238.67.59. Redistribution subject to AIP license or copyright; see http://proceedings.aip.org/proceedings/cpcr.jsp

METHOD

In order to measure Y the spectrometer's neutron flux F has to be determined and its relation (p) to Y has to be known. This is described in detail in Ref. [2], and simplified in Equation 1.

$$Y = \int_t R \,\partial t = \int_t F \cdot p^{-1} \,\partial t = \int_t \frac{C}{e} \cdot p^{-1} \,\partial t \qquad (1)$$

where p depends on the neutron emission profile (NEP), C is the spectrometer count rate, t is the integration time and e is its efficiency. Besides the terms given in Equation 1, material effects, such as scattering, attenuation and transmission have to be taken into account.

The uncertainties in this paper are relative and divided into systematic (λ), random (σ) and total (Δ), where $\Delta = \sqrt{\lambda^2 + \sigma^2}$. The uncertainty of Y and R, ΔY and ΔR, is given by the uncertainty of the parameters in Equation 1 combined with the uncertainties in the material effects. To evaluate these uncertainties two different ITER lines of sight (LOS) have been investigated. One is for the ITER HRNS reference position in equatorial port cell 1 and the other is for a hypothetical tangential LOS.

C and e have to be known in order to determine the flux at the spectrometer. As reference an MPR type spectrometer with a 4 % resolution setting was used. The systematic uncertainty of the efficiency, λ_e, for the MPR is 2.6 % [2] and similar or better performance is expected for a dedicated ITER spectrometer. ΔC is dominated by counting statistics, which gives σ_R.

In this work the NEP have a quasi-parabolic shape (see Equation 2) and is assumed to consist of 10 nested elliptical iso-emissivity contours (IECs)[1]. Each IEC has a centre in the poloidal plane and a neutron emission (NE).

$$\mathrm{NE}(r_n) = \mathrm{NE}_0 \left(1 - (r_n)^2\right)^{\alpha}, \qquad n = 1 \ldots 10 \qquad (2)$$

where n is the index of the IEC, r_n is the normalized distance to the plasma centre, NE_0 is the peak neutron emission and α is the peaking factor. In this work the radial position of the common centre has been fixed to 6.2 m. The height above the mid-plane (Z) of the centre was varied between 0 and 1.2 m and the peaking factor was varied between 0 and 10.

The λ_p depends on the NEP and its magnitude is determined by λ_Z, λ_{NE} and the uncertainty in the alignment of the LOS, where as σ_p depends on σ_Z and σ_{NE}. The propagation of the LOS and plasma position uncertainties was calculated by varying the centre of the NEP and evaluating how p changes with Z. The ITER requirement for the overall uncertainty in the determination of the NE in each IEC is 10 % [1]. λ_{NE} has still to be evaluated and is dependent on the characteristics of the ITER neutron camera. For this work three different scenarios have been examined with ΔNE of 2 %, 5 % and 10 %, where Δp was determined for a wide range of NEPs. This was done by reconstructing each IEC using ΔNE as the standard deviation and NE as the mean in a Gaussian random number generator and thereby producing a randomized NEP for which p was evaluated. This was repeated 1000 times with the spread in p giving Δp and hence ΔY.

In order to assess the material effects a MCNP [3] model of ITER and the MPR collimator have been set up to calculate the amount of scattered and transmitted[2]

---

[1] The ITER requirement for the spatial resolution is $a/10$, where a is the minor radius.

[2] Those neutrons penetrating the collimator

Downloaded 01 Sep 2008 to 130.238.67.59. Redistribution subject to AIP license or copyright; see http://proceedings.aip.org/proceedings/cpcr.jsp

neutrons reaching the spectrometer. The amount of attenuation and scattering in the vacuum window has also been assessed. The model consists of a conical steel collimator with a radius of 17 mm at the foil and a radius of 150 mm at the first wall and a 5 mm vacuum window 5 m from the plasma edge. The neutron source in the model has full toroidal and poloidal coverage in order to correctly calculate the scattering contributions. MCNP point detectors (F5 tallies) were used [3].

RESULTS

The uncertainty for different parameters varies with changing plasma conditions. Figure 1a shows how ΔY varies as a function of α and ΔNE. The difference between using a radial and a tangential LOS is also illustrated. Figure 1b shows the Y dispersion in Z, $\partial Y / \partial Z$, as a function of Z and α, giving $\Delta Y = \partial Y / \partial Z \cdot \Delta Z$.

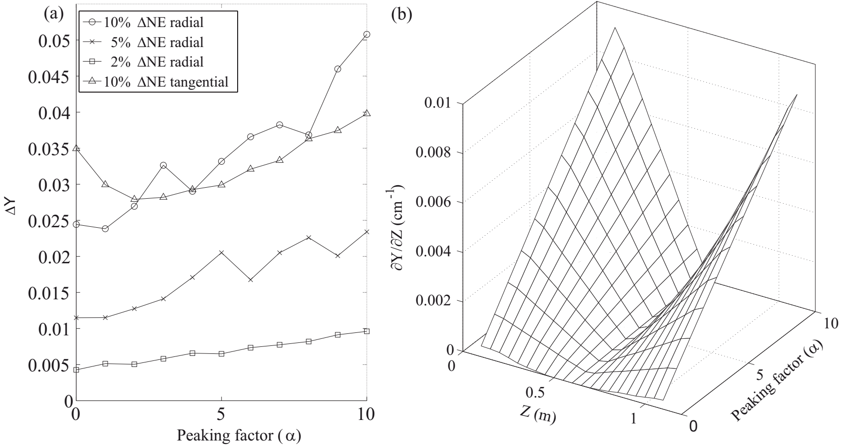

FIGURE 1. (a) ΔY as a function of α. **(b)** The $\partial Y_n / \partial Z$ as a function of Z and α.

A well-designed collimator should minimize the scattered and transmitted flux. It was found that a conical collimator where the angle and the size of the cone increase towards the plasma fill these criteria. In addition, the flux at surfaces close to the spectrometer should be minimized in order to reduce the scattered flux at the foil. It was established that scatters in the vacuum window gives a very small contribution (0.05 % of the direct flux), due to its distance from the plasma. This number would have to be re-evaluated if a vacuum window was placed close the plasma. Back-scattered neutrons (central column) is the only unavoidable scattering contribution.

A summary of the different contributions to λ_Y can be seen in Table 1 for a plasma (p1) with Z = 0.4, $\alpha = 2$ and λ_{NE} = 5 % and for an extreme plasma (p2) with Z = 0, $\alpha = 5$ and λ_{NE} = 10 %.

TABLE 1. Parameter sizes and their contribution to λ_Y

Contributor	**Magnitude**	**λ_Y (p1)**	**λ_Y (p2)**
Scattered neutrons	0.4 %	0.04 %	0.04 %
Transmitted neutrons	0.25 %	0.025 %	0.025 %
Attenuation (5 mm port)	8 %	0.4 %	0.4 %
λ_{NE} (see Fig.1a)	5 % / 10 %	1.3 %	3.2 %
λ_Z (see Fig. 1b)	1 cm	0.3 %	1.2 %

Downloaded 01 Sep 2008 to 130.238.67.59. Redistribution subject to AIP license or copyright; see http://proceedings.aip.org/proceedings/cpcr.jsp

LOS alignment uncertainty	0.5 cm	0.1 %	0.4 %
Efficiency	$1.44 \cdot 10^{-5}$	2.6 %	2.6 %
SUM (in quadrature)	-	3.0 %	4.3 %

If the system is used to measure R a significant contribution to the total uncertainty comes from σ_C and σ_{NE} [4], which both are time dependent.

TABLE 2. Parameter sizes and their contribution to ΔR for a 400MW plasma

Time resolution	σ_{NE}	$\sigma_R(\sigma_{\mathrm{NE}})$	$\sigma_R\ (\sigma_C)$	$\lambda_R=\lambda_Y$	$\Delta R=\sqrt{\sigma_R^2(\sigma_{NE})+\sigma_R^2(\sigma_C)+\lambda_R^2}$
1 ms	5 %	1.3 %	3.5 %	3.0 %	4.8 %
10 ms	2 %	0.5 %	1.1 %	3.0 %	3.2 %
100 ms	2 %	0.5 %	0.4 %	3.0 %	3.1 %

DISCUSSION AND CONCLUSION

The results given in Table 1 supports the idea that a HRNS with a broad central LOS combined with a neutron camera can determine Y with an accuracy (3.0 %) well below the ITER requirements. Consequently, the system could be used as an independent absolute calibration of the ITER neutron monitors. The uncertainty in the reconstructed NEP is an important contribution to λ_Y. Therefore, a research effort to evaluate the systematic uncertainties associated to the ITER camera should be pursued. λ_e is the dominating term for λ_Y and hence the choice of HRNS is very important. Thin foil HRNSs like the MPR have the advantage of e mainly depending on the well-known hydrogen cross section, which reduces the uncertainty.

ACKNOWLEDGEMENTS

The work leading to this article was funded by the European Atomic Energy Community and is subject to the provisions of the European Fusion Development Agreement

.REFERENCES

1. ITER Design Description Document N 55 DDD 2 01-07-05 W 0.3
2. H.Sjöstrand et al. 2006 UU-NF ISSN 1401-6269, http://www.inf.uu.se/Reports/Internal.html
3. MCNP manual, LA-UR-03-1987, Los Alamos
4. B. Esposito et al. ITPA Meeting-Moscow, 2006.04.11

Downloaded 01 Sep 2008 to 130.238.67.59. Redistribution subject to AIP license or copyright; see http://proceedings.aip.org/proceedings/cpcr.jsp

Paper VII

IOP PUBLISHING JOURNAL OF PHYSICS D: APPLIED PHYSICS
J. Phys. D: Appl. Phys. **41** (2008) 129801 (1pp) doi:10.1088/0022-3727/41/12/129801

Corrigendum

Triton burn-up neutron emission in JET low current plasmas
Henrik Sjöstrand, Giuseppe Gorini, S Conroy,
G Ericsson, L Giacomelli, H Henriksson,
A Hjalmarsson, J Källne, D Palma, S Popovichev,
M Tardocchi, M Weiszflog and EFDA JET contributors
2008 *J. Phys. D: Appl. Phys.* **41** 115208

In the unnumbered equation in the second column on page 2 an equals sign is missing and the subscript 0 in the denominator should be subscript f. The corrected equation is

$$t(W_\mathrm{f}) = \frac{2}{3}\frac{1}{\beta}\ln\frac{\frac{\alpha}{\beta} + W_0^{3/2}}{\frac{\alpha}{\beta} + W_\mathrm{f}^{3/2}}.$$

© 2008 IOP Publishing Ltd Printed in the UK

IOP PUBLISHING JOURNAL OF PHYSICS D: APPLIED PHYSICS

J. Phys. D: Appl. Phys. **41** (2008) 115208 (10pp) doi:10.1088/0022-3727/41/11/115208

Triton burn-up neutron emission in JET low current plasmas

Henrik Sjöstrand[1], Giuseppe Gorini[2], S Conroy[1], G Ericsson[1], L Giacomelli[1], H Henriksson[1], A Hjalmarsson[1], J Källne[1], D Palma[2], S Popovichev[3], M Tardocchi[2], M Weiszflog[1] and EFDA JET contributors[4,5]

[1] Department of Neutron Research, Uppsala University, BOX 525, SE-75120 Uppsala, Sweden
[2] INFM, Department of Physics, University of Milano-Bicocca, Milano, Italy
[3] UKAEA Fusion Association, Culham Science Centre, Abingdon, Oxon, UK
[4] JET-EFDA, Culham Science Centre, OX14 3DB, Abingdon, UK

Received 15 January 2008, in final form 19 March 2008
Published 16 May 2008
Online at stacks.iop.org/JPhysD/41/115208

Abstract

The 14 MeV neutron emission from JET deuterium discharges is analysed on the basis of the information on all neutron diagnostics available on JET. This emission is due to the $d + t \rightarrow \alpha + n$ reaction, mainly, the triton burn-up process, and is used to determine the fast triton confinement. A simplified model for triton burn-up neutron emission has been used and provides an adequate description of the 14 MeV emission. First orbit triton losses are found to amount to 50%, 20% and 10% at $I_p = 1$ MA, 2 MA and 3 MA, respectively. Neutron emission spectroscopy measurements with the magnetic proton recoil neutron spectrometer have detected a contribution to the 14 MeV emission due to residual tritium. For the selected (low impurity) discharges analysed in this paper 15% of the 14 MeV emission comes from the residual tritium reactions. It is also found that the residual tritium concentration tends to increase with increasing impurity content.

(Some figures in this article are in colour only in the electronic version)

1. Introduction

The study of fast charged fusion reaction products in high temperature plasmas is of intrinsic interest and has an important bearing on the physics of fusion α-particles. In particular, 1 MeV tritons from the $d + d \rightarrow t + p$ reaction have similar orbits to 3.5 MeV αs, which makes them suitable for simulation of certain α particle confinement properties, e.g. prompt losses. For this reason triton burn-up neutrons (TBN) have long been used to infer the confinement properties of α particles in tokamaks. This is described in [1] (and references therein) as well as in [2–9]. Only confined tritons can contribute to the TBN emission; hence, triton losses will lead to a reduction in the TBN emission, which can be observed experimentally.

For a given plasma device, triton losses depend mainly on the plasma current. The triton burn-up studies carried out on JET in the 1980s [8] explored mainly the plasma current range 3–6 MA, representing very high confinement conditions compared with those of previous studies on smaller devices [10–13]. In more recent years, new plasma regimes have been investigated on JET with plasma currents in the range 1–3 MA. This provides a new plasma operation range where fast ion confinement can be investigated experimentally, e.g. by triton burn-up studies. A further motivation for triton burn-up studies on JET is the general improvement in the neutron emission and other plasma diagnostic measurements leading to a more accurate triton burn-up analysis than the previous studies could attain.

In this paper the results of the analysis of TBN measurements in a set of low current H-mode plasmas of JET are presented. These plasmas provide a benchmark for triton burn-up studies at low plasma currents in so far as they indicate the accuracy that these studies can achieve in terms of comparison between experiment and theory and the required plasma conditions. A unique circumstance at JET is that residual tritium from previous DT-experiments is present, which contributes to the total 14 MeV neutron emission. This was regularly monitored using neutron spectrometry to ensure a correct interpretation of the triton burn-up results.

---

[5] See the appendix of Watkins M L *et al* 2006 *Proc. 21st Int. Conf. on Fusion Energy 2006 (Chengdu, 2006)* (Vienna: IAEA).

© 2008 IOP Publishing Ltd Printed in the UK

2. The triton burn-up model

The triton burn-up process has been extensively described in the past so it will only be briefly reviewed here. It is important to point out some approximations underlying the so-called 'classical' triton burn-up model.

2.1. Overview of the triton burn-up process

The TBN emission is the combined result of triton production, confinement, slowing down process and burn-up. Triton burn-up is manifested in the 14 MeV TBN emission intensity and its time evolution. A comparison of measured and theoretical time-resolved TBN emission is performed here with the help of a model describing the triton burn-up process.

Tritons of 1.01 MeV average energy are created in the reaction d + d → t + p at nearly the same rate as the routinely measured 2.5 MeV neutrons from the d+d → ^{3}He+n reaction. The fraction of these tritons that is lost promptly depends on the plasma geometry, the triton birth profile and on the plasma current and can be calculated by simulating the particle orbit motion in the plasma.

The tritons describe orbiting trajectories with a Larmor radius (L_R) determined by $L_R = p/(qB) = \sqrt{2E \cdot m}/(qB)$, where p is the momentum, E is the particle energy, q is the particle charge and m is the particle mass. This gives 7.4 cm for a B field of 3.4 T. As usual orbits can be circulating or trapped and their width increases in inverse proportion to the poloidal magnetic field; therefore, the orbits are better confined in a high-current plasma. Some tritons hit the plasma first wall during their first orbit and are lost. This kind of loss is referred to as 'prompt' since it takes place on the time scale of the orbit period, which is of the order of microseconds.

A useful quantity describing the confining properties of plasmas is the triton confined fraction f_c. This is the fraction of tritons that is not lost due to prompt losses. For fixed plasma geometry, f_c increases with current and decreases with increasing width of the triton emissivity profile. On JET, f_c is close to unity for plasma currents above 3 MA. The calculation procedure of f_c is outlined in section 2.3.

The fast tritons confined in the plasma are slowed down to thermal energies through Coulomb collisions. The slowing down equation for fast ions is [14]

$$-\dot{W} = \frac{\alpha}{\sqrt{W}} + \beta W,$$

where W is the triton energy and the coefficients are determined from the general expressions for the slowing down due to ions and electrons. These are

$$\dot{W}\,|_{\mathrm{i}} \cong -\left[\frac{2^{3/2}\pi q_{\mathrm{e}}^4}{m_{\mathrm{p}}^{1/2}}\right] \ln\Lambda_{\mathrm{i}} Z^2 A^{1/2} \sum_j \frac{n_j Z_j^2}{A_j} \frac{1}{\sqrt{W}} \equiv -\frac{\alpha}{\sqrt{W}},$$

$$\dot{W}\,|_{\mathrm{e}} \cong -\left[\frac{16}{3}\sqrt{\frac{\pi}{2}}\frac{q_{\mathrm{e}}^4 m_{\mathrm{e}}^{1/2}}{m_{\mathrm{p}}}\right] \ln\Lambda_{\mathrm{e}} \frac{Z^2}{A}\frac{n_{\mathrm{e}}}{T_{\mathrm{e}}^{3/2}} W \equiv -\beta W,$$

where Z, A are the triton charge and mass number, n_j, Z_j, A_j are the density, charge and mass number of each ion species in the plasma, q_e is the electron charge, m_e is the electron mass, m_p is the proton mass and $\ln\Lambda_e$ and $\ln\Lambda_i$ are the electron and ion Coulomb logarithms, respectively.

For the special case of constant coefficients the slowing down equation can be integrated to determine the time, t, at which the triton energy is reduced from its initial energy W_0 to a chosen energy W_f:

$$t(W_{\mathrm{f}})\frac{2}{3}\frac{1}{\beta}\ln\frac{\frac{\alpha}{\beta} + W_0^{3/2}}{\frac{\alpha}{\beta} + W_0^{3/2}}.$$

The triton slowing down time is defined as the time τ_S at which $\tau_S \equiv t(W_f \cong T_i)$. For these energies $\alpha/\beta \gg W_f$; hence $\tau_S \propto \ln(\beta)/\beta$ which results in a gross scaling of the slowing down time $\tau_S \sim T_e/n_e$ due to the combined T_e dependence of β and the logarithmic term. The slowing down time is not used in the triton burn-up analysis but its value and scaling are useful for error estimates. The 1 MeV tritons are slowed down on the time scale 0.1–3 s for typical JET plasma conditions.

During the slowing down, a fraction of the confined tritons undergo nuclear fusion (burn-up) reactions t + d → α + n, resulting in the 14 MeV TBN emission. The effective dt cross section is peaked at a triton energy of 170–200 keV depending on the deuteron temperature [15]. As a result, the burn-up probability peaks with a time delay (relative to the birth time) of the order of the slowing down time. This is reflected in a characteristic delay of the TBN emission relative to the 2.5 MeV neutron emission. This delay is an important observable to be reproduced in the simulations.

The 14–2.5 MeV neutron production ratio, which is the triton burn-up fraction ρ, is a function of the slowing down of the tritons as well as of their containment. The comparison between the measured burn-up fraction, ρ_{exp}, and the theoretical burn-up fraction, ρ_{th}, provides means to test the classical triton burn-up model. With the installation of silicon diodes at JET the 14 MeV neutron emission can be measured with adequate time resolution [9]. Time-resolved measurements have also been performed at JT-60U [4] and DIII-D [16]. Time resolution enables an accurate test of the classical triton burn-up model due to a detailed comparison of measured and simulated time-resolved TBN emission. Finally, the TBNs have a characteristic neutron emission spectrum [17, 18]; this is essential in order to identify the TBN emission unambiguously and distinguish it from other 14 MeV neutron emission processes due to residual tritium contamination of JET (see below).

The level of detail for modelling the triton burn-up process depends on the desired accuracy level. Since the TBN data have uncertainties at the 10% level and, furthermore, the triton burn-up model depends on the plasma parameters with uncertainties at the 10–20% accuracy level, we set at the 10% level the accuracy of the triton burn-up model. In this way many details of the triton burn-up process can be simplified or completely disregarded.

It is interesting to observe that in the region of the performed experiments ($n_e = (2\text{–}8) \times 10^{19}\,\mathrm{m}^{-3}$ and $T_e =$ 2–8 keV) a coarse scaling of the burn-up fraction is $\rho \sim f_c \cdot T_e \cdot n_d/n_e$. Thus, the uncertainties in T_e and in the density ratio n_d/n_e will propagate linearly to the result of any triton burn-up model simulation, no matter how accurate is the model. On the other hand, the characteristic time delay of the TBN emission scales as T_e/n_e. The combined availability of observables with different parametric dependences is sometimes useful for validating the accuracy of the input plasma parameters used in the simulations.

2.2. Model assumptions

The starting point of the triton burn-up model calculation is the time-resolved 'birth' distribution of tritons in the available phase space. It is assumed that the triton velocity distribution is isotropic; this is not true for plasmas with NBI and/or ICRH heating but the resulting error in the TBN emission is small [19]. The triton energy spectrum is broadened due to the kinetic energy of the reacting deuterons, but this has little consequence for the triton burn-up process. There is also a small spectral shift [20], which is disregarded here. The triton birth profile is assumed to be constant on a magnetic flux surface.

Since the two dominant branches of the dd-fusion reaction have nearly equal probability, the 2.5 MeV neutrons and the 1.01 MeV tritons have the same birth profile. Therefore, the 2.5 MeV neutrons provide the means to determine the triton birth profile experimentally using time-resolved data from the neutron camera system (see below).

Individual tritons orbits are calculated without any approximation to determine the triton confined fraction f_c. In principle, f_c varies with time for transient plasma conditions but for the purpose of this work f_c is determined once per plasma discharge.

The slowing down of tritons is calculated taking into account the time dependence of T_e and n_e as provided by diagnostic measurements. There is also a spatial dependence of the T_e and n_e values, which vary along each triton orbit. The approximation made here is to model the effect of the varying plasma parameters along the triton orbit by broadening the triton birth profile (i.e. by redistributing the tritons over a radial width chosen here to be 10% of the plasma minor radius) after which the tritons are assumed to slow down at this new location.

An effect that is not included in the present triton burn-up model is the occurrence of triton losses during the slowing down process. These are referred to as delayed losses. An example is the so-called neoclassical losses due to triton deflections by Coulomb collisions resulting in a change in orbit. These losses have been investigated numerically especially in relation to alpha particle confinement in plasma equilibria with a current hole [21]. The actual triton burn-up (where the triton undergoes a fusion reaction and emits a 14 MeV neutron) occurs with a probability given by the expression

$$\mathrm{d}p/\mathrm{d}t = \sigma_{\mathrm{dt}} n_{\mathrm{d}} v,$$

where σ_{dt} is the dt cross section, n_d is the deuterium density and v is the triton velocity. The time dependence of $\sigma_{\mathrm{dt}} n_d$ and v as the triton slows down is taken into account without any approximation, but σ_{dt} is calculated assuming the deuterons are at rest. The spatial dependence of n_d is dealt with in the same way as is done for T_e and n_e in the slowing down.

Since the density ratio n_d/n_e is not a directly measured quantity it must be derived from other experimental data. Here we determine n_d/n_e from Z_{eff} as provided by visible bremsstrahlung. It is further assumed that Z_{eff} and n_d/n_e are uniform and that one impurity species (usually carbon) of charge number Z is dominant. Under these assumptions the density ratio is related to Z_{eff} by

$$n_d/n_e = (Z_{\mathrm{eff}} - Z)/(1 - Z).$$

From this the uncertainty can be calculated:

$$\frac{\Delta(n_d/n_e)}{n_d/n_e} = \frac{\Delta Z_{\mathrm{eff}}}{Z - Z_{\mathrm{eff}}}.$$

The uncertainty in Z_{eff} from the visible bremsstrahlung is estimated to be 20–30%. This gives a 15–20% uncertainty in the deuterium concentration and hence in the triton burn-up fraction for a $Z_{\mathrm{eff}} = 2.5$.

A fixed 5% correction for the presence of small admixtures of hydrogen and beryllium is also included.

2.3. Numerical codes

The simplified triton burn-up model used for the data analysis is implemented by two separate simulation codes. The triton confined fraction, f_c, is determined once per plasma discharge from first orbit simulations performed with the Monte Carlo code McOrbit. The code uses the experimental magnetic equilibrium and the neutron emissivity profile to calculate the triton orbits. Examples of McOrbit calculations are shown in figures 1 and 2.

These are so-called 'fat banana' orbits of tritons in plasmas with different currents. For comparison α-particle orbits are also shown. Note that McOrbit calculates the exact trajectory and not its guiding centre approximation. One can see that these orbits are very wide and indeed are not confined in the low current case (see figure 2).

By generating a large number of these orbits the triton confined fraction, f_c, is determined. Typically 30 000 orbits are launched. The code can be used for more detailed studies, an example being shown in figure 3, which features the computed radial distribution of the tritons that are lost to the wall.

The second code used for triton burn-up simulation is called TRAP-T. It was developed in the late 1980s [9] and is still in use. It calculates the time evolution of the TBN emission assuming no triton losses using the assumptions described earlier. Each triton slows down and reacts at its birth point; that is, no orbit effect is included in the simulation, but the 2.5 MeV emissivity and other plasma parameter profiles affecting the triton slowing down are taken into account. For this purpose the model divides the plasma into a number of toroidal shells with T_e, n_e and the neutron emissivity specified by diagnostic measurements (usually the LIDAR Thomson scattering system and the neutron cameras). The deuterium density is derived from Z_{eff}. The model is time dependent and allows one to

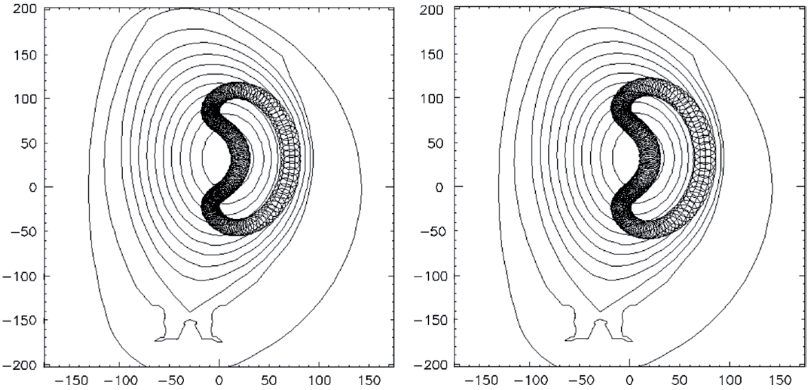

Figure 1. Example of 'fat banana' orbits of a 1 MeV triton (left) and a 3.5 MeV α-particle (right) with the same initial position ($x = 0$ cm, $z = 3$ cm) and pitch angle ($\theta = 75^\circ$). The magnetic equilibrium used in the simulation is taken from JET discharge #52958 at time $t = 21.86$ s. The plasma current was 2.6 MA. The x and y coordinates are the distance in cm from the geometrical centre of the vacuum vessel.

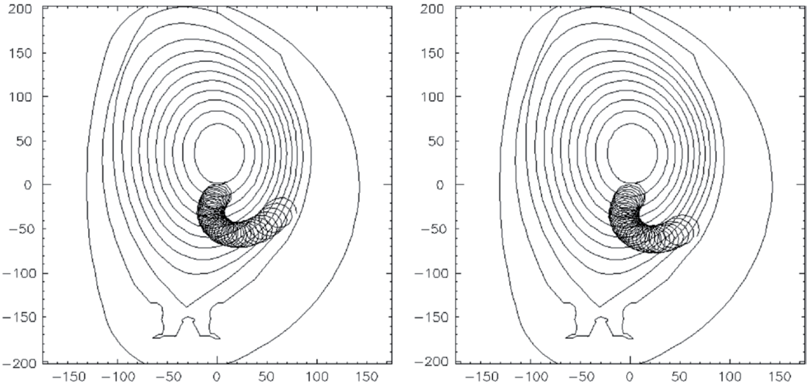

Figure 2. Same as figure 1 but for a 1.6 MA discharge (#52771, $t = 18$ s). The particles are no longer confined.

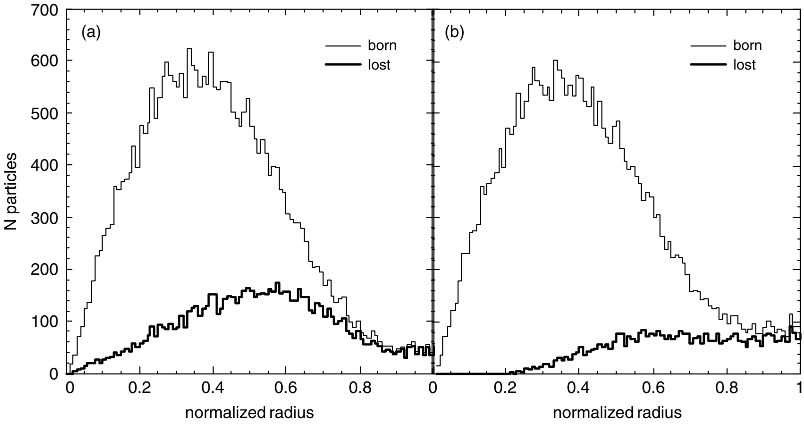

Figure 3. Examples of radial profiles of simulated tritons in JET plasmas at (*a*) low current (#52771 at $t = 18$ s, $I_\mathrm{p} = 1.6$ MA, total losses 29%) and (*b*) medium current (#52958 at $t = 22$ s, $I_\mathrm{p} = 2.6$ MA, total losses 15%).

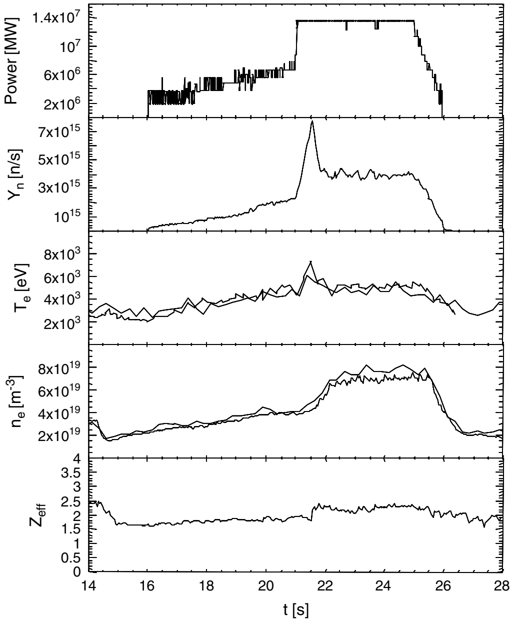

Figure 4. Time traces of some plasma parameters for JET discharge #52958, which was an H-mode discharge with plasma current $I_p = 2.6$ MA and toroidal magnetic field $B_T = 2.6$ T. Shown from the top are the traces of neutral beam injection power, total neutron yield, peak electron temperature from LIDAR and ECE, peak density from LIDAR and interferometry and Z_{eff} from visible bremsstrahlung.

determine the TBN yield as a function of time. The model was used extensively for the high current (above 3 MA) plasmas of JET [9] where triton losses could hardly be observed. Here we extend its use to currents as low as 1 MA by combining it with independent calculations of the triton confined fraction, which, however, must not vary in time and space. The systematic error introduced by neglecting the spatial variation of the losses (see figure 3) is further addressed in section 5.

3. Experiment

The measurements analysed in this paper were carried out in the period October 2000–May 2002. During this period JET was operated in different modes and here we analyse the discharges, most of which were intended to achieve H-mode conditions. These discharges have long periods of nearly steady-state conditions. Time traces of a typical discharge are shown in figure 4.

All data have uncertainties at the 10–20% level except for the NBI power. Some of the data shown are subsets of the data used as an input for the TRAP-T simulations. This includes the total (2.5 and 14 MeV) neutron yield measured by a set of fission chambers, which in practice coincides with the 2.5 MeV yield since the 14 MeV contribution is at the 1% level. Neutron emissivity profiles (not shown) were also measured routinely with the two JET neutron cameras and used in the simulations. The 14 MeV neutron yield was measured with a silicon detector working on the following principle. The (n, α) and (n, p) reactions in silicon can be used for monitoring the 14 MeV neutron flux from JET discharges because the reaction thresholds are above the 2.5 MeV neutron energy from dd reactions. The energetic reaction products are retained within the silicon and produce signals much greater than those from the simple scattering of neutrons and those due to gamma rays. Silicon diodes are therefore suitable for monitoring the 14 MeV neutron emission at all intensities [22], from triton burn-up to full DT-plasma experiments, with limitations due to radiation damage. At JET for D-plasma operation an Si detector with a 450 mm^2 active area and a 1 mm sensitivity depth is usually in use for TBN measurements.

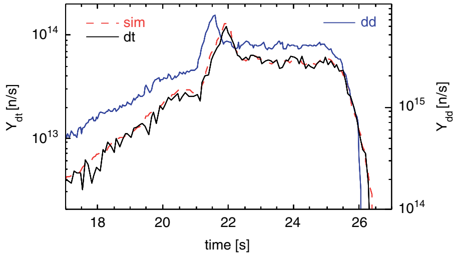

Figure 5. Time-resolved 2.5 MeV (left scale) and 14 MeV (right scale) neutron yields for JET plasma discharge #52958 ($I_p = 2.6$ MA) plotted on log scale. The dashed line is the simulated 14 MeV yield from triton burn-up. The time difference between the 2.5 MeV and the 14 MeV traces is due to the slowing down time of the tritons.

All neutron measurement systems are calibrated by comparison with absolute, time-integrated neutron measurements performed with an activation system [23]. An example of calibrated 2.5 and 14 MeV time traces is shown in figure 5, which also shows the result of a TRAP-T simulation. The agreement between data and simulation is very close in this particular example.

The yield and emissivity measurements are complemented by neutron spectrometry measurements of 14 MeV neutrons performed with the MPR spectrometer [24]. These measurements have the important task of establishing the presence of 14 MeV neutron emission processes different from the TBN emission. The MPR rates are very low in deuterium plasmas and data from many (of order 100) plasma discharges need to be added to achieve adequate statistics. Under these conditions the MPR is set so that the spectrum of the analog to digital converter (ADC) for each hodoscope detector is recorded. An example of an ADC spectrum is shown in figure 6 (left). It features a high-energy peak above channel 400 due to np scattering from a CH$_2$-conversion foil depositing their full energy in the scintillator. The intensity of this peak and similar peaks in the ADC spectra of other hodoscope detectors is plotted in the form of a position histogram in figure 6(*b*).

This histogram is finally analysed by folding the detector response with the model neutron energy spectra. This method has been used previously for low rate observations of TBN [17]

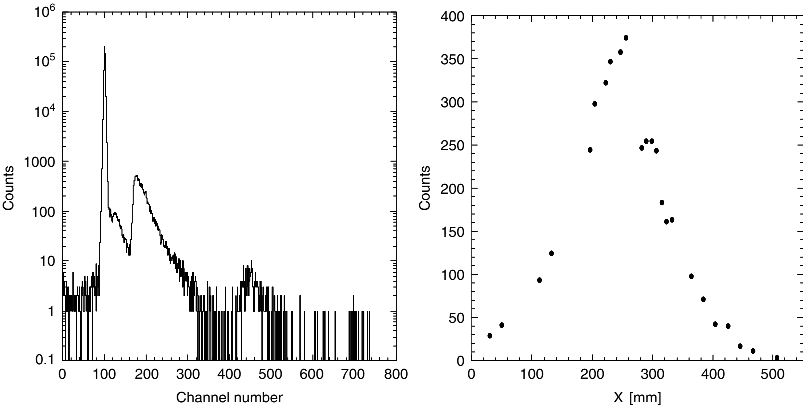

Figure 6. Examples of neutron spectrometry data. The data refer to all plasma discharges for which MPR data were recorded. To the left the ADC spectrum for hodoscope detector #17 (hodoscope coordinate $X = 248$ mm) features a well separated high-energy peak above channel 400. The intensity of this peak and similar peaks in ADC spectra of other hodoscope detectors is plotted in (the right panel) as a position histogram.

and is known to provide data with accuracy at the 5% level. However, for some of the channels the data were of too poor quality and they could not be included in the analysis.

4. Measurements and analysis

4.1. Data selection

A set of 112 discharges was selected from a total of hundreds by applying the following selection criteria. First, a practical threshold of 2×10^{15} in the total neutron yield was imposed in order to achieve sufficient statistics in the 14 MeV neutron measurements. Second, only plasmas with $Z_{\rm eff} < 2.5$ were included in the analysis. The reason for this threshold in $Z_{\rm eff}$ is the uncertainty in the $n_{\rm d}/n_{\rm e}$ ratio. Higher $Z_{\rm eff}$ values mean larger uncertainties in $n_{\rm d}/n_{\rm e}$, which propagate linearly to the simulated burn-up fraction. Finally, some discharges had to be rejected because of the poor quality of some diagnostic data required for the analysis.

The data set selected for analysis covers the range of plasma currents 1–3 MA. The data show some variability in this range as illustrated by the measured burn-up fraction values, $\rho_{\rm exp} = N_{\rm dt}/N_{\rm dd}$, where $N_{\rm dt}$ and $N_{\rm dd}$ are the total (time integrated) 14 and 2.5 MeV yields. The $\rho_{\rm exp}$ values are plotted in figure 7 as a function of plasma current. The data show a trend given approximately by $\rho_{\rm exp}[\%] = I_{\rm p}[{\rm MA}]/2$ with a large scatter around this trend. The current dependence of $\rho_{\rm exp}$ is mainly a manifestation of a well-known correlation between plasma current and electron temperature.

4.2. Results of data analysis

Code simulations were run for all plasma discharges in the database. An example where the agreement between simulation and data is remarkable is shown in figure 5. This was a 2.6 MA discharge for which we expect most of the triton to be confined. Another example of a high current discharge is shown in figure 8. The agreement is very good regardless of the detailed shape of the 2.5 MeV neutron time trace. In particular, the transients in the TBN trace are well reproduced, indicating that the relevant input data and the model assumption have adequate accuracy.

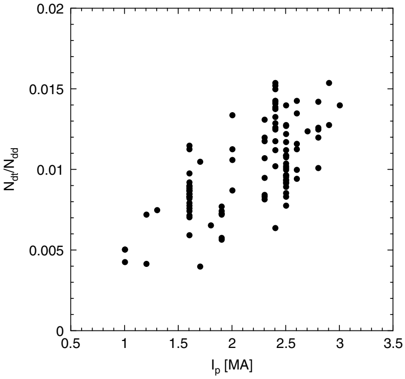

Figure 7. The ratio of 14 MeV and 2.5 MeV neutron yields from selected plasma discharges (see text) plotted versus plasma current.

At lower plasma currents the TRAP-T simulation is systematically above the experiment. This is not surprising and we expect it to be explained in terms of triton losses not included in the TRAP-T simulation. An example is shown in figure 9 where the plasma current is rather low. The log scale plot shows that a scale factor can account for the mismatch between simulation and data; however, the statistics is too low to provide conclusive evidence in the rise and fall phases of the 14 MeV neutron emission, which would be most sensitive to deviations from the model assumptions.

Evidence of triton losses manifests itself in the TBN data by taking the ratio $\rho_{\rm exp}/\rho_{\rm sim}$ between the experimental

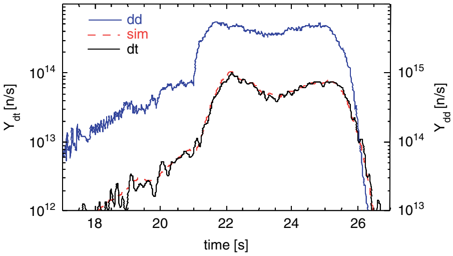

Figure 8. Time-resolved 2.5 MeV (left scale) and 14 MeV (right scale) neutron yields for JET plasma discharge #53718 ($I_p = 2.5$ MA) plotted on the log scale. The dashed line is the simulated 14 MeV yield from triton burn up.

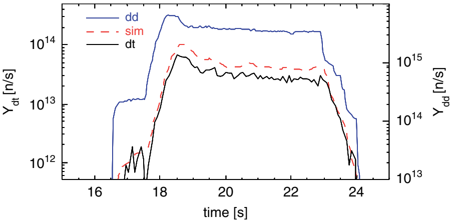

Figure 9. Same as figure 8 but for JET plasma discharge #52771 ($I_p = 1.6$ MA).

ρ_{exp} values and the corresponding simulated value ρ_{sim} from TRAP-T, which assumes no losses. The ratio is plotted in figure 10 versus the plasma current for the same plasma discharges as in figure 7. The dashed line marks the unity ratio expected under conditions of perfect triton confinement. Open and full triangles are for total 2.5 MeV neutron yields below and above 10^{16} neutrons, respectively. No obvious correlation of the ratio with the neutron yield is observed, but a clear current dependence is seen.

A similar current dependence is found (figure 11) in the confined fraction, f_c, determined from orbit simulations using the McOrbit code. Losses at the 50% level are found to be typical of 1 MA plasmas; at 2 MA and 3 MA the losses are about 20% and 10%, respectively. There is some scatter of the f_c values about the average current dependence, which can be attributed to various causes including different neutron emissivity profiles for the same total plasma current. Before drawing conclusions from the data of figures 10 and 11 we must however consider the contamination of the 14 MeV neutron data by residual tritium.

5. The role of residual tritium

Neutron spectrometry provides evidence of a non-negligible amount of 14 MeV neutrons emitted by residual tritium. Figure 12 shows the analysis of an intensity histogram in terms of components of the neutron spectrum obtained by adding data from a large number of (over 300) discharges for this study for which data are available. The fitted line is the sum of a broad component of known shape [18] from the triton burn-up (labelled TBN) and a narrow component (labelled thermal) that is assumed to be of thermonuclear shape (i.e. Gaussian [20]). There is also a third low energy component. The thermal component is attributed to residual tritium from previous DT-experimental campaigns [24].

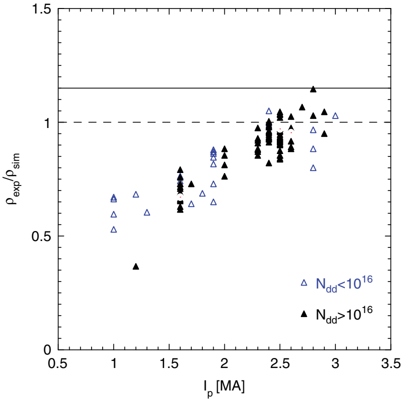

Figure 10. Ratio of experimental and simulated burn-up fractions for the same plasma discharges as in figure 7 plotted versus plasma current. Open and full triangles are for total 2.5 MeV neutron yields below and above 10^{16} neutrons, respectively. The circles mark the three discharges used as examples throughout this paper. The dashed line marks the unity ratio expected under conditions of perfect triton confinement. The full line marks the level expected due to contamination from residual tritium (see text).

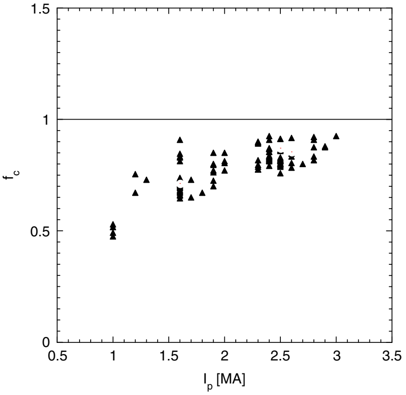

Figure 11. Confined fraction of tritons according to first orbit simulations for the same plasma discharges of figure 7 plotted versus plasma current. The symbols have the same meaning as in figure 10.

The thermal component has been observed to decrease with time over the 6 year period following the DT-experiments in 1997 (see figure 13). The trend is in agreement with results from the residual gas analyzer [25]. The TBN/(thermal+TBN) ratio for this data set is $\eta = 0.68$. In other words, about one-third of the 14 MeV neutron emission was not due to the triton burn-up in the time period of these measurements.

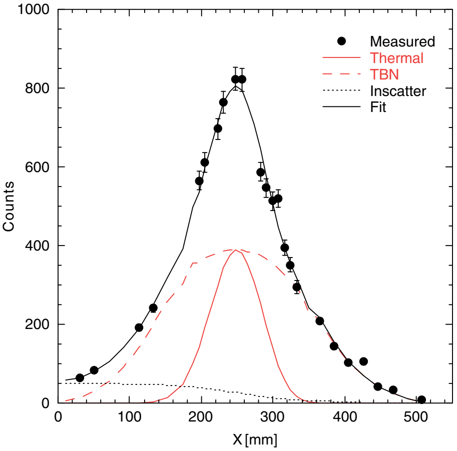

Figure 12. Analysis of the neutron spectrum for an inclusive set of plasma discharges (see text). The fitted line is the sum of a broad component from the triton burn-up (TBN) and a narrow component due to residual tritium (thermal). There is also a third low energy component. The TBN/(thermal+TBN) ratio is $\eta = 0.68$.

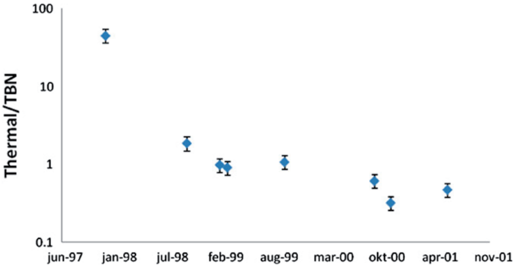

Figure 13. The time evolution of the JET residual tritium (thermal) concentration after DTE1.

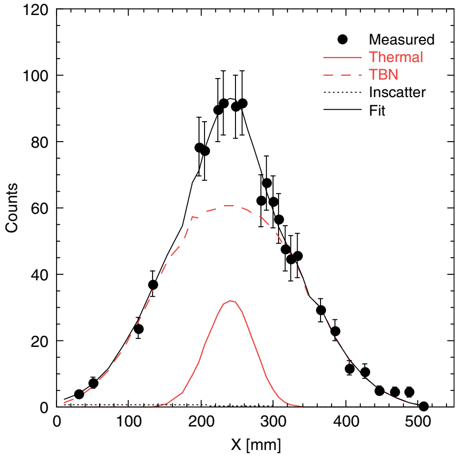

Figure 14. Same as figure 13 but for a set of selected plasma discharges with $Z_{\text{eff}} < 2.5$ (see text). The TBN/(thermal+TBN) ratio is $\eta = 0.85$.

This thermal component is an important contribution to the total 14 MeV rate. Therefore, a detailed investigation is undertaken and presented in figure 14, where the neutron spectrum obtained by adding up data from discharges belonging to the data set of the triton burn-up analysis is shown. The statistics is worse but sufficient to prove that the residual tritium emission is about 15%. This is about a factor of 2 lower than the average value for that period, which could be explained if we assume that plasmas with higher Z_{eff} have also a higher content of residual tritium. The triton burn-up data set has $Z_{\text{eff}} < 2.5$ and a 15% neutron yield from residual tritium, whereas higher average values of both Z_{eff} and residual tritium are found in the enlarged data set. No other evidence of a correlation of the residual tritium content with plasma operation and conditions has previously been reported.

The 15% average contamination level of the 14 MeV yield from residual tritium must be included in the triton burn-up analysis of the previous section. Actually one wonders how a 15% contribution can go undetected in the time trace analysis. Indeed the TBN (from burn-up) and thermal (from residual tritium) 14 MeV yields have different time traces. The TBN is delayed relative to the 2.5 MeV emission whereas the thermal 14 MeV emission should more or less follow the 2.5 MeV neutron time trace. This should provide a way, independent of neutron spectrometry, to separate the two neutron emission components. It turns out that the sensitivity level of the time trace analysis is not good enough. Figure 15 shows an expanded view of the measured and simulated 14 MeV yield for JET plasma discharge #52958 (from figure 5). Also shown is the simulated 14 MeV time trace for a model case where 30% of the total 14 MeV neutron emission is assumed to be thermal. As one can see, a 30% admixture would be detectable, whereas a 15% admixture gives a time trace (not shown) that is practically undistinguishable from the pure TBN case.

The effect of an average 15% residual tritium contribution to the 14 MeV yield is to raise the ‘perfect agreement’ line in figure 7 to the level marked by a full line. With this effect taken into account the data show that the experimental TBN yield is roughly half of what is expected at $I_{\text{p}} = 1$ MA and approaches the expected value at the highest currents. This is in fair agreement with the f_{c} trend of figure 11.

A more quantitative comparison of the current dependences seen in figures 10 and 11 is obtained by introducing a corrected burn-up fraction $\rho'_{\text{exp}} = (N_{\text{dt}}/N_{\text{dd}}) \cdot \eta$ and the corresponding simulated quantity $\rho'_{\text{sim}} = \rho_{\text{sim}} \cdot f_{\text{c}}$. The ratio $\rho'_{\text{exp}}/\rho'_{\text{sim}}$ is shown in figure 16. The ratio is convincingly close to unity at high current. At lower currents the data are scattered but suggest $\rho'_{\text{exp}} < \rho'_{\text{sim}}$ by 10–20% (although $\rho'_{\text{exp}}/\rho'_{\text{sim}} = 1$ is not incompatible with the data given the large uncertainties). Neoclassical triton losses [21] are a likely mechanism for additional reduction of TBN at low currents. Is it also possible that some additional losses of tritons at low current could be due to MHD activity such as those described in [16] and [26]. However there was no obvious difference in the MHD behaviour in these discharges compared with those

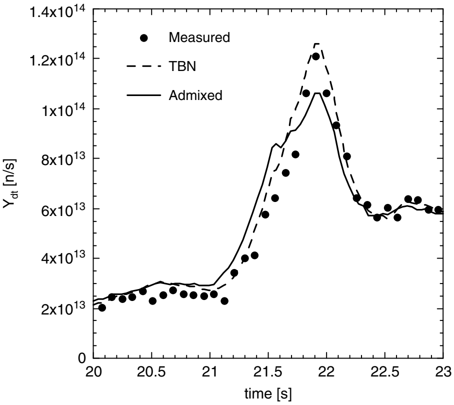

Figure 15. Expanded view of the measured and simulated 14 MeV yield for JET plasma discharge #52958 (from figure 5). Also shown is the simulated 14 MeV time trace for a model case where 30% of the total 14 MeV neutron emission is due to residual tritium. The total 14 MeV yield is the same in both simulations.

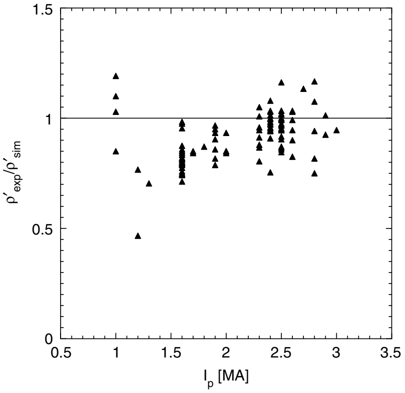

Figure 16. The ratio $\rho'_{\text{exp}}/\rho'_{\text{sim}}$ for the same plasma discharges of figure 7 plotted versus plasma current. Here $\rho'_{\text{exp}} = \rho_{\text{exp}} \cdot \eta$ and $\rho'_{\text{sim}} = \rho_{\text{sim}} \cdot f_c$ where $\rho_{\text{exp}} = N_{\text{dt}}/N_{\text{dd}}$ and ρ_{sim} are the (uncorrected) experimental and simulated burn up fractions, respectively, $\eta = 0.85$ is a correction factor for residual tritium and f_c is the confined fraction of tritons from MCOrbit simulation.

with standard confinement. They were normal sawtoothing discharges with moderate levels of MHD fluctuations and no detectable levels of fishbone or Alfvén instabilities.

One should also bear in mind the limitations introduced by the model assumptions. In particular, the assumption of uniform triton losses across the plasma seems questionable with a 50% loss level. This, however, cannot explain a $\rho'_{\text{exp}} < \rho'_{\text{sim}}$ result because the burn-up probability is larger in the (hotter) plasma core. Hence, the model tends to underestimate the TBN emission, which leads us to believe that there may indeed be additional triton losses at a level that is best investigated by a more sophisticated model than the one used in the present analysis.

The uncertainty associated with ρ_{sim} is dominated by the uncertainty in the input parameters in the model calculations. Besides the 15–20% uncertainty due to Z_{eff}, the determination of T_e also gives an 10% uncertainty. ρ_{exp} is dominated by the 10% systematic uncertainty in the calibration of the silicon diodes.

6. Discussion

The work has shown that there are significant losses of tritons at low currents. At currents of 3 MA about 10% of the tritons are lost and losses of 60% were observed at 1 MA current. This loss reduces the plasma heating with the same amount indicating that operations at low currents will effectively reduce the alpha heating. At currents >2.2 MA, there is no evidence of non-prompt losses; for smaller currents other loss-mechanisms could not be excluded. Mechanisms responsible for such losses could be, for example, field ripple diffusion, MHD activity or large angle Coulomb scattering. The non-prompt loss-levels at JET are small in comparison with what has been observed at TFTR [7].

In general, the uncertainties associated with the triton burn-up method are to a large degree given by the uncertainties in the input parameters. One major uncertainty contributor is the difficulty in determining the deuterium density, due to large uncertainties in Z_{eff}. Previously, experiments have shown that the deuterium density can be determined using neutron spectroscopy [27].

7. Conclusion

The 14 MeV neutron emission from H-mode deuterium discharges with $Z_{\text{eff}} < 2.5$ and plasma currents $1 < I_p < 3$ MA has been studied on the basis of all neutron diagnostics available on JET. A simplified model for triton burn-up neutron (TBN) emission has been used and provides an adequate description of the 14 MeV emission. Prompt (first orbit) triton losses are found to amount to typically 50%, 20% and 10% at $I_p = 1$ MA, 2 MA and 3 MA, respectively. Below 2 MA additional losses (such as due to 'neoclassical' Coulomb collisions) could also play a role and should be investigated theoretically.

These results verify findings from machines other than JET, but also highlight the possibilities offered by neutron measurements to supply information outside their traditional field of study. In particular, the ability of a high-resolution neutron spectrometer to separate the triton burn-up and residual triton neutron emission components is useful in this context. Measurements with the MPR spectrometer have detected a contribution to the 14 MeV emission due to residual tritium. It is found that its concentration increases with the increasing impurity content being at the 15% level for the selected (low Z_{eff}) discharges analysed in this paper. This level does not preclude a useful triton burn-up analysis. For the higher Z_{eff} values frequently observed in JET the triton burn-up analysis faces a number of difficulties and more direct approaches (see, for example [28]) for fast ion studies should be considered, which are not dependent on the detailed knowledge of the tritium contamination of the plasma and the deuterium density ratio.

Acknowledgment

This work was carried out within the framework of the European Fusion Development Agreement.

References

[1] Heidbrink W W and Sadler G J 1994 *Nucl. Fusion* **34** 535
[2] Isobe M *et al* 1997 *Nucl. Fusion* **37** 437
[3] Jarvis O N 1997 *Plasma Phys. Control. Fusion* **39** 1571
[4] Nishitani T 1996 *Plasma Phys. Control. Fusion* **38** 355
[5] Tobita K 1997 *Nucl. Fusion* **37** 1583
[6] Strachan J D *et al* 1996 *Nucl. Fusion* **36** 1189
[7] Barnes C W *et al* 1998 *Nucl. Fusion* **38** 597
[8] Kallne J *et al* 1988 *Nucl. Fusion* **28** 1291
[9] Conroy S *et al* 1988 *Nucl. Fusion* **28** 2127
[10] Heidbrink W W *et al* 1983 *Nucl. Fusion* **23** 917
[11] Strachan J D *et al* 1986 Basic physical processes of toroidal fusion plasmas *Proc. Workshop (Varenna, 1985)* vol 2 (Brussels: CEC) p 699
[12] Batistoni P, Martone M, Pillon M, Podda S and Rapisarda M 1987 *Nucl. Fusion* **27** 1040
[13] Pillon M and Vannucci P 1987 *Nucl. Instrum. Methods* A **255** 188
[14] Stix T H 1972 *Plasma Phys.* **14** 367
[15] Gorini G, Ballabio L and Källne J 1997 *Plasma Phys. Control. Fusion* **39** 61
[16] Duong H H and Heidbrink W W 1993 *Nucl. Fusion* **33** 211
[17] Frenje J *et al* 1998 *Plasma Phys. Control. Fusion* **40** 1211
[18] Ballabio L *et al* 2000 *Nucl. Fusion* **40** 21
[19] Gorini G, Batistoni P, Bittoni E, Kallne J, Podda S and Taroni A 1987 *JET Report JET*-P(87) (Abingdon, Oxfordshire: JET Joint Undertaking) p 35
[20] Ballabio L, Kallne J and Gorini G 1998 *Nucl. Fusion* **38** 1723
[21] Yavorskij V *et al* 2003 *Nucl. Fusion* **43** 1077
[22] Elevant T *et al* 1986 *Rev. Sci. Instrum.* **57** 1763
[23] Bertalot L *et al* 1999 *Rev. Sci. Instrum.* **70** 1137
[24] Ericsson G *et al* 2001 *Rev. Sci. Instrum.* **72** 759
[25] Andrew P *et al* 1999 *J. Nucl. Mater.* **266–269** 153
[26] Marcus F B *et al* 1994 *Nucl. Fusion* **34** 687
[27] Olsson M *et al* 1993 *Plasma Phys. Control. Fusion* **35** 179
[28] Zweben S J *et al* 1995 *Nucl. Fusion* **35** 893